UCRL-ID-123306

RECEIVED
JUN 24 1996
OSTI

Soft X-Ray Generation in Gases with an Ultrashort Pulse Laser

T. R. Ditmire

January 8, 1996

Lawrence Livermore National Laboratory

This is an informal report intended primarily for internal or limited external distribution. The opinions and conclusions stated are those of the author and may or may not be those of the Laboratory.
Work performed under the auspices of the U.S. Department of Energy by the Lawrence Livermore National Laboratory under Contract W-7405-Eng-48.

MASTER

DISTRIBUTION OF THIS DOCUMENT IS UNLIMITED

DISCLAIMER

This document was prepared as an account of work sponsored by an agency of the United States Government. Neither the United States Government nor the University of California nor any of their employees, makes any warranty, express or implied, or assumes any legal liability or responsibility for the accuracy, completeness, or usefulness of any information, apparatus, product, or process disclosed, or represents that its use would not infringe privately owned rights. Reference herein to any specific commercial product, process, or service by trade name, trademark, manufacturer, or otherwise, does not necessarily constitute or imply its endorsement, recommendation, or favoring by the United States Government or the University of California. The views and opinions of authors expressed herein do not necessarily state or reflect those of the United States Government or the University of California, and shall not be used for advertising or product endorsement purposes.

This report has been reproduced
directly from the best available copy.

Available to DOE and DOE contractors from the
Office of Scientific and Technical Information
P.O. Box 62, Oak Ridge, TN 37831
Prices available from (615) 576-8401, FTS 626-8401

Available to the public from the
National Technical Information Service
U.S. Department of Commerce
5285 Port Royal Rd.,
Springfield, VA 22161

Soft X-Ray Generation in Gases

with an Ultrashort Pulse Laser

by

Todd Raymond Ditmire
BA Harvard University, 1991
MS University of California, Davis, 1993

DISSERTATION

Submitted in partial satisfaction of the requirements for the degree of

DOCTOR OF PHILOSOPHY

in

Applied Science

in the

GRADUATE DIVISION

of the

UNIVERSITY OF CALIFORNIA

DAVIS

Approved:

Committee in Charge

1995

Soft X-Ray Generation in Gases

with an Ultrashort Pulse Laser

Copyright © 1995

by

Todd Raymond Ditmire

The Government reserves for itself and others acting on its behalf a royalty free, nonexclusive, irrevocable, world-wide license for governmental purposes to publish, distribute, translate, duplicate, exhibit, and perform any such data copyrighted by the contractor.

Acknowledgments

The work described in this thesis represents the results of collaborations with many people, all of whom I owe a great debt of gratitude. I have had a unique opportunity as a graduate student to work with some of the best scientists in the field and I have learned and benefited from all of them.

First I want to thank Mike Perry. Mike has aided me through my graduate career in too many ways to summarize here. I have learned many things, both in science and otherwise, from Mike. Mike was a very strong supporter of me and my efforts from the earliest days in his group, and I immensely value his support, suggestions and complements. Mike is also to be lauded for supplying me with a world class atmosphere to do physics. He has gone beyond the call of duty in providing me with intellectual as well as physical resources that are unparalleled for most graduate students.

Next, I need to thank the many other people I have had the opportunity to work with while at Livermore. I have had a gratifying experience working with many high quality, talented people over the last four years. I owe much of my laboratory skills to Donna Strickland who showed great patience with me as an eager and inexperienced young graduate student. I want to thank Hoang Nguyen for aid in the construction of the LiSAF laser as well as the many other tasks he performed during my experiments. I also greatly appreciated the assistance of Russ Jones. I enjoyed working with John Crane and always appreciated his input on experiments and papers. Sasha Rubenchik has been

very helpful to me and I want to thank him for his theoretical assistance. I have had a very enjoyable time working with Tom Donnelly over the last year. His assistance in the lab was much appreciated and his presence added a bit of joviality (and cynicism) to our toils in the lab that was lacking prior to his arrival.

Finally I want to thank my parents and my wife Nancy. I owe a great debt to my parents, who supported and fostered my interest in science and things scholarly from my youth. Most of all, I want to thank Nancy for many things. Nancy exhibited unparalleled patience with me during the last four years. I am deeply in debt to her for her endless assistance and support.

Todd Ditmire
December 1995
Applied Science

Soft X-Ray Generation in Gases

with an Ultrashort Pulse Laser

Abstract

An experimental investigation of soft x-ray production resulting from the interaction of intense near infra-red laser radiation with gases is presented in this thesis. Specifically, soft x-ray generation through high order harmonic generation or exploiting intense inverse bremsstrahlung heating is examined. Most of these studies are conducted with a femtosecond, terawatt class Cr:$LiSrAlF_6$ (LiSAF) laser, though results derived from studies with other laser systems are presented as well. The majority of this work is devoted to experimental investigations, however, theoretical and computational models are developed to interpret the data. These studies are motivated by the possibility of utilizing the physics of intense laser/matter interactions as a potential compact source of bright x-rays. Consequently, the thrust of many of the experiments conducted is aimed at characterizing the x-rays produced for possible use in applications.

In general, the studies of this manuscript fall into three categories. First, a unique 130 fs, 8 TW laser that is based on chirped pulse amplification, is described, and its performance is evaluated. In particular, a detailed analysis of flashlamp pumping large aperture (> 1 cm) LiSAF amplifiers is given. The effects of pulse propagation of laser pulses in chirped pulse amplifier lasers is also carefully examined and modeled.

The generation of x-rays through high order harmonics is then discussed with emphasis on characterizing and optimizing harmonic generation. These studies include

an examination of the wavelength range attainable with harmonics, the spatial profiles of the harmonics, the spectral linewidths of the harmonics, and the energy yields of the harmonics.

Finally, the generation of strong, incoherent x-ray radiation by the intense irradiation of large (> 1000 atom) clusters in gas jets, is explored. The physics of laser energy absorption by clusters illuminated with intensities of 10^{15} to 10^{17} W/cm^2 is considered in detail. X-ray spectroscopy of the hot plasmas that result from the irradiation of the clusters is conducted, and energy transport and kinetics issues in these plasmas are discussed.

Table of Contents

Acknowledgments ..... **iii**

Abstract ..... **v**

Table of Contents ..... **vii**

I Introduction **1**

I.1 Short Pulse Lasers and Intense Laser/Atom Interactions 1

I.2 High Field Physics and the Breakdown of Perturbation Theory 3

I.3 Tunneling Ionization and Quasi-Classical Electrons 5

I.4 Energetic Electrons and Soft X-Ray Production 7

I.5 Motivation and Plan of the Thesis 10

II Design and Performance of a Multi-Terawatt Cr^{3+}:$LiSrAlF_6$ Laser **12**

II.1 Chirped Pulse Amplification and Design of a Terawatt Laser 12

II.2 Advantages of Cr:$LiSrAlF_6$ in Femtosecond Chirped Pulse Amplification Systems 16

II.3 Design and Performance of the Cr:LiSAF Laser System 18

II.3.A Laser Front End 18

II.3.B Ring Regenerative Amplifier 20

II.3.C Power Amplifier Chain Design and 9.5 mm LiSAF Amplifier Performance 25

II.3.D Performance and Modeling of the 19 mm LiSAF Amplifier 31

II.3.E Pulse Recompression and Focused Brightness 41

II.4 Modeling the Propagation of Stretched Pulses in Chirped Pulse Amplification 44

II.4.A Theory of Stretched Pulse Propagation Through the Amplifier Chain 44

II.4.B Gain Saturation Effects 49

II.4.C Self Phase-Modulation Effects 57

II.5 Conclusion 64

III. Physics of the Interaction of Short, Intense Laser Pulses with Atoms in a Gas 66

III.1 Strong Field Laser-Atom Interactions and the Ponderomotive Potential 66

III.2 High Order Harmonic Generation: Laser Driven Oscillations in Atoms 68

III.2.A Nonlinear Polarization of Strongly Driven Atoms 68

III.2.B Quasi-Classical Model of Strong Field Harmonic Generation 71

III.2.C Propagation Equations in the Weak Field Limit 75

III.3 Plasma Formation During the Intense Irradiation of a Gas 77

III.3.A Tunnel Ionization of Atoms in a Strong Laser Field 78

III.3.B Other Ionization Mechanisms 84

III.3.C Plasma Formation Effects on the Propagation of a Short Pulse Through a Gas 84

III.4 Heating Mechanisms in an Optically Ionized Plasma 92

III.4.A Heating During Ionization: Above Threshold Ionization 93

III.4.B Heating by Driving Plasma Waves: Stimulated Raman Scattering 97

III.4.C Heating Through Coulomb Collisions: Inverse Bremsstrahlung 113

III.5 Conclusion 127

IV Studies and Characterization of Coherent X-Ray Production By High Order Harmonic Generation 128

IV.1 Harmonic Generation: Overview of Experimental Aspects 128

IV.1.A Harmonics as a Source of Coherent X-Rays 128

IV.1.B Experimental Studies of Harmonic Generation 130

IV.2 Accessible Wavelength Range With High Order Harmonics 133

IV.3 Spatial Distribution Properties of the High Order Harmonics 136

IV.3.A Studies of Harmonic Spatial Profiles at Intensity Around the Saturation Intensity 136

IV.3.B The Effects of Plasma Formation on the Harmonic Spatial Distributions 146

IV.4 Linewidths and Blueshifting of the Harmonics 152

IV.5 Energy Yield and Conversion Efficiency Measurement of Harmonics Produced by the 600 fs Nd:glass Laser 157

IV.5.A Experimental Scheme for Harmonic Energy Yield Measurements 157

IV.5.B Energy Yield Comparison Between 1053 nm and 526 nm Laser Light 159

IV.5.C Energy Yield Comparison Between Harmonics Produced in Ne and He at 526 nm 162

IV.5.D Energy Yield Variation with Focal Geometry 164

IV.5.E Energy Yields and Conversion Efficiency as a Function of Peak Laser Intensity 166

IV.6 Theoretical Calculations of Harmonic Energy Yields 167

IV.6.A Harmonic Yield Model Description 167

IV.6.B Comparison of the Harmonic Yield Calculations with the Energy Measurements 173

IV.7 Harmonics in Applications: High Order Harmonics Used in Photoionization Studies 177

IV.8 Amplification of a Harmonic in a Ga X-Ray Laser 183

IV.8.A X-Ray Lasers as Amplifiers for Harmonics 183

IV.8.B Experimental Set-Up 184

IV.8.C Harmonic Amplification Experimental Results 187

IV.8.D Harmonic Gain Analysis 191

IV.9 Conclusion 193

V Strong X-Ray Production from Plasmas Produced By the Intense Irradiation of Atomic Clusters 194

V.1 Introduction and Background 194

V.2 Cluster Formation in a Gas Jet 197
V.3 The Theory of Short Pulse Laser Interactions with Clusters 199
V.3.A Ionization Mechanisms within the Cluster 200
V.3.B Cluster Heating Mechanisms 203
V.3.C Cluster Expansion Mechanisms 207
V.3.D Electron-Ion Thermalization in the Cluster 212
V.4 Numerical Modeling of the Laser-Cluster Interaction 212
V.5 Properties of an Underdense Plasma Heated by Laser Irradiation of Clusters 222
V.5.A X-Ray Emission Mechanisms 223
V.5.B Plasma Cooling Mechanisms 224
V.6 Experimental Apparatus 227
V.7 Cluster Condensation Onset and Size Measurement by Rayleigh Scattering 231
V.7.A Experimental Set-Up 231
V.7.B Rayleigh Scattering Results in the Mach 8 Gas Jet 232
V.8 Soft X-Ray Emission Characteristics of the Various Gases 234
V.9 Helium/Cluster Mixture Emission Characteristics 240
V.9.A Lyman α Enhancement with Clusters 240
V.9.B Lyman α Backing Pressure Dependence 243
V.9.C Lyman α Time History 243
V.10 50 - 100 Å Emission in Krypton 247
V.11 Short Wavelength Emission in Argon 251
V.12 Prepulse Experiments 255
V.12.A Fast Time History of Kr Emission With and Without a Prepulse 256
V.12.B Cluster Emission Control with a 14 ns Prepulse 256
V.13 X-Ray Yields for Long and Short Pulses 261
V.14 Conclusion 263

VI Conclusion and Future Directions 264
VI.1 Summary 264
VI.2 Future Directions 266

VI.2.A High Average Power Short Pulse Lasers 266

VI.2.B Time Resolved Probing of Plasma Kinetics with Harmonics 268

VI.2.C High Average Power Cluster Based Soft X-Ray Source 269

VI.3 Conclusion 271

References **272**

Chapter I

Introduction

I.1 Short Pulse Lasers and Intense Laser/Atom Interactions

The interaction of electromagnetic radiation with matter represents one of the fundamental aspects of modern physics. Studies of these interactions range from the scattering of high energy gamma rays off of elementary particles and nuclei to the propagation of very low frequency radio waves through low density plasmas in the ionosphere. The invention of the laser in 1960 permitted the study of light interactions with matter with very high photon densities and high electric field strengths [120]. The observation of the first multiphoton phenomena followed shortly after this invention with the demonstration of second harmonic generation [66]. This experiment marked the beginning of a long quest to find ways to efficiently generate short wavelength radiation with optical frequency lasers.

The progress made in laser technology in the last ten years has made possible the generation of intensities in which the laser electric field becomes comparable to the electric field felt by an electron in an atom. This accesses a new regime of exotic laser-matter interaction physics [152]. These intensities have become possible through rapid advancement of ultra-short pulse laser technology. Amplification of pulses of less than 1 ps in duration permits the generation of very high brightness with modest energy. The technology of short pulse, high brightness lasers, which was developed at first using dye

lasers [132], was accelerated dramatically in 1985 with the first demonstration of chirped pulse amplification (CPA) [182].

Prior to the development of CPA the energy of short laser pulses was limited by the high peak powers associated with the short pulse duration. High peak power can result in self-focusing which may damage the laser. The peak power density of lasers directly amplifying a pulse are limited to less than a few GW/cm^2. The technique of chirped pulse amplification circumvents this problem. By stretching a short pulse before amplification, the pulse can be safely amplified to energies far above that which would be possible if the short pulse is amplified directly. The pulse is then recompressed after amplification. The use of CPA extended the technology of short pulse lasers to peak powers of above a TW (10^{12} W) on a "table-top" scale [152].

The advent of new laser materials during the last ten years has extended the technology of these terawatt CPA systems to laser pulse widths of 100 fs or shorter. Focused intensity of $>10^{18}$ W/cm^2 is routinely achievable with this new class of ultra-short pulse lasers [152]. At these intensities the electric field of the laser is stronger than the characteristic atomic field and the interaction of such intense light with matter is dramatically different then the standard "weak field" interactions that have been studied through the majority of this century. Thus, the development of a femtosecond, terawatt class laser is strongly motivated by an ability to access exotic aspects of light-matter interactions. The development of such a system is described in this thesis.

The various exotic interactions accessed by this class of lasers are numerous. Perhaps one of the most important is the possibility of bright short wavelength generation through the interaction of the intense laser pulse with matter [116]. For example, it became clear in the early days of harmonic generation research that higher laser intensities would permit higher conversion efficiency of higher order harmonics of an optical frequency laser [162]. In fact it was found in the middle 1980's that with high enough intensities, and a clever choice of the medium for generating harmonics, producing light

with wavelengths extending down into the x-ray region is possible through optical harmonic generation [19, 126]. Since the development of terawatt class lasers, the possibility of producing bright, efficient x-rays with intense laser pulses has been an active field of investigation. It is the generation of x-ray radiation through the exploitation of the interaction of intense laser pulses with atoms in a gas that is the primary subject of this thesis.

I.2 High Field Physics and the Breakdown of Perturbation Theory

The first complication that arises in trying to understand these high field interactions and how they can be used to produce x-rays is that the classic perturbation theory description of the light interaction with atoms and free electrons breaks down at high intensity. This occurs because the strong laser field is no longer a small perturbation on the atomic system. In fact, at an intensity of 3 x 10^{16} W/cm^2 the peak laser field is equal to the characteristic atomic field of the hydrogen atom ($\sim e/a_0^2$). At intensity well above this, the electron motion is dominated not by the atomic nuclei but by the oscillating laser field. Clearly in this intensity regime all predictions made from a perturbative treatment of the light field will be incorrect.

One of the earliest manifestations of this non-perturbative behavior occurred in 1979 with the observation of above threshold ionization (ATI) [3]. In classic, perturbative multiphoton ionization of atoms in a laser field, a bound electron absorbs enough laser photons to liberate it from the atom. Perturbation theory predicts that the electron will then have kinetic energy equal to $q'\hbar\omega_0 - I_p$ where q' is the minimum number of photons required for ionization, $\hbar\omega_0$ is the energy of a single laser photon, and I_p is the atom's ionization potential. This is just a generalized multiphoton version of the

classic photoelectric effect. Perturbation theory predicts that electrons with kinetic energy corresponding to $q > q'$ will occur with exponentially decreasing probability. Studies of electron energies resulting from multiphoton ionization at intensity $>10^{13}$ W/cm^2 deviated from this prediction, however, with higher energy electrons, corresponding to the absorption of more than the minimum number of photons required for ionization, appearing with comparable probability to the lowest energy electrons [125, 68].

From the standpoint of short wavelength generation, a similar manifestation of this non-perturbative behavior occurs in the harmonic generation of the laser in gases. Perturbation theory predicts that increasingly higher order of harmonics (i.e. increasing multiples of the laser frequency) will be generated with exponentially decreasing efficiency. This behavior was observed initially [162] and even at high laser intensity holds true for the low order (q>7) harmonics [102]. However, a deviation from this behavior was first observed in 1987 when a high intensity 248 nm laser produced harmonics out to the 17th order in neon, a wavelength of 146 Å [126]. The harmonic spectrum produced exhibited an initial drop in efficiency with the first few orders out to the 9th order, and was then followed by a plateau in the harmonic orders in which the higher orders were all produced with comparable efficiency. This behavior was also observed with a 1064 nm laser soon afterwards [63, 111]. This non-perturbative behavior of the harmonics has been the subject of intense investigation since then by a number of groups around the world and is the subject of a large portion of this work. The greatest motivation of these studies is that these harmonics produced at high intensities may provide an efficient means of coupling laser light into soft x-rays.

Another important consequence of the non-perturbative nature of intense laser matter interactions on short wavelength generation is the large absorption of laser energy by free electrons in a plasma through scattering off of charged nuclei. When the laser field strongly drives electrons, their motion is dominated by the laser. The electron, however, absorbs no energy from the laser field. A perturbation on the electron motion by an

encounter with a charged nucleus can cause the electron to absorb laser energy. In strong laser fields, the electron can absorb many laser photons worth of energy in a single scattering event. This process is called multiphoton inverse bremsstrahlung [172]. Consequently, if the medium is of sufficient density that these scattering encounters occur frequently, this process can transfer large amounts of energy from the intense laser field to free electrons. Through a clever choice of medium and conditions these energetic free electrons can be exploited to produce x-rays in the plasma.

In some sense, both harmonic generation and inverse bremsstrahlung are similar in that they both involve the interaction of an electron, a charged nucleus, and an intense laser field to couple laser energy to electron energy. Both processes can be thought of as the absorption of many laser photons by an electron in the presence of a charged nucleus. In harmonic generation, the charged nucleus is the parent atom core; in the case of inverse bremsstrahlung the nuclei is one of the ions in a plasma. Both of these non-perturbative processes represent avenues to short wavelength generation. Though the manner in which short wavelengths are generated with each of these processes is quite different, the efficient coupling of laser energy to electrons is the common theme in their study.

I.3 Tunneling Ionization and Quasi-Classical Electrons

In the study of both of these processes we speak of multiphoton absorption by an electron from the laser field. As we have mentioned, however, the multiphoton picture of the laser matter interaction at high intensity is not strictly correct since it implies a lowest order perturbation theory approach to the problem. At optical frequencies and sufficiently high intensity the interactions can be more accurately described by quasi-classical interpretations. Keldysh was the first to recognize this transition from multiphoton interactions to a quasi-classical picture of the electron motion and interaction in the laser

field in the process of ionization of atoms by optical frequency light [86]. Keldysh demonstrated that at low intensity and high laser frequency, the ionization of atoms can be described as the absorption of many laser light photons by an electron in the Coulomb field of the parent ion. However, at low frequencies and high intensity, the ionization can be described by the tunneling of the bound electron wave packet out of the atomic binding potential that has been distorted by the strong laser field.

These two pictures of strong field ionization correspond to large and small values of the so-called Keldysh parameter, defined as [86]

$$\gamma = \omega/\omega_{tun} \tag{1.1}$$

Here ω is the laser oscillation frequency and ω_{tun} is the tunnel ionization frequency, the inverse of the characteristic time for an electron wave packet to tunnel out of the atomic potential. When the tunneling frequency significantly exceeds the optical frequency, (i. e. $\gamma << 1$) then tunnel ionization will predominate. Multiphoton ionization predominates in the other limit of γ. For the majority of the situations considered in this work, in which ionization is achieved with near infra-red wavelength lasers with intensity $> 10^{15}$ W/cm^2, the tunneling mechanism of ionization will predominate.

This regime of tunnel ionization suggests a very powerful simplification in the consideration of strong field interactions. The picture of an electron tunneling out of the atomic potential implies that we treat the electron as a wave packet with a well defined position. Another way to look at this interaction is to say that in the strong field limit ($\gamma << 1$) the electron motion is dominated by the laser field, not the atomic field. Tunnel ionization occurs when the laser field is strong enough to pull the electron free from the binding potential of the atom. In this case it is accurate to treat the trajectory of the electron classically. The validity of this assertion can be confirmed by considering the uncertainty relation

$$\Delta x \Delta p \sim \hbar \tag{1.2}$$

For an electron in a typical laser intensity of 10^{16} W/cm^2 the electron momentum oscillates from 0 to 2 x 10^{-18} g cm/s. Thus if $\Delta p = 2 \times 10^{-18}$ g cm/s, this implies that $\Delta x \sim .05$ Å which is, in general, much smaller that the size of an atomic orbital, characterized by the Bohr radius (0.53 Å). So it is a reasonable approximation to treat the electron as a particle (or more correctly a wave packet) of well defined position during the ionization process as well as after ionization in the laser field. This concept of quasi-classical electron motion can be exploited to simplify the calculations of both harmonic generation and inverse bremsstrahlung. These simplifications will be elaborated on later in the thesis.

I.4 Energetic Electrons and Soft X-Ray Production

Soft x-ray photons are those photons with energy from about 30 eV to about 1 keV. It is, therefore, natural to expect that we must impart energies of this order to electrons in order to generate these energetic photons in the encounters between electrons and ions. Since the oscillation energy of electrons in laser fields with intensity between 10^{15} and 10^{17} W/cm^2 corresponds to this energy range, it is clear that laser pulses in this intensity range will be advantageous in generating photons of these energies.

We can, for example, understand harmonic generation by considering the classical motion of electrons freed by tunnel ionization in the strong laser field. When an oscillating electron has a sizable amount of kinetic energy from the driving field upon its return to its parent nucleus after it is ionized, it can emit a harmonic photon of energy equal to the sum of its kinetic energy and the laser ionization potential. In strong laser fields the electrons can have sufficient energy to generate photons in the x-ray range. This concept of harmonic generation was first forwarded by Corkum [32] and Kulander et. al. [96].

Strong incoherent x-ray radiation is also possible in a medium if electrons of sufficient energy are present. Energetic electrons can either collisionally excite or collisionally ionize atoms in the medium [74]. If these collisional processes are rapid and the electrons have sufficient energy they will create high atomic charge states in which the resonance transitions occur in the x-ray range. Upper levels of ions can be populated by recombination or by collisional excitation [74]. Radiation from radiative decay of these upper levels results. Although the x-ray radiation is incoherent and emitted into all directions with equal probability, this mechanism provides an avenue to shorter wavelengths than are possible with harmonic generation. This mechanism of x-ray generation exploits the production of plasmas through inverse bremsstrahlung. Bright x-ray production using this approach over the last decade has been largely confined to solid targets heated to temperatures of ~ 1 keV [137, 29]. How collisional heating can be increased in a low density gas, however, making possible plasma temperatures sufficient for efficient x-ray generation, will be discussed at length in this thesis.

Finally, I would like to note that the collisional processes in a plasma with energetic electrons can also be exploited for coherent x-ray generation as well. Coherent x-ray production can be achieved in a hot plasma with a collisionally pumped X-ray laser [56]. Such a laser was first demonstrated at LLNL in 1985 in Se by Matthews and coworkers using the Novette laser [124]. The energy level scheme for such an x-ray laser is illustrated in figure I.1. In brief, a plasma must be heated to collisionally ionize the constituent atoms to a high charge state. The original laser utilized Ne-like ions. Recently Ni-like [117] and Pd-like schemes [110] have been demonstrated as well. Hot electrons collisionally excite both levels u and l from the ground state. Since the upper level is chosen such that it is not a dipole allowed transition to the ground state (3p-2p in the Ne -like case) and is therefore metastable while the lowest level is dipole allowed to the ground state (3s-2p in the Ne-like case) and therefore empties rapidly by radiative decay to

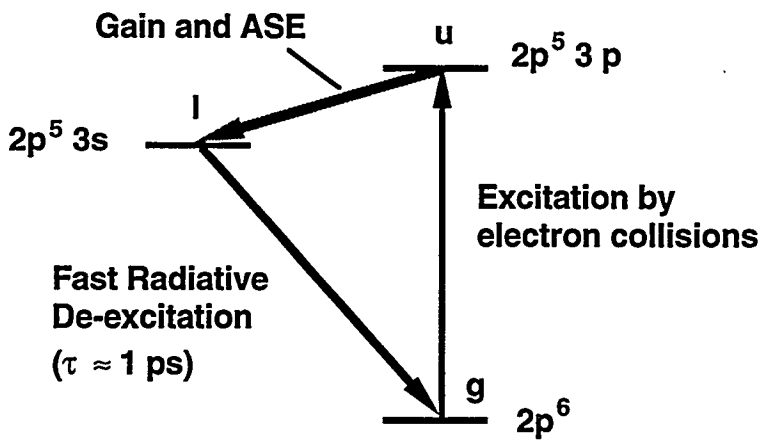

Figure I.1: Simplified energy level schematic of a collisionally pumped soft x-ray laser. The level designations are for the Ne-like scheme.

the ground state, an inversion between u and l naturally develops. For large Z atoms (Z > 8) this transition will occur in the x-ray range.

Using this approach, lasing has been demonstrated with wavelengths in the water window [118]. Furthermore, very high conversion efficiency from laser light to x-ray light has been achieved with these schemes when large (> 500 J) pump lasers heating a solid slab or foil target are used. Using this approach over 1 mJ of x-rays at 155 Å have been produced in a yttrium, Ne-like laser [40]. The use of such a collisionally pumped x-ray laser to amplify a harmonic of a picosecond laser will be described later in this thesis.

I.5 Motivation and Plan of the Thesis

The purpose of this thesis is to experimentally examine the coupling mechanisms between intense laser pulses in the near IR wavelength range to soft x-rays. Though the majority of this work is devoted to experimental investigations, theoretical work as well as extensive numerical modeling is included where appropriate to explain the physical

phenomena. These investigations are primarily aimed at understanding and characterizing the physics of soft x-ray generation by short, intense pulses in gases. However, an eye is always kept on the possibility of exploiting the process to optimize it for potential applications.

In general, the studies of this work fall into three categories. First, since experimental studies in intense field, x-ray generation require a terawatt class laser system, a unique 100 fs, terawatt class laser utilizing a novel amplifier material, Cr^{3+}:$LiSrAlF_6$ (LiSAF) has been developed and is described in this manuscript. The generation of x-rays through high order harmonics is then examined with emphasis on characterizing and optimizing the harmonic generation. Finally, the possibility of generating strong, incoherent x-rays at wavelengths shorter than possible with harmonics by utilizing the enhanced laser absorption exhibited by large atomic clusters, is explored. In the studies of both mechanisms of x-ray generation, the importance of electron collisional processes in the laser field are emphasized. The effects of plasma formation by optical ionization of atoms in the gas are explored in the context of both mechanisms of x-ray production. This exploration includes studies of plasma effects on the laser and its propagation through the gas, as well as studies of energy transport and kinetics issues in the plasma formed after the laser has passed through the medium.

The general plan of the manuscript is as follows. The presentation of results begins with chapter II in which the design, development and performance of the LiSAF laser is detailed. This chapter is followed by a chapter in which many of the physical principles described or alluded to in this chapter are put on a more quantitative footing. This includes tunnel ionization, the quasi-classical picture of harmonic generation and collisional inverse bremsstrahlung heating. This chapter investigates the importance of other heating mechanisms as well in the interaction of the intense pulse with the ionized gas as well as the effects of plasma formation on pulse propagation.

In chapter IV a detailed experimental investigation of strong field, high order harmonic generation is presented. This chapter describes a number of different experiments and descriptive models aimed at understanding the various characteristics of the soft X-rays generated. The chapter also includes a demonstration of the use of harmonics in an application experiment and a description of an experiment demonstrating the amplification of a harmonic in a collisionally pumped x-ray laser amplifier. Chapter V details an investigation of soft x-ray generation by plasmas produced when atomic clusters are irradiated with intensity from 10^{15} to 10^{17} W/cm^2. We experimentally and computationally explore the large laser absorption of these clusters and show that using clusters as a target is an efficient way to convert laser light into short wavelength x-rays. Chapter VI concludes the thesis, summarizing its results, and discussing potential directions and applications of this work.

Chapter II

Design and Performance of a Multi-Terawatt Cr^{3+}:$LiSrAlF_6$ Laser

II.1 Chirped Pulse Amplification and the Design of a Terawatt Laser

To achieve the intensities that are required to access the physical phenomena introduced in the last chapter it is necessary to construct a laser with peak power on the order of 1 TW. These peak powers can be easily achieved in table-top scale laser systems through the amplification of short (< 1 ps) pulses to moderate energies (0.1 - 10 J). To amplify pulses of this temporal width a gain medium of sufficient bandwidth is required. Previous to 1985, the most common manner of amplifying ultrashort pulses was in dye laser amplifiers [132, 151]. Dyes, however, are limited in their ability to produce pulse energy >100 mJ because of their low saturation fluence (~ 1 mJ/cm^2). Use of solid-state amplifier materials can solve this problem due to their much higher saturation fluence which ranges from 1 to 10 J/cm^2 depending on the material. Consequently, efficient energy extraction with output energy on the order of 1 J from an amplifier can be achieved with reasonably small aperture rods.

However, it is easy to see that the propagation of a short pulse at this energy fluence results in very high intensity. For example, a 100 fs at 0.1 J/cm^2 results in an intensity of 10^{12} W/cm^2. Not only will pulses of this intensity damage optics, but the

effects arising from the nonlinear refractive index of the materials in the amplifier chain will be very important. Small-scale self -focusing of perturbations on the beam, for example, can cause catastrophic damage in long amplifier rods for intensity > 1 GW/cm^2. The way to defeat this problem is through the utilization of the technique of chirped pulse amplification (CPA) [182]. In this technique, a short pulse is generated and stretched by a large factor, (typically 1000 - 10,000 times) before amplification in the laser chain. The peak power is now reduced to a safe level to permit the extraction of large energy from the amplifiers. After amplification the pulse is then recompressed. This stretching and compressing is achieved by inducing a large amount of dispersion on the pulse and reversing the dispersion after amplification to compress it.

Though the initial lasers designed around CPA used a fiber to chirp (and add bandwidth to) the initial pulse [121, 140], recently designed systems utilize ultrashort pulse oscillators, such as a Kerr lens mode-locked Ti:sapphire laser [176], to generate the initial pulse which is then dispersed directly with a pair of gratings. When this approach is used, one only needs a short pulse oscillator, a grating stretcher and a grating compressor to implement CPA in an amplifier chain. The original grating compressor design of Treacy can be generalized for use in both stretcher and compressor [186]. The stretching can be achieved with a pair of gratings and a pair of lenses designed in the configuration shown in figure II.1a. The compressing is accomplished with a second set of gratings in the configuration shown in figure II.1b. Inspection of the ray paths of the various wavelengths in figures II.1a and II.1b illustrate the way in which a broadband pulse may be stretched. In the compressor design, the blue light travels a shorter distance than the red light, inducing a negative chirp (i.e. canceling positive chirp). The stretcher utilizes a one-to-one telescope between the gratings to reverse the sign of the chirp, to make the initial chirp positive.

Large stretching ratios are possible, with ratios of ~10,000 having been demonstrated [169,183]. The effective time delay for a typical pulse can be estimated

(a)

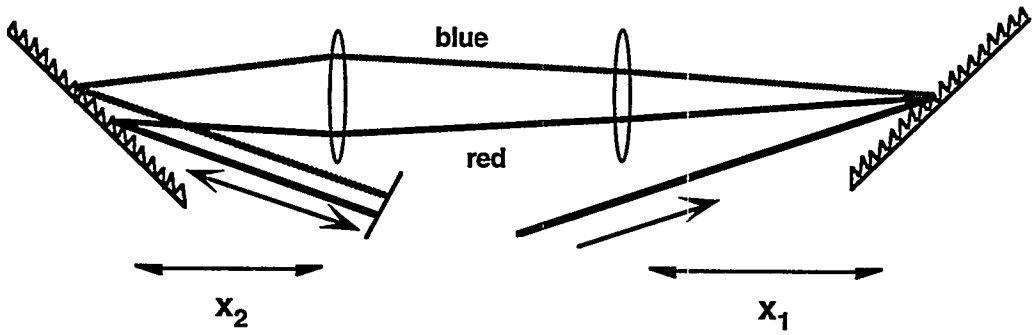

(b)

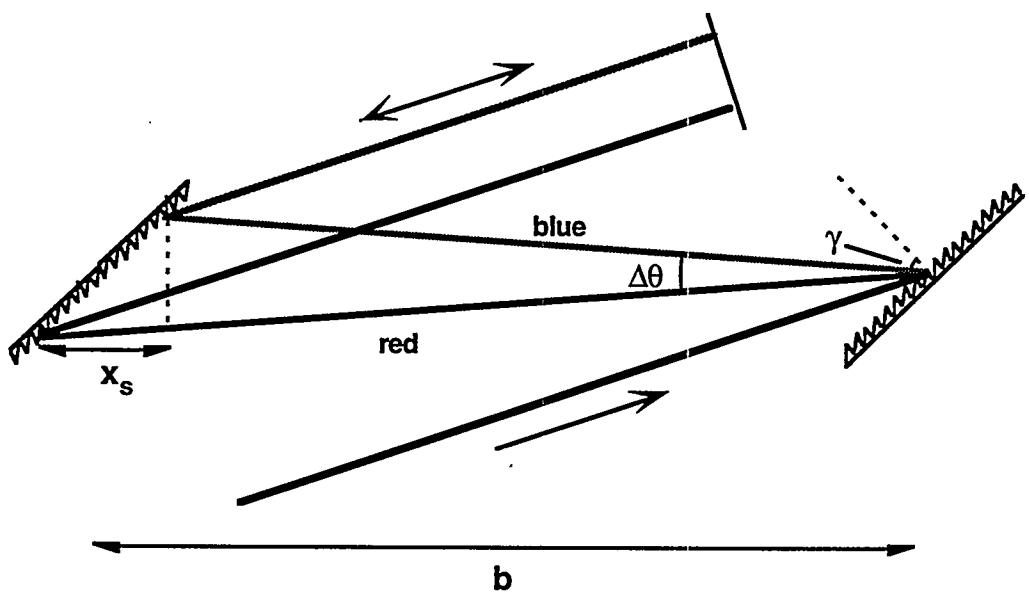

Figure II.1: **(a)** Optical layout of a two-grating, two lens pulse stretcher. **(b)** Optical layout of a two-grating pulse compressor.

from the geometry of the grating pair. First consider the case of the compressor grating pair (figure II.1b). The angular dispersion of the grating can be estimated from the grating equation, $m\lambda = d(\sin\gamma_{in} + \sin\gamma_{out})$:

$$\Delta\theta \approx \frac{\Delta\lambda}{d\cos\gamma} \tag{2.1}$$

where d is the grating line spacing, $\Delta\lambda$ is the laser pulse bandwidth, and γ is the angle of incidence on the grating (see figure II.1b for geometry). The time delay between red and blue frequency components for a double pass through the configuration is then given by

$$\begin{aligned} \tau_s &\approx 4x_s / c \\ &\approx \frac{4\Delta\lambda}{cd\cos\gamma\tan(\pi/2-\gamma)} b \end{aligned} \tag{2.2}$$

So to compress a 100 fs pulse ($\Delta\lambda = 90$ Å) at 825 nm that has been stretched to 500 ps with gratings of $d = (1800 \text{ lines/mm})^{-1}$ operated at the Littrow angle requires a grating separation, b, of ~ 1.4 m. Although this simple analysis implies that the compressor compensates the nearly linear chirp imparted by the stretcher, it can be shown that the dispersion of the stretcher configuration can be compensated to all orders of dispersion if the angles of the compressor gratings with respect to the input beam are the same as the angles of the stretcher gratings [186, 123].

The stretching factor can be determined from eq. (2.2) by using an appropriate effective grating separation, b. Simple ray tracing analysis shows that the effective grating spacing for the stretcher configuration, figure II.1a is

$$b_{eff} = 2f - x_1 - x_2 \tag{2.3}$$

where f is the focal length of the lenses and x_1 and x_2 are distances between the gratings and the lens closest to the respective grating.

II.2 Advantages of $Cr:LiSrAlF_6$ in Femtosecond Chirped Pulse Amplification Systems

To amplify broadband pulses that have been stretched requires an amplifier material that is itself of wide enough bandwidth to support the amplification of the initial pulse without any significant gain narrowing of the pulse spectrum. Any spectral narrowing results in recompressed pulses that are longer than the initial pulse. The choice of amplifier material will, consequently, be limited to those with large enough bandwidth for the desired pulse width.

The technique of CPA was first applied to picosecond Nd:glass based systems [121, 140, 170, 196]. The neodymium based systems are limited to pulse widths greater than approximately 500 femtoseconds at the terawatt level due to gain narrowing [153]. Recent systems using both Ti:sapphire and Nd:glass amplifiers have demonstrated multi-terawatt pulses with pulse width of < 400 fs [165]. Laser systems amplifying 100 fs pulses, however, require amplifier media of greater bandwidth than Nd:glass. The two solid state materials most promising for 100 fs chirped pulse amplification systems are Ti:sapphire [135] and $Cr:LiSrAlF_6$ [143]. The parameters of relevance for the design of

	Cr:LiSAF	**Ti:sapphire**	**Nd:glass**
Tuning Range (nm)	750 - 950	660 - 1100	1043 - 1063
Gain Cross Section (x 10^{-20} cm^2)	3.0	30	4.0
Saturation Fluence (J/cm^2)	7	0.8	4.9
Storage Lifetime (μs)	67	3.2	350
n_2 (x 10^{-13} esu)	.50	1.3	1.5
Thermal Diffusivity (cm^2/s)	.019	.15	.003

Table II.1: Comparison of the important properties of the amplifier materials commonly used in chirped pulse amplification.

CPA lasers for the three most commonly used materials in chirped pulse amplification are compared in Table II.1. For 100 fs lasers the most common material used is Ti:sapphire [91, 184]. Systems using Ti:sapphire with recompressed pulse widths a short as 30 fs have been demonstrated [10]. Though Ti:sapphire exhibits broad tunability, a large gain cross section and good thermal properties when compared to Nd:glass, the short upper state lifetime of Ti:sapphire (3.2 μs) requires rapid pumping most commonly achieved with a secondary pump laser (see table II.1). This limits the practical size of Ti:sapphire lasers, limiting their output to an energy of ≤ 0.25 J [184] unless a large scale, frequency doubled Nd based system is utilized for pumping, dramatically limiting the repetition rate and increasing the system complexity [191].

Cr:$LiSrAlF_6$, (Cr:LiSAF, or LiSAF), a material developed at LLNL [143], offers an important alternative to Ti:sapphire in the design of a femtosecond CPA laser. It has a broad emission cross section (tunable from 750 nm to 950 nm), comparable to Ti:sapphire. Unlike Ti:sapphire, however, LiSAF has a sufficiently long upper state lifetime (67 μs) to allow direct flashlamp pumping. Furthermore, the absorption spectra of LiSAF exhibits good overlap with the emission of most xenon flashlamps suggesting that high flashlamp pumping efficiency is possible. The ability to flashlamp pump LiSAF makes it an attractive candidate for compact table-top terawatt systems [179, 14] since it permits straightforward scaling to high output energy amplifiers through a simple scaling to large (>1 cm) aperture [49, 15, 48]. LiSAF also exhibits low nonlinear refractive when compared to Ti:sapphire, (see table II.1) minimizing deleterious nonlinear effects during amplification. Furthermore, the moderate thermal diffusivity ($\alpha = 0.019$ cm^2/sec) and low thermal lensing of LiSAF permits moderate repetition rates (= 1 Hz for a 1 cm diameter LiSAF rod and 0.05 Hz for a 19 mm rod [48]). For these reasons we have chosen to pursue the use of LiSAF in the design of our terawatt femtosecond laser.

Since it has become widely available, Cr:LiSAF has been demonstrated in many tunable and short pulse laser applications. LiSAF has been used in short pulse, mode

locked oscillators [57, 163]. A number of groups have demonstrated lasing with diode pumping [173]. Recently, use of diode pumped Cr:LiSAF in a self mode-locked oscillator was achieved [69]. Flashlamp pumped regenerative amplifiers have been demonstrated [154, 13], and the recent availability of large Cr:LiSAF crystals has made possible terawatt systems which include the use of a large energy storage Cr:LiSAF power amplifier to amplify the output of a Ti:sapphire system [190]. Pulse energy as high as 750 mJ has been demonstrated in a femtosecond Cr:LiSAF system employing a 25 mm diameter flashlamp-pumped amplifier [15]. This system utilized two 25x115 mm Cr:LiSAF rods placed end to end pumped with 5 kJ of electrical energy to produce a single pass gain of 2.4 with a maximum repetition rate of 1 pulse every 10 minutes.

In the following section the design of a system based solely on flashlamp pumped Cr:LiSAF amplifiers with increasing aperture up to 19 mm is described [51, 49, 48]. This system produces pulses with energy up to 1.7 J pulses before compression and yields compressed 130 fs pulses with energy > 1 J at a repetition rate of 0.05 Hz. This description is then followed by an analysis of propagation effects in chirped pulse amplification with particular emphasis on gain saturation and self-phase modulation effects. The effects that these phenomena have on the performance of the LiSAF system are then discussed.

II.3 Design and Performance of the Cr:LiSAF Laser System.

II.3.A Laser Front End

Shown in figure II.2, the system begins with a self mode-locked Ti:sapphire oscillator (Coherent Mira 900) which produces transform limited, 110 fs (full width at half maximum, FWHM) pulses of 5 nJ at 76 MHz ($\Delta\nu\Delta\tau = 0.38$). This pulse train is collimated with an f = 1.6 m lens and injected into a diffraction-grating pulse stretcher

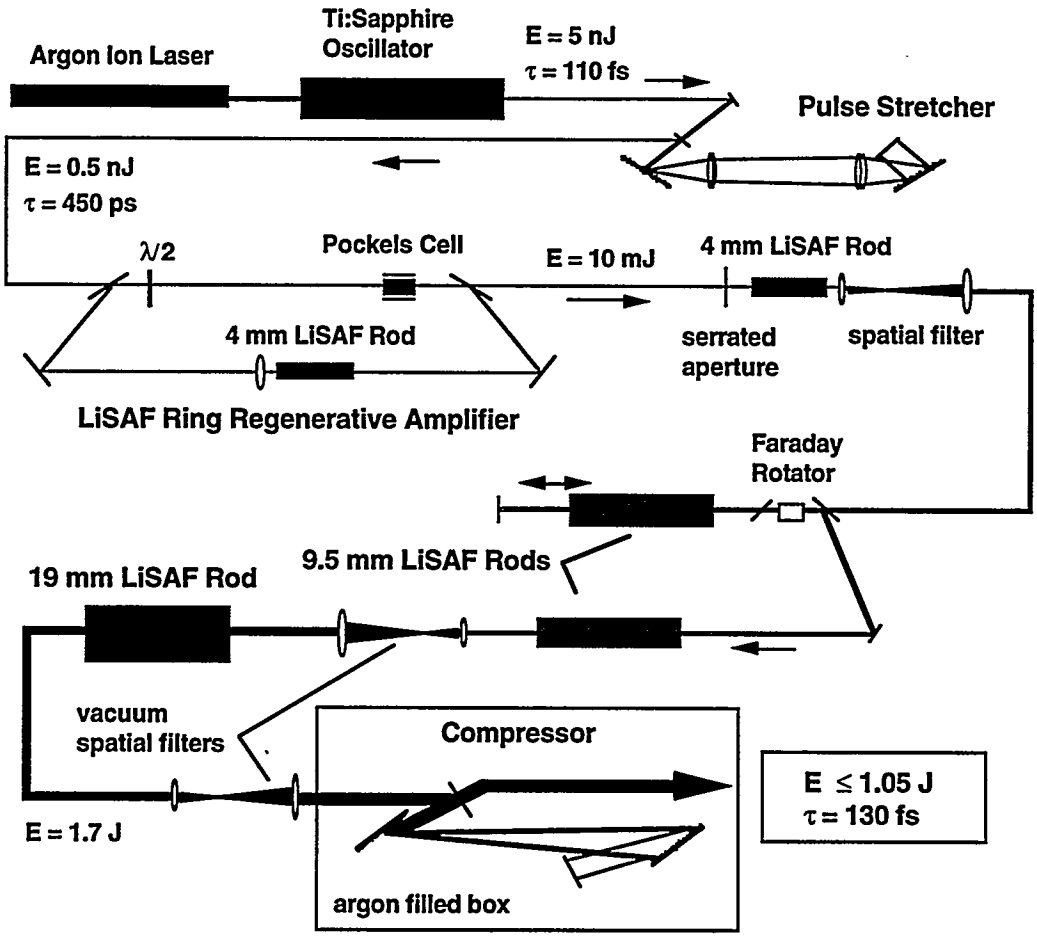

Figure II.2: Optical schematic of the Cr:LiSAF laser system.

based on the design of Martinez [123] like that shown in figure II.1a. This stretcher employs two 1800-line/mm gold coated holographic diffraction gratings and two 60-cm focal length cemented achromatic doublet lenses, corrected for spherical and chromatic aberration at 825 nm. The gratings reflect ~90% of the incident pulse energy into the first diffracted order. Each grating is located 25 cm on either side of the lens pair. Four passes through the stretcher produce enough positive group velocity dispersion to widen the pulses from 110 fs to 450 ps. The stretched pulse shape and pulse spectrum are shown in figure II.3. This 5000 x pulse stretching is necessary to avoid deleterious self focusing and self phase modulation in the amplifiers. The input pulse energy is reduced to 0.5 nJ due to losses on the gratings and other optics. Direct recompression of these stretched pulses result in pulses of 120 fs FHWM indicating that there is some small loss of spectral bandwidth in the stretcher. This small loss of spectrum is attributed to the finite aperture of the 10 cm diameter stretcher lenses.

II.3.B Ring Regenerative Amplifier

At this point the p-polarized pulses are injected into a ring regenerative amplifier cavity. The cavity employs broadband thin-film polarizers and a zero-order half-wave plate to provide a broad gain profile. The regenerative amplifier [154], (figure II.2) utilizes a single 4 mm x 50 mm flashlamp-pumped 2% doped Cr:LiSAF rod ($N_{Cr} = 1.9 \times 10^{20}$ cm^{-3}) as the amplifying medium. A single pulse is selected for amplification by applying half wave voltage (5800 V) to a KD^*P Pockels cell placed inside the cavity. Combined with the zero order half-wave plate, the trapped pulse experiences a full-wave retardation between the two polarizers while the Pockels cell is on. Dropping the voltage on the Pockels cell back to ground then cavity-dumps the amplified pulse after the desired number of round trips in the cavity. Timing synchronization with the Pockels cell is achieved with the use of a slow diode monitoring the pulse train from the self mode-locked Ti:sapphire oscillator. The output of the diode is amplified and passed through an

(a)

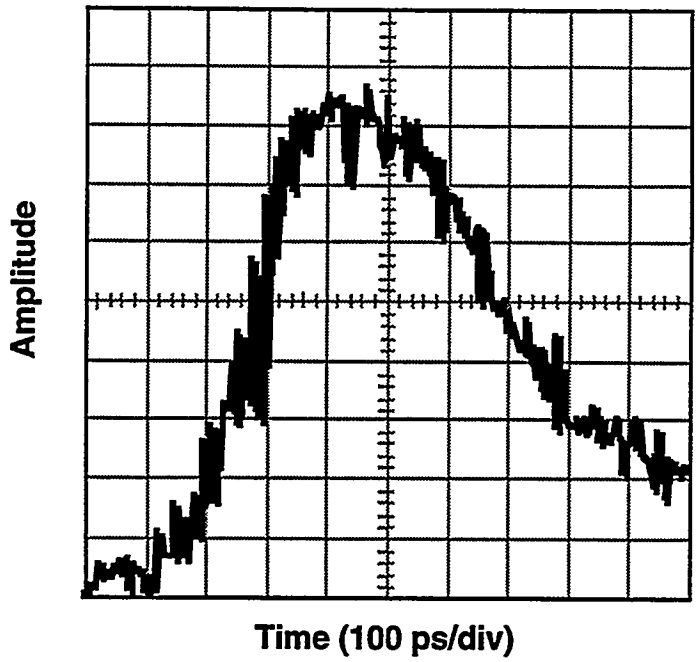

(b)

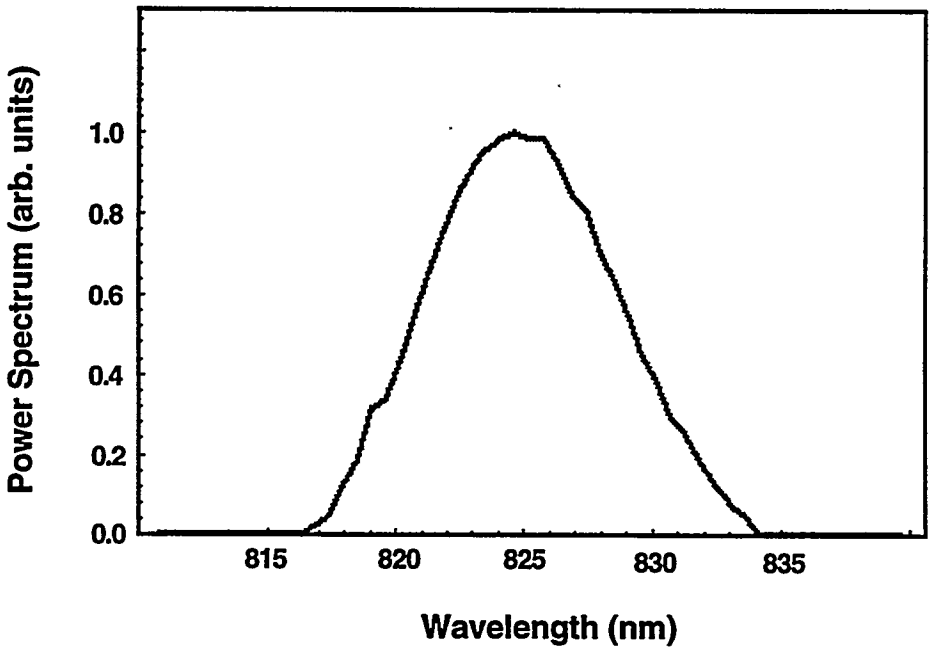

Figure II.3: **(a)** Stretched laser pulse monitored by a fast photo-diode and sampling oscilloscope. **(b)** Spectrum of the stretched pulse which seeds the regenerative amplifier.

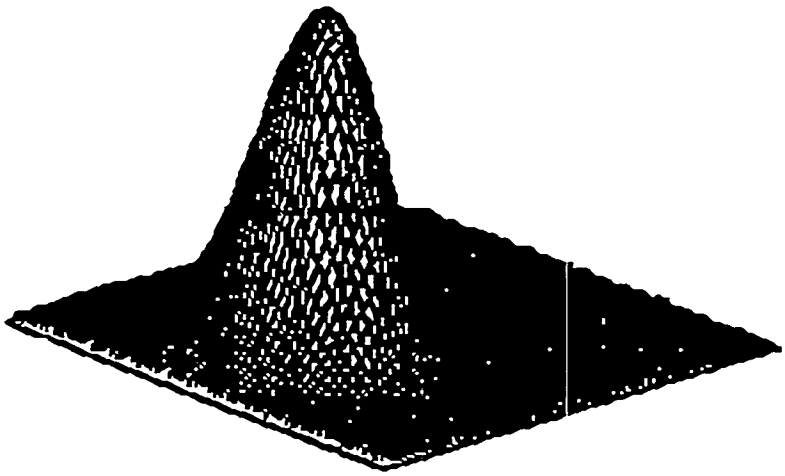

Figure II.4: TEM_{00} spatial profile of the 12 mJ output from the regenerative amplifier.

RF filter; a frequency scalar is used to fire the Pockels cell in phase with the RF to sub-nanosecond accuracy. The Pockels cell is triggered at the peak of the single pass gain in the LiSAF amplifier which follows the flashlamp light pulse.

The 4 m long ring cavity is TEM_{00} stable, defined by a 1.5 m lens and a 2 mm aperture in the cavity. This design is superior to the confocal design (where $l = 2f = 3$ m) since the 4 m cavity lies well within the cavity stability diagram ($g_1\, g_2 = 0.33$), and the effective spot size is larger inside the amplifier head than for the confocal design. Furthermore, the cavity exhibits lower divergence than the confocal design, desirable when one requires a large number of passes through polarization dependent elements. The ring configuration permits the easy use of polarizers in reflection upon each transit around the cavity, (a geometry in which broadband polarizers have better spectral characteristics), and it allows a longer cavity resulting in a larger Gaussian mode size. The mode size in the amplifier rod for our cavity is 1.9 mm (FW $1/e^2$), and the cavity divergence is .86 mrad. Mode discrimination is achieved by the insertion of a single hard aperture at the waist of the cavity. This aperture also serves to limit amplified spontaneous emission. The resulting output is a low divergence Gaussian mode, shown in figure II.4.

The LiSAF amplifier head is normally pumped by 60 J of electrical energy and exhibits a single pass gain of 2.8. The single pass gain as a function of pump energy in this amplifier is shown in figure II.5. The measured gain corresponds to a pump efficiency of 2.4% from electrical to stored energy with 60 J of electrical pump energy. Although we have safely achieved 20 mJ from this regenerative amplifier, it is normally run with an output of 10 to 12 mJ. Cavity losses reduce the net round-trip gain in the cavity to 1.5, making 36 round trips necessary to achieve the total net gain of 5×10^6.

Gain narrowing in the LiSAF regenerative amplifier is negligible. The multipass transmission function of the waveplate and polarizers, however, limit the effective gain profile observed in the Q-switched (unseeded) pulse to a FWHM of 20 nm centered at 832 nm for 36 round trips in the cavity (shown in figure II.6a). Consequently, a small amount of narrowing is imposed on the output spectrum. This can be seen in figure II.6. The spectrum of the stretched pulses seeding the regenerative amplifier is shown in figure II.3. Figure II.6b, curve 1 shows the spectrum calculated using the regenerative amplifier small signal gain profile and the seed pulse spectrum. This is compared to the measured

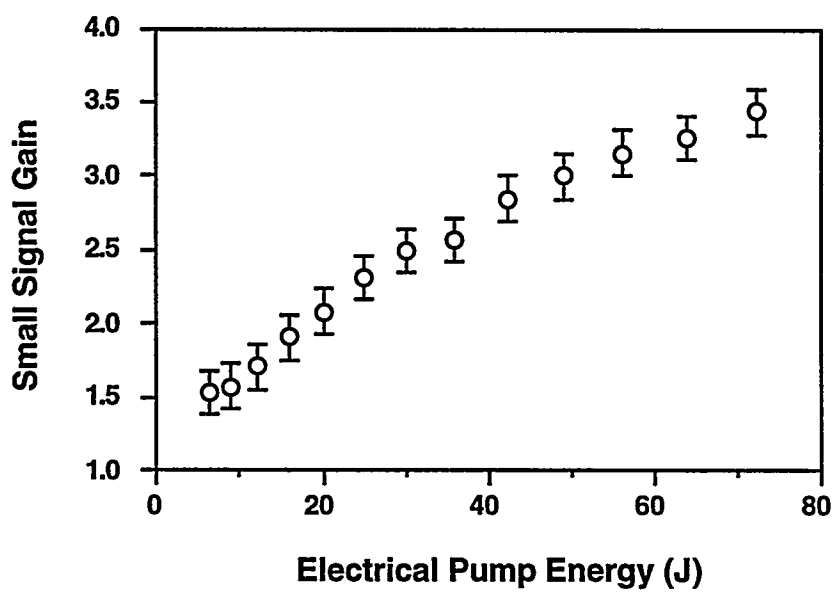

Figure II.5: Measured small signal gain in the 4 mm LiSAF amplifier as a function of electrical pump energy.

(a)

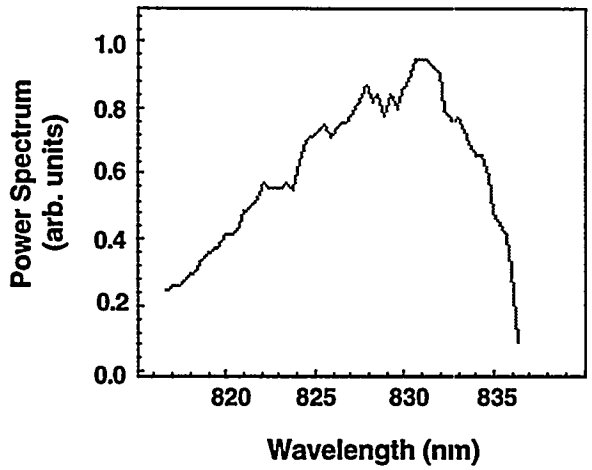

(b)

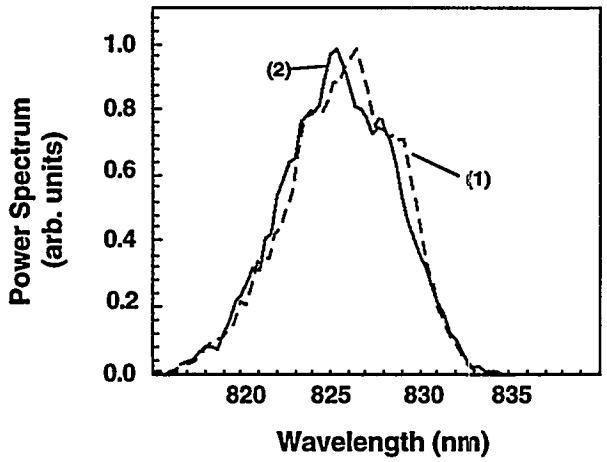

(c)

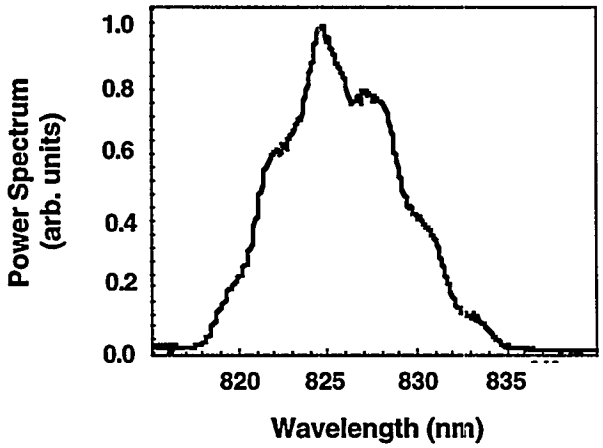

Figure II.6: **(a)** Spectrum of a Q-switched light pulse from the unseeded, free-lasing regenerative amplifier. **(b)** Curve 1 is the spectrum calculated from the seed spectrum and gain profile of the regenerative amplifier. Curve 2 is the actual measured spectrum of the laser pulse after amplification to 12 mJ. **(c)** Spectrum of the laser after amplification.

spectrum at 12 mJ in figure II.6b curve 2; the two exhibit very close agreement. The amplified spectrum from the regenerative amplifier exhibits 7.0 nm of bandwidth at FWHM.

The pulse buildup inside the regenerative amplifier is shown in figure II.7. The gain in the cavity is exponential up to the pulse switch-out. This small signal gain behavior is expected since the saturation fluence of LiSAF is approximately 7 J/cm^2, well above the pulse fluence of ~ 1 J/cm^2 during the final pass around the cavity. The operation of a chirped pulse regenerative amplifier in the small signal regime is necessary in order to avoid pulse shape distortion resulting from saturation of the amplifier. For chirped pulses, temporal distortion results in spectral distortion. A detailed analysis of gain saturation effects in chirped pulse amplification is given in section II.3.B.

II.3.C Power Amplifier Chain Design and 9.5 mm LiSAF Amplifier Performance

The design goal in our system, as is the case in any short pulse solid state laser

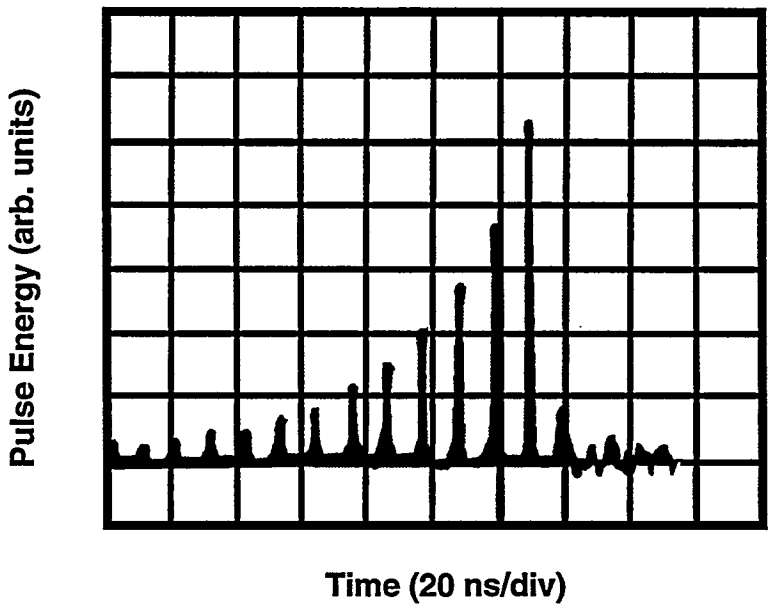

Figure II.7: Oscilloscope trace of a fast photodiode monitoring the pulse energy buildup inside the ring regenerative amplifier cavity.

amplifier system, is to extract as much energy as is possible from the large amplifiers while keeping pulse intensities at a level that minimize undesirable effects of self focusing and self phase modulation [150]. Maximum energy extraction for rod amplifiers can be achieved by propagating a near flat-top spatial profile through the amplifier chain. This profile permits a greater fill-factor in the rods without diffraction effects than does a Gaussian profile. For this reason a flat top spatial profile is generated after the regenerative amplifier by truncating the Gaussian spatial profile with a 2.0 mm serrated aperture. The Gaussian output from the regenerative amplifier is propagated 3 m allowing it to slightly diverge, and the aperture is illuminated with a 3.2 mm diameter ($1/e^2$) Gaussian, passing 45% of the 10 mJ output from the regenerative amplifier. Propagation of the flat-top is achieved by relay imaging the aperture through the remainder of the system [81]. The near field image plane of each stage of the system is placed near the damage prone optics in the system to minimize diffraction ripples.

Immediately after the aperture, the pulse is single passed through a second 4 mm diameter LiSAF amplifier exhibiting a single pass gain of 2.0. This amplifier essentially restores the energy lost on the serrated aperture. The image of the aperture is then relayed by an air spatial filter to the next amplification stage. The magnification of this spatial filter is 2.9 and the resulting beam diameter is 6.1 mm. The filter uses an f = 35 cm focusing lens (f/#=170), an f = 100 cm recollimating lens and a 1.5 mm pinhole in the far field of the spatial filter. The 6.1 mm diameter beam is then passed to the amplifier section of the system. The image of the serrated aperture is relayed by this spatial filter to the output face of the second 9.5 mm amplifier rod since it is at this point that the pulse energy fluence is at a maximum.

After the first spatial filter, the pulsed is double passed through a 9.5 mm diameter x 115 mm long flashlamp pumped LiSAF rod and then single passed through a second 9.5 mm rod. The actual flashlamp arc length in the 9.5 mm amplifiers is 100 mm. There are two issues that arise in the flashlamp pumping of large diameter (> 9 mm) LiSAF

amplifiers. The first is of gain uniformity across the diameter of the rod and the second involves the attainable stored energy as a function of flashlamp light pulse duration. Special care has been taken to optimize our LiSAF power amplifiers with respect to both considerations. We have developed flashlamp heads and pulse forming networks specifically for our large aperture LiSAF amplifiers to optimize these performance aspects [49, 48].

Both amplifiers utilize an intermediately coupled four lamp head. The flashlamp pulse forming network delivers up to 600 J in a 140 μs pulse (measured with a photodiode and shown in figure II.8) . The measured single pass, small signal gain in the first of the two 9.5 mm amplifier rods is shown in figure II.9 as a function of electrical pump energy discharged through the flashlamps. With a pump energy of 600 J we observe a gain of 7.5. This corresponds to a pump efficiency of 1.7% from electrical to stored energy. The second amplifier, which is pumped by a slightly longer flashlamp pulse and lower flashlamp discharge current, exhibits a gain of 5.3. The energy of the pulse after the second 9.5 mm rod is 400 mJ.

To optimize the gain in the large LiSAF amplifiers we found it necessary to reduce

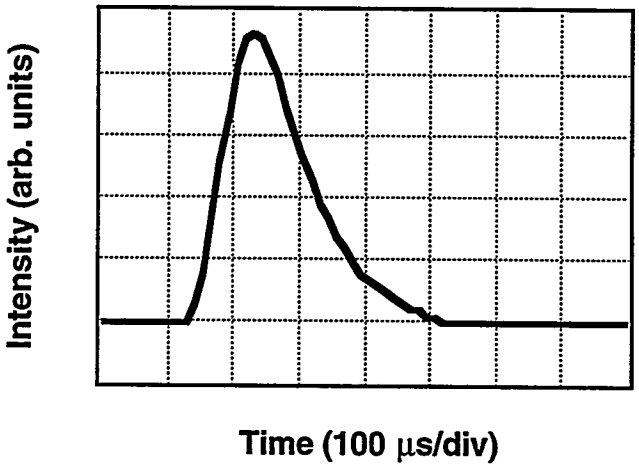

Figure II.8: Flashlamp light pulse of the 9.5 mm LiSAF amplifier head.

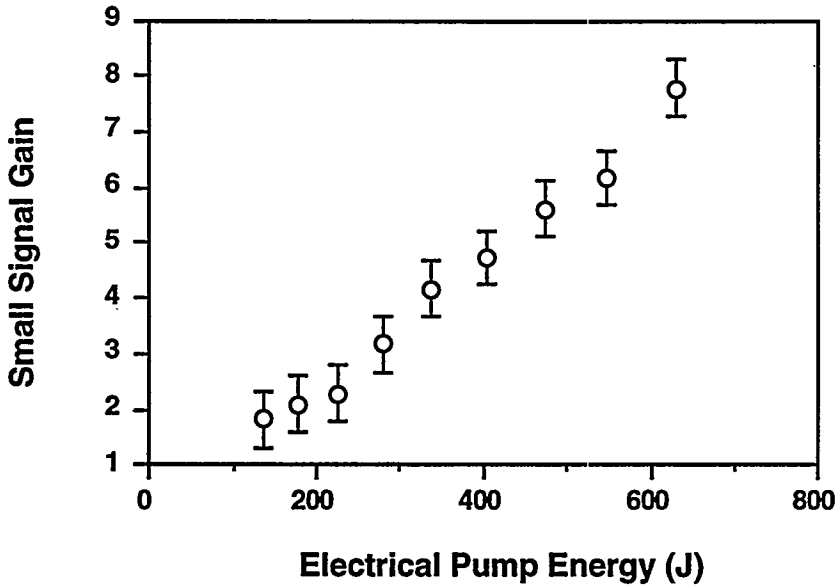

Figure II.9: Measured small signal gain in the 9.5 mm LiSAF amplifiers as a function of electrical energy delivered to the flashlamps.

the pulse width of the flashlamp pulse in our amplifier heads from that used in commercially available flashlamp pulse forming networks to more closely match the upper state lifetime of the LiSAF. Commercially available electronics typically utilize flashlamp pulses with widths of the order of 200 - 300 μs. The lifetime of the LiSAF, however, is only ~ 70 μs so a significant amount of the stored energy in the LiSAF will decay before the termination of the flashlamp pump.

To illustrate the advantage gained by shortening the flashlamp pulse we have modeled the efficiency of flashlamp pumping LiSAF as a function of flashlamp pulse width with a simple rate equation model. This model determines the time dependent stored energy density in the LiSAF amplifier rod as a function of the flashlamp pulse duration and the flashlamp electrical to radiant conversion efficiency. The model finds the time dependent inversion density inside the amplifier rod by numerically solving the rate equation,

$$\frac{dN(t)}{dt} = -\frac{N(t)}{\tau_s} + \alpha W_{pump}(t) \tag{2.4}$$

as a function of flashlamp pulse width. Here $N(t)$ is the time dependent inversion density, τ_s is the spontaneous decay lifetime of LiSAF, $W_{pump}(t)$ is the time dependent flashlamp pumping rate (for these calculations the flashlamp pulse shape from a critically damped LC pulse forming circuit [122], with a pulse width t_{lamp} is assumed), and α is the pumping conversion efficiency. For these simple estimates we assume that α is constant with varying flashlamp pulse duration. In general this is not true. The effect of a variable pump efficiency resulting from the spectral shifting of the flashlamp light will be considered in the next section in the context of the 19 mm LiSAF rod which utilizes higher current density in the flashlamps than used in the 9.5 mm amplifier heads.

The relative maximum inversion density as a function of flashlamp pulse width calculated from this model is plotted in figure II.10. The calculated small signal gain values resulting from these inversion densities are shown on the same plot in figure II.10 for the estimated pump efficiency, α, of our 9.5 mm heads. These calculations indicate that a dramatic increase in the pumping efficiency in a LiSAF amplifier is achieved by shortening the pump pulse duration from 250 μs to <150 μs.

Because of this increase in pump efficiency with a decrease in flashlamp pulse widths, a flashlamp pulse forming network that produces a 140 μs critically damped flashlamp pulse was developed. Experimental results agree well with the predictions of the model. Preliminary work with large flashlamp pumped LiSAF amplifiers utilized a 200 μs flashlamp pulse, and the model predicts an 18% increase in pump efficiency by shortening the flashlamp pulse duration from 200 μs to 140 μs. This 18% increase in pump efficiency increases the small signal gain as $G^{1.18}$. This predicted increase in pump efficiency agrees very well with the experimentally observed pump efficiency increase of 15% . The model also indicates that maximum gain in the LiSAF amplifier should be achieved at 30 to 40 μs after the peak of the flashlamp pulse for a pulse width of 140 μs.

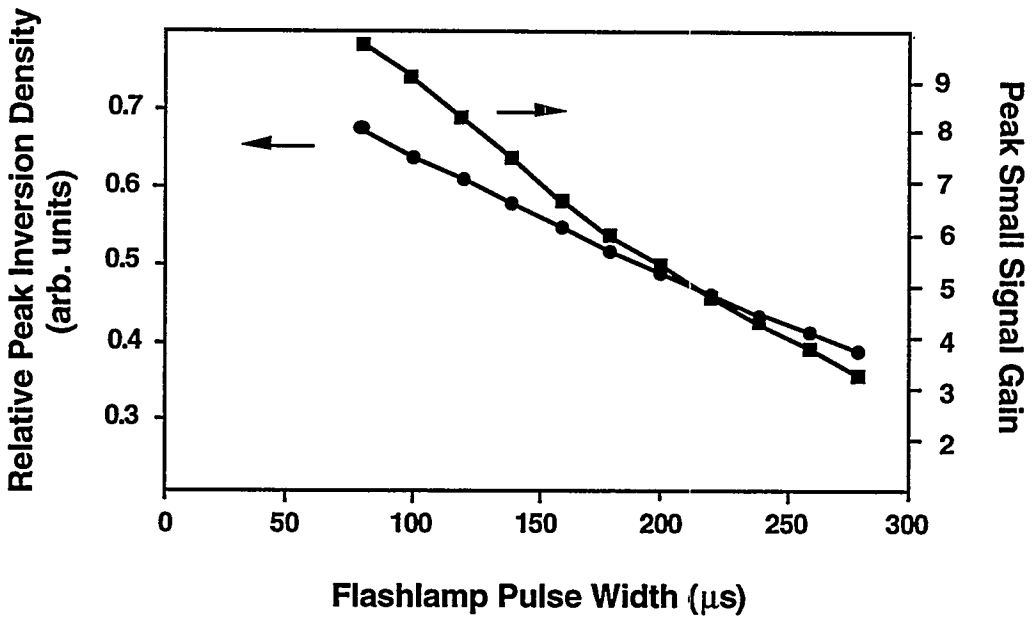

Figure II.10: Calculated relative inversion density achievable in a flashlamp pumped LiSAF amplifier as a function of flashlamp pulse width (circles, left axis). The corresponding small signal gain achievable in our 9.5 mm LiSAF amplifier is plotted on the right axis (squares).

Experimentally, the gain peaks roughly 25 μs after the peak of the flashlamp pulse, a value that agrees well with the calculated gain time history. Shortening the flashlamp pulse further can cause a UV-shift in the emission spectrum of the flashlamp lowering the pumping efficiency, an effect that will be discussed below.

The other concern in the design of the large aperture LiSAF amplifiers was that of maintaining the gain uniformity across the aperture of the rod. The results of gain uniformity measurements of the first 9.5 mm LiSAF amplifiers are shown in figure II.11. This LiSAF rod contained a Cr concentration of 0.8 mole %, corresponding to an ion concentration of about 1.0×10^{20} ions/cm^3. The small signal, single pass gain is plotted as a function of radius for the central 7 mm inside the 9.5 mm rod. As can be seen here the gain profile is constant to within 10%, though slightly higher gain is observed near the edges of the rod.

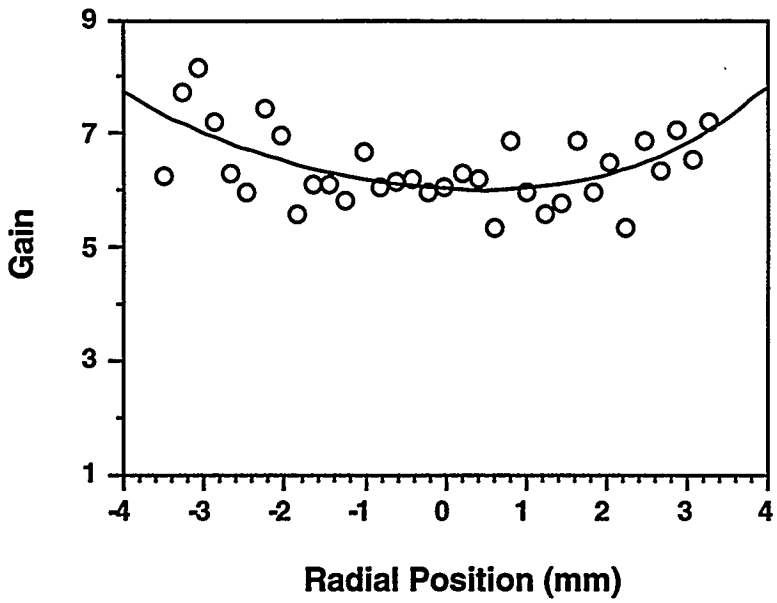

Figure II.11: Small signal gain as a function of radial position inside the 9.5 mm LiSAF amplifier when pumped with 600 J through four flashlamps.

II.3.D Performance and Modeling of the 19 mm LiSAF Amplifier

After amplification in the 9.5 mm amplifiers a vacuum spatial filter expands the beam by a factor of 2 for amplification in the 19 mm LiSAF amplifier. This spatial filter consists of an f = 25 cm focusing lens, a 50 μm pinhole located in a vacuum chamber to smooth the beam profile, and an f = 60 cm lens for recollimation.

- GAIN PERFORMANCE OF THE 19 MM AMPLIFIER

The performance of the 19 mm LiSAF amplification stage has been carefully optimized to yield high brightness pulses with energy of above 1 J [48]. By using a relatively short rod (length ≤ 11 cm) it is possible to obtain material of high optical quality with clear apertures of >20 mm and we have obtained a LiSAF rod of 19 x 110 mm with low scatter and reasonable phase front quality. A head was specifically designed for pumping this short amplifier rod. The head uses 8 lamps in a cylindrical pump cavity and delivers up to 3 kJ of electrical pump energy in a 160 μs flashlamp pulse (shown in figure

II.12). The amplifier head is water cooled and the amplifier rod thermally recovers within 20 seconds after being pumped with the full 3 kJ of energy. The gain of this amplifier for a full aperture beam (14 mm) as a function of input electrical energy is shown in figure II.13. At low pump energies, the pump efficiency is high (1.6%), but at the higher pump energies this efficiency begins to drop. The result is that the small signal gain grows slightly slower than linearly with increasing pump energy.

- UV SHIFTING IN THE FLASHLAMP PUMP LIGHT OF THE 19 MM AMPLIFIER

We attribute this drop in the pump efficiency to the shift of the Xe flashlamp light spectrum toward the ultraviolet with increasing electrical pump energy. This shifts the flashlamp light away from the LiSAF absorption bands and lowers the excitation efficiency. To model this effect, we use the fact that the spectral characteristics of small bore Xe flashlamps can be well approximated by that of a plasma column emitting radiation with a single effective blackbody temperature [187, 87] given by the empirical formula [157]:

$$T(J) = 9300 J^{0.18} D^{0.092} P^{-0.017} \tag{2.5}$$

where T is in °K, D is the Xe plasma column diameter in centimeters, P is the Xe fill pressure in torr (= 800 torr for our lamps), and J is the current density in the lamps in kA/cm^2. The actual emitted flashlamp spectrum is given by the relation [157]:

$$I(\lambda) = I_{BB}(\lambda, T) F(\alpha(\lambda) d) \tag{2.6}$$

where $I_{BB}(\lambda, T)$ is the black-body spectrum at a temperature T, $\alpha(\lambda)$ is the wavelength dependent absorption of the Xe plasma and d is the Xe plasma diameter (taken to be 5 mm for our lamps [187]). $F(\alpha(\lambda)d)$ is the angle averaged emissivity function of the Xe flashlamps and has been calculated in reference [157]. For the parameters that are relevant for the 19 mm LiSAF head, the emissivity is generally quite flat over the wavelength range

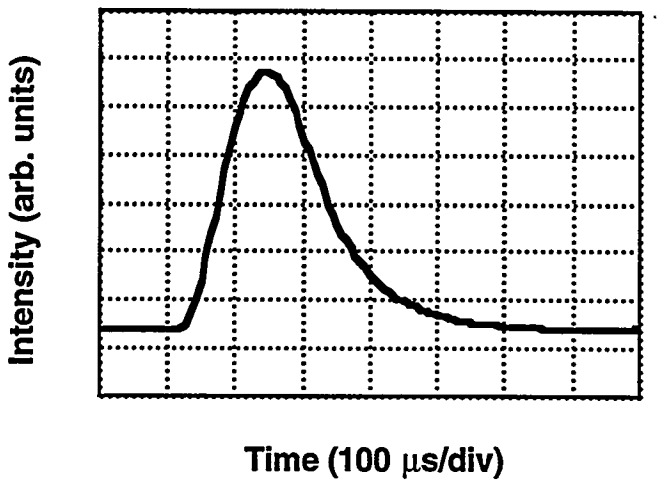

Figure II.12: Flashlamp light pulse of the 19 mm LiSAF amplifier head.

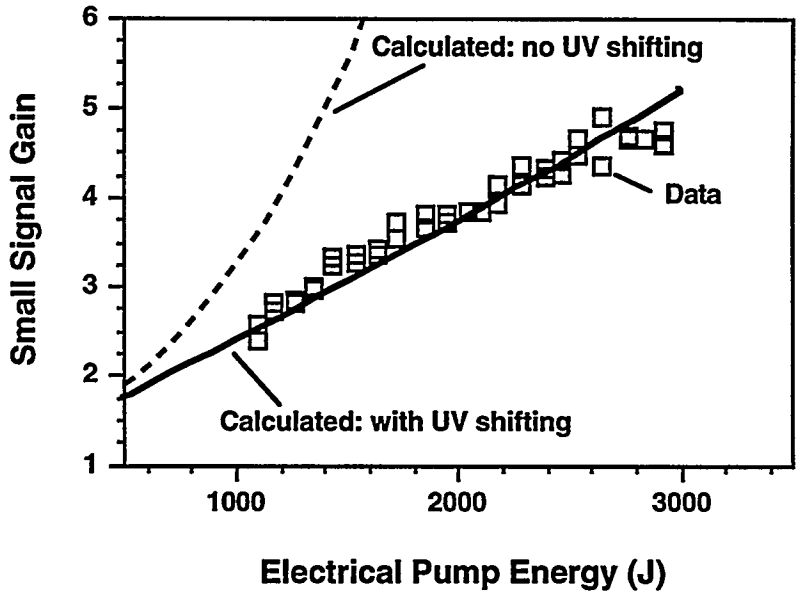

Figure II.13: Measured small signal gain in the 19 mm LiSAF amplifier as a function of electrical pump energy discharged through the flashlamps (squares). The dashed line is the calculated small signal gain assuming a constant 1.8% pump efficiency and the solid line is the calculated gain when the UV shift of the Xe spectrum is taken into account.

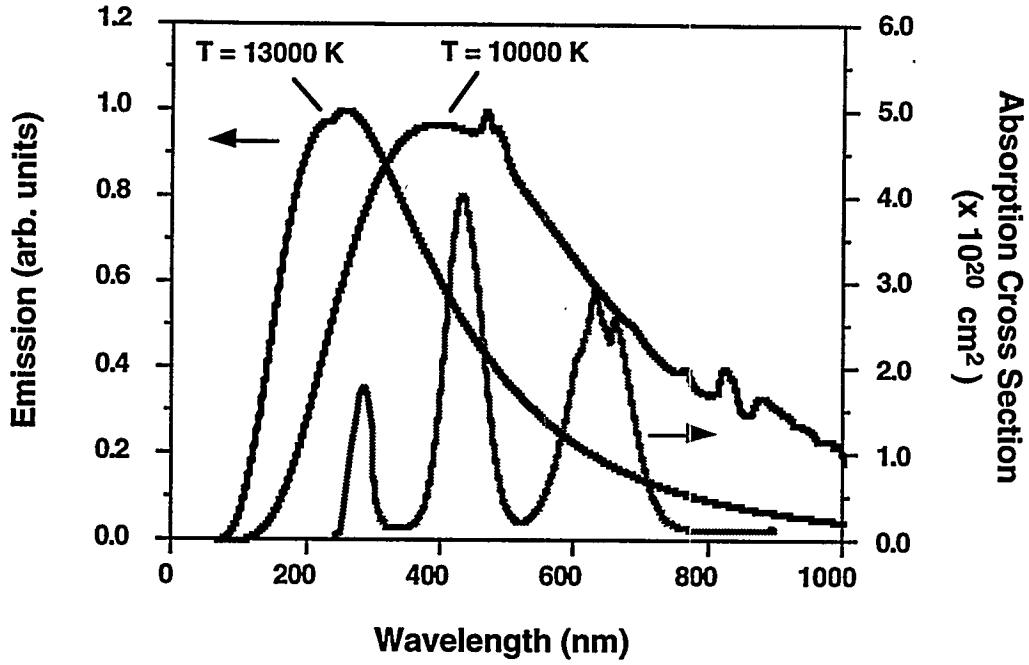

Figure II.14: The gray line is the absorption spectrum of LiSAF (right axis). The calculated emission spectra of Xe flashlamps at 10000 K and 13000 K temperatures are compared to show the relative overlap with the LiSAF absorption.

of interest for LiSAF pumping. The time dependent current density, J, is calculated from the time dependent behavior of the LRC circuit which produces the flashlamp pulse [122]. The effect of the UV shifting of the flashlamp spectrum is illustrated in figure II.14. Here the calculated flashlamp emission spectra, from eq. (2.6), for plasma temperatures of 13000 K and 19000 K are compared to the absorption spectrum of the LiSAF. These temperatures correspond to the spectra at the peak of the flashlamp discharge output for 60 and 350 J discharged per lamp in a 160 μs pulse respectively. As this figure illustrates, the bulk of the flashlamp emission is pushed away from the primary LiSAF absorption band at 425 nm toward the UV at the higher pump energy.

To accurately calculate the stored energy in the LiSAF rod, we need to know how much flashlamp power is absorbed by a volume element dV in the LiSAF rod. If there is power P_0 incident on a volume element dV with thickness dr, then the power absorbed is

$$dP = P_0(1-\exp(-N\sigma d\rho)) \approx P_0 N\sigma d\rho \tag{2.7}$$

which means that the time rate of change of the inversion density from pumping is given by:

$$\left.\frac{dn}{dt}\right|_{pump} = \frac{P_0 N\sigma\, d\rho}{\hbar\omega\, dV} = \frac{P_0 N\sigma}{\hbar\omega\, dA} \tag{2.8}$$

We assume that the rod is bathed in a uniform, isotropic pump field. To calculate the fraction of the power emitted per unit area on the surface of the rod that makes it to a point inside the rod we assume exponential absorption of the light and consider only one spectral component of the pump light distribution. If P' is the flashlamp power per unit incident on the rod surface a distance ρ away from the point inside the rod, then the fractional power incident on the area dA of the volume element dV from the surface element dS on the surface of the rod is:

$$P_0 = \frac{dA}{\rho^2} P' e^{-N\sigma\rho} \cos\varphi\, dS \tag{2.9}$$

where φ is the angle between the normal to dS and the ray between dS and the volume element inside the rod. If we now insert (2.9) into (2.8) we have for the time rate of change of the inversion density:

$$\left.\frac{dn}{dt}\right|_{pump} = \frac{N\sigma}{\hbar\omega} P' \frac{e^{-N\sigma\rho}}{\rho^2} \cos\varphi\, dS \tag{2.10}$$

In cylindrical coordinates we have that $\rho = \sqrt{r^2 + R^2 - 2rR\cos\theta + z^2}$ and $\cos\varphi = (R - r\cos\theta)/\sqrt{r^2 + R^2 - 2rR\cos\theta + z^2}$ if we choose the coordinate system such that the point of interest inside the rod r, θ', z' is centered in the rod with $\theta' = z' = 0$. θ and z are the coordinates of the rod surface, and R is the rod radius.

Now $W'(t)d\lambda$ is the total power emitted by the flashlamps incident on the rod surface for a give spectral range $d\lambda$ (which is time dependent since the current in the lamps varies with time). We need to integrate equation (2.10) over the surface of the rod, and we need to integrate over all emitted wavelengths. This integration is weighted by a normalized flashlamp wavelength distribution $P_{kT}(\lambda)$ defined as $P_{kT}(\lambda) = I(\lambda)\Big/\int I(\lambda)d\lambda$ where $I(\lambda)$ is defined in equation (2.6). Performing these integrations on equation (2.10) we get:

$$\left.\frac{dn}{dt}\right|_{pump} = NW'(t)\int_0^\infty \frac{P_{kT}(\lambda)\sigma\lambda}{hc}\left[\int_{-l/2}^{l/2}\int_0^{2\pi}\frac{\exp(-N\sigma\rho)}{\rho^3}(R - r\cos\theta)Rd\theta dz\right]d\lambda \qquad (2.11)$$

From this analysis we see that the changing emission spectrum resulting from the time dependence of the current density and the plasma temperature results in a time-dependent pumping efficiency, $\gamma(r,t)$. Since the rod length in our case, (l = 100 mm), is much greater than the rod radius, (R = 9.5 mm), it is a good approximation to extend the limits of the integration in eq. (2.11) over the length to $\pm\infty$ which yields for the pump efficiency:

$$\gamma(r,t) = \int_0^\infty \frac{P_{kT}(\lambda)\sigma_a(\lambda)\lambda}{hc} \times$$
$$\left[\int_{-\infty}^{\infty}\int_0^{2\pi}\frac{\exp\left(-N\sigma_a(\lambda)\sqrt{r^2+R^2-2rR\cos\theta+z^2}\right)}{\left(r^2+R^2-2rR\cos\theta+z^2\right)^{3/2}}(R - r\cos\theta)Rd\theta dz\right]d\lambda \qquad (2.12)$$

where we have accounted for the wavelength dependence of the absorption cross section.

The calculated value of $\gamma(r,t)$ at the center of the rod (r=0) and the peak of the flashlamp pulse as a function of discharged energy is shown in figure II.15. This pump efficiency drops by an appreciable amount as the pump energy is increased from 500 to 3000 J (from 0.35 to 0.2).

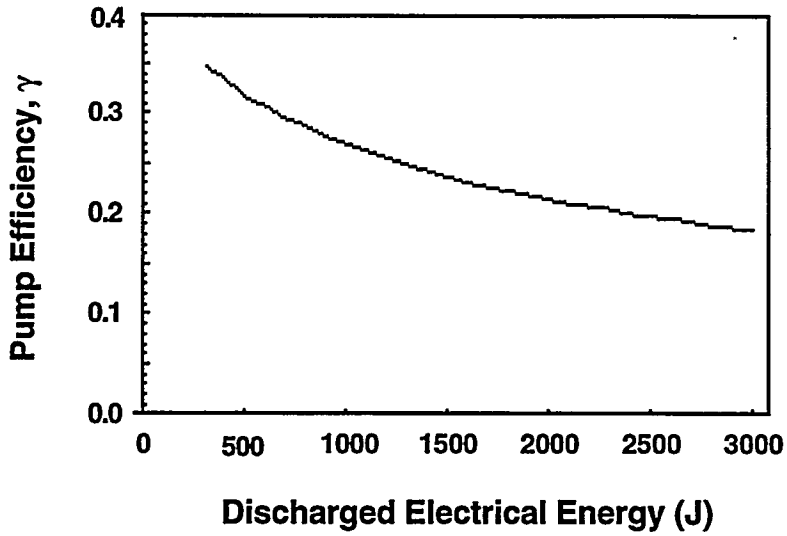

Figure II.15: Calculated pump efficiency using equation (2.12) as a function of discharged energy into eight flashlamps. The efficiency is evaluated at the peak of the flashlamp pulse for the rod center (r=0).

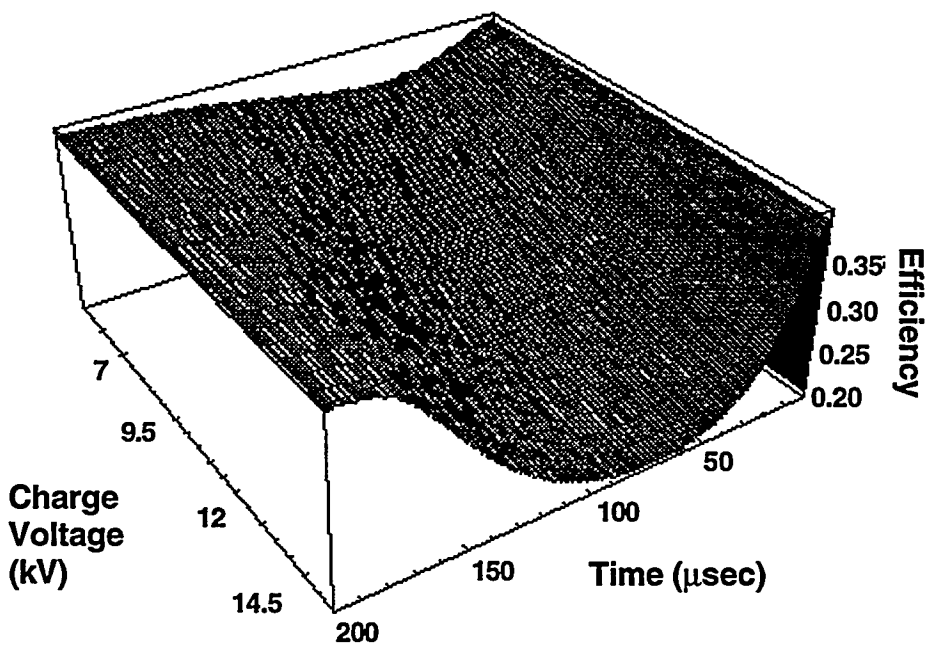

Figure II.16: Calculated pump efficiency using equation (12) as a function of time during the flashlamp discharge over a range of stored energy voltages. (Capacitance = 25 μF)

The time dependence of this pumping efficiency during the actual flashlamp pulse is illustrated in figure II.16 over the range of voltages used in the 19 mm pulse forming network. (The pulse forming network utilizes a 25 μF capacitor. Thus, a charge voltage of 15000 V corresponds to a discharged energy of 3 kJ). As can be seen from this figure, the pump efficiency dips because of the spectral UV shift during the peak of the pulse due to the increased current in the flashlamps. The magnitude of this dip increases with increasing discharged energy.

The time dependent inversion density, $n(r,t)$, (which is now radially dependent as well) is then obtained by solving the inversion population rate equation which includes both the pumping from the flashlamps as well as the decay of the upper level:

$$\frac{dn(r,t)}{dt} = -\frac{n(r,t)}{\tau} + \alpha_{cav}\gamma(r,t)W(t)N \tag{2.13}$$

Here τ is once again the upper state lifetime of the LiSAF, N is the Cr^{3+} ion density. Now, α_{cav} is a fitting parameter that characterizes the overall efficiency of the pump cavity. This equation is similar to eq. (2.4) except that the pump efficiency is now a function of time. The small signal gain experienced by a flat-top beam, calculated at the time when the inversion density is maximum, is then given by:

$$G = \frac{1}{\pi a^2}\int_0^a \exp\left(n(r,t)\sigma_e l\right)2\pi r dr \tag{2.14}$$

with a beam radius of $a = 7$ mm.

The calculated small signal gain as a function of pump energy is shown as a solid line in figure II.13. For comparison, the gain calculated assuming a constant pump efficiency of 1.8% for all pump energies is shown as a dashed curve in figure II.13. Inclusion of the UV shifting in our model accurately predicts the observed small signal gain in this head for pump energies between 1 kJ and 3 kJ as well as the linear increase of the gain with increasing electrical pump energy. From these measurements we conclude

that it is the UV shifting that sets the limit on flashlamp pump efficiency in large aperture LiSAF amplifiers. Furthermore, since the UV shift varies with the flashlamp current, further shortening of the flashlamp pulse width would increase the current density in the lamps and would not necessarily improve the single pass gain performance significantly. It is for this reason that we have chosen a flashlamp pulse that is 160 μs instead of one that more closely matches the 67 μs lifetime of the LiSAF. The calculated gain in the 19 mm head as a function of flashlamp pulse width is shown in figure II.17. This calculation suggests that a further decrease in the flashlamp pulse width results in very modest increases in gain. For example with 3 kJ of electrical energy into our eight flashlamps, shortening the pulse width to 70 μs would result in only a slight increase in gain from 5 to 5.6. Below this value the calculated gain begins to drop. Concerns about the lifetime of the flashlamps would also become important with shorter pulse widths. We operate our lamps at an explosion fraction of 0.25, a value above which Xe flashlamp lifetime begins to decrease rapidly [156].

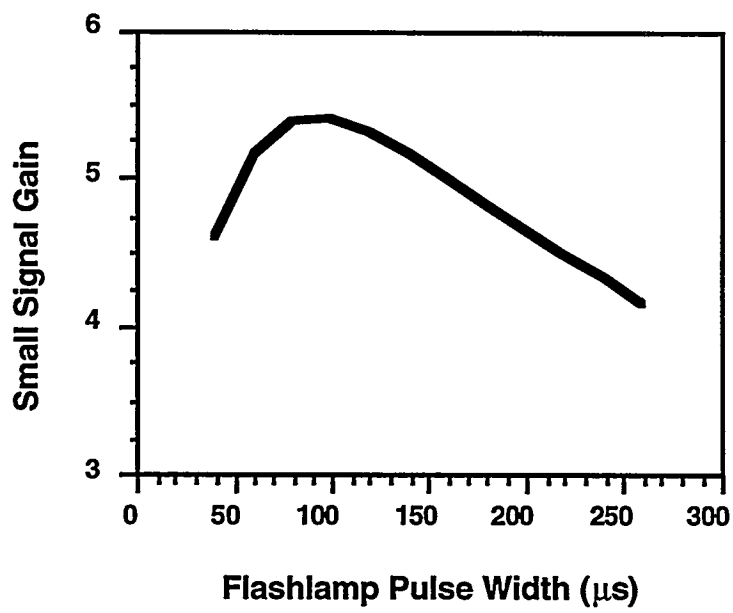

Figure II.17: Calculated gain in the 19 mm head as a function of flashlamp pulse width for a fixed pump energy of 2800 kJ.

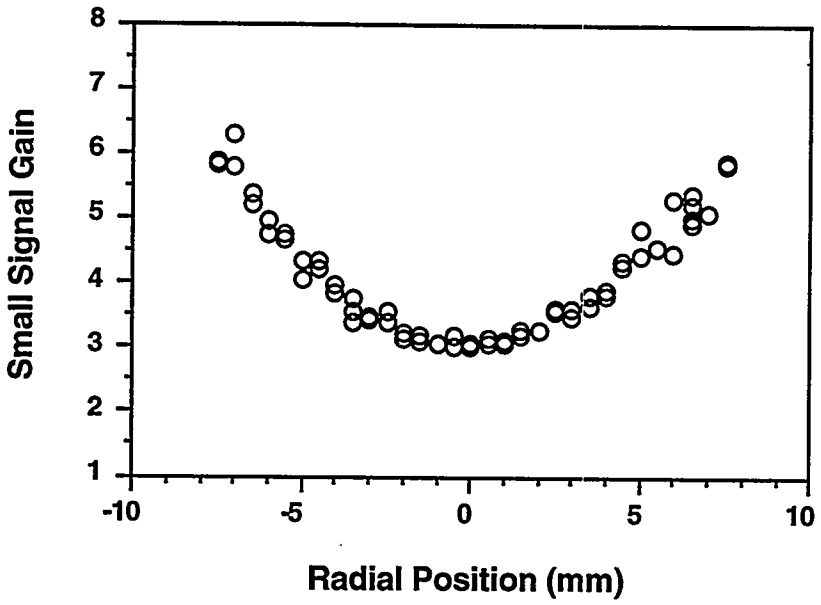

Figure II.18: Measured small signal gain as a function of radial position in the 19 mm amplifier.

- RADIAL GAIN PROFILE OF THE 19 MM ROD

Our 19 mm rod has a Cr^{3+} ion doping of 0.6% corresponding to an ion density of 0.8×10^{20} ions/cm^3. This doping provides a good compromise between absorption efficiency and gain uniformity. The measured radially dependent small signal gain in the rod at an electrical pump energy of 2.7 kJ is shown in figure II.18. The gain varies from 3.5 at the center of the rod to 6.5 at the outer edge of the beam ($r = 7$ mm) This gain variation, can be compensated by generating a signal pulse which exhibits an intensity profile opposite to the gain profile. We accomplish this by a choice of the aperture size in the front stage of the relay imaging described above. The near field profile of the amplified beam is shown in figure II.19 illustrating that a flat-top profile is roughly the result of the relay imaging and the laser amplifier chain gain profile. The modulation in the profile is a result of the phase aberrations in the large amplifier rods. This aberration has some effect on the brightness achievable and is discussed below.

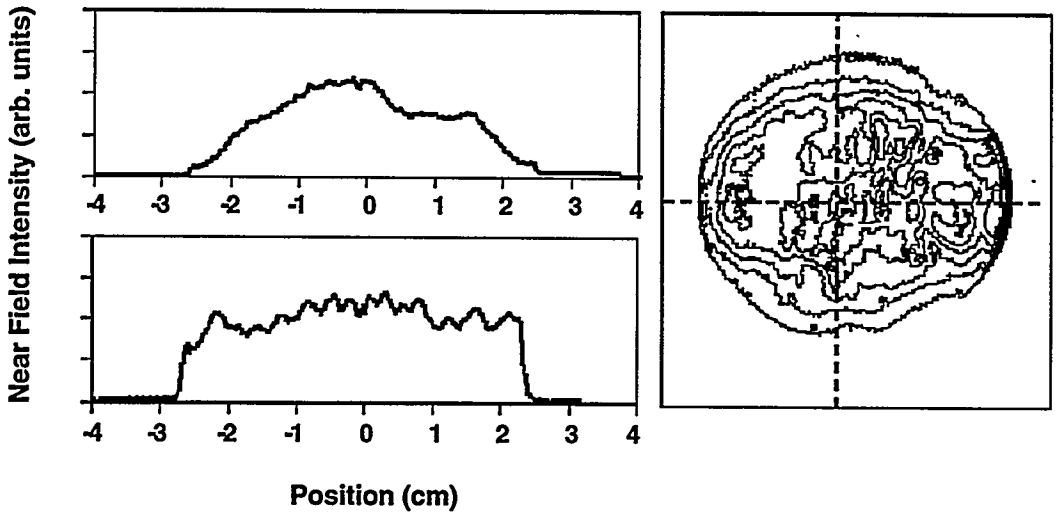

Figure II.19: Near field beam profile after amplification to 1 J.

II.3.E Pulse Recompression and Focused Brightness

The amplified pulse (up to an energy of 1.7 J) is injected into a double-pass grating pair pulse compressor. The 1800 l/mm gratings were designed for high diffraction efficiency in the -1 order for 825 nm light [21]. The gratings each exhibit a diffraction efficiency of ~ 90% resulting is a compressor through-put of 63% and a recompressed pulse with an energy of up to 1.05 J. The amplified spectrum (figure II.6c) exhibits a width of 7.0 nm, narrowed from 9.5 nm by factors already discussed. The measured autocorrelation of the amplified pulse, shown in figure II.20, exhibits a width of 195 fs. A $sech^2$ deconvolution of the autocorrelation suggests a pulse FWHM of under 130 fs and a resulting time bandwidth product $\Delta\nu\Delta\tau = 0.40$. A numerical Fourier transform of the amplified pulse spectrum was performed and the corresponding transform limited autocorrelation calculated. The results of this calculation suggest a transform limited pulse width of 125 fs and a resulting autocorrelation of 190 fs, (shown in Figure II.20), indicating that the recompressed pulse is very nearly transform limited. A curve fit to the measured autocorrelation indicates a shape characteristic of a $sech^2$ pulse near the peak and

characteristic of a Gaussian in the wings. This intermediate behavior is not unexpected in light of the time bandwidth product that lies between the values of a transform limited $sech^2$ (0.36) and Gaussian (0.44).

The intensity of the recompressed pulse at this point is in excess of 400 GW/cm^2 and any propagation in air would result in significant self phase-modulation and spatial beam break-up. To circumvent this problem the compressor is enclosed in a chamber filled with argon. Argon has a substantially lower nonlinear refractive index than air, ($n_2^{(air)} = 1.2 \times 10^{-16}$ esu, $n_2^{(Ar)} = 0.2 \times 10^{-16}$ esu). Subsequent propagation of the recompressed pulse to the experiment is in argon.

- BEAM FOCUSABILITY

Of equal importance to the peak power in high irradiance systems is the focusability of the beam. Because of a desire to achieve high brightness with this laser system we have paid special attention to beam quality and aberrations. In particular we

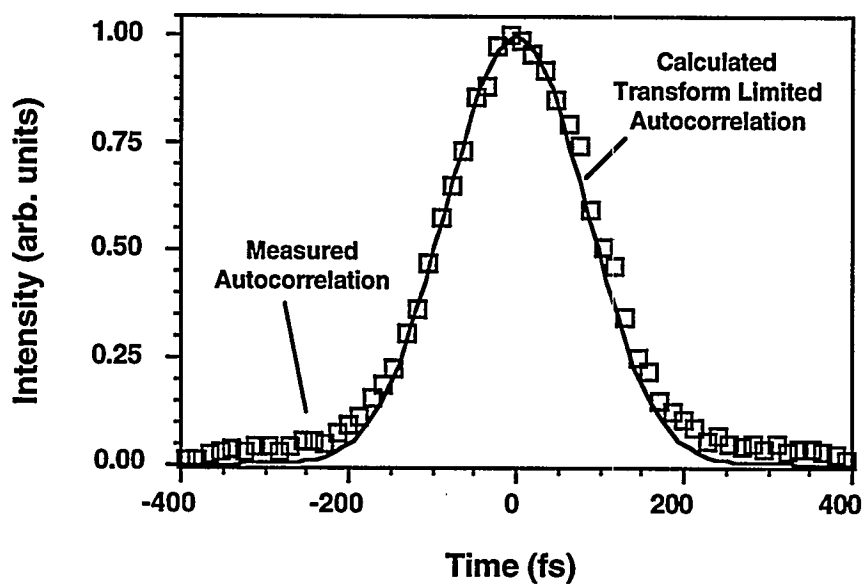

Figure II.20: Measured autocorrelation trace after compression (circles). The FWHM of is 195 fs. The solid line is the calculated transform limited autocorrelation based on the measured spectrum.

have made an effort to use the highest optical quality LiSAF amplifier rods that can be currently fabricated. Transmission interferograms of early generation LiSAF indicated that 1 cm rods exhibited less than acceptable optical quality ($>\lambda/2$ over a 1 cm aperture). Since then the wave front quality of large LiSAF crystals has improved somewhat and the material used for our 9.5 mm rods is representative of this newer material. It has been hypothesized that the distortions we observed in the material arise from stresses in the crystal caused by residual particles of lithium fluoride [27]. The two 9.5 mm rods currently used in our system each impose roughly a $\lambda/4$ distortion across the aperture of the rod.

The 19 x 110 mm Cr:LiSAF rod exhibits an overall peak to valley phase aberration of approximately $\lambda/5$. This is not the limiting distortion in our system. Instead, it is the double pass in the first 9.5 mm amplifier resulting in a phase front distortion of $\approx \lambda/2$ that is responsible for the primary limit on focusability. Far field and pinhole measurements of the focal spot produced with an f/25 lens indicate that ~ 50% of the focused pulse energy is contained in a near diffraction limited spot of 50 μm ($1/e^2$ diameter). The remainder of the pulse energy is contained in wings that extend out to a diameter ~ 100 μm. The measured far field focal spot profile is shown in figure II.21 On the basis of this measurement we can say the far field intensity is 2 to 2.2 times diffraction limited.

The actual peak intensity of the focused laser has also been examined by observing the maximum charge state produced in a low density gas by tunneling ionization [49]. A time of flight experiment was performed in which the laser was focused by an f/20 optic (f = 85 cm) into a low density (pressure $< 10^{-6}$ torr) gas, a situation in which the ionization dynamics are not affected by collisions and the ion yields are determined solely by tunneling ionization due to the laser's strong electric field. The results of this measurement will be described in chapter III. On the basis of a theoretical fit to this data with standard tunneling ionization rate formulas, we have determined that the peak intensity at the focus of the laser is roughly 4 - 5 times lower than that expected if the

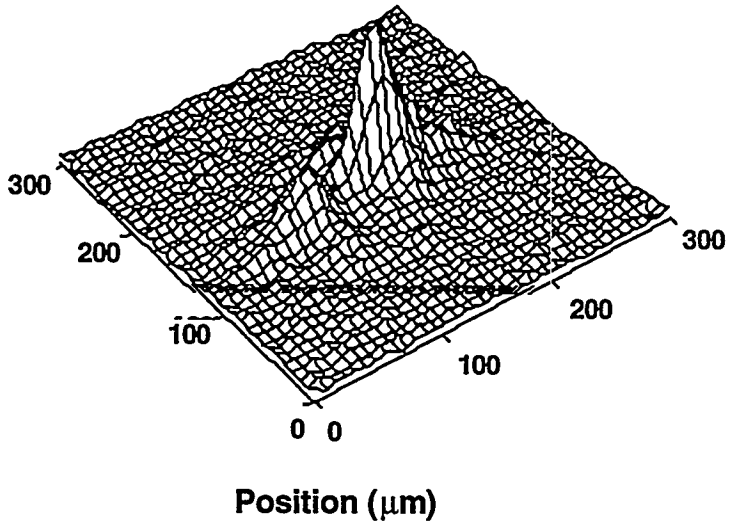

Figure II.21: Measured far field profile of the LiSAF laser focused with an f/25 lens.

focus were a diffraction limited Gaussian. This agrees well with our assertion that the focus spot is approximately twice diffraction limited.

II.4 Modeling the Propagation of Stretched Pulses in Chirped Pulse Amplification

II.4.A Theory of Stretched Pulse Propagation Through the Amplifier Chain

As mentioned in the previous sections, it is very important to maintain the integrity of the pulse spectrum throughout the propagation of the stretched pulse through the amplifier chain. It is for this reason that we require a broadband amplifier material so that gain narrowing of the spectrum does not occur and broaden the resulting recompressed pulse. There are other factors that can contribute to broadening of the recompressed pulse as well. First, if the compressor does not compensate the dispersion of the stretched pulse to all orders, then residual dispersion will remain on the compressed pulse causing its

compressed width to be larger than the theoretical bandwidth limit. In principle, if the angles and the separation of the compressor and the stretcher are perfectly matched, their dispersion will cancel to all orders. However, due to chromatic aberrations in the lenses this is, in practice, not possible for stretchers that utilize lenses. For pulses much shorter than 100 fs, the problem of chromatic aberration is important [109]. For the pulse width of the LiSAF laser, however, it is of secondary importance.

More important for our system are the effects that the propagation of the stretched pulse through the amplifier chain itself has on distorting the pulse. Though the dispersion of the material in the amplifier chain, such as optics, amplifier rods, and Pockels cells, is significant, for a pulse width of <100 fs we can largely ignore the dispersion of the material above the second order. The second order material dispersion can be compensated relatively easily by a change in the compressor dispersion without a significant mismatch of the stretcher. However, nonlinear effects within the amplifier chain are not insignificant and their effects, in general, can not be compensated by a simple retuning of the stretcher/compressor pair [150].

The nonlinear effects on the pulse can be separated into amplitude and phase modulation. The first arises from gain in the amplifier chain that is not linear across the pulse envelope due to gain saturation. The second arises from the intensity induced refractive index of the material in the chain, imparting a phase on the stretched pulse which is nonlinear with time. To examine these two effects, it is necessary to conduct numerical simulations since the equations describing the effects are not solvable analytically. For these calculations it is convenient to use a simplified pulse envelope analysis in which the transverse profile of the pulse is ignored. This simplified view permits easy access to the physics and allows us to circumvent a complete solution of the wave equation for the pulse propagating through the amplifier chain.

We begin by assuming that the initial pulse electric field before stretching, $\mathsf{E}(\mathbf{r},t)$, is described by a transform limited pulse that is immediately separable into a transverse

term and a slowly varying amplitude $E(t)$.

$$\mathsf{E}(\mathbf{r},t) = F(x,y)E(t)\left[\frac{1}{2}\left(e^{-i\omega_0 t} + c.c.\right)\right] \tag{2.15}$$

We consider a time coordinate that moves with the envelope of the pulse: $t = t' - nz/c$. The frequency spectrum of the electric field is found through a Fourier transform (we ignore the transverse term):

$$\tilde{E}(\omega) = \Im\left\{E(t)\left[\frac{1}{2}\left(e^{-i\omega_0 t} + c.c.\right)\right]\right\} \tag{2.16}$$

To find the field of the stretched pulse, we apply the frequency dependent phase function characteristic of a stretcher, $e^{i\phi_s(\omega)}$, by multiplying it with the initial pulse spectrum. The electric field of the stretched pulse is then found by inverse Fourier transform:

$$E_s(t) = \Im^{-1}\left\{\tilde{E}(\omega)e^{i\phi_s(\omega)}\right\} \tag{2.17}$$

At this point, we determine the effects of the propagation of the laser pulse through the amplifier chain by solving the generalized nonlinear Schrödinger equation for the electric field [22]:

$$i\frac{\partial E_s}{\partial z} = i\frac{\alpha}{2}E_s + \frac{1}{2}\frac{\partial^2 k}{\partial \omega^2}\omega_0\frac{\partial^2 E_s}{\partial t^2} - \beta|E_s|^2 E_s \tag{2.18}$$

where α is the gain associated with the amplifiers, $\omega_0\,\partial^2 k/\partial\omega^2$ is the dispersion of the group velocity in the amplifier chain optical materials, and β, in CGS units, is related to the nonlinear refractive index, γ, by $\beta = \frac{n_0\omega_0}{8\pi}\gamma$. (Here γ is defined as $\Delta n = \gamma I$.)

In general, eq. (2.18) requires numerical solution. We can simplify this solution, however, by exploiting the fact that the dispersion induced by the stretcher is much larger than the material dispersion, represented by the second term on the right hand side. We can, then solve eq. (2.18) by ignoring the dispersion and solving only for the nonlinear contribution to the stretched pulse envelope, applying the material dispersion afterwards.

Doing this means that we can solve two independent equations for the stretched pulse amplitude, $A(t)$, and the accumulated phase, $i\phi_a(t)$, where $E(t) = A(t)e^{i\phi_a(t)}$. The equations for these quantities becomes

$$\frac{\partial A}{\partial z} = \frac{\alpha}{2} A \tag{2.19}$$

$$\frac{\partial \phi_a}{\partial z} = \beta A^2 \tag{2.20}$$

We shall consider the nature and size of both the amplitude and phase effects later in this section.

To find the recompressed pulse shape, we find the spectrum of the amplified, phase modulated pulse, apply the compressor phase function and inverse Fourier transform:

$$E_c(t) = \Im^{-1}\left\{e^{-i\phi_c(\omega)}\Im\left\{G(t)e^{-i\phi_a(t)}E_s(t)\right\}\right\} \tag{2.21}$$

where $G(t)$ is the time dependent gain found from eq. (2.20). We assume that the compressor phase completely compensates the phase from both the stretcher and material dispersion:

$$\phi_c(\omega) = \phi_s(\omega) + \phi_m(\omega) \tag{2.22}$$

which is possible when third order dispersion terms are unimportant.

We now consider the case of stretching a Gaussian pulse. The intensity profile of such a pulse is:

$$I(t) = I_0 e^{-2t^2/\tau^2} \tag{2.23}$$

where the full width at half maximum of the pulse is: $\tau_{FWHM} = \tau\sqrt{2\ln 2}$. We assume the pulse is initially transform limited so its electric field is described by:

$$E(t) = E_0 e^{-t^2/\tau^2} e^{-i\omega_0 t} \tag{2.24}$$

and its spectrum is

$$\tilde{E}(\omega) = \frac{E_0 \tau}{\sqrt{2}} e^{-(\omega-\omega_0)^2 \tau^2/4} \tag{2.25}$$

To find the stretched pulse shape we apply the stretcher phase function. The phase function for two parallel gratings has been derived by Treacy [186]; we can use this function if we substitute for the effective grating spacing of the stretcher, eq. (2.3). This phase is described, to second order, by the formula:

$$\phi_s(\omega) = \xi(\omega - \omega_0) - \mu(\omega - \omega_0)^2 \tag{2.26}$$

$$\xi = \frac{b}{c}(1+\cos\theta); \qquad \mu = \frac{b\lambda_0^{\ 3}}{4\pi c^2 d^2} \frac{1}{1-(\lambda_0 / d - \sin\gamma)} \tag{2.27}$$

Here θ and γ are the angles defined in figure II.1b and b is the effective grating spacing given by eq. (2.3). Use of this phase yields for the stretched pulse envelope (ignoring the linear phase in eq. (2.26)):

$$E_s(t) = \frac{E_0 \tau}{2} \frac{1}{\sqrt{\tau^2/4 + i\mu}} \exp\left[-\frac{t^2(\tau^2 - i4\mu)}{\tau^4 + 16\mu^2} - i\omega_0 t \right] \tag{2.28}$$

which implies that the FWHM of the stretched pulse is

$$\tau_s^{(FWHM)} = \sqrt{2\ln 2\left(\tau^2 + 16\mu^2/\tau^2\right)} \tag{2.29}$$

Most CPA systems utilize large stretching ratios (>1000) so $\mu^2 / \tau^4 >> 1$. Eq. (2.29) predicts, for example, that the stretcher used in the LiSAF system, with a $b \approx 4(2\times 60 - 25 - 25) = 280$ cm (for a four pass stretcher), d=(1800 lines/mm)$^{-1}$ and $\sin\gamma \approx 0.9$, will produce a stretched pulse width of 460 ps, in good agreement with the

observed value. The original pulse and the calculated shape of the stretched pulse for the parameters of the LiSAF laser stretcher is shown in figure II.22.

At this point, to continue requires numerical calculations. First we shall consider the effects of amplitude modulation of the pulse by gain saturation, an effect found to be unimportant in the LiSAF laser, and then we shall consider the effect of self phase-modulation and compare the numerical model with experimental measurements. This second effect is, in fact, quite important in the LiSAF laser.

II.4.B Gain Saturation Effects

Since CPA critically depends upon large stretching, effectively mapping the pulse spectrum into time, any temporal pulse shape distortion occurring during amplification will have a corresponding effect on the pulse spectrum amplitude. This distortion can adversely affect pulse recompression [80]. For this reason, it is important to examine the effects of gain saturation on pulses in a CPA scheme. Furthermore, solving the rate equations for a laser amplifier allow one to predict the actual gain of the amplifiers in the laser system; a gain value which may differ significantly from the small signal gain. It has

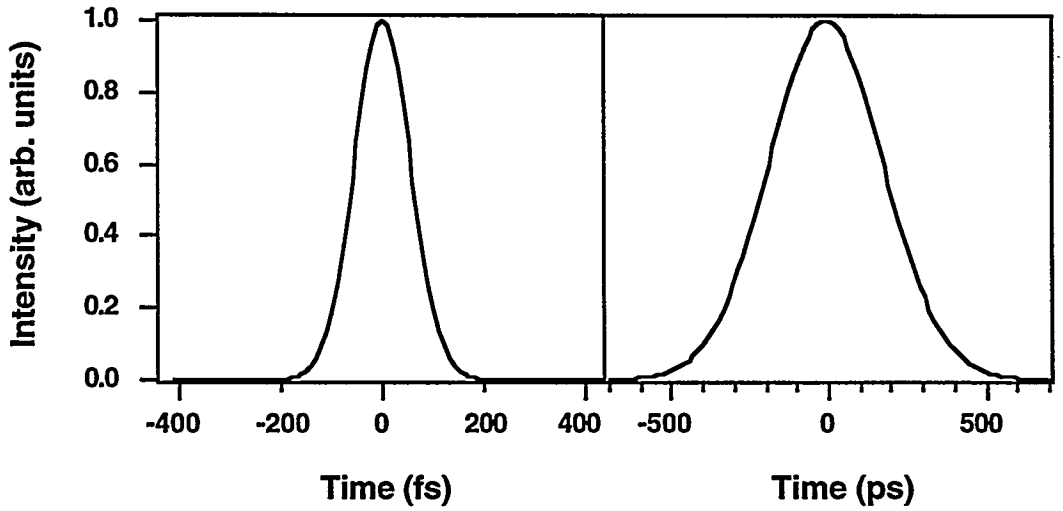

Figure II.22: Initial pulse (left curve) and calculated stretched pulse (right curve) for the grating stretcher used in the LiSAF laser.

been shown previously that the rate equations for a pulse in an amplifier are easily solvable if some simplifying assumptions are made [67]. We shall solve the equations through straightforward integration in a manner similar to that used in ref. [174].

- GENERAL THEORY OF GAIN SATURATION OF A LASER PULSE IN AN AMPLIFIER

We start with the equations that determine the time dependence of the number of photons per unit volume, $\phi(x,t)$, and the population inversion density, $N(x,t)$, in a laser amplifier. Here t is the time and x is the length along the laser amplifier rod parallel to the direction of light propagation. For a two level laser $N=N_2-N_1$ where N_2 is the population density of the upper laser level and N_1 is the population of the lower level. For simplicity, we consider only four level laser schemes like LiSAF; thus pumping the medium populates the upper level infinitely fast and the lower levels empties at an infinite rate.

The time rate of change of the inversion density is given by three terms. In all terms we assume that the upper and lower laser level have the same degeneracy. The first term is due to stimulated emission between levels 2 and 1 and is given by $N\phi\sigma c$. σ is the net cross section for stimulated transitions from level 1 to 2. The second term in the equation accounts for spontaneous decay with a characteristic time, t_f. These mechanisms include but are not restricted to the spontaneous emission rate of the upper state. Finally there is a pumping rate of the upper laser level, W_p. Thus we have:

$$\frac{\partial N}{\partial t} = -cN\phi\sigma - \frac{N}{t_f} + W_p \tag{2.30}$$

Next we have the equation for the photon density rate of change. This rate includes a term due to photon propagation, given by $c\,\partial\phi/\partial x$, a rate due to stimulated emission, and a rate due to spontaneous emission. We can generalize all losses due to other factors such as scatter and absorption in a term: $-\alpha\phi$. The photon equation is:

$$\frac{\partial \phi}{\partial t} + c\frac{\partial \phi}{\partial x} = c\phi\sigma N + \frac{N}{t_s} - \alpha\phi \tag{2.31}$$

To analytically solve these simultaneous, partial differential equations it is necessary to neglect some of the terms. We assume that the rate of stimulated emission in the amplifier is much greater than either the pumping rate or the rate of spontaneous emission so we can drop these contributions. It has been shown that these equations can be solved with the photon loss term included in the equations [7], but for simplicity we shall neglect this effect. This approximation is very good for modern, high quality, solid state laser materials in which the scattering losses are very low. We are therefore left with equations describing pulse propagation in a solid state amplifying medium. We wish to solve the equations for the intensity, I (where $I = \phi\hbar\omega$), and so the equations become.

$$\frac{\partial I}{\partial t} + c\frac{\partial I}{\partial x} = \sigma c N(x,t) I(x,t) \tag{2.32}$$

$$\frac{\partial n}{\partial t} = -\frac{\sigma}{\hbar\omega} N(x,t) I(x,t) \tag{2.33}$$

These equations can be easily integrated if we transform to a coordinate system that moves with the laser pulse:

$$\chi = x / c;$$
$$\tau = t - x / c$$

The rate eqs. (2.27) and (2.28) become:

$$\frac{\partial I}{\partial \chi} = \sigma c N(\chi,\tau) I(\chi,\tau) \tag{2.34}$$

$$\frac{\partial N}{\partial \tau} = -\frac{\sigma}{\hbar\omega} N(\chi,\tau)\, I(\chi,\tau) \tag{2.35}$$

The variable $\eta(\tau)$ is now introduced,

$$\eta(\tau) = c\int N(\chi,\tau)\, d\chi \tag{2.36}$$

$\eta(\tau)$ represents an averaged inversion density along the length of the amplifier rod. Using this definition, equation (2.34) can be easily integrated to give an expression for the output pulse shape.

$$I_{out}(t) = I_{in} e^{\sigma\eta(t)} \tag{2.37}$$

Finding the time dependence of the averaged inversion density solves the problem. To do this, integrate equation (2.35) over χ and substitute equation (2.34) for NI.

$$\frac{\partial}{\partial\tau}\int N\,d\chi = -\frac{\sigma}{\hbar\omega}\int N I\,d\chi \tag{2.38}$$

$$\frac{\partial\eta}{\partial\tau} = -\frac{1}{\hbar\omega c}\int\frac{\partial I}{\partial\chi}d\chi \tag{2.39}$$

$$\frac{\partial\eta}{\partial\tau} = -\frac{1}{\hbar\omega c}\left(I_{out}(\tau) - I_{in}(\tau)\right) \tag{2.40}$$

Use of the expression derived for the output intensity pulse shape, equation (2.37) renders a simple differential equation for $\eta(t)$.

$$\frac{\partial\eta}{\partial\tau} = -\frac{1}{\hbar\omega c}\left(e^{\sigma\eta(\tau)} - 1\right)I_{in}(\tau) \tag{2.41}$$

This equation is most easily solved if a parameter U is introduced:

$$U(\tau) = \int_{-\infty}^{\tau} I_{in}(\tau')d\tau' \tag{2.42}$$

U represents the input energy fluence. The solution for $\eta(t)$ now becomes:

$$e^{\sigma\eta(\tau)} = \frac{1}{1-\left(1-e^{-\sigma\eta_0}\right)e^{-\sigma U/\hbar\omega}} \tag{2.43}$$

We can now write the general expression for pulse propagation in an amplifier:

$$I_{out}(t - x/c) = I_{in}(t)\frac{1}{1-\left(1-e^{-\sigma\eta}\right)e^{-U/U_{sat}}} \tag{2.44}$$

where we have introduced the saturation fluence, $U_{sat} = \hbar\omega / \sigma$.

It is clear from this expression that U_{sat} serves to scale the effects of the input fluence, U. It is interesting to note that this saturation fluence depends only on the laser photon energy and the gain cross section. There is no dependence on the length of the laser rod itself or the initial inversion density. The resulting pulse shape, assuming an initial stretched pulse shape of that in figure II.22 is shown in figure II.23 for a number of total input energy fluences calculated from eq. (2.44). When $U \sim U_{sat}$ the pulse exhibits asymmetry as well as steepening on the leading edge. This steepening of the pulse, and therefore the spectrum, result in the production of wings in the compressed pulse. This can be understood when one considers a square spectrum (i.e. a very fast rise in the spectrum). The temporal pulse, a sinc^2 function, exhibits significant pre- and post- pulses from the lobes of the sinc function. From figure II.23, we see, however, that this is not significant for a fluence much below the saturation fluence.

To explore these effects in greater detail a code was developed to examine an arbitrary pulse propagating in a medium subject to equation (2.44) including the effects of gain depletion (which may be important in a multi-pass regenerative amplifier). This code numerically solves for the pulse phase and amplitude profile by using the formalism described in section II.4.A. To isolate the effects of the gain saturation on the pulse shape we ignore the nonlinear phase accumulation on the stretched pulse. The effects of the self-phase modulation on the stretched pulse will be considered in section II.4.C.

- NUMERICAL MODELING OF GAIN SATURATION

To illustrate the effects of the gain saturation we present calculations of the pulse shape distortion in the LiSAF regenerative amplifier. It is at this point in the laser chain that the energy fluence actually reaches its highest level (≥ 1 J/cm^2). For all LiSAF simulations the stretched pulse profile shown in figure II.22 is used. The amplifier rod, itself, has been given a small signal gain of 3.0 corresponding to an inversion density of

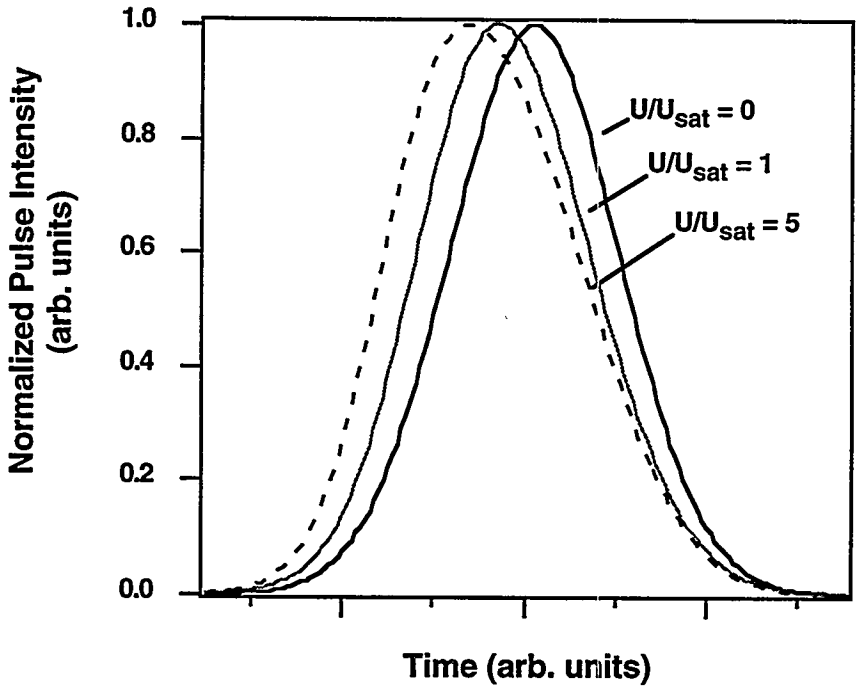

Figure II.23: Calculated pulse shapes for a pulse amplified in a gain rod with a small signal gain of 10 for three values of the input pulse energy fluence.

6.6×10^{18} cm^{-3} in a 5 cm long LiSAF rod. The effective gain cross section in LiSAF is reduced from 5.0×10^{-20} cm^2 to 3.3×10^{-20} cm^2 because of some excited state absorption [144]. Thus the effective saturation fluence of the LiSAF is 7.3 J/cm^2. Cavity losses have been set at 50%, and the spot size used in the simulation is 2 mm, approximating that of the LiSAF regenerative amplifier cavity described in section II.3.B. For simplicity, the effects of the spectral characteristics of optics in the regenerative amplifier were ignored as was any spectral narrowing from the LiSAF itself (which is in fact, negligibly small). The cavity is seeded with 0.5 nJ of energy.

Figure II.24 shows the calculated pulse energy as a function of round trips in the regenerative amplifier cavity. The energy predicted after 36 round trips in the cavity is

about 9 mJ, in good agreement with the experimental value of the extracted energy from the LiSAF regenerative amplifier. Figure II.25a compares the initial stretched pulse envelope that seeds the cavity with the calculated amplified pulse envelope with 8.6 mJ extracted from the cavity. (The seed pulse used in these calculations is that calculated in the previous section.) From this comparison it is clear that saturation effects are very small in the LiSAF regenerative amplifier. The recompressed pulse compared with the ideal Gaussian initial 120 fs pulse are shown in figure II.25b. The amplified pulse follows the ideal pulse over better than four decades of intensity. From this we conclude that saturation effects are negligible for the energies normally obtained with the

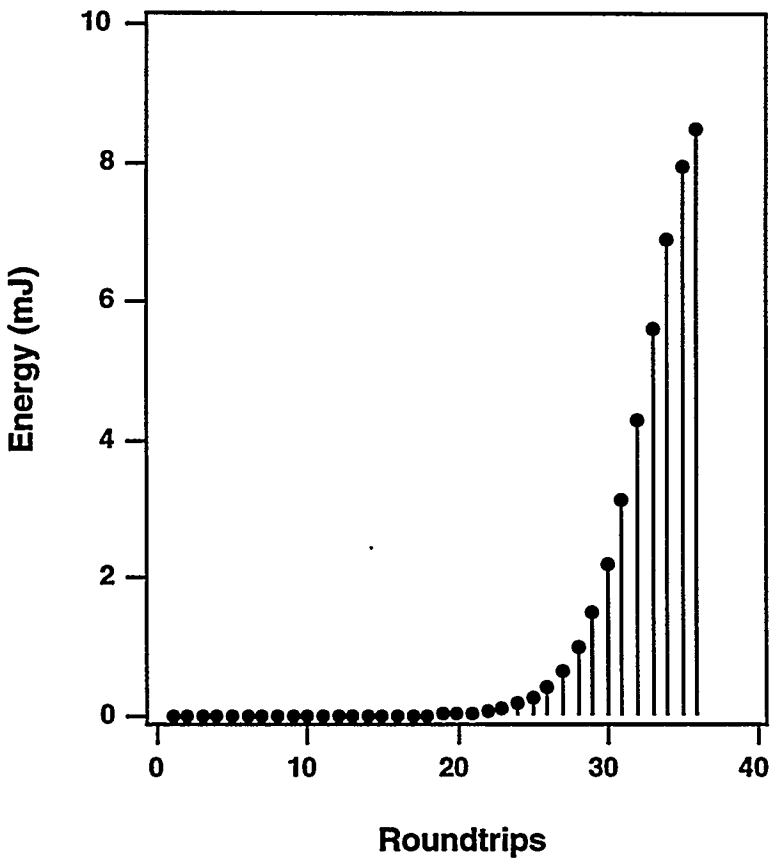

Figure II.24: Calculated energy after each round trip in the regenerative amplifier.

(a)

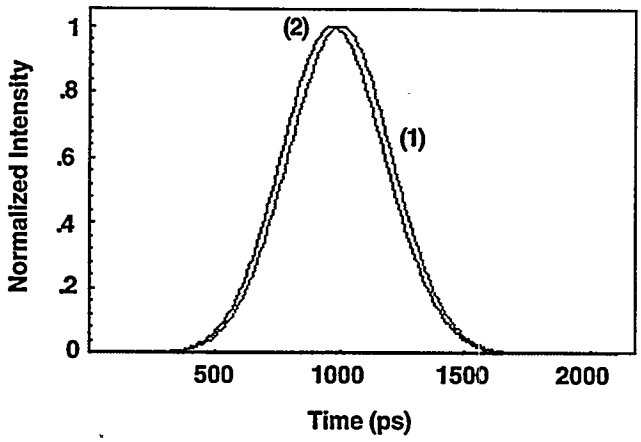

(b)

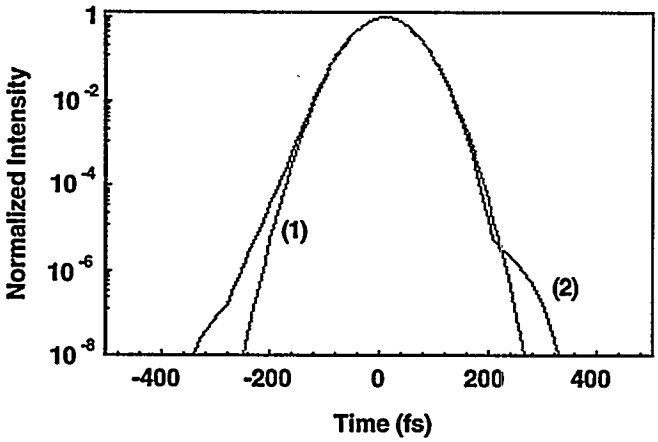

Figure II.25: **(a)** Calculated stretched pulse shape for the Cr:LiSAF system before (1) and after (2) amplification. **(b)** Recompressed pulse shape (2), and initial pulse shape (1).

(a) (b)

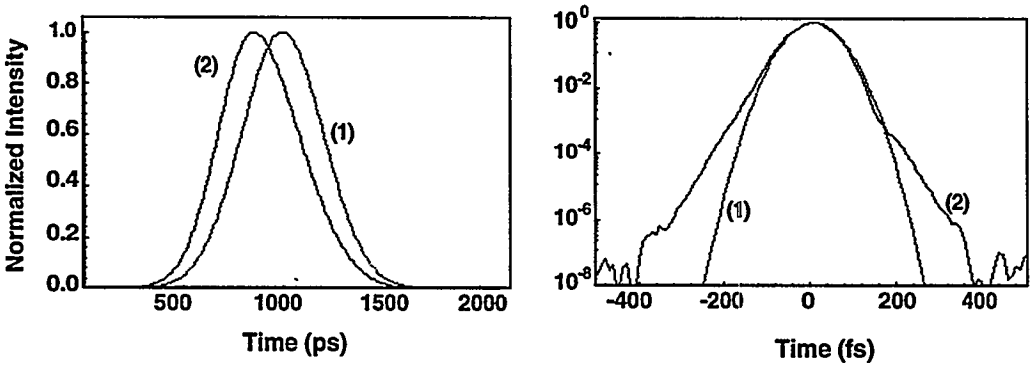

Figure II.26: The same calculation as in figure II.24 instead performed with a Ti:sapphire amplifier with an initial small signal gain of 10.

regenerative amplifier and that the recompressed pulse contrast should be better than 10^8:1 if other effects are ignored. This calculation is corroborated by the spectrum observed after amplification (figure II.6b). We observe no spectral pulling of the amplified spectrum which would indicate distortion from gain saturation.

For the sake of comparison with a different amplifier material, this calculation was also carried out for a similar regenerative amplifier utilizing Ti:sapphire, which has a much lower saturation fluence (~0.8 J/cm^2). For the sake of comparison the same cavity parameters as were used in the calculation described above with the exception that the amplifying medium was a Ti:sapphire rod with a single pass gain of 10. The results of a pulse amplified to 10 mJ after 10 round-trips are shown in figures II.26a and II.26b. Since we see no significant narrowing of the stretched pulse we do not observe any real broadening of the compressed pulse. However, it is clear from figure II.24a that saturation effects are much more significant for this case, and that, though the full width at half maximum of the pulse is not altered, the pulse contrast is seriously degraded. Though the amplified pulse follows the 100 fs Gaussian in the first two decades of intensity, the wings of the amplified pulse have been drastically increased. The sharpening of one edge of the spectrum (stretched pulse) has resulted in a severe deterioration of the pulse contrast ratio. For example, at 200 fs before the peak of the pulse the amplified pulse intensity is 10^3 times higher than the initial pulse.

II.4.C Self Phase-Modulation Effects

While gain saturation effects are unimportant in affecting the LiSAF laser, another nonlinear effect is, in fact, quite important. This effect arises from the accumulation of phase on the stretched pulse during its propagation through the amplifier chain due to the induced nonlinear refractive index of the material in the chain. This nonlinear phase, or B-integral is defined as:

$$B = \frac{2\pi}{\lambda}\int_0^L \gamma I(x)dx \tag{2.45}$$

where γ is the nonlinear index of refraction of the material through which the laser is propagating. In the design of any laser amplifier chain, the total, integrated nonlinear phase accumulated by a pulse upon amplification needs to be minimized. In CPA the nonlinear phase is minimized by stretching the pulse by a large factor (> 1000 x) prior to amplification thus reducing the peak intensity in the laser amplifiers. Nevertheless, some B-integral is inevitably accumulated even for large stretching ratios. The effects of temporal self phase modulation upon a pulse that is nearly transform limited are well known and the effect of this nonlinear phase on the pulse spectrum is well documented [82, 181]. Because of the dramatic manipulation of phase in chirped pulse amplification, however, the effects of self phase modulation on the broadband, laser pulse after recompression are significantly different [30, 130, 150].

Because of the mapping of frequency into time, any temporal phase modulation on the stretched pulse will manifest itself as spectral phase modulation on the compressed pulse. The resulting compressed pulse shape will then exhibit amplitude modulations similar to those exhibited by the spectrum of a phase modulated, initially transform limited pulse [181]. To estimate the extent of the pulse distortion caused by self-phase modulation we have analytically calculated the value of t^2 averaged over the compressed laser pulse subject to a B-integral of B_0 at the peak of the pulse by using the method of steepest descents [166]. The ratio of $\langle t^2 \rangle$ for the phase modulated pulse to that of the transform limited pulse can be written approximately as

$$\frac{\langle t_{B_0}{}^2 \rangle}{\langle t_0{}^2 \rangle} \cong 1 + \frac{4}{3\sqrt{3}} B_0{}^2 \tag{2.46}$$

This assumes a Gaussian initial pulse stretched to a pulse width that is much larger than the initial pulse width and that the stretcher and compressor gratings are perfectly matched

for a pulse experiencing no self-phase modulation. This result shows that a pulse will exhibit serious broadening for even moderate phase modulation (i.e. $B \approx 1$). Furthermore, because the phase modulation is not linear in time, it is not possible to effectively compensate for the phase distortion with the compression gratings [166].

To further investigate these effects a simple, one-dimensional numerical model was developed similar to the model of gain saturation. The stretched pulse shape and phase of the calculation in figure II.21 was used for the initial pulse. The resulting stretched pulse is propagated through the laser system by use of the nonlinear equations (2.19) and (2.20). Gain saturation effects have been ignored in this calculation. We assume, once again, that the phase function of the compressor grating-pair exactly cancels the phase of the stretcher gratings and the dispersion in the laser material to all orders so as to isolate the effect of the self phase modulation in the calculation.

The results of a calculation for a number of different B-integral values are shown in figure II.27. The calculated recompressed pulses are shown for the cases of B-integrals equal to zero (transform limited case), $B = \pi/4$ and $B = \pi/2$. The integrated energy in each pulse is normalized to that of the transform limited pulse. The effects of even a moderate amount of nonlinear phase are significant, reducing the peak power of the pulse with respect to the transform limited case and broadening the wings of the phase modulated pulse significantly. These calculations indicate that for a B-integral value of $\pi/2$, the peak intensity of the pulse is reduced by 25% and the pulse contrast is seriously degraded. The intensity 400 fs before the pulse peak for the $B = \pi/2$ case is over one order of magnitude higher than that for the $B = 0$ case.

To experimentally confirm this pulse broadening, we examined the autocorrelation of the recompressed pulse as a function of B-integral in the LiSAF regenerative amplifier [150]. The experimental configuration is shown in figure II.28. For these measurements, the amplifier chain was bypassed to preserve the Gaussian beam profile of the regenerative amplifier. The pulse is amplified up to 20 mJ and the output of the regenerative amplifier

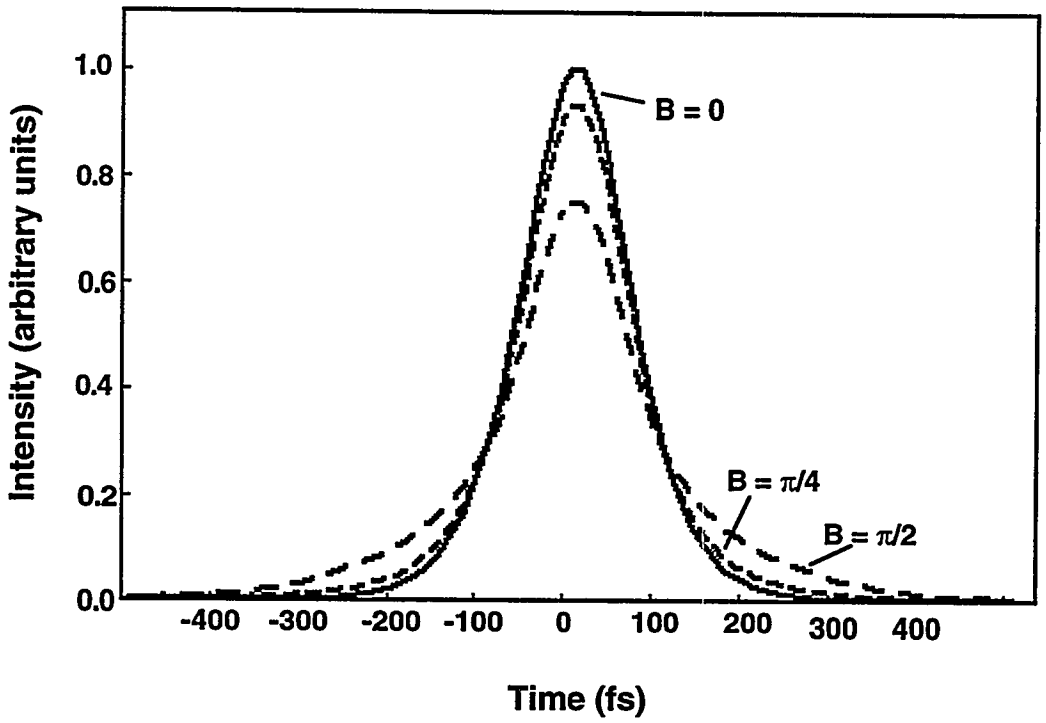

Figure II.27: Numerically calculated recompressed pulse shapes for a 130 fs pulse, initially stretched to 450 ps and subject to three different values of nonlinear phase, B = 0, B = $\pi/4$, and B = $\pi/2$.

is immediately recompressed. By keeping the number of round trips in the cavity constant and by varying the gain in the LiSAF amplifier rod, the energy fluence, and therefore the total B-integral, is varied without changing the amount of dispersive material traversed by the pulse. Furthermore, the TEM_{00} character of the regenerative amplifier cavity assures a very smooth beam and helps eliminate any uncertainty in the laser fluence or any spatial inhomogeneities that might effect the single shot autocorrelation measurement. The autocorrelation was taken from the central part of the Gaussian beam profile so as to probe the highest intensities.

To directly measure the variation of B-integral with output energy the Gaussian spatial mode of the output pulse from the regenerative amplifier was monitored on a CCD camera on a shot to shot basis. Whole beam self-focusing inside the regenerative amplifier cavity causes a small variation in the size of the output beam [183]. A simple

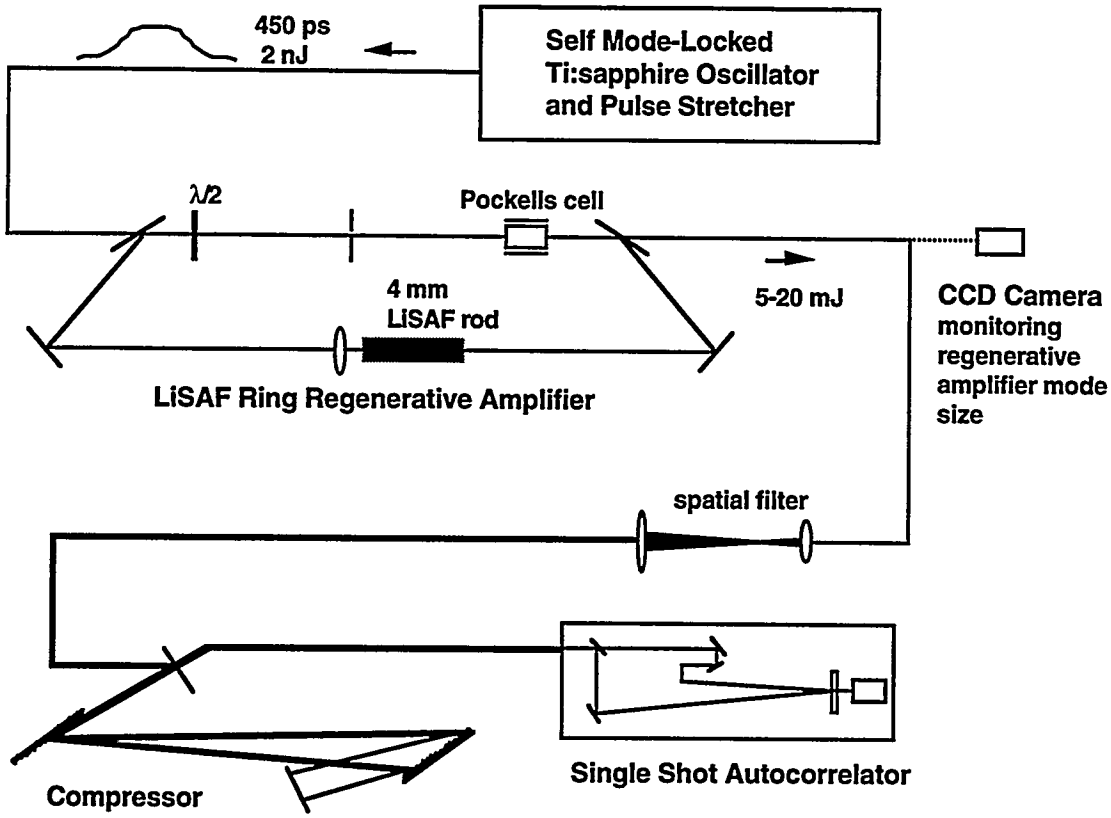

Figure II.28: Experimental layout for the measurement of self-focusing and self-phase modulation of a stretched pulse.

cavity mode analysis including self-focusing inside both the laser rod and the Pockels cell KDP crystal yields an accurate estimation of the total B-integral accumulated inside the cavity. The measured $1/e^2$ diameter of the output beam as a function of output energy is shown in figure II.29. A solid line representing the cavity analysis model is shown fit to these data points. The model has a single adjustable parameter, the nonlinear refractive index of the LiSAF. The solid line in figure II.29 was obtained with $n_2 = 5 \times 10^{-14}$ esu, in good agreement with earlier calculated estimates [142].

After the amplified beam was recompressed, the second order intensity autocorrelation was measured. Two measured autocorrelations at low and high output fluence are shown in figure II.30a, both normalized to a peak value of one. One curve is the autocorrelation at 1.5 mJ ($B \approx 0.1$) representing a clean 130 fs pulse. The second

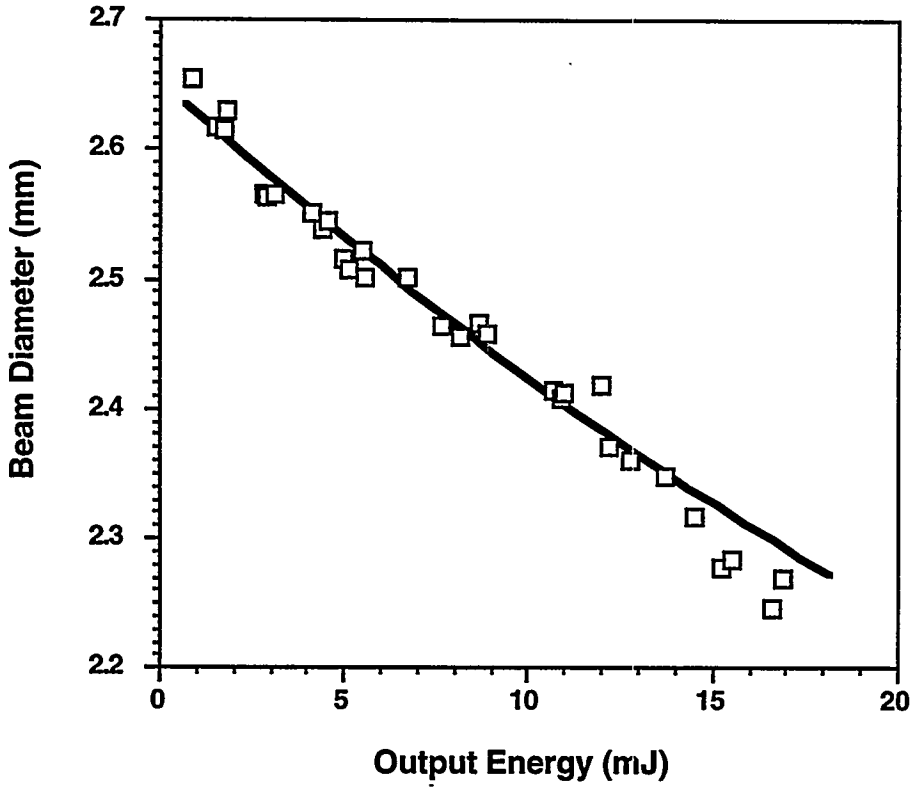

Figure II.29: Measurement of the Gaussian beam size 230 cm from the waist inside the regenerative amplifier cavity as a function of output energy. The solid line is the beam size predicted using a cavity analysis model that accounts for the whole beam self-focusing inside the cavity.

curve is an autocorrelation trace at 16.9 mJ from the regenerative amplifier cavity ($B \approx 1.3$). The broadening of the pulse is clearly evident as is the severe degradation of the pulse contrast. The autocorrelations for these B-integral values calculated from the model are also shown on this plot as solid lines. The experimental curves show very good agreement with the calculated autocorrelation curves. The 16.9 mJ compressed pulse has a peak intensity that is reduced by roughly 27% from that of a transform limited pulse shape, in good agreement with the one-dimensional model.

(a)

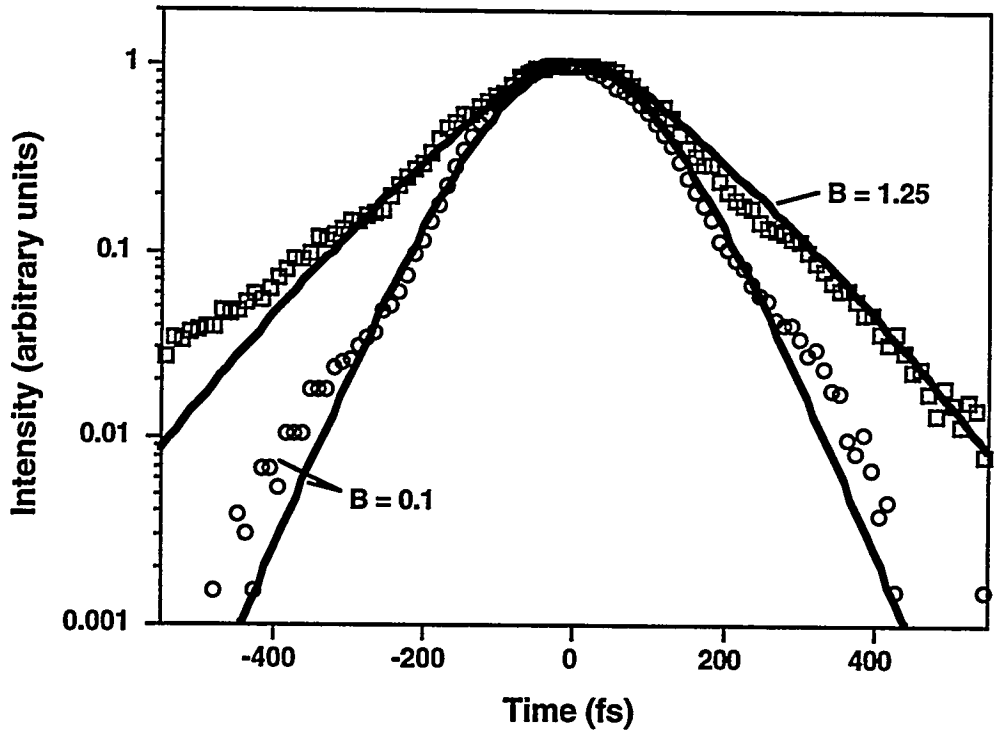

(b)

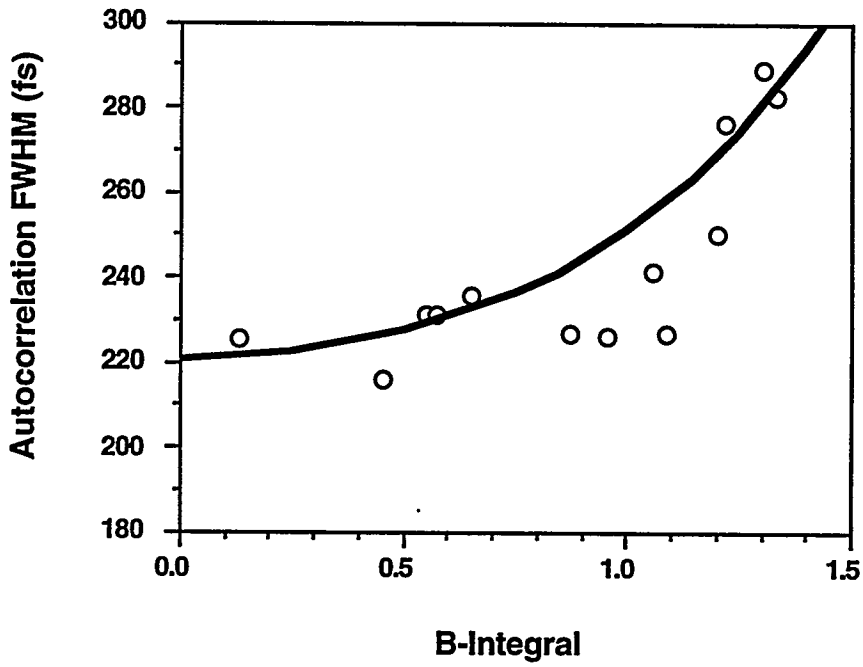

Figure II.30: **(a)** Comparison of the measured autocorrelation profiles with the results of the 1-D calculation for two different values of the B-integral. The points are the data and the solid lines are the calculation. **(b)** Comparison of the measured autocorrelation full width at half maximum with the calculated width as a function of the accumulated B-integral in the regenerative amplifier cavity.

Using the model we calculated the expected autocorrelation full width at half maximum as a function of total B-integral. This curve is compared with the measured autocorrelation full width as a function of B-integral in figure II.30b. As can be seen here, our data is in good agreement with the numerically calculated autocorrelation widths. The measured pulse width begins to noticeably broaden with B-integral values above 1.0.

We observe negligible modification of the pulse spectrum with the increasing width of the autocorrelation. This is because the frequency modulation resulting from self-phase modulation is determined by the time derivative of the nonlinear phase: $\omega(t) = \omega_0(t) - \partial B / \partial t$. Therefore, the fractional increase in bandwidth is: $\Delta\lambda_B / \Delta\lambda_0 \approx B\tau_p / \tau_s$. For our stretcher $\tau_p / \tau_s \approx 2 \times 10^{-4}$ so the change in bandwidth is negligible. Nonetheless, this analysis and data illustrate the dramatic effect that moderate phase modulation can have on the recompression of pulses in CPA. These effects are independent of initial pulse width; they depend only on the value of the peak B-integral and the fact that the pulse has been stretched by a large factor.

The most important feature of the phase modulation effect is a significant distortion of the recompressed pulse shape for even a modest integrated nonlinear phase. Significant energy can be removed from the central peak of the pulse and pushed into the pulse wings, severely degrading pulse contrast and lowering the pulse peak intensity. Consequently, the design of CPA systems must take into consideration these consequences which become important at B-integral levels that are typically considered safe for most amplifier systems.

II.5 Conclusion

In this chapter we have described a compact Cr:LiSAF laser system capable of producing femtosecond pulses with an energy of one joule. The system employs a

flashlamp pumped, 19 x 110 mm amplifier producing a radially averaged single pass gain of 4.8 for a pump energy of 3 kJ. This permits amplification of stretched pulses to an energy of 1.7 J at a repetition rate of one shot every 20 sec. Recompression results in a transform-limited 125 fs, 1.05 J pulse with a corresponding peak power of 8.5 TW. We have shown that flashlamp UV shifting sets an upper limit on the pump efficiencies that are possible with LiSAF. Though good pump efficiencies (~ 1.5 %) are possible, further shortening of the flashlamp light or discharge of higher energies will not necessarily increase the gains possible in large aperture LiSAF amplifiers.

We have also examined some of the consequences of nonlinear propagation effects on the recompression of pulses in chirped pulse amplification. In particular, the effects of gain saturation and self phase modulation were examined with a simple 1-D numerical code. We found that gain saturation effects were unimportant in the LiSAF system but that the phase modulation can be very important. We confirmed the predictions of the phase modulation code experimentally by examining the intensity autocorrelation of pulses amplified in a LiSAF ring regenerative amplifier. The most important feature of the phase modulation effect are a significant distortion of the recompressed pulse shape for even a modest integrated nonlinear phase. Significant energy can be removed from the central peak of the pulse and pushed into the pulse wings, severely degrading pulse contrast and lowering the pulse peak intensity.

Chapter III

Physics of the Interaction of Short, Intense Laser Pulses with Atoms in a Gas

III.1 Strong Field Interactions and the Ponderomotive Potential

The primary topic of this work is the examination of soft x-ray generation through the interaction of intense, short laser pulses with atoms and clusters in a gas. Before moving on to the specifics of these investigations it is useful to examine some of the general aspects of strong field interactions of laser pulses with atoms and plasmas. The purpose of this chapter is to introduce some of the basic concepts that are relevant for the investigations of the next two chapters.

First we shall consider the consequences of driving an electron in an atom in a strong laser field. Due to the anharmonic nature of the atomic binding potential, such laser driven oscillations will give rise to electron oscillations at harmonics of the laser frequency. When the atom is driven with a field that is of sufficient strength, this phenomenon can give rise to high order harmonic generation in which the harmonic wavelength lies within the soft x-ray region. Second we shall examine the manner in which a plasma is formed during the interaction of an intense laser with a gas. We will consider the consequences that this has on the laser pulse itself during propagation

through the plasma. We will, also, investigate a variety of electron heating mechanisms in the plasma in detail and consider the magnitude of each one under the conditions of interest for x-ray generation.

The heating of a plasma is of interest because the ability to convert laser light to x-ray photons relies on the fact that the laser field can efficiently couple many photons worth of energy to an electron during the laser pulse. That an intense focused laser pulse is optimum for producing electrons with large kinetic energies can be seen when one considers that electrons oscillating in a strong laser field can have kinetic energy far above that of the typical binding energies of neutral atoms. If we assume that the electron oscillates in free space in the absence of an atomic ion, the classical electron motion can be described by the equation

$$m_e \ddot{x}(t) = eE_0 \sin \omega_0 t \tag{3.1}$$

The electron's kinetic energy due to oscillations in the laser field is

$$\tfrac{1}{2} m_e \, \mathrm{v}(t)^2 = \frac{e^2 E_0^{\,2}}{2 m_e \omega_0^{\,2}} \cos^2 \omega_0 t \tag{3.2}$$

The cycle averaged kinetic energy of the electron, or the so called quiver or ponderomotive energy of the electron, is

$$U_p = \tfrac{1}{2} m_e \langle \mathrm{v}^2 \rangle = \frac{e^2 E_0^{\,2}}{4 m_e \omega_0^{\,2}} \approx 9.33 \times 10^{-14} I(W/cm^2)(\lambda(\mu m))^2 \tag{3.3}$$

Thus, at an intensity of 10^{16} W/cm^2 in a laser of $\lambda = 1$ μm, the electron quiver energy is 1 keV, 1000 times larger than the energy of a laser photon.

This oscillation energy is not permanently transferred to the electron during the laser pulse if no other force acts on the electron. Thus, if the electron starts at rest and the laser pulse is turned on slowly over many cycles, a case that is well satisfied for all visible wavelength pulses with Gaussian or similar pulse envelopes with width of 100 fs or

greater, then the electron will return to a state of rest after the laser pulse passes. Only if another force is present to break the adiabaticity of the pulse rise and fall, such as that from the presence of a charged ion, can some of this coherent oscillation energy be transferred to the electron.

III.2 High Order Harmonic Generation: Laser Driven Oscillations in Atoms

III.2.A Nonlinear Polarization of Strongly Driven Atoms

The first interaction of a short, intense laser pulse with the atoms in a gas that we shall consider is that in which the laser drives oscillations of the electron wavefunction in the presence of the anharmonic potential of an atom. This gives rise to harmonic generation due to the induced dipole of the electron - ion pair [22, 162]. The emitted radiation from a medium with these oscillating electrons comes from the polarization of the individual atoms adding coherently. This polarization is

$$\mathbf{P}(t) = N_0 \mathbf{d}(t) \tag{3.4}$$

where N_0 is the density of emitters in the medium and $\mathbf{d}(t)$ is the atomic dipole moment. This dipole moment is found from the wavefunction of the electrons driven by the laser field:

$$\mathbf{d}(t) = \langle \psi(t) | e\mathbf{r} | \psi(t) \rangle \tag{3.5}$$

where $\psi(t)$ is the wavefunction of the electron in the laser field. This wavefunction is found from the time dependent Schrödinger equation (in the dipole approximation):

$$i\hbar | \psi(t) \rangle = -\frac{\hbar^2}{2m_e} \nabla^2 | \psi(t) \rangle + V_{atom} | \psi(t) \rangle - exE(t) | \psi(t) \rangle \tag{3.6}$$

Here V_{atom} is the potential of the atom felt by the oscillating electron and $E(t)$ is the electric field of the laser. We can describe this field as $E(t) = E_0 \sin \omega_0 t$.

At low field strengths, the electron oscillates only at the fundamental frequency of the laser, ω_0. In stronger fields, the electron oscillations contain higher frequency components due to the fact that the atomic potential is anharmonic. In the absence of any additional fields to break the symmetry of the atom, the electron can only oscillate at odd integer multiple of the laser frequency. The atomic dipole can be expanded in a Fourier series containing these higher oscillation frequencies:

$$\mathbf{d}(t) = \sum_{q=odd} \left[\mathbf{d}(q\omega_0) e^{-iq\omega_0 t} + c.c. \right] \tag{3.7}$$

We assume that the temporal variation of $\mathbf{d}(q\omega_0)$ is much slower than any harmonic oscillation. The polarization of the medium can then be expanded as

$$\mathbf{P}(t) = N_0 \sum_{q=odd} \left(\mathbf{d}(q\omega_0) e^{-iq\omega_0 t} + c.c. \right) \tag{3.8}$$

It is this nonlinear polarization that gives rise to harmonic generation.

First, we shall consider the situation when the field is not too large, (i. e. it is small with respect to the field of the atom). In this case we can expand the nonlinear polarization in powers of the induced electric field [22]:

$$\mathbf{P}_q = 2^{1-q} N_0 \chi_q(-q\omega_0; \omega_0, \omega_0, \ldots, \omega_0) |\mathbf{E}|^{q-1} \mathbf{E} \tag{3.9}$$

where we have defined the qth order susceptibility, $\chi_q(-q\omega_0; \omega_0, \omega_0, \ldots, \omega_0)$. The picture of harmonic generation in this weak field, perturbative limit is illustrated in figure III.1. The generation of the qth harmonic can be seen as an absorption of q laser photons by the atom followed by an emission of one photon of energy $q\hbar\omega_0$. The reason for odd harmonic generation can also be understood in this perturbative view. The transition from

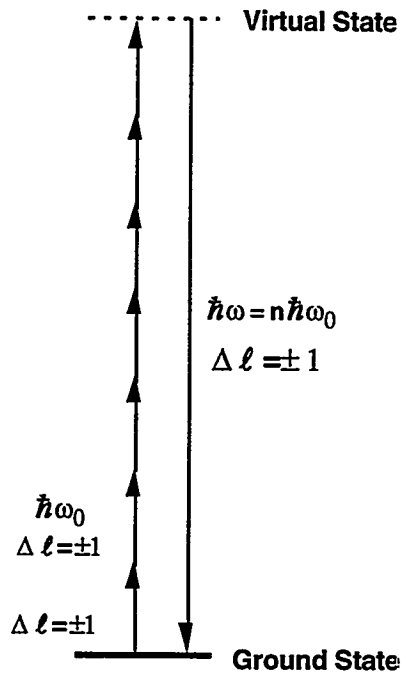

Figure III.1: Schematic of the multiphoton picture of high harmonic generation by a linearly polarized laser pulse.

the virtual state to the atom ground state in the harmonic emission process must be a dipole allowed transition, i. e. $\Delta\ell = \pm 1$. Only the absorption of an odd number of photons will allow this condition to be satisfied.

The physical origin of harmonics from an electron oscillating in an anharmonic potential can also be seen by a very simple exercise. Consider a particle driven by a sinusoidal force in a symmetric anharmonic potential according to the equation:

$$\ddot{x} + \gamma\dot{x} + \Omega^2 x + \varepsilon x^3 = E\cos\omega_0 t \tag{3.10}$$

The harmonic spectrum of such a system can be retrieved by a Fourier transform of the particle displacement, x. The Fourier spectrum from a numerical solution of this equation with γ=1, ω_0=10Ω, ε=200, and E = 600 is shown in figure III.2. A comb of harmonics extending out to the 41st order results. This calculation also exhibits some of

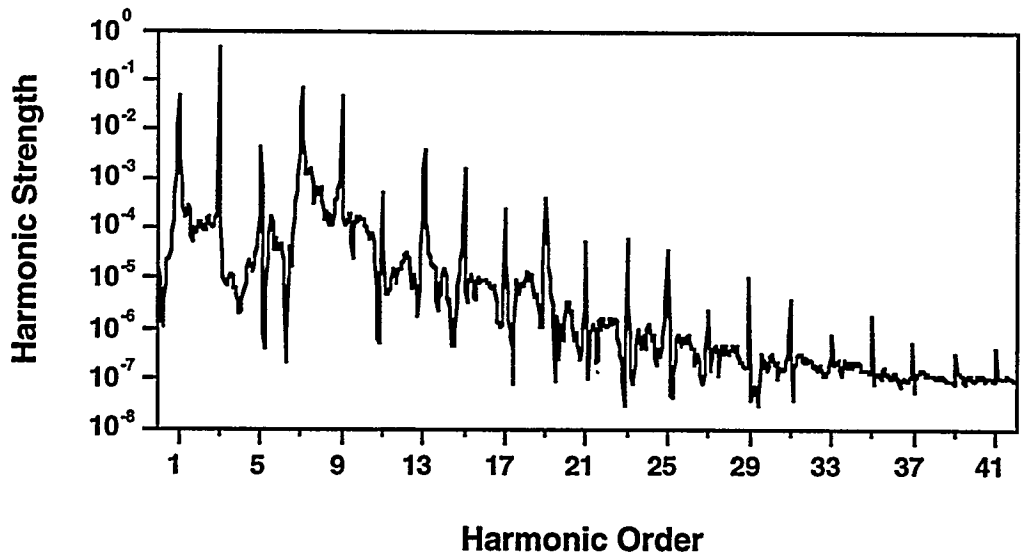

Figure III.2: Calculated harmonic spectrum from a classical, anharmonic oscillator driven by a strong field.

the characteristics of strong field harmonic generation. In particular, the spectrum exhibits harmonics that drop off rather slowly with increasing harmonic order.

III.2.B Quasi-Classical Model of Strong Field Harmonic Generation

Though the perturbative, "multiphoton" picture of harmonic generation illustrated in figure III.1 is informative, when the laser field strength becomes comparable to the atomic field strength, this picture breaks down as we discussed in chapter I. This strong field regime begins with laser intensity roughly $\geq 10^{14}$ W/cm^2. The perturbative picture predicts that the yield of successively higher order harmonics will decrease exponentially. Though this is experimentally observed for the first few orders of harmonics (i. e. $q \leq 7$) the higher orders typically do not fall off this fast [102]. This phenomena can be seen in the classical particle of figure III.2 which roughly corresponds to a "strongly driven" case.

Since the perturbative picture breaks down in the high field regime, in general, a full solution of the Schrödinger equation is required to retrieve the harmonic spectrum. This has been performed by a number of people and the nonperturbative behavior of the

harmonics has been recreated in these simulations [94]. These calculations are cumbersome, however, and a more intuitive view of the high field harmonic generation process is desirable.

One such model, first proposed by Corkum [32] and later expanded by Kulander et. al. [96], takes advantage of the fact that, in high field strengths, the electron typically acquire large oscillation velocity and have a characteristic oscillation amplitude that is larger than the atom itself. We can then utilize a simplification which we will find very useful later in this chapter to explain a host of physical processes. We can treat the electron trajectory classically. In this model, the electron is freed from the atom by direct ionization in the laser field. The electron follows a classical oscillation trajectory. If the electron was born at a phase of the field such that it returns to the atom nucleus, it can recombine and emit a harmonic photon. The energy of this photon will be equal to the ionization potential of the atom, if we assume that the electron drops back to the atom ground state, plus the kinetic energy the electron acquired in the laser field.

To treat this process quantitatively we need only consider the classical trajectory of an electron in the laser field. We shall assume that the electron is "born" through tunnel ionization at a well defined phase in the field. This time of ionization is t_0. We assume the electron is born with zero velocity at the position of the atom. After ionization we shall ignore the force of the atom on the electron; this is a good assumption since the laser field strongly drives the electron oscillation. The electron is subject to a force:

$$F(t) = eE_0 \sin \omega_0 t \tag{3.11}$$

Using the fact that $\mathrm{v}(t_0) = 0$, the electron velocity is

$$\mathrm{v}(t) = -\frac{eE_0}{m_e \omega_0}\left(\cos \omega_0 t - \cos \omega_0 t_0\right) \tag{3.12}$$

which implies that the electron's instantaneous kinetic energy, $K(t)$, is given in terms of the ponderomotive potential as:

$$K(t) = 2U_p\left(\cos\omega_0 t - \cos\omega_0 t_0\right)^2 \tag{3.13}$$

The electron position with respect to the stationary atom is

$$x(t) = -\frac{eE_0}{m_e\omega_0^{\,2}}\left(\sin\omega_0 t - \sin\omega_0 t_0 - \omega_0\left(t - t_0\right)\cos\omega_0 t\right) \tag{3.14}$$

To find the harmonic spectrum, we merely need to find the phase of ionization that allows the electron to return to the nucleus and emit a harmonic photon. This is done by finding the zeros of eq. (3.14). The energy of the harmonic photon for each return to the nucleus is found by summing the instantaneous kinetic energy, eq. (3.13), with the ionization potential of the atom. To generate a "harmonic" spectrum, we histogram the energy for the electron returns for a range of ionization times, t_0. The energy is weighted by the probability of ionization at the phase $\omega_0 t_0$. The ionization is through tunnel ionization in the laser field, a process that will be discussed in greater detail in the next section. For the simple calculation we use the simple DC tunneling rate formula for a hydrogenic atom [104]:

$$W_{DC} = 4\omega_a\left(\frac{I_p}{I_H}\right)^{5/2}\frac{E_a}{E(t)}\exp\left[-\frac{2}{3}\left(\frac{I_p}{I_H}\right)^{3/2}\frac{E_a}{E(t)}\right] \tag{3.15}$$

where I_p is the atom ionization potential, I_H is hydrogen's ionization potential (= 13.6 eV), ω_a is the atomic unit of frequency (= 4.1 x 10^{16} s^{-1}) and E_a is the atomic field strength (= 5.1 x 10^9 V/cm). Finally we weight the histogram by the probability of a returning electron to recombine. For a hydrogenic atom this probability is proportional to $\sim 1/\Delta E_{if}^{\,3}$.

A "harmonic spectrum" calculated by this classical trajectory method is shown in figure III.3 for a laser intensity of 5 x 10^{14} W/cm^2 and an atom with an ionization

potential of 15.7 eV (which corresponds to argon). The most striking aspect of this spectrum is a relatively flat plateau that extends to an abrupt cut-off at an energy value of:

$$\hbar\omega_{max} \approx I_p + 3.2U_p. \tag{3.16}$$

This cut-off results from the fact that $3.17U_p$ is the highest energy that the electron can have upon return to the atom and is a consequence of equations (3.13) and (3.14). This harmonic cut-off law was first proposed by Krause et.al. [94] as an empirical scaling derived from numerical solution of the Schrödinger equation.

Experimental results on harmonic generation typically mirror this plateau and cut-off behavior [102]. An experimental study of this law is presented in chapter IV. The validity of this quasi-classical model of harmonic generation has also been confirmed in

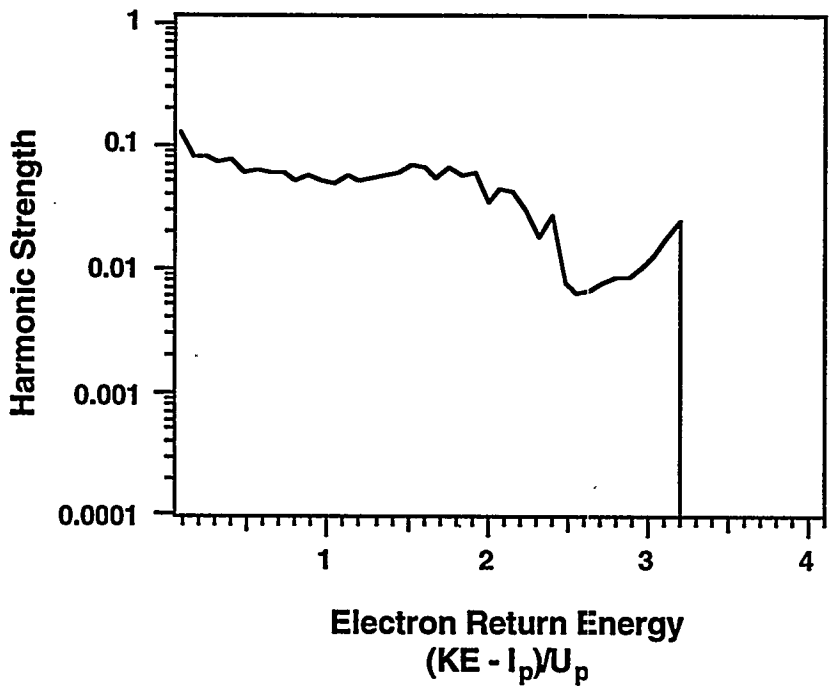

Figure III.3: Harmonic spectrum calculated by the classical trajectory method for a laser intensity of 5 x 10^{14} W/cm^2 and an atom with an ionization potential of 15.7 eV. This represents a histogram of electron energies upon return to the atom's nuclei for many different phases of the electron's birth by tunneling in the laser field.

studies of harmonic dependence on laser ellipticity. Since a small amount a ellipticity on the laser field will prevent the ionized electron from coming back to the vicinity of the nucleus to emit a harmonic photon, the harmonic yield should be sensitive to this parameter. This has been confirmed experimentally by a number of groups [24, 26].

Most importantly, this analysis indicates that harmonics are a means of producing soft X-ray radiation. For example, the cut-off law, eq. (3.16), predicts that a helium atom (I_p = 24.6 eV) illuminated by an 825 nm laser at an intensity of 5 x 10^{14} W/cm^2 (Up = 46.6 eV) will be able to produce harmonics with energy up to 180 eV, a wavelength of 70Å. This is the greatest attraction of the study of high order harmonics: the coupling of laser energy to soft x-ray radiation.

III.2.C Propagation Equations In the Weak Field Limit

Before moving on to the description of other phenomena it is useful to consider the propagation equation of the harmonics. Since harmonic generation is a parametric process, the manner in which the various frequency fields propagate is of importance in determining the net harmonic yield and coherence of the radiation generated . A general solution of the wave equation for the harmonics produced by a strong field will be presented in chapter IV. To gain some insight into this physics, however, we now consider the wave equation for harmonics produced by a focused Gaussian beam in the weak field, perturbative limit. We do this merely for illustrative purposes. This analysis is, in general, not applicable to the strong field harmonic generation but does yield some useful insight into the geometrical effects of focusing on phase matching.

The paraxial wave equation for the field amplitude of the qth harmonic, E_q, in the weak field limit is [22]:

$$2ik_q \frac{\partial E_q}{\partial z} + \nabla_\perp{}^2 E_q = -\frac{4\pi\omega_q}{c^2}\chi_q E_0{}^q e^{i\Delta kz} \tag{3.17}$$

where we have introduced the phase mismatch $\Delta k = k_q - qk_0$. If the laser beam can be described by a focused Gaussian beam with a spot size w_0, then we can describe the harmonic field as a product of an amplitude that varies with z and a radially dependent term:

$$E_q(r,z) = a_q(z)\frac{1}{1+2iz/b}\exp\left[-\frac{qr^2}{w_0^{\,2}(1+2iz/b)}\right] \tag{3.18}$$

Upon substitution of eq. (3.18) into eq. (3.17) we have that the harmonic amplitude is described by

$$a_q(z) = \frac{i2\pi q\omega_0}{c}\chi_q E_0^{\,q}\int_{-l/2}^{l/2}\frac{e^{i\Delta kz'}}{(1+2iz'/b)^{q-1}}dz' \tag{3.19}$$

This integral is the well known phase matching integral [22]. We have assumed that the laser is focused in the center of a medium with length l. Since we are concerned with the optimization of the harmonic generation, we wish to minimize the effects of the geometric phase mismatch in determining the harmonic amplitude. This geometric phase mismatch arises from the π phase shift associated with a Gaussian beam passing through a focus [174]. Thus, when the confocal parameter is short with respect to the medium, the harmonics generated on one side of the focus will destructively interfere with the harmonics generated on the other side of the focus. This effect can be seen in eq. (3.19) when $z'/b >> 1$; in this case the integral goes to zero for an odd q. This effect can be avoided, however, with "weak focusing" in which the laser is focused such that the confocal parameter, b, is much longer than the medium interaction length, l. In this limit, the phase matching integral can be evaluated to yield

$$\left|a_q(z)\right| = \frac{2\pi q\omega_0}{c}\chi_q E_0^{\,q} l\frac{\sin(\Delta kl/2+(q-1)l/b)}{(\Delta kl/2+(q-1)l/b)} \tag{3.20}$$

From this equation, it is clear that a phase mismatch arising from differences in the refractive indices of the laser and the harmonic can cause a limitation on the harmonic generation through the $\sin(\Delta kl/2)/(\Delta kl/2)$ term. The implications of this dependence for a phase mismatch arising from the presence of a free electron plasma will be considered in detail in chapter IV. Furthermore, we see that an additional term is added to the phase mismatch. This term, equal to $(q-1)l/b$ arises from the geometrical phase mismatch. Consequently, the harmonics produced by a focused Gaussian beam have an effective coherence length, $L_{coh} \approx \pi b/2q$ [102]. Radiation generated in the qth harmonic will only interfere constructively when produced over this coherence length. It can be shown that this coherence length is also approximately correct for harmonics produced in the strong field limit as well [102].

III.3 Plasma Formation During the Intense Irradiation of a Gas

In addition to harmonic generation, another consequence of focusing intense pulses in a gas is the rapid optical ionization of the atoms in the gas. This process competes with the harmonic generation in a strong laser field. The result is rapid plasma formation during the time frame of the laser pulse. A description of this plasma formation is necessary to understand its effects on the harmonic generation (which will be considered in chapter IV) as well as the other mechanisms of x-ray generation considered in this work. For example, the formation of a plasma through ionization during the laser pulse can have deleterious effects on the propagation of the laser pulse itself through self-phase modulation and refraction.

III.3.A Tunnel Ionization of Atoms in a Strong Laser Field

In the regime of interest for our experiments, the Keldysh parameter is typically less than one, as discussed in the introduction. Consequently the optical ionization of atoms is primarily though tunneling. As we discussed in chapter I, this picture of tunneling is consistent with our quasi-classical picture of the electron motion in the field. A schematic of the physics of tunnel ionization is shown in figure III.4. An electron bound by the coulombic potential of the atom is shown in figure III.4a. When a laser field is applied, it distorts the potential in the manner shown in figure III.4b. The electron may then tunnel through the barrier on a time scale much faster than the laser oscillation and free itself from the atomic binding potential.

The intensity at which this rate becomes significant can be easily estimated by calculating the intensity required for the laser field to lower the barrier down to the electron binding energy. This "barrier suppression model," first proposed by Augst et. al. [6], has been shown to be in reasonable agreement with ionization experiments conducted with a 1 ps laser [6]. To calculate this barrier suppression intensity we say that the potential seen by an electron in a coulomb potential with a field of E_0 is

$$V(r) = -\frac{Ze^2}{r} - eE_0 r \tag{3.21}$$

From this we find the peak of the potential:

$$\frac{\partial V}{\partial r} = \frac{Ze^2}{r^2} - eE_0 = 0 \tag{3.22}$$

which implies that the coulomb barrier is suppressed at a radius of

$$r_{peak} = \sqrt{\frac{Ze}{E_0}} \tag{3.23}$$

To find the electric field required for ionization we set the potential at the peak equal to the ionization potential of the atom:

(a)

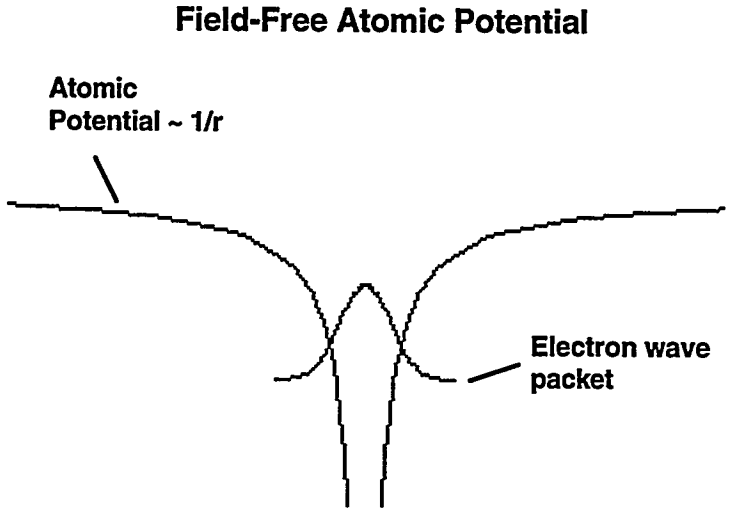

(b)

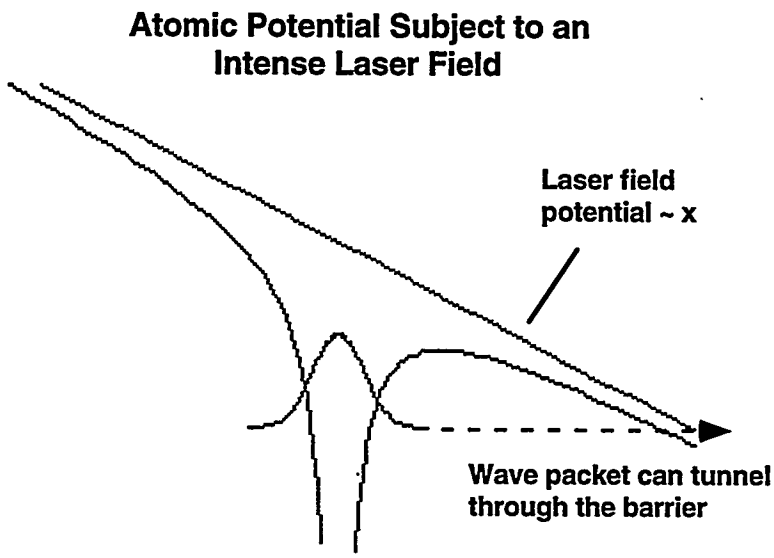

Figure III.4: **(a)** Illustration of a bound electron wavepacket in the coulomb potential of an atom. **(b)** Distorted potential of an atom with a strong laser field present. The laser potential oscillates back and forth. When the laser field is sufficiently strong, the wavepacket can tunnel through the barrier and ionize.

$$V(r_{peak}) = -2Z^{1/2}e^{3/2}E_0^{1/2} = -I_p \tag{3.24}$$

Since the laser intensity is given as $I = (c/8\pi)|E_0|^2$, then the threshold intensity for the barrier suppression of the atom is

$$I_{thresh} = \frac{cI_p^{\,4}}{128\pi Z^2 e^6} = 4.0\times10^9 \frac{\left[I_p(eV)\right]^4}{Z^2} \quad (W/cm^2) \tag{3.25}$$

This relation suggests, for example, that Ar (I_p = 15.7 eV) will ionize with an intensity of 2.5 x 10^{14} W/cm^2, He (I_p = 24.6 eV) will ionize with an intensity of 1.5 x 10^{15} W/cm^2 and Ar^{8+} (I_p = 422 eV) will ionize with an intensity of 1.5 x 10^{18} W/cm^2.

This relation is useful for estimating the appearance intensity of a particular charge state by tunneling. It, however, does not accurately predict the actual ionization rate for tunneling. The general relation for the tunneling rate of an electron in a complex atom has been worked out by Ammosov, Delone and Krainov [5]. From their work, the tunnel ionization rate (the so-called ADK rate) is given as:

$$W_{tun} = \omega_a \frac{(2l+1)(l+|m|)!}{2^{|m|}|m|!(l+|m|)!}\left(\frac{2e}{n^*}\right)^{n^*}\frac{1}{2\pi n^*}I_p \times \left(\frac{2E}{\pi(2I_p)^{3/2}}\right)^{1/2}\left(\frac{2(2I_p)^{3/2}}{E}\right)^{2n^*-|m|-1}\exp\left[\frac{2(2I_p)^{3/2}}{3E}\right] \tag{3.26}$$

Here, l and m are the angular momentum quantum numbers (the rate is averaged over m for a shell), ω_a is the atomic frequency (ω_a=4.13 x 10^{16} s^{-1}), n^* is the effective principal quantum number, $n^* = Z\left(2I_p(eV)\right)^{-1/2}$, E is the field of the laser in atomic units and I_p is the ionization potential of the charge state in atomic units. This expression has been derived by averaging the tunneling rate over a single optical oscillation. The ADK rate is very nonlinear with laser field exhibiting a sharp "threshold like" behavior in a manner similar to the simple barrier suppression model. The intensity at which this rate

reaches 10^{13} s^{-1} (i.e. nearly complete ionization will occur in 100 fs) for neutral Ar, for example, is ~ 3 x10^{14} W/cm^2. This is in good agreement with the simple barrier suppression model prediction.

- EXPERIMENTAL CONFIRMATION OF THE TUNNELING RATE IN HELIUM

The validity of this rate has been confirmed many times by a number of groups [6]. We have measured the ionization yields of helium with the LiSAF laser and compared them to the predicted yields of the ADK model [49]. The experimental set-up utilized for these measurements is shown schematically in figure III.5. This apparatus has been described previously [148]. Briefly, the ion yields from tunneling in the laser field are measured by a time-of-flight technique. The laser is focused with an f/20 lens into a chamber filled with a low density of gas (typically 10^{-7} - 10^{-5} torr). This low density assures that inter-atom collisions are not important so as to isolate the single atom contribution to the ionization. The laser is focused between two grids with an accelerating voltage (1000 V) placed across them. This field accelerates any ions produced by the laser into a 1 m long, field free, drift region. The ions are then detected by a dual micro-

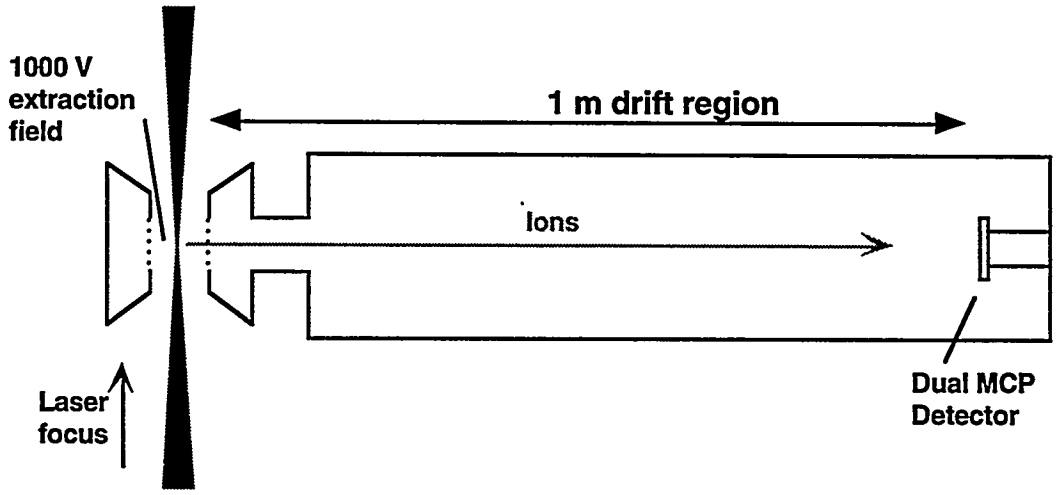

Figure III.5: Experimental schematic of the ion time-of-flight apparatus.

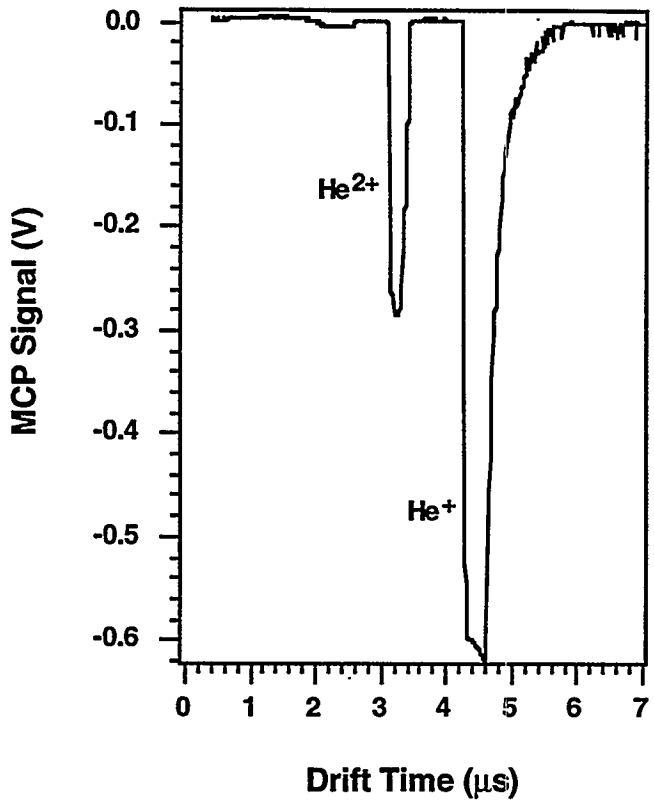

Figure III.6: Characteristic data from the time-of-flight spectrometer showing ions produced at 1 x 10^{16} W/cm^2 in helium.

channel plate detector. The charge to mass ratio of the ions is determined by their drift time from focus to detection. A fast transient digitizer digitizes the signal from the MCP detector. A computer sums the total ion signal on each shot.

Figure III.6 illustrates characteristic data from this apparatus showing ions produced at 1 x 10^{16} W/cm^2 in helium. The two peaks in this data correspond to the production of He^+ and He^{2+} in the laser focus from tunneling. The measured ion yield in helium as a function of laser intensity is shown in figure III.7. Each point on these curves represents the average of more than 30 laser shots in a 5% energy bin. The calculated ion yields using the ADK ionization rate integrated over the focal volume of the laser assuming a Gaussian focus [148] is shown in this figure as well. The measured ion yields have been shifted in yield and intensity (though not with respect to each ion stage,

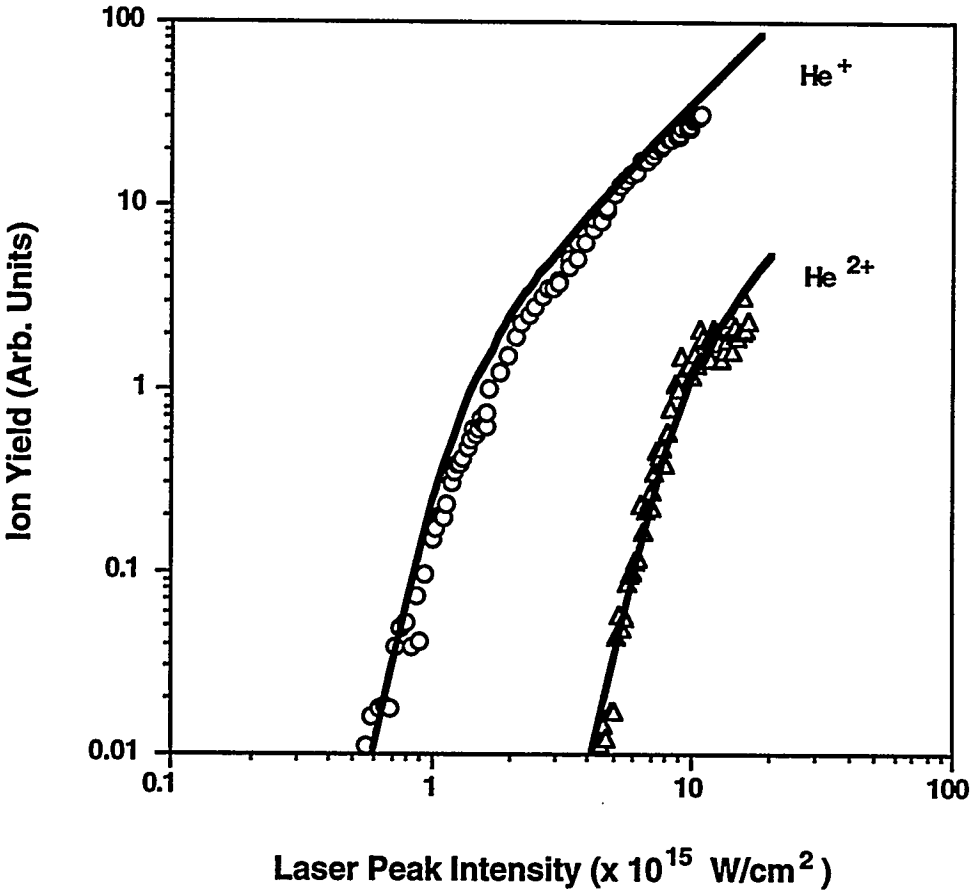

Figure III.7: Measured ion yields of He^+ and He^{2+} as a function of laser intensity.

however) to correspond to the ADK curves. The initial nonlinear growth of the ion yield at low intensity is characteristic of the nonlinear nature of eq. (3.26). The use of this measurement to estimate the laser peak intensity was discussed in chapter II.

III.3.B Other Ionization Mechanisms

Other ionization mechanisms are possible in the low density plasma that is produced by the initial tunnel ionization of electrons. For example ionization from the collisions of electrons with atoms and ions is possible. To calculate this rate we can use the empirically determined collisional ionization rate formula of Lotz [114]. This rate per ion averaged over a Maxwellian electron distribution is [114]

$$W_{kT} = n_e \frac{a_i q_i}{I_p (kT_e)^{1/2}} \int_{I_p/kT_e}^{\infty} \frac{e^{-x}}{x} dx \tag{3.27}$$

where n_e is the electron density, I_p is the ionization potential in eV, a_i is an empirical constant = 4.5 x 10^{-14} eV^2 cm^{-3}, and q_i is the number of electrons in the outer shell of the ion. For the conditions that prevail in typical gases, this rate is quite low on the time scale of the plasma decay. For example, in a gas with an electron density of $n_e = 1 \times 10^{18}$ cm^{-3} and a temperature of 10 eV the rate for ionization of He^+ to He^{2+} (I_p = 54.4 eV) is ~ 0.01 ns^{-1}. Only when the plasma is hot does this rate become important in a low density gas. For example, the rate rises to 5 ns^{-1} when the temperature is increased to 100 eV in the He plasma. When the density is enhanced to solid density this ionization mechanism will dominate. (This is discussed at length in chapter V).

III.3.C Plasma Formation Effects on the Propagation of a Short Pulse Through a Gas

A consequence of the rapid ionization of the atoms in a gas through tunneling is the formation of a plasma during the laser pulse. This plasma formation can then affect the propagation of the laser pulse itself. As a plasma is formed by ionization during the

laser pulse the refractive index of the medium is altered. The refractive index of a plasma is given by [95]

$$n_{plasma} = \sqrt{1 - \frac{\omega_p^{\ 2}}{\omega_0^{\ 2}}} = \sqrt{1 - \frac{4\pi e^2 n_e}{m_e \omega_0^{\ 2}}}$$
$$\approx 1 - \frac{2\pi e^2 n_e}{m_e \omega_0^{\ 2}} \tag{3.28}$$

where the last step is valid if the plasma frequency is much less then the laser frequency $\omega_p << \omega_0$, a situation found in a low density plasma ($n_e < 10^{19}$ cm^{-3}).

The ionization causes the electron density, n_e, to change with time. The variation of the refractive index with the changing electron density can lead to phase modulation on the laser pulse. Furthermore, the radially varying intensity of a focused laser beam leads to a radially varying electron density. This radial change in the electron density can cause refraction of the laser beam. The consequences of each of these effects will now be considered.

- PHASE MODULATION CAUSED BY A TEMPORALLY VARYING ELECTRON DENSITY

The first effect we will consider is that of the time dependence of the electron density on the laser pulse phase. Due to the highly nonlinear behavior of the tunnel ionization rate, as the intensity in the pulse rises, the electron density will rapidly rise. This rise in the electron density corresponds to a drop in the refractive index of the medium, resulting in a blue shifting of the laser spectrum. This effect has been studied by a number of groups and has been shown to be quite significant for short pulses propagating in an ionizing medium with a density of $>10^{18}$ cm^{-3} [193, 105].

We can estimate the magnitude of the spectral blue shifting by noting that the laser field E(t) can be written as a product of an amplitude and a phase:

$$E(t) = A(t)\exp\left[-i\omega_0 t - i\Delta\phi_p\right] \tag{3.29}$$

where $\Delta\phi_p$ is the additional, time dependent phase accumulated by the laser pulse propagating through the plasma. The actual instantaneous frequency of the laser then is given by (if we assume that the envelope, $A(t)$, varies slowly with respect to the field oscillations):

$$\omega = -\frac{\partial\phi}{\partial t} = \omega_0 + \frac{\partial}{\partial t}\Delta\phi_p \tag{3.30}$$

$$\omega = \omega_0 + \frac{\partial}{\partial t}\left[k_0 l\sqrt{1-\frac{n_e(t)}{n_{crit}}}\right] \tag{3.31}$$

$$\omega \approx \omega_0 + \frac{\omega_0 l}{2cn_{crit}}\frac{\partial n_e}{\partial t} \tag{3.32}$$

where we have introduced the critical density, $n_{crit} = m_e\omega_0^2/4\pi e^2$, and have assumed $n_e << n_{crit}$ in the last step. l is the plasma length through which the laser propagates. The wavelength shift can be written

$$\Delta\omega = -2\pi\frac{c}{\lambda^2}\Delta\lambda \tag{3.33}$$

$$\Delta\lambda \approx -\frac{\lambda l}{2cn_{crit}}\frac{\partial n_e}{\partial t} \tag{3.34}$$

where we have, once again, used the fact that $n_e << n_{crit}$. This relation implies that if the electron density rises to $0.001\ n_{crit}$ (i. e. rises from zero to about 2 x 10^{18} cm^{-3} for a wavelength of 800 nm) during a time of 100 fs with a plasma length of 1 mm then the laser pulse will experience a spectral shift of $\Delta\lambda \sim 10$ nm which is comparable to the bandwidth of a transform limited 100 fs pulse. This analysis suggests that this blue shifting can be an important effect for the parameter range in which our experiments are carried out.

To illustrate this point in a more quantitative fashion we have calculated the electron density as a function of time due to argon gas irradiated by a 100 fs pulse of a

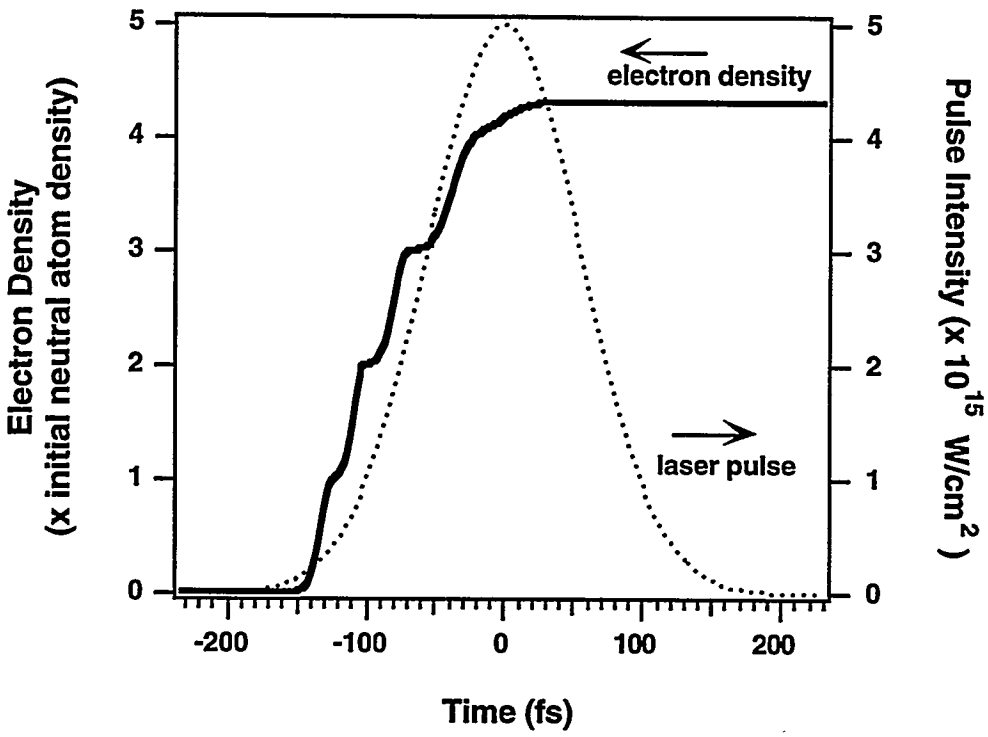

Figure III.8: Calculated electron density as a function of time (solid line) due to argon gas irradiated by a 100 fs pulse (dashed line) with a peak intensity of 5 x 10^{15} W/cm^2.

peak intensity of 5 x 10^{15} W/cm^2 in figure III.8. This calculation was conducted by assuming sequential ionization of the atoms by tunneling. We therefore solve the rate equations for the various charge states:

$$\frac{dn_0}{dt} = -W_{01}n_0 \tag{3.35a}$$

$$\frac{dn_1}{dt} = W_{01}n_0 - W_{12}n_1 \tag{3.35b}$$

$$\vdots$$

$$\frac{dn_i}{dt} = W_{i-1,i}n_{i-1} - W_{i,i+1}n_i \tag{3.35c}$$

where $W_{i,i+1}$ is rate of ionization from the ith charge state to the i+1 charge state, and n_i is the density of the ith charge state. We use the tunneling ionization rate of eq. (3.26) for these calculations. The electron density is derived from

$$n_e = n_1 + n_2 + \ldots n_i \tag{3.36}$$

The steps seen in figure III.8 result from the ionization of successive ionization states of the Ar.

The calculated phase due to the free electrons of an argon plasma with a gas of density 10^{18} cm^{-3} subject to the conditions of figure III.8 after propagation through an argon gas of 1 mm in length is shown in figure III.9. The initial spectrum of the transform limited pulse is compared to the spectrum of the pulse after modulation in figure III.10. As can be seen, the laser spectrum undergoes a sizable shift of some of the spectral energy to the blue side of the spectrum. The blue shifting occurs during the time of the laser pulse in which the tunnel ionization is significant. This corresponding to the

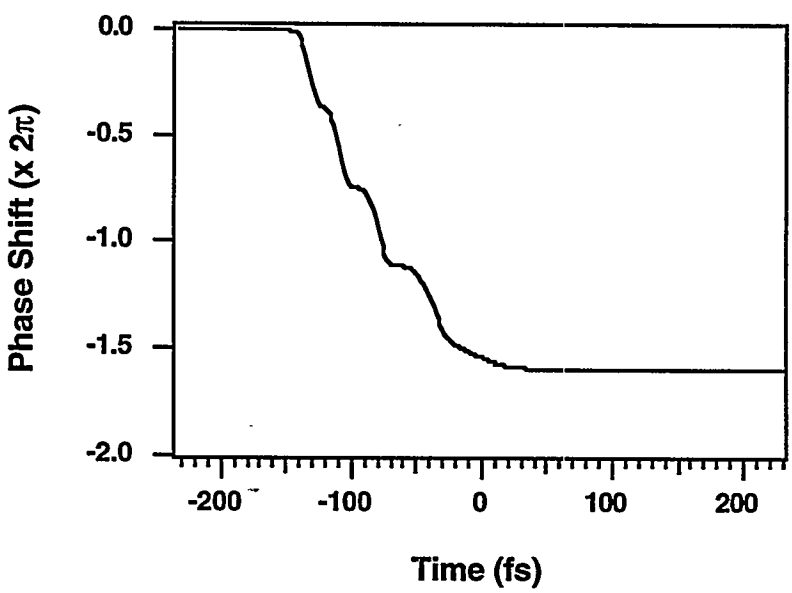

Figure III.9: Calculated phase imparted to the laser pulse as a function of time due to the formation of a free electron plasma in argon with a gas of density 10^{18} cm^{-3}, a pulse of peak intensity 5 x 10^{15} W/cm^2, and a gas of 1 mm in length.

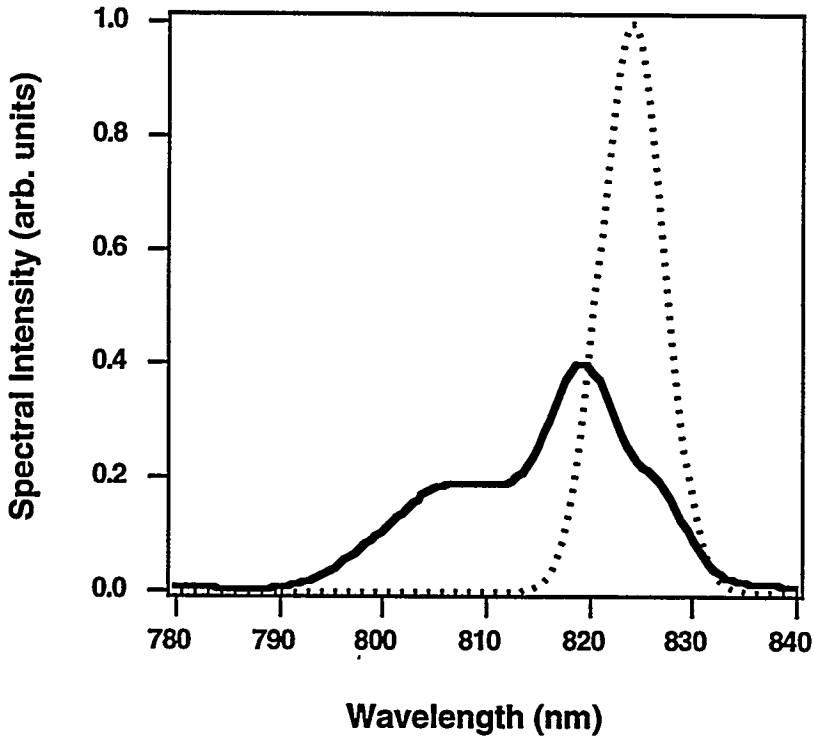

Figure III.10: Calculated initial spectrum of a transform limited pulse (dotted line) compared to the spectrum of the pulse after modulation by the phase in figure III.9 (solid line).

time in which the harmonics are generated, so we expect that this spectral shifting will manifest itself in some spectral shifting of the harmonics as well.

We have experimentally confirmed the presence of this spectral modulation in the gas jets used in our experimental studies. The schematic set-up of this experiment is shown in figure III.11. The LiSAF laser pulse was focused with an f/20 lens into a sonic gas jet nozzle which produces a gas density of between 1 and 10 x 10^{18} cm^2 [34]. The laser far field was imaged onto the slit of a 0.25 m spectrometer allowing a measurement of the spectrum on every laser shot. Figure III.12a illustrates the measured spectrum of the laser with an energy of 10 mJ (corresponding to an intensity of roughly 2 x 10^{15} W/cm^2) when no gas is released from the gas jet. This illustrates the case in which no spectral modulation occurs. Figure III.12b shows the measured spectrum for the same

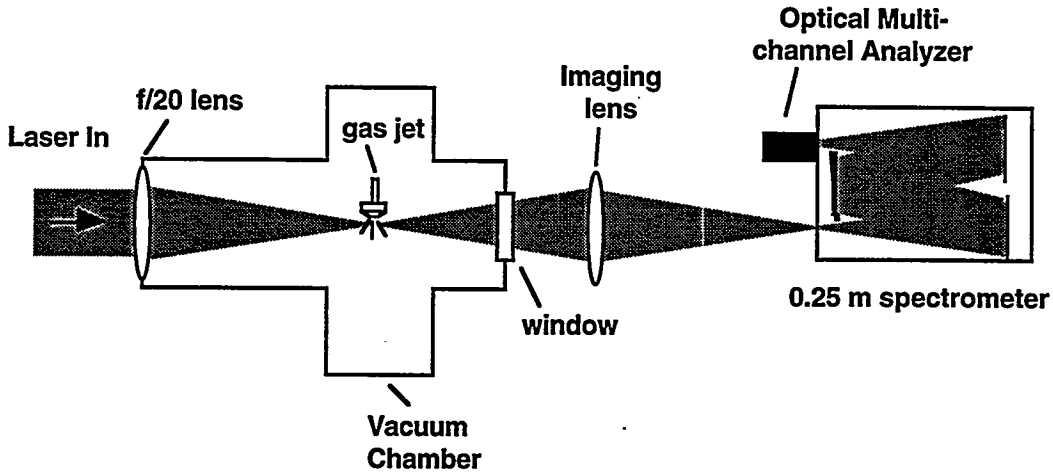

Figure III.11: Experimental set-up for measuring the ionization induced blue-shift on the LiSAF laser spectrum.

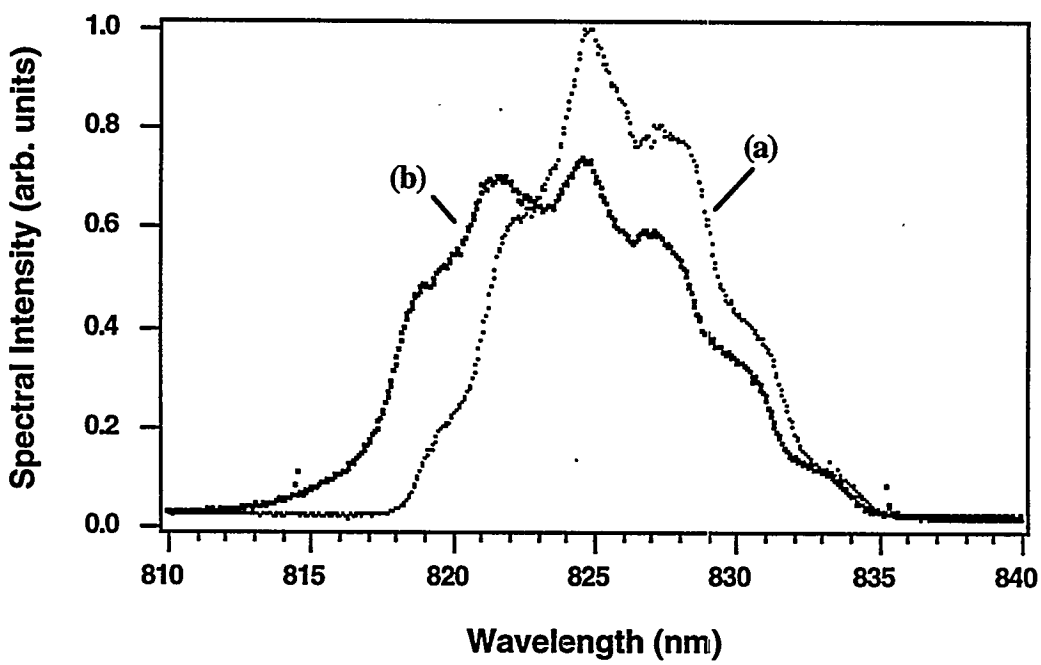

Figure III.12: **(a)** Measured spectrum of the laser with an intensity of roughly 2 x 10^{15} W/cm^2 when no gas is released from the gas jet. **(b)** Measured spectrum for the same laser intensity but with argon gas released when the gas jet is backed with 50 psi of pressure.

laser energy but with argon gas released when the gas jet is backed with 50 psi of pressure. A sizable fraction of the laser energy has been shifted toward the blue side of the spectrum. As we will see in chapter IV, this shifting will have an important effect on the characteristics of the high order harmonic spectral profiles at high intensity.

- LASER BEAM REFRACTION CAUSED BY A RADIALLY VARYING ELECTRON DENSITY

The second effect that the free electron refractive index can have on the laser pulse propagating through the underdense gas plasma is laser beam refraction [161, 108]. This arises from the fact that the electron density caused by an optically ionized plasma is not radially uniform. Since the focused laser pulse has a radial intensity profile that is peaked in the center and drops off further from the axis, the electron density will also be peaked in the center. Since the refractive index of a plasma is lower for a higher electron density, an electron density profile that is peaked in the center will act as a negative lens, causing a defocusing of the laser beam. This effect not only clamps the peak laser intensity that can be achieved but it also limits the length of the plasma through which the focused laser can propagate.

The ionization induced refraction of a focused short pulse has been studied both numerically and experimentally by a number of groups [161, 108, 134]. An extensive analysis of this effect is beyond the scope of this work. However, we can make an estimate on the range of conditions in which this refraction will be important. To do this we perform the analysis of Rankin et.al. [161]. We assume that the electron density exhibits a step radial profile. The characteristic length for refraction will occur when the central portion of the beam experiences a phase shift of $\pi/2$ with respect to the outer part of the beam (where the electron density is zero). This occurs when

$$kl_{char}\Delta n = \pi / 2 \tag{3.37}$$

where Δn is the difference between the refractive index in the center, where the electron density is δn_e, and the outer region, where the electron density is zero. Thus

$$\begin{aligned}\Delta n &= 1-\sqrt{1-\delta n_e/n_{crit}} \\ &\approx \delta n_e/2n_{crit}\end{aligned} \tag{3.38}$$

Here we have, once again, used the fact that $n_e << n_{crit}$. Thus

$$l_{char} \approx \frac{\lambda n_{crit}}{2\delta n_e} \tag{3.39}$$

Refraction will be significant when this characteristic length of refraction is comparable to the Rayleigh range of the laser focus, $2\pi w_0^2 / \lambda$. This implies that the condition for significant refraction is

$$\frac{\delta n_e}{n_{crit}} \sim \frac{\lambda^2}{4\pi w_0^2} \tag{3.40}$$

For an 800 nm laser focused to a spot of 50 μm, this condition will be satisfied when δn_e is $>10^{17}$ cm^{-3}. Since the majority of the experiments conducted in this work occur within gases of atomic density $> 10^{18}$ cm^{-3}, it follows that the ionization induced refraction will be a significant effect when the fractional ionization reaches a few percent. As we will see in the next chapter, this refraction can have a significant effect on the far field spatial profiles of the high order harmonics.

III.4 Heating Mechanisms in an Optically Ionized Plasma

As we have alluded to in the introduction to this work, one avenue to short wavelength generation with a short pulse is to couple a significant amount of energy to the electrons in the plasma. These energetic electrons can then produce x-ray photons through collisions with the atoms and ions in the plasma. If we desire x-rays with photon energies

of > 100 eV, we clearly need to couple comparable energy into each electron to get significant x-ray yields. Consequently, the manner in which an electron can acquire energy from the laser field inside the plasma is a central issue to our studies. Consequently, a detailed study of each of the relevant heating mechanisms in a low density, optically ionized plasma is informative. As we will illustrate, the efficiency in which laser energy is coupled into electrons in a low density, optically ionized plasma is rather low. A technique in which this coupling efficiency can be increased will be described in chapter V. Now we shall consider the theory of each of these heating mechanisms in an optically ionized plasma and present numerical calculations estimating their magnitudes under the conditions of interest.

III.4.A Heating During Ionization: Above Threshold Ionization

The first heating mechanism that we shall consider is above threshold ionization (ATI) [54]. This heating is a single atom effect and results from the additional energy that the electron receives from the laser field during the ionization process. From a perturbative standpoint, this process can be seen as the absorption by an ionizing electron of more than the minimum number of laser photons required to ionize the atom [54]. The additional photons absorbed result in an increase in electron kinetic energy after ionization. There have been a broad range of studies in this field since ATI was first observed in 1979 [3]. In general, in the strong field limit, a full solution of the Schrödinger equation is required to determine the actual magnitude of the ATI. Such a study is beyond the scope of this work and has been presented by a number of other authors [171].

We can however, simplify the consideration of ATI when the ionization of the atoms take place in the tunneling regime [131]. If this is the case, we can resort to the quasi-classical treatment of the electron dynamic in a manner similar to that used in the study of the high harmonic spectrum presented earlier. Such an analysis was first proposed by Burnett and Corkum [25]. We once again, assume the electron is born

through tunnel ionization at a well defined phase of the field. We assume that the electron is born at rest. If the time at which the electron is born in the field is t_0 then we recall the solution for the electron velocity:

$$v(t) = \frac{eE_0}{m_e \omega_0}\left(\cos\omega_0 t - \cos\omega_0 t_0\right) \tag{3.41}$$

where the first term is simply the oscillation velocity of the electron and the second term is the residual drift velocity associated with the ATI. This implies that the electron ATI energy is given by

$$K_{ATI} = 2U_p \sin^2 \Delta\varphi \tag{3.42}$$

where $\Delta\varphi$ is the phase from the peak of the e-field at which the electron is born. Note that the probability of tunneling is highest at the peak of the e-field, corresponding to the acquisition of no ATI energy. Thus we expect that, for a linearly polarized field, the majority of tunnel ionized electrons will be born with $\Delta\varphi$ near zero. Consequently, the ATI energy will tend to be a small fraction of the ponderomotive potential.

This process is shown schematically in figure III.13. The calculated velocity of an electron born at two different phases during a Gaussian laser pulse are shown in figures III.13b and III.13c subject to the pulse in figure III.13a. Figure III.13b shows the electron born at the peak of a laser cycle. The electron oscillates but as the field falls to zero amplitude, the electron velocity also falls to zero. However, when the electron is born at a phase of $\pi/4$ off of the peak (figure III.13c) the electron still has some residual velocity after the laser pulse intensity has fallen to zero. We can extend this analysis to a realistic laser pulse (100 fs) and combine this estimate for the acquisition of ATI energy with a full rate equation model of the ionization like that employed in eqs. (3.35a) to (3.35c). The calculated energy distribution of helium atoms subject to an 800 nm, 100 fs pulse with a peak intensity of 10^{17} W/cm^2 is shown in figure III.14. The distribution is very non-Maxwellian, strongly peaked at E = 0. The "temperature" of this distribution,

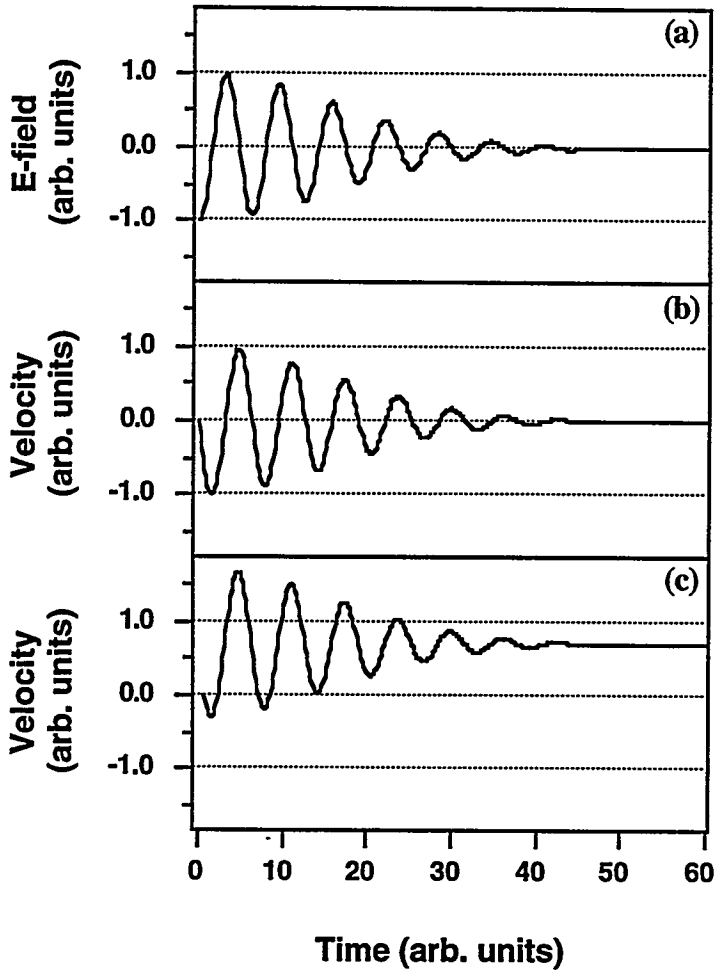

Figure III.13: **(a)** Electric field of the test laser pulse. **(b)** Calculated velocity of an electron subject to the laser field in (a) when the electron is born at the electric field peak. **(c)** Calculated velocity of the electron when it is born $\pi/4$ off of the field peak.

(defined as $kT_e = 2/3\langle E\rangle_{avg}$) is about 40 eV. Experimental results have confirmed this picture of cold plasma production [71] at low density with non-Maxwellian electron distributions [70].

Further calculations indicate that, in general, for a linearly polarized laser pulse, the temperature of an optically ionized electron is given roughly as

$$kT_e \approx 0.1U_p \tag{3.43}$$

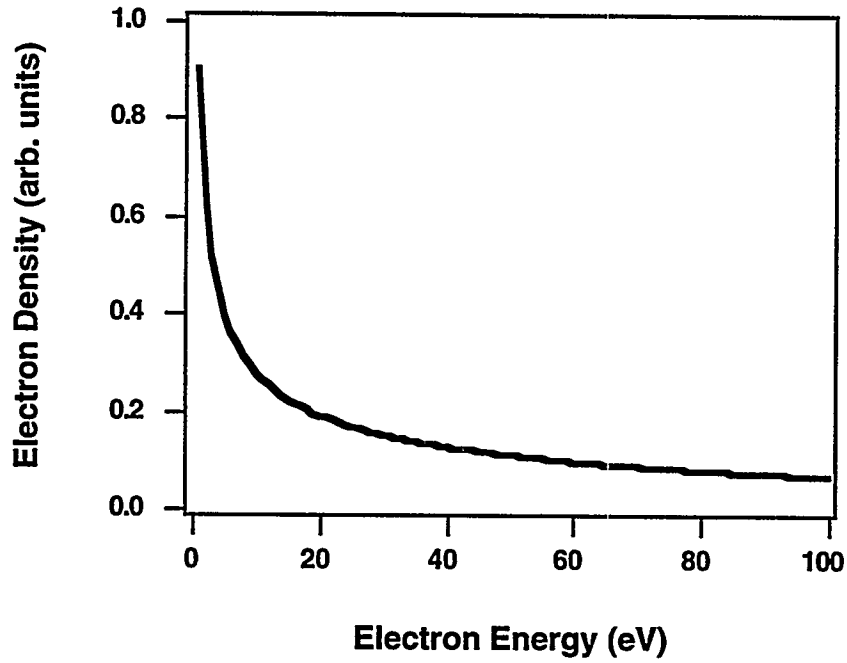

Figure III.14: Calculated energy distribution of helium atoms subject to an 800 nm, 100 fs pulse with a peak intensity of 10^{17} W/cm^2, found using the quasi-classical ATI model.

where U_p is the ponderomotive potential at the time the electron is ionized. Figure III.15 shows the calculated temperature of a plasma formed from ionization of He, Ar and Kr, as a function of peak intensity for a 100 fs (full width at half maximum), 800 nm linearly polarized pulse, based on the model of Burnett and Corkum and a numerical integration of the DC tunneling rate. The steps in the temperature correspond to the intensities at which each additional electron is stripped from the ion. In general, the plasma temperature does not exceed 50 eV in any of these gases for intensities below ~10^{17} W/cm^2. From this analysis it is clear that simple ATI heating is an ineffective manner in which to couple energy into the electron plasma. For example, figure III.15 illustrates that, though the ponderomotive energy of the electrons at an intensity of 10^{17} W/cm^2 is 6 keV, the electron temperature never exceeds 50 eV.

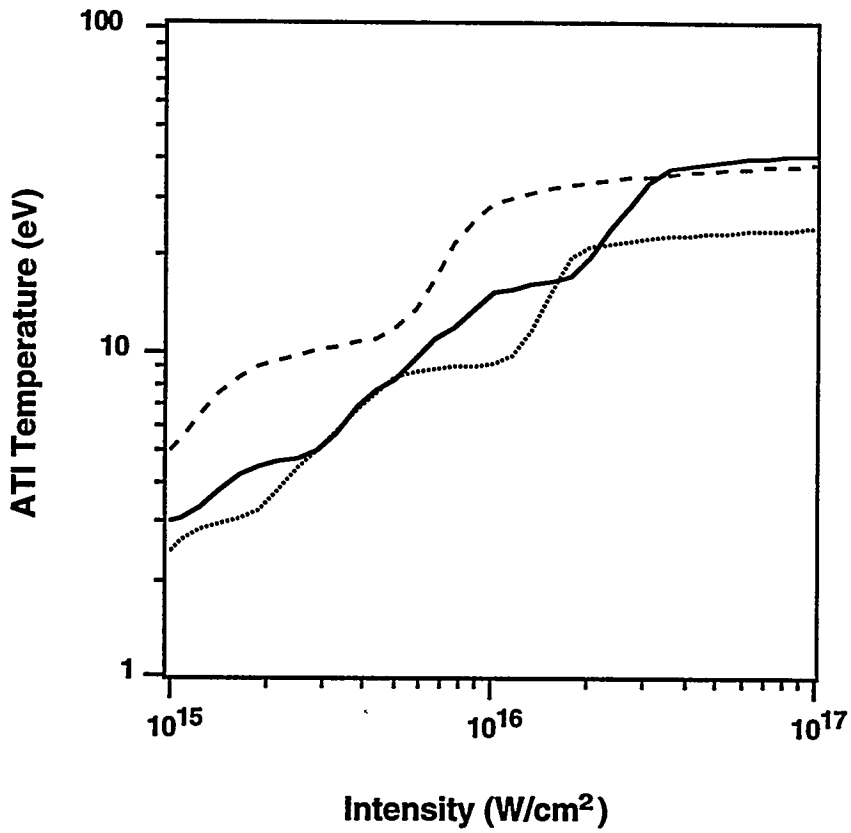

Figure III.15: Calculated ATI temperature of a plasma formed from ionization of He (dashed line), Ar (solid line) and Kr (dotted line), as a function of peak intensity for a 100 fs (full width at half maximum), 800 nm linearly polarized pulse.

III.4.B Heating by Driving Plasma Waves: Stimulated Raman Scattering

- UNDERLYING PHYSICS

A second process that can contribute to the plasma heating is one resulting from a bulk plasma phenomena. In this process the laser drives an electron plasma wave [53, 192]. After the laser has passed, the energy given from the laser to this electron density wave will ultimately thermalize and heat the plasma [95]. At sufficiently high intensity, the process of laser scattering off of the plasma wave exhibits feedback and is therefore stimulated. We might therefore expect that because of the exponential growth of the

plasma wave due to this feedback, very large amounts of energy can be coupled into the plasma during even a very short laser pulse. However, as we will show, this occurs only at very high intensities for short (< 1 ps) pulses [38, 33] and is, therefore, rather inefficient at coupling laser energy [35]. This is due to the fact that with short pulses there is insufficient time for the plasma wave to grow from the thermal noise. It is, however, informative to examine this process in detail and make some accurate calculations of the magnitude of plasma heating due to this process.

Following the nomenclature of nonlinear optics, this scattering is called stimulated Raman scattering. When the laser pulse propagates through an underdense plasma, it can scatter off of plasma waves already present because of thermal noise in the plasma. The plasma oscillates at its eigenfrequency, ω_p (the usual plasma frequency) while the laser drives transverse oscillations in the plasma at the laser frequency, ω_0. These two waves can beat together to produce oscillations at the difference of these two frequencies, namely $\omega_s = \omega_0 - \omega_p$. Thus an electromagnetic wave, the Stokes wave, is created at a frequency that is slightly down shifted from the frequency of the laser light (assuming $\omega_0 >> \omega_p$). Finally, the downshifted Stokes wave can beat together with the laser field to resonantly drive the plasma wave at $\omega_p = \omega_0 - \omega_s$, completing a feedback loop. This feedback loop can also be understood from a quantum mechanical point of view. The presence of plasma phonons at ω_p stimulate the decay of a laser photon, with energy ω_0, into a photon with energy ω_s and another plasma phonon. This three wave mixing process is illustrated schematically in figure III.16.

- DERIVATION OF THE COUPLED EQUATIONS DESCRIBING STIMULATED RAMAN SCATTERING IN A PLASMA FOR A SHORT PULSE.

I shall follow a derivation of the equations governing SRS that is similar to that of Kruer [95]. Consider a plane electro-magnetic wave propagating through a slab of homogeneous plasma. We can describe the fields by using Ampere's Law:

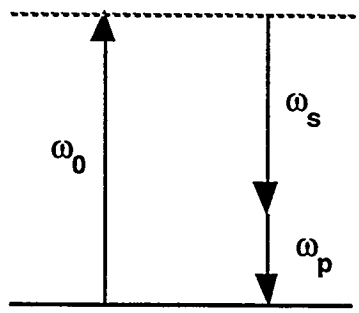

Figure III.16: Schematic of the stimulated Raman scattering of laser light in a plasma, where a photon from the laser field at frequency ω_0 decays into a stokes wave at ω_s and an electron plasma wave phonon at the plasma frequency, ω_p.

$$\nabla \times \mathbf{B} = \frac{4\pi \mathbf{J}}{c} + \frac{1}{c}\frac{\partial \mathbf{E}}{\partial t} \tag{3.43}$$

We can write the magnetic and electric fields in terms of the usual scalar and vector potentials with the following relations,

$$\mathbf{E} = -\frac{1}{c}\frac{\partial \mathbf{A}}{\partial t} - \nabla\varphi \tag{3.44}$$

$$\mathbf{B} = \nabla \times \mathbf{A} \tag{3.45}$$

Using eqs. (3.44) and (3.45) Ampere's Law (3.43) becomes,

$$\nabla \times \nabla \times \mathbf{A} = \frac{4\pi \mathbf{J}}{c} - \frac{\partial^2 \mathbf{A}}{\partial t^2} - \frac{1}{c}\frac{\partial}{\partial t}(\nabla\varphi) \tag{3.46}$$

If we choose the gauge such that $\nabla \cdot \mathbf{A} = 0$ this becomes,

$$\nabla^2 \mathbf{A} - \frac{1}{c^2}\frac{\partial^2 \mathbf{A}}{\partial t^2} = -\frac{4\pi \mathbf{J}}{c} - \frac{1}{c}\frac{\partial}{\partial t}(\nabla\varphi) \tag{3.47}$$

We wish to eliminate φ from eq. (3.47). To do this we can use the conservation of charge relation

$$\frac{\partial \rho}{\partial t} + \nabla \cdot \mathbf{J} = 0 \tag{3.48}$$

and Poisson's relation for the scalar potential,

$$\nabla^2 \varphi = -4\pi\rho \tag{3.49}$$

These relations yield:

$$\nabla \cdot \frac{\partial}{\partial t}(\nabla \varphi) = 4\pi \nabla \cdot \mathbf{J} \tag{3.50}$$

At this point it is useful to decompose the current density $\mathbf{J}$ into a transverse component (parallel to the oscillating laser field) and a longitudinal component such that $\mathbf{J} = \mathbf{J}_t + \mathbf{J}_l$. Because the transverse current is due merely to the oscillation of electrons in the laser field, we have that

$$\nabla \cdot \mathbf{J}_t = 0 \tag{3.51}$$

Thus eq. (3.50) becomes:

$$\frac{\partial}{\partial t}(\nabla \cdot \varphi) = 4\pi \mathbf{J}_l \tag{3.52}$$

and the wave equation for the vector potential, eq. (3.47), becomes:

$$\nabla^2 \mathbf{A} - \frac{1}{c^2}\frac{\partial^2 \mathbf{A}}{\partial t^2} = -\frac{4\pi \mathbf{J}_t}{c} \tag{3.53}$$

If $\mathbf{u}$ is the electron plasma velocity (which can also be decomposed into transverse and longitudinal components, $\mathbf{u}_e = \mathbf{u}_l + \mathbf{u}_t$) and n_e is the electron density then the transverse current density is

$$\mathbf{J}_t = -n_e e \mathbf{u}_t \tag{3.54}$$

The transverse electron velocity is related to the vector field by:

$$\dot{\mathbf{u}}_t = -\frac{e}{m}\mathbf{E} = -\frac{e}{m}\left(-\frac{1}{c}\frac{\partial \mathbf{A}}{\partial t}\right) \tag{3.55}$$

$$\mathbf{u}_t = \frac{e}{mc}\mathbf{A} \quad \Rightarrow \quad \mathbf{J}_t = -\frac{n_e e^2}{mc}\mathbf{A} \tag{3.56}$$

Substituting this into eq. (3.53) yields the wave equation for the vector potential in a plasma:

$$\nabla^2 \mathbf{A} - \frac{1}{c^2}\frac{\partial^2 \mathbf{A}}{\partial t^2} = -\frac{4\pi n_e e^2}{mc^2}\mathbf{A} \tag{3.57}$$

Now we require a relation for the density fluctuations in the plasma. To derive this we start with the continuity and momentum equations. The electron density conservation equation is

$$\frac{\partial n_e}{\partial t} + \nabla \cdot (n_e \mathbf{u}_e) = 0 \tag{3.58}$$

and the electron momentum equation reads

$$\frac{\partial \mathbf{u}_e}{\partial t} + \mathbf{u}_e \cdot \nabla \cdot \mathbf{u}_e = -\frac{e}{m}\left(\mathbf{E} + \frac{\mathbf{u}_e}{c} \times \mathbf{B}\right) - \frac{\nabla p_e}{n_e m} \tag{3.59}$$

Since

$$\begin{aligned} \mathbf{u}_e &= \mathbf{u}_l + \mathbf{u}_t \\ &= \mathbf{u}_l + \frac{e\mathbf{A}}{mc} \end{aligned} \tag{3.60}$$

we can write eqs. (3.58) and (3.59) in terms of $\mathbf{u}_l$. Using eq. (3.60) in eqs. (3.58) and (3.59), some lengthy algebra yields for the two moment equations:

$$\frac{\partial n_e}{\partial t} + n_e \nabla \cdot \mathbf{u}_l + \mathbf{u}_l \cdot \nabla n_e = 0 \tag{3.61}$$

$$\frac{\partial \mathbf{u}_l}{\partial t} + \frac{1}{2}\nabla\left(\mathbf{u}_l + \frac{e\mathbf{A}}{mc}\right)^2 = \frac{e}{m}\nabla\varphi - \frac{\nabla p_e}{n_e m} \tag{3.62}$$

Equations (3.57), (3.61), and (3.62) completely describe the laser/electron plasma interaction.

At this point we can simplify these fluid equations by introducing small perturbations to each quantity and linearizing the equations in the standard way [95]. We introduce the following definitions:

$$n_e = n_0 + \tilde{n}_e \tag{3.63}$$

$$\mathbf{u}_l = \tilde{\mathbf{u}}_l \tag{3.64}$$

Here $\tilde{n}_e$ is a small, time dependent perturbation to the background electron density denoted by n_0. We treat the electron velocity as a small perturbation as well. The following analysis is justified if the driven electron density fluctuations are small compared to the total electron density and the longitudinal electron velocity is small compared to the transverse velocity driven by the laser.

We also introduce a small perturbation to the vector potential:

$$\mathbf{A} = \mathbf{A}_L + \tilde{\mathbf{A}} \tag{3.65}$$

where $\mathbf{A}_L$ is the large laser field and $\tilde{\mathbf{A}}$ is a small amplitude scattered wave. We introduce the quantities in eqs. (3.63) - (3.65) into the fluid equations (3.61) and (3.62) and drop all terms that are second order or higher in the small perturbations. Using the fact that the plasma is homogeneous and, therefore, $\nabla n_0 = 0$, the relation for the electron density perturbation becomes

$$\frac{\partial \tilde{n}_e}{\partial t} + n_0 \nabla \cdot \tilde{\mathbf{u}}_l = 0 \tag{3.66}$$

The relation for the electron longitudinal velocity becomes:

$$\frac{\partial \tilde{\mathbf{u}}_l}{\partial t} = \frac{e}{m}\nabla\varphi - \frac{1}{2}\nabla\left(\frac{2e^2}{m^2c^2}\mathbf{A}_L \cdot \tilde{\mathbf{A}}\right) - \frac{\nabla p_e}{n_e m} \tag{3.67}$$

(Note that the convective term $\mathbf{u}_e \cdot \nabla \cdot \mathbf{u}_e$ drops out of the equations altogether since it is second order in the small perturbation $\tilde{\mathbf{u}}_l$.) We can then take the time derivative of equation (3.66) , $\nabla \cdot$ of eq. (3.67) and substitute for $\frac{\partial}{\partial t}(\nabla \cdot \tilde{\mathbf{u}}_l)$ to derive a wave equation for $\tilde{n}_e$. This operation yields:

$$\frac{\partial^2 \tilde{n}_e}{\partial t^2} + \omega_p{}^2 \tilde{n}_e - \nabla^2 \frac{p_e}{m} = \frac{n_0 e^2}{m^2 c^2}\nabla^2\left(\mathbf{A}_L \cdot \tilde{\mathbf{A}}\right) \tag{3.68}$$

where the fact that $\nabla^2\varphi = 4\pi e\tilde{n}_e$ has been used. We must make an assumption about an equation of state to get an expression for the electron pressure, p_e. Assuming the adiabatic equation of state, we find that

$$\begin{aligned} p_e &= 3mv_e{}^2\tilde{n}_e \\ &= 3k_B T_e \tilde{n}_e \end{aligned} \tag{3.69}$$

with which the electron density equation becomes

$$\frac{\partial^2 \tilde{n}_e}{\partial t^2} + \omega_p{}^2 \tilde{n}_e - \frac{3k_B T_e}{m}\nabla^2 \tilde{n}_e = \frac{n_0 e^2}{m^2 c^2}\nabla^2\left(\mathbf{A}_L \cdot \tilde{\mathbf{A}}\right) \tag{3.70}$$

Returning to the vector potential wave equation (eq. (3.57)) and linearizing as well we get an equation for the scattered light field:

$$\nabla^2 \tilde{\mathbf{A}} - \frac{1}{c^2}\frac{\partial^2 \tilde{\mathbf{A}}}{\partial t^2} = \frac{4\pi n_0 e^2}{mc^2}\tilde{\mathbf{A}} + \frac{4\pi e^2}{mc^2}\mathbf{A}_L \tilde{n}_e \tag{3.71}$$

or, after introducing the usual plasma frequency, $\omega_p{}^2 \equiv \frac{4\pi n_0 e^2}{m}$, eq. (3.71) becomes

$$\nabla^2 \tilde{\mathbf{A}} - \frac{1}{c^2}\frac{\partial^2 \tilde{\mathbf{A}}}{\partial t^2} - \frac{\omega_p{}^2}{c^2}\tilde{\mathbf{A}} = \frac{4\pi e^2}{mc^2}\mathbf{A}_L \tilde{n}_e \tag{3.72}$$

The equation for the pump laser field, $\mathbf{A}_L$, is irrelevant since we shall assume that the pump field is large and undepleted by the scattering process.

Equations (3.70) and (3.72) are the two coupled equations that describe the plasma wave and the scattered field usually found in the literature [65]. To model the effect of a short laser pulse, it is possible to derive first order, coupled equations for the envelopes of the scattered light field and the electron oscillation amplitude. To do this we define the scattered wave and the electron density wave as products of a fast, oscillating term and a slowly varying envelope:

$$\tilde{\mathbf{A}} = \mathbf{a}_s(x,t)e^{i(k_s x - w_s t)} + c.c. \tag{3.73}$$

$$\tilde{n}_e = n(x,t)e^{i(k_e x - w_e t)} + c.c. \tag{3.74}$$

$$\mathbf{A}_L = \mathbf{a}_L(x,t)e^{i(k_0 x - w_0 t)} + c.c. \tag{3.75}$$

where $\mathbf{a}_s(x,t)$, $n(x,t)$, and $\mathbf{a}_L(x,t)$ all vary slowly with respect to the oscillating exponential term. For simplicity, we consider only one dimension in the spatial coordinates. This is adequate for a plane wave incident on a homogeneous plasma.

Substituting relations (3.73), (3.74) and (3.75) into the linearized equation for the scattered light field, eq. (3.72). yields (having ignored the complex conjugate terms)

$$\begin{aligned}\frac{\partial^2}{\partial x^2}\left(a_s e^{i(k_s x - \omega_s t)}\right) - \frac{1}{c^2}\frac{\partial^2}{\partial t^2}\left(a_s e^{i(k_s x - \omega_s t)}\right) - \frac{\omega_p{}^2}{c^2} a_s e^{i(k_s x - \omega_s t)} \\ = \frac{4\pi e^2}{mc^2} a_L n^* e^{i[(k_0 - k_e)x - (\omega_0 - \omega_e)t]}\end{aligned} \tag{3.76}$$

Considering the first term:

$$\frac{\partial^2}{\partial x^2}\left(a_s e^{ik_s x}\right) = \left(\frac{\partial^2 a_s}{\partial x^2} + 2ik_s \frac{\partial a_s}{\partial x} - k_s{}^2 a_s\right)e^{ik_s x} \tag{3.77}$$

Since we know that the envelope of the field, a_s, varies slowly with respect to the field oscillations it is a very good approximation to assume that

$$\frac{\partial^2 a_s}{\partial x^2} << ik_s \frac{\partial a_s}{\partial x} \tag{3.78}$$

and we can effectively drop the second derivative term. An identical argument can be made for the time derivative term in equation (3.76) and we can drop the second temporal derivative as well since

$$\frac{\partial^2 a}{\partial t^2} << i\omega_s \frac{\partial a}{\partial t}. \tag{3.79}$$

Finally we note that in the plasma $\left(\omega_s^2 - \omega_p^2\right)/c^2 - k_s^2 = 0$ (because the refractive index is $\sqrt{1-\omega_p^2/\omega_s^2}$). I have, then, the equation for the Stokes field:

$$\frac{\partial a_s}{\partial x} - \frac{\omega_s}{k_s c}\frac{\partial a_s}{\partial t} = \frac{2i\pi e^2}{k_s m c^2} a_L n^* e^{i\Delta kx} \tag{3.80}$$

having defined the wave mismatch $\Delta k \equiv k_0 - k_s - k_e$.

Inserting relations (3.73) - (3.75) into the electron plasma wave equation (3.70) we get

$$\begin{aligned}\frac{\partial^2 n}{\partial t^2} + 2i\omega_e \frac{\partial n}{\partial t} - \omega_e^2 n + \omega_p^2 n + \frac{3k_B T_e}{m} k_e^2 n \\ = \frac{n_0 e^2}{m^2 c^2}\frac{\partial^2}{\partial x^2}\left(a_L a^* e^{i[(k_0-k_s)x-(\omega_0-\omega_s)t]}\right) e^{-i(k_e x - \omega_e t)}\end{aligned} \tag{3.81}$$

where we have dropped all space derivative terms of the density in the thermal correction term. The space derivative term represents a temperature dependent group velocity of the electron plasma wave. This means that for a hot plasma, the plasma wave is nonstationary and will have a group velocity due to the thermal velocity of the oscillating electrons. For our plasmas this term is very small ($kT_e k_e^2/_e << \omega_p^2$) and is completely negligible during the time frame of the short laser pulse.

We wish to drop the second time derivative term of the electron wave envelope using the same slowly varying envelope argument used in deriving equation (3.80). We

shall do this but it should be noted that this is not nearly as good as an approximation. The electron oscillates at a frequency near ω_p which is typically much smaller than the laser frequency. Therefore if the growth rate of the electron plasma wave is large enough, (which it may be if the driving laser field is very large) then

$$\frac{\partial^2 n}{\partial t^2} \leq i\omega_p \frac{\partial n}{\partial t} \tag{3.82}$$

may be a poor approximation. The inclusion of the second derivative term represents a phase slip of the plasma wave with respect to the driving wave. Nonetheless, we shall restrict our discussion to the cases in which this term is negligible.

If we assume that the electrons oscillate at their eigenfrequency, namely that

$$\omega_e^{\ 2} = \omega_p^{\ 2} + \frac{3k_B T_e}{m} k_e \tag{3.83}$$

then the equation for the plasma wave becomes

$$\frac{\partial n}{\partial t} = \frac{i n_0 e^2}{2m^2 c^2}\left((k_0 - k_s)^2 a_L a^* + 2i(k_0 - k_s)\frac{\partial}{\partial x}\left(a_L a^*\right)\right)e^{i\Delta kx} \tag{3.84}$$

(after having applied the slowly varying envelope approximation to the driving term on the right hand side.)

Examination of eqs. (3.80) and (3.84) reveals that the growth of the Stokes field and the plasma wave will be largest if $\Delta k = 0$. This relation, $k_0 - k_s - k_e = 0$, essentially represents the conservation of momentum condition for the three wave stimulated scattering process. The conservation of energy relation reads: $\omega_s = \omega_0 - \omega_e$. One should also note that the driving term for the growth of the plasma wave is proportional to $(k_0 - k_s)^2$. Thus the growth is maximum when the Stokes wave number, k_s, is of opposite sign to the wave vector of the laser field, k_0. In other words, the back scatter will be far larger than the forward scatter. In fact, since $k_s \approx k_0$, the forward scatter is

essentially negligible at the intensities that we shall consider (though it becomes important at higher intensity [33]).

Equations (3.80) and (3.84) represent the coupled equations for the envelopes of the scattered Stokes wave and the longitudinal plasma oscillation. They are valid in the limits of strong laser pump field and moderate growth. The approximations leading up to these equation break down if the growth rate is too large or the amplitudes of the waves becomes very large.

- DESCRIPTION OF THE NUMERICAL MODEL OF SRS AND COMPUTATIONAL RESULTS

To examine the physics of stimulated Raman scattering in a plasma the coupled equations derived in the previous section are solved numerically for a variety of plasma parameters. The code solves the equations (3.80) and (3.84). A fourth order Runge-Kutta algorithm is used to propagate the equations in time. The equations are solved on a grid of 500 points in the x axis and 150 points in the time axis. Each time step is 3 fs and each space step is $v_g \cdot \Delta t$, where v_g is the group velocity of the laser light in the plasma. Thus the laser pulse propagates one space step for each time step. This assures numerical stability by satisfying the Courant (CFL) condition [158].

The incident laser field is taken to be a Gaussian profile:

$$\mathbf{a}_L(x,t) = a_0 \exp\left[-\frac{\left(t - x/v_g\right)^2}{\tau^2}\right] \tag{3.85}$$

where τ is chosen to correspond to an intensity variation with a 100 fs full width at half maximum. The laser is set in the middle of the space grid for the initial time step. We initially assume a homogenous amplitude for the plasma oscillation. This represents the thermal noise of the plasma contained in the mode resonant with the laser. For these runs, we assume an initial plasma density fluctuation that is 10^{-10} times the electron density. This corresponds to roughly 3×10^{-4} of the initial plasma thermal energy in the resonant mode for a 100 eV plasma (a fairly high value for the initial thermal energy in the resonant

mode; it is probably more like 10^{-8} for an experimental plasma [192]). Nonetheless, we can derive a growth factor for the electron plasma wave from these parameters. We also assume that there is no energy in the Stokes field initially.

The results of a typical calculation are shown in figure III.17. For this run, the electron density was 1×10^{18} cm^{-3}, and the peak laser intensity was 1×10^{18} W/cm^2. The laser pulse was a transform limited 100 fs pulse with a vacuum wavelength of 825 nm. Figure III.17a shows the initial and final positions of the laser pulse in the calculation. The plots in figure III.17b show the envelope of the Stokes field at various time steps and the plot in figure III.17c shows the electron wave amplitude at the end of the run. In these runs the laser pulse propagates to the right; as it does, the amplitude of the Stokes field grows and begins to propagate toward the left. The plasma wave amplitude also grows but is stationary. The result is a long Stokes pulse that grows to its maximum value during the laser pulse and exits the plasma in the direction from which the laser came. The growth of the Stokes field amplitude is shown in figure III.17d. The amplitude growth is initially exponential as it grows from the noise but levels off at later times as it propagates out of the laser pulse to the left. The result is that the amplitude of the plasma wave has grown by a factor of 3.4×10^5 or, in other words, by 12.7 e-foldings.

In figure III.18 is plotted the growth of the plasma wave as a function of incident laser intensity for a 100 fs, 825 nm laser pulse; the electron density was 1×10^{18} cm^{-3}. We define the growth as the factor by which the plasma wave amplitude has grown over the initial noise level. As can be seen in this figure for intensity below 10^{17} W/cm^2, the growth of the plasma wave above the noise is less than a factor of 100. As pointed out earlier, only $\sim 10^{-8}$ of the plasma thermal energy is contained in the unstable modes. Thus, we expect that significant heating will occur only when the growth factor is comparable to 10^8. Clearly, this condition is not achieved with intensity below 10^{17} W/cm^2. Only when the intensity approaches 10^{18} W/cm^2 does the SRS growth become significant.

(a)

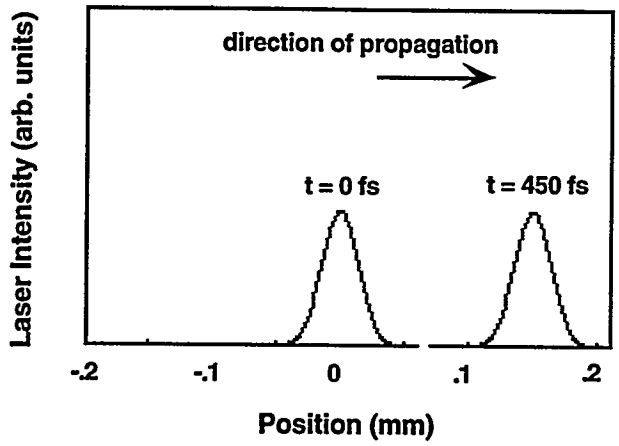

(b)

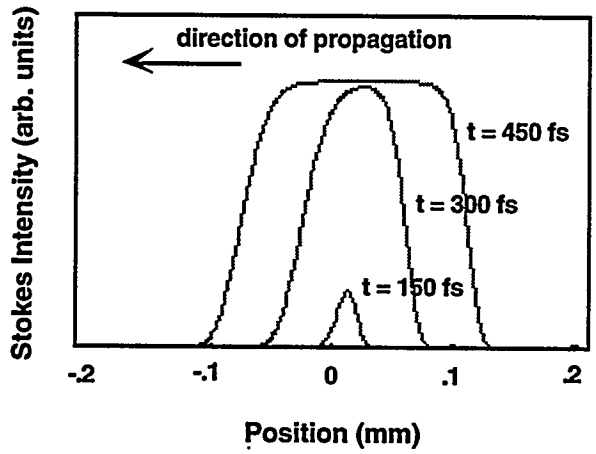

Figure III.17: Results of a run with a plasma density of 1×10^{18} cm^{-3}, a laser peak intensity of 1×10^{18} W/cm^2, and a laser wavelength of 825 nm. **(a)** Driving laser pulse position in the plasma for two times, initial position and the pulse position after 450 fs. **(b)** Scattered Stokes field intensity for three different times illustrating the initial growth and final saturation as the scattered wave propagates out of the laser pulse toward the left.

(c)

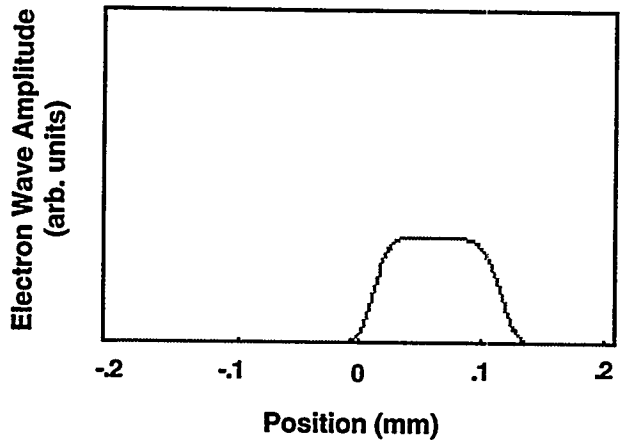

(d)

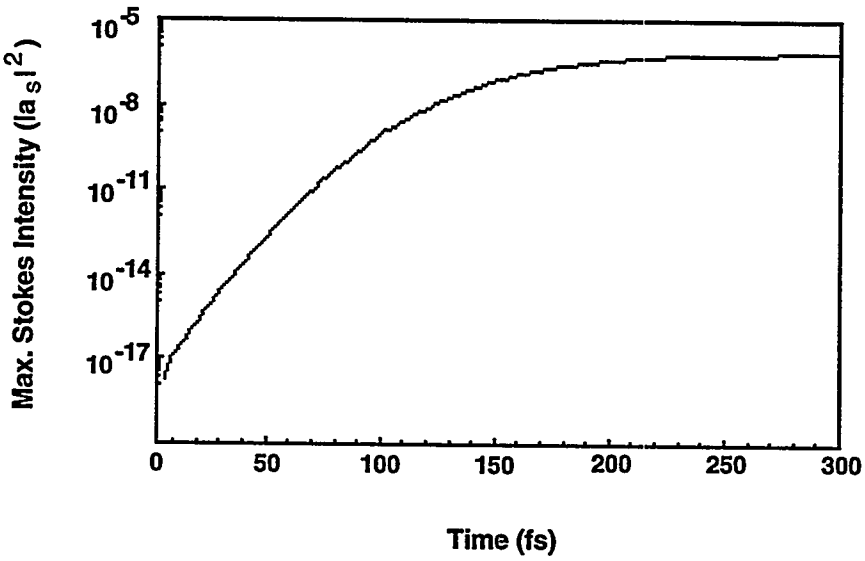

Figure III.17: **(c)** Amplitude of the plasma wave after 450 fs; the initial homogeneous noise level is too low to be seen on this graph. **(d)** Plot of the growth of the stokes field amplitude (in units of the vector potential squared, which is statvolts^2).

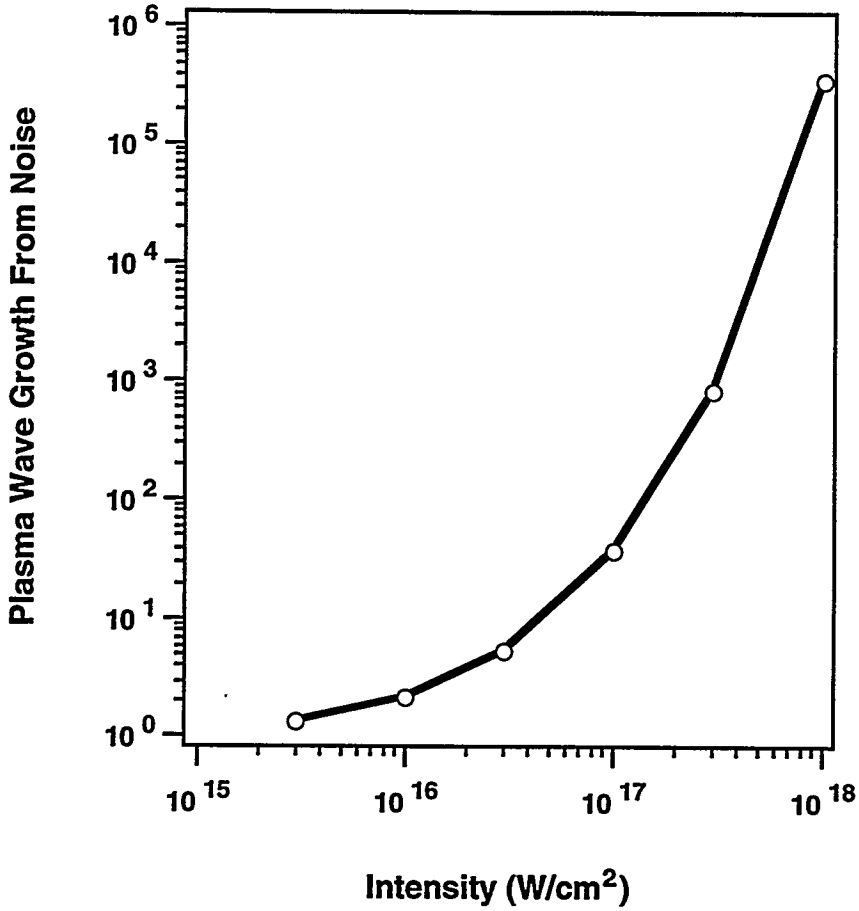

Figure III.18: Growth of a plasma wave from the thermal noise as a function of incident laser intensity for a 100 fs, 825 nm laser pulse in an electron density of 1 x 10^{18} cm^{-3}.

This is in keeping with the experimental results of Blyth et. al. [18] and Crane. et. al. [35] who observed significant plasma heating at high intensity.

The plasma wave growth as a function of electron density is shown in figure III.19 for an intensity of 10^{17} W/cm^2 and a wavelength of 825 nm. The increase in growth with density is not as dramatic as it is with intensity. The plot in figure III.19 demonstrates that for this parameter range, significant growth does not occur until the plasma density approaches 10^{20} cm^{-3} or $n_e \approx n_{crit}/10$.

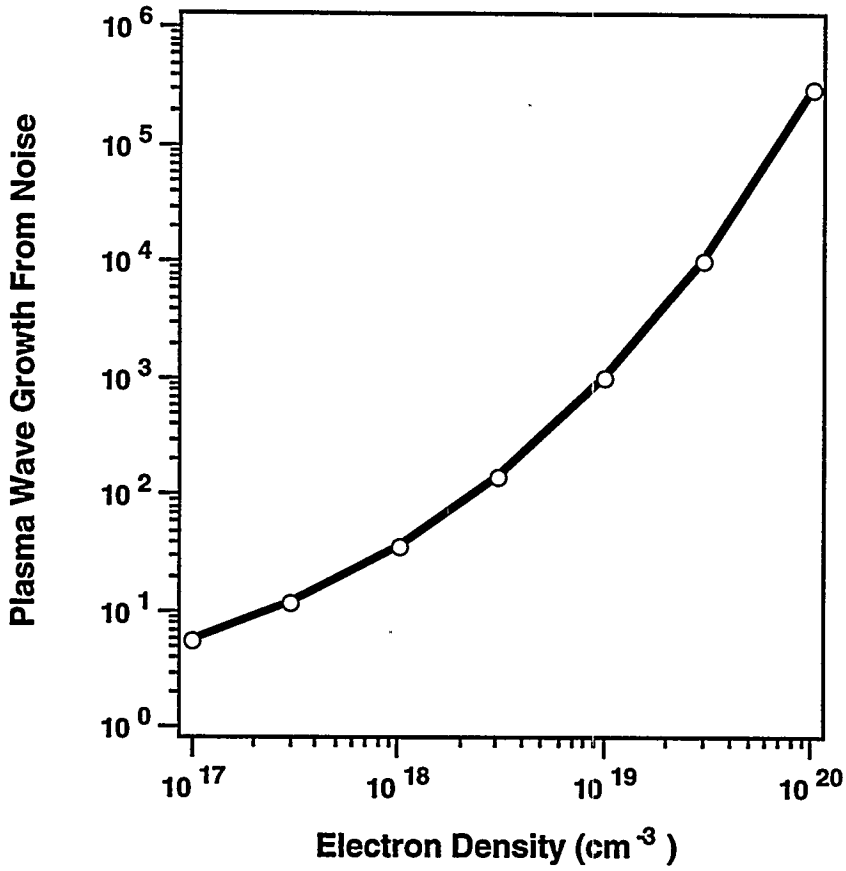

Figure III.19: Growth of a plasma wave from the thermal noise as a function of electron density for a 100 fs, 825 nm laser pulse with a peak intensity of 1 x 10^{17} W/cm^2.

- ANALYSIS AND EXPERIMENT

From these calculations it is clear that SRS is not important mechanism for 100 fs pulses of 825 nm light in underdense plasma when the intensity is at or below 10^{17} W/cm^2. We would typically expect that a growth of the electron plasma wave by a factor of $>10^7$ would be required to provide any significant heating of the plasma. This large growth is not achieved with the intensity and density typically used in our experiments.

We made an experimental search for the back scattered Raman signal that would be indicative of significant SRS heating. No scattered SRS was observed in the plasmas formed with a sonic gas jet up to an intensity of 5 x 10^{16} W/cm^2. Though this negative

result does not necessarily prove that SRS heating is negligible in our experiments, it is consistent with our calculations which indicate that this is so. Our measurements are also consistent with the measurements of Crane et. al. [35] on the 600 fs, $\lambda = 1$ μm, laser which showed that SRS heating becomes important only at intensity above 10^{17} W/cm^2.

III.4.C Heating Through Coulomb Collisions: Inverse Bremsstrahlung

The third method of electron plasma heating that we will consider is collisional heating or inverse bremsstrahlung heating [85]. As we discussed in the introduction, this heating occurs when an oscillating electron encounters a charged ion. The result is that the electron can absorb energy from the laser field. Once again, we can gain significant insight into the collision process by treating the motion of the electron classically. Figure III.20 illustrates the effect of a collision on a classical oscillating electron. As we discussed before, in the absence of a perturbation, the electron energy will return to zero as the field falls to zero. However, if the electron undergoes a collision, illustrated in figure III.20 as a 90° collision that occurs instantaneously, the electron maintains energy after the laser has passed. When these collisions occur often enough, significant energy can be transferred to the electrons.

At this point it is informative to consider the dynamics of the classical electron undergoing collisions in the field. This will give us some insight into the collisional heating process and allow us to derive an expression for the magnitude of the collisional heating per unit time in the plasma. The following analysis is a more detailed presentation of that originally published by Pert [155].

- DYNAMICS OF ELECTRONS UNDERGOING COLLISIONS IN THE LASER FIELD

We start by considering the motion of an electron in an oscillating electric field. The velocity of the particle will have both a coherent oscillation and a thermal velocity component. The oscillatory motion of the electron is described by:

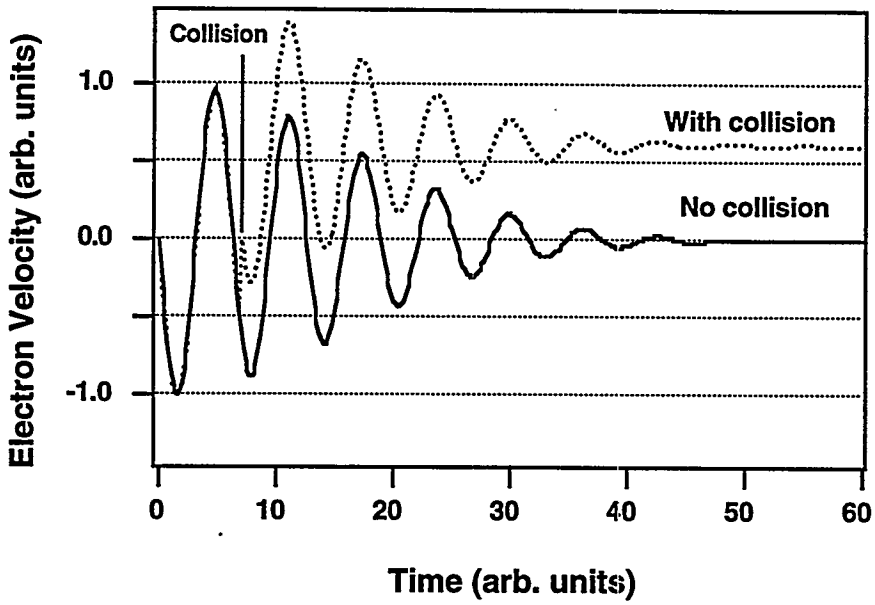

Figure III.20: Calculated velocity of an electron in the laser field illustrated in figure III.13a. The velocity of an electron born at rest at the peak of the field is compared to the case when the same electron undergoes a collision at t =7.

$$\mathbf{u}(t) = \mathbf{u}_0 \sin \omega t \tag{3.86}$$

where the peak velocity, as before, is given by:

$$\mathbf{u}_0 = \frac{e\mathbf{E}_0}{m_e \omega} \tag{3.87}$$

$\mathbf{E}_0$ is the peak laser field strength, and ω is the frequency of the laser field. If $\mathbf{v}_T$ is the thermal velocity of the electron then the total velocity of the electron is

$$\mathbf{v} = \mathbf{v}_t + \mathbf{u}(t) \tag{3.88}$$

and the electron kinetic energy is

$$\begin{aligned} E &= \tfrac{1}{2} m_e |\mathbf{v}|^2 \\ &= \tfrac{1}{2} m_e \left(\mathbf{v}_t^2 + u^2 + 2\mathbf{v}_t \cdot \mathbf{u} \right) \end{aligned} \tag{3.89}$$

For laser fields of optical frequencies it is a good assumption that the laser field oscillates much faster than the mean time between collisions $\delta t \sim \nu_{ei}^{-1}$ if ν_{ei} is the mean rate of electron-ion collisions in the plasma. If this is true, it is apparent that the term in eq. (3.89) that varies as $\mathbf{v}_t \cdot \mathbf{u}$ will average to zero over a time $\delta t \sim \nu_{ei}^{-1}$. Consequently, the electron energy is

$$E \approx \tfrac{1}{2} m_e \mathrm{v}_t^2 + \tfrac{1}{2} m_e u^2 \tag{3.90}$$

We now consider what happens after a collision of an electron with an ion (which is assumed stationary because of its much greater mass). If the electron velocity before the collision is given by eq. (3.88) and its velocity after the collision is given by

$$\mathbf{v}' = \mathbf{v}_t' + \mathbf{u}'(t') \tag{3.91}$$

then the total change in the thermal energy of the electron is:

$$\Delta E_t = \tfrac{1}{2} m_e \left(\mathrm{v}_t'^2 - \mathrm{v}_t^2 \right) \tag{3.92}$$

We can make two very good approximations at this point. First, we assume that the time of the collision is much shorter than the oscillation time of the field. Consequently the oscillation velocity is well defined and we can assume that

$$\mathbf{u}'(t') = \mathbf{u}(t) \tag{3.93}$$

We also assume that the collision is elastic and that the total energy is conserved:

$$\mathrm{v}'^2 = \mathrm{v}^2 \tag{3.94}$$

Using relations (3.88), (3.91), (3.93) and (3.94), the net change in thermal energy, eq. (3.92), can be written as

$$\Delta E_t = m_e \left(\mathbf{v}_t - \mathbf{v}_t' \right) \cdot \mathbf{u} \tag{3.95}$$

We now need to write an expression for the total thermal energy gained by the plasma per unit time. This energy gain will be given by the product of the collision rate and the net change in thermal energy per collision averaged over all possible scattering outcomes (i. e. scattering angles). Thus the net rate of thermal energy gain by the plasma is:

$$\delta E = \int d\Omega \, \nu_{ei} \Delta E_t \tag{3.96}$$

where the integration is over all possible scattering angles. ΔE_T is given by eq. (3.95). The differential rate scattering into a solid angle $d\Omega$ is given by the product of the differential scattering cross section, the velocity of the incoming electron, the density of ion scatterers and a differential unit of time. This quantity is then weighted by the number of electrons with thermal velocities between v_T and $\mathrm{v}_T + d\,\mathrm{v}_T$ which is given by the electron distribution function. The scattering rate, then, is:

$$\nu_{ei}(\mathrm{v}_t) = \frac{d\sigma}{d\Omega} d\Omega \, \delta t \, \mathrm{v} \, n_i \, f(\mathrm{v}_t) d\,\mathrm{v}_t \tag{3.97}$$

Using eqs. (3.92) and (3.97) in relation (3.96) yields for the heating rate:

$$\delta E = \delta t \, n_i f(\mathrm{v}_t) d\,\mathrm{v}_t \frac{m_e}{2} \int \frac{d\sigma}{d\Omega} \mathrm{v} \left(\mathrm{v}_t'^2 - \mathrm{v}_t^2 \right) d\Omega \tag{3.98}$$

Recalling eq. (3.95), we note that:

$$\tfrac{1}{2}\left(\mathrm{v}_t'^2 - \mathrm{v}_t^2 \right) = (\mathbf{v} - \mathbf{v}') \cdot \mathbf{u} \tag{3.99}$$

With this fact we can simplify the integral in (3.98). We introduce a coordinate system detailed in figure III.21. θ' is the angle between $\mathbf{v}$ and $\mathbf{u}$, while θ, ϕ are the angles between $\mathbf{v}$ and $\mathbf{v}'$, and $\mathbf{v}'$ and the $\mathbf{vu}$ plane respectively (see figure III.21). With these definitions, (3.99) becomes:

$$(\mathbf{v}-\mathbf{v}')\cdot\mathbf{u}=\mathbf{u}\cdot\mathbf{v}(1-\cos\theta)-u\,\mathrm{v}\sin\theta'\sin\theta\cos\phi \tag{3.100}$$

Since the differential scattering cross section will be independent of ϕ, the second term in (3.100) will average to zero when introduced into (3.98) because of the $\cos\phi$ dependence. Thus we have for the heating rate:

$$\delta E=\delta t\, n_i f(\mathrm{v}_t)d\mathrm{v}_t\, m_e\int_0^{\pi}\frac{d\sigma}{d\Omega}\mathrm{v}\,\mathbf{u}\cdot\mathbf{v}(1-\cos\theta)\sin\theta\, d\theta \tag{3.101}$$

- HEATING BY ELASTIC COULOMB SCATTERERS

Eq. (3.101) is completely general and, in principle, any appropriate scattering cross section can introduced to obtain a heating rate. An average over all thermal velocities will then yield a total plasma heating rate. We are most interested in the case in which the scattering cross section is given by the formula for coulomb scattering. In that

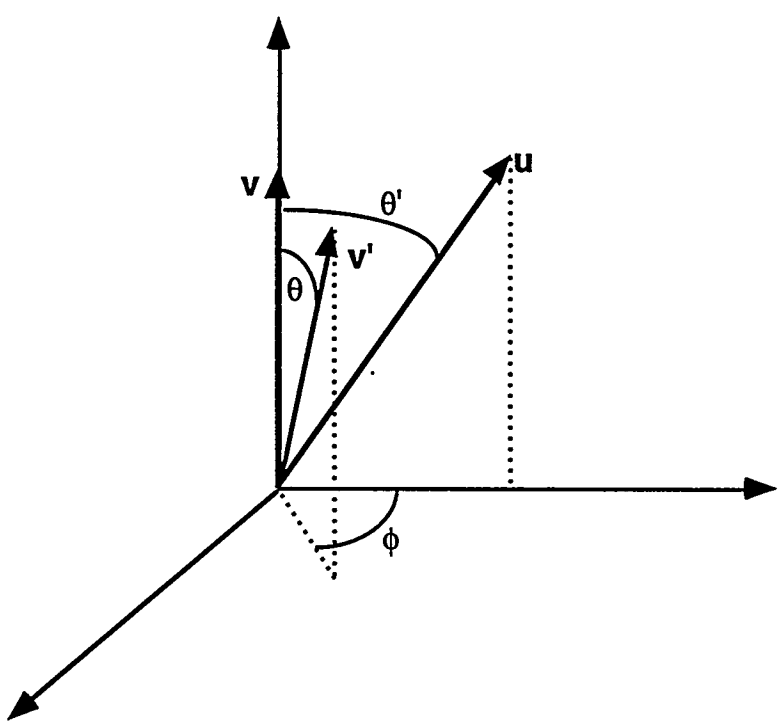

Figure III.21: Coordinate system describing the scattering of an electron.

case the differential cross section can be written [72]:

$$\frac{d\sigma}{d\Omega} = \frac{Z^2 e^4}{\left(2m_e \mathrm{v}^2\right)^2 \sin^4 \theta/2} \tag{3.102}$$

It is clear that an integration from 0 to π over the coulomb cross section in eq. (3.101) will diverge. At this point it is necessary to follow the standard treatment of coulomb scattering in a plasma by introducing a cutoff on the minimum scattering angle. To do this we need the relation between the impact parameter of the scattered electron, b, and the scattering angle, θ. This is given by [72]

$$b = \frac{Ze^2}{m_e \mathrm{v}^2} \cot\left(\theta/2\right) \tag{3.103}$$

Following the standard treatment, we shall set the maximum impact parameter to that distance over which the coulomb field of the scatterer is shielded by the plasma, namely the Debye length, given by [95]:

$$\lambda_D = \sqrt{\frac{k_B T}{4\pi n_e e^2}} \tag{3.104}$$

We can, furthermore, assume that the minimum scattering angle is very small (to a very good approximation). Using relations (3.103) and (3.104) the minimum scattering angle is:

$$\begin{aligned} \theta_{\min} &= 2\cot^{-1}\left(\frac{m\mathrm{v}^2 \lambda_D}{Ze^2}\right) \\ &\approx \frac{2Ze^2}{m\mathrm{v}^2 \lambda_D} \end{aligned} \tag{3.105}$$

With this shielded coulomb cutoff, eq. (3.101) becomes:

$$\frac{\delta E}{\delta t} = n_i f(\mathrm{v}_t) d\mathrm{v}_t m_e \frac{Z^2 e^4}{\left(2m_e \mathrm{v}^2\right)^2} \mathrm{v}\mathbf{u}\cdot\mathbf{v} \int_{\theta_{\min}}^{\pi} \frac{(1-\cos\theta)\sin\theta}{\sin^4 \theta/2} d\theta \tag{3.106}$$

The integral in (3.106) can be evaluated:

$$\int_{\theta_{\min}}^{\pi} \frac{(1-\cos\theta)\sin\theta}{\sin^4 \theta/2} d\theta = 4\ln\left(\frac{2}{1-\cos\theta_{\min}}\right)$$

$$\approx 4\ln\left(\frac{4}{\theta_{\min}^2}\right) \tag{3.107}$$

$$\approx 8\ln\Lambda$$

where I have introduced the standard coulomb logarithm, given by

$$\Lambda \equiv \frac{m_e \mathrm{v}^2 \lambda_D}{Ze^2} \tag{3.108}$$

Finally, equation (3.106) becomes:

$$\frac{\delta E}{\delta t} = n_i f(\mathrm{v}_t) d\mathrm{v}_t m \frac{4\pi Z^2 e^4}{m_e^2} \frac{1}{\mathrm{v}^3} \mathbf{u}\cdot\mathbf{v}\ln\Lambda \tag{3.109}$$

At this point we must now average over all angles between $\mathbf{v}$ and $\mathbf{u}$. In general this cannot be done analytically because of the v^2 dependence in $\ln\Lambda$. We can, however, derive an approximate solution to (3.109) if we simply ignore the slow dependence in the logarithm. This approximation will be good in the limit of a very high laser field. In the case of very large oscillation velocity we can approximate, inside the logarithm, $\mathrm{v}^2 \approx u^2$ and pull the logarithm out of the integral in (3.109). The integral can then be evaluated and gives:

$$\int_1^{-1} \frac{1}{\mathrm{v}^3} \mathbf{u}\cdot\mathbf{v}\, d(\cos\theta') = \int_1^{-1} \frac{u\mathrm{v}_T\cos\theta' + u^2}{\left(2u\mathrm{v}_T\cos\theta' + u^2\mathrm{v}_T^2\right)^{3/2}} d(\cos\theta')$$

$$= \frac{2}{u} \qquad \mathrm{v}_T < u \tag{3.110}$$

$$= 0 \qquad \mathrm{v}_T > u$$

This result yields for the heating rate of electrons with thermal velocity v_T:

$$\frac{\delta E}{\delta t} = n_i f(\mathrm{v}_T) d\mathrm{v}_T \frac{8\pi Z^2 e^4}{m_e} \ln\Lambda \frac{1}{u} \qquad u > \mathrm{v}_T$$
$$= 0 \qquad u < \mathrm{v}_T \tag{3.111}$$

To ascertain the validity of the above approximation, I compare in figure III.22 a plot of the heating rate verses oscillation velocity u/v_t given by equation (3.111) and the result obtained by numerically integrating the general relation in (3.109). As can be seen, the approximate treatment of (3.111) predicts no heating of electrons with quiver velocity of less than the thermal velocity while the more rigorous result correctly predicts the heating for these low velocity electrons. The approximate result over-estimates the heating rate at quiver velocities such that $u \sim \mathrm{v}_T$. However, the two results converge to nearly the same value for $u/\mathrm{v}_t \geq 3$. Thus, as expected, the approximation is particularly good in the case of large oscillation velocities.

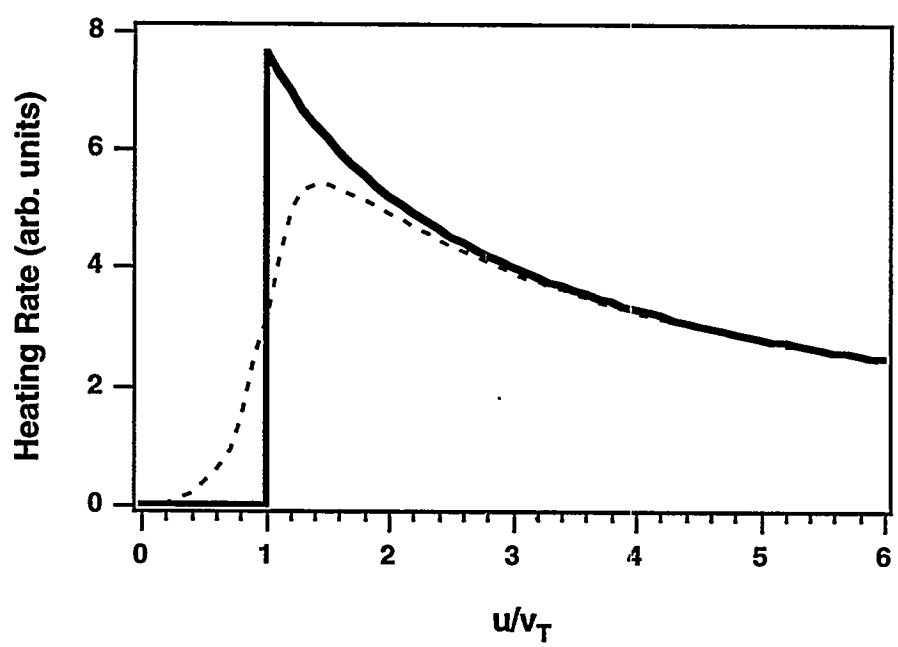

Figure III.22: Functional form of the heating rate verses oscillation velocity u/v_t given by equation (3.111) (solid line) and the result obtained by numerically integrating the general relation in (3.109) (dashed line).

Finally, we need to average eq. (3.111) over a laser cycle to retrieve the average energy deposited from the field into the electrons per unit time. We average eq. (3.111) by integrating in the first equation over the part of the cycle in which the velocity is greater than v_T. To evaluate this integral we assume that $u_0 >> v_T$ (a strong field approximation):

$$\int_{\sin^{-1} v_T/u_0|_1}^{\sin^{-1} v_T/u_0|_2} \frac{1}{u_0 \sin\phi} d\phi = \frac{1}{u_0} \ln\left| \frac{\tan\left[\sin^{-1}((\pi - v_T/u_0)/2)\right]}{\tan\left[\sin^{-1}(v_T/2u_0)\right]} \right| \approx \frac{1}{u_0} \ln\left[\frac{2u_0}{v_T}\right] \tag{3.112}$$

The cycle averaged energy deposited per unit time then becomes

$$\frac{\delta E}{\delta t} = n_i n_e \frac{8Z^2 e^4}{m_e} \ln\Lambda \frac{1}{u_0} \ln\left[\frac{u_0}{v_T}\right] \qquad u_0 > v_T$$
$$= 0 \qquad u_0 < v_T \tag{3.113}$$

where we have ignored the slow variation of the logarithm and averaged over the electron energy distribution.

From this analysis we can make some important generalizations about collisional heating in a plasma. First, we see from eq. (3.113) that in high field strengths, the heating rate actually decreases with increasing oscillation velocity (which is proportional to $I^{1/2}$). This behavior is a consequence of the fact that the coulomb cross section drops with electron velocity as v^{-4}. Eq. (3.113) also indicates that the maximum heating rate occurs when the oscillation velocity is comparable to the thermal velocity. In experiments in which we wish to heat the electrons to temperatures of 100 to 1000 eV, this result implies that it is desirable to heat with a pulse of ponderomotive energy of 100 to 1000 eV. This implies an optimum intensity of between 10^{15} W/cm^2 and 10^{17} W/cm^2.

- NUMERICAL CALCULATIONS

The rate of energy deposition derived in eq. (3.113) is identical to the rate of

collisional heating derived in a more sophisticated analysis by Jones and Lee in the strong field limit (i. e. when the oscillation velocity is larger than the electron thermal velocity) [85]. This rate predicts that for a 10 eV He plasma, with an ion density of 10^{18} cm^{-3} at an intensity of 10^{16} W/cm^2 the heating rate is approximately ~3 eV/ps. So the contribution to the heating of gases is, in general, quite small [160].

To gain some additional insight into the magnitude of the collisional heating and the scaling with some laser parameters, we have performed numerical calculations using the general heating equations of Jones and Lee. We calculate the heating of electrons of a single initial thermal velocity and ignore electron-electron collisions (i. e. ignore thermalization). These calculations are only meant to indicate the relative values of the collisional heating and do not constitute a complete description of the plasma. To do that would require solving the full Fokker-Planck equation [95].

For the following calculation parameters that are of interest in short pulse, optically ionized plasmas have been assumed. We assume the initial electron thermal energy to be 10 eV. We consider the case of a doubly ionized helium plasma (Z=2) with an ion density of 5 x 10^{18} $ions/cm^3$. We calculate the heating due to a 100 fs (full width at half maximum), high intensity laser pulse. The heating as a function of laser peak intensity for a laser wavelength of 825 nm is shown in figure III.23 for a 10 eV initial electron temperature. Eq. (3.113) predicts a weak dependence of the heating on intensity (roughly $\sim I^{-1/2}$). This dependence can be seen in figure III.23 where the heating falls from 7 eV for a peak intensity of 10^{16} W/cm^2 to a heating of just above 3 eV for a peak intensity of 10^{18} W/cm^2. The most important result of this calculation is that at low density, the collisional heating is quite low.

III.4.D Monte Carlo Simulations of Laser Plasma Heating

Though we have made some estimates for the relative magnitude of the various heating mechanisms, it is desirable to conduct a calculation that incorporates the most

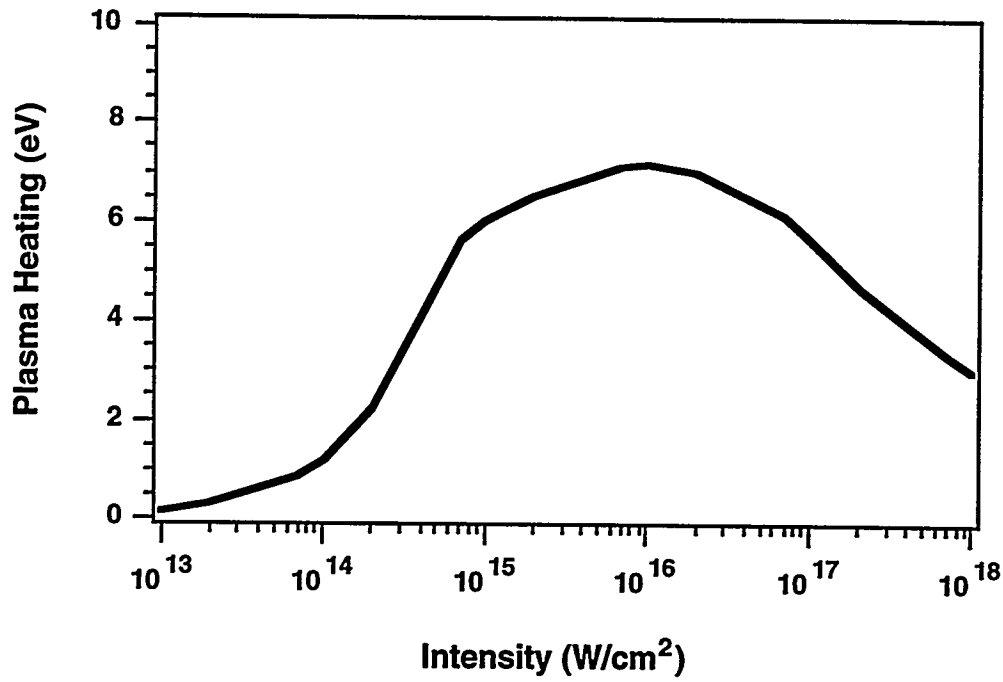

Figure III.23: Heating as a function of laser peak intensity for a 100 fs laser pulse with a wavelength of 825 nm. The atom density is taken to be 10^{19} cm^{-3} and the initial temperature is 10 eV. The plasma is assumed to be singly ionized (Z = 1).

important heating mechanisms. To do this in a code that includes both ATI heating and collisional heat, we have developed a Monte Carlo algorithm that includes both of these effects [50].

The code utilizes the quasi-classical concept of the ATI heating. The ionization rate equations are solved (eqs. (3.35a-c)) for an oscillating field. When the ionization rate becomes significant for a certain charge state, a number of test particles are generated at the time step of ionization with each electron weighted according to the ionization probability at the time in which it is born. The velocities of these test electrons are then propagated in the laser field according to Newton's equation. At each time step, we define a probability of each test electron undergoing a coulomb collision. A random number determines whether the test electron undergoes a coulomb collision. If it does, a second random number, used in conjunction with the differential scattering cross section for a

coulomb collision, determines the angle through which the electron is scattered. This treatment assumes instantaneous collisions within the laser field.

This treatment ignores electron-electron collisions, and therefore, ignores electron thermalization. This is a good approximation, since the thermalization time of the electrons oscillating in the field is much longer than the laser pulse width [178]. This code tracks only the velocities of the test particles; it assumes that the plasma is uniform. This is only a good approximation when the laser focal spot is large enough that the ponderomotive gradient does not move the electrons radially by any significant amount during the laser pulse [147]. This criteria is well satisfied for 100 fs pulses focused to intensity below 10^{18} W/cm^2 with a focal spot that is larger than 10 μm.

For the sake of illustration, we shall discuss the predicted electron temperatures for a gas of helium. As before, we define the plasma temperature as $kT_e = 2/3\langle E\rangle_{avg}$. First we shall consider the calculated temperature of a helium plasma subject to an 800 nm, 100 fs pulse focused to 2 x 10^{16} W/cm^2. This calculation is shown in figure III.24. At an atom density below about 10^{18} cm^{-3} the temperature is merely determined by the single atom ATI temperature, which in this case is about 35 eV. This is in good agreement with the simple calculation of ATI heating in He presented in section III.4.A. Only when the atom density approaches 10^{20} cm^{-3} does the heating from collisions play an important role. These densities are typically much higher than those used in the experiments described in the next two chapters.

The role of the collisional heating is also manifest when we consider the electron energy distribution function for various initial atom densities. Figure III.25 illustrates the calculated electron energy distributions for densities of 10^{17}, 10^{19} and 10^{20} cm^{-3} for a helium plasma subject to an 800 nm, 100 fs pulse focused to 2 x 10^{16} W/cm^2. At the low density, the temperature and the distribution function are characteristic of the single atom ATI distribution. However, as the atom density is increased, the collisional heating becomes more important as we saw in figure III.24. The non-Maxwellian character of the

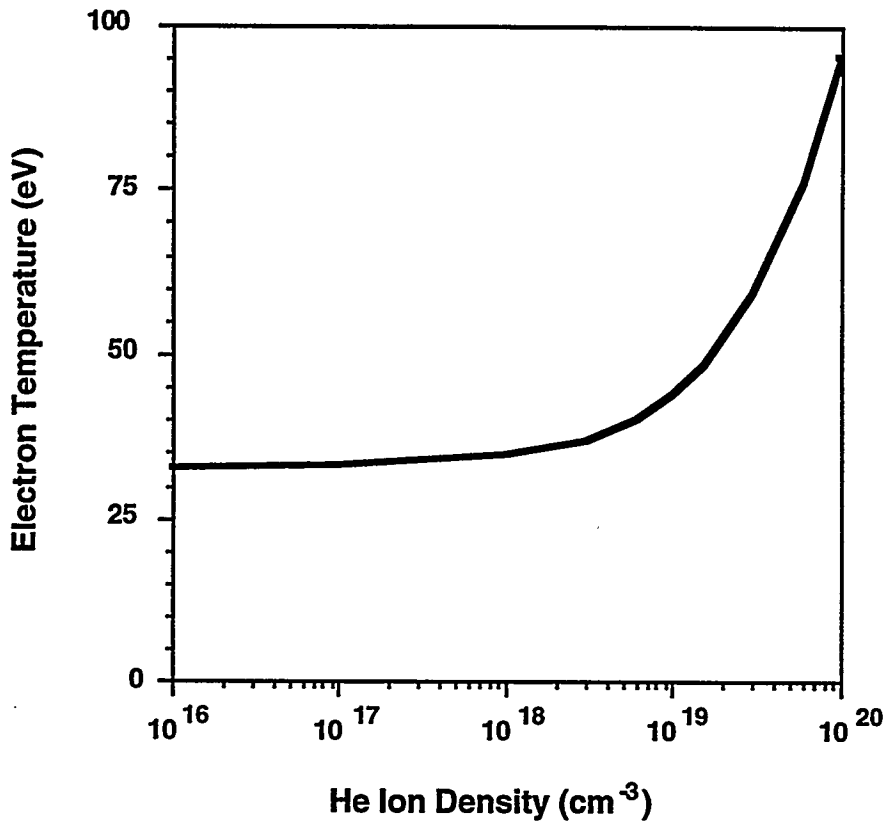

Figure III.24: Calculated temperature of a helium plasma as a function of initial He density ionized by an 800 nm, 100 fs pulse focused to 2 x 10^{16} W/cm^2.

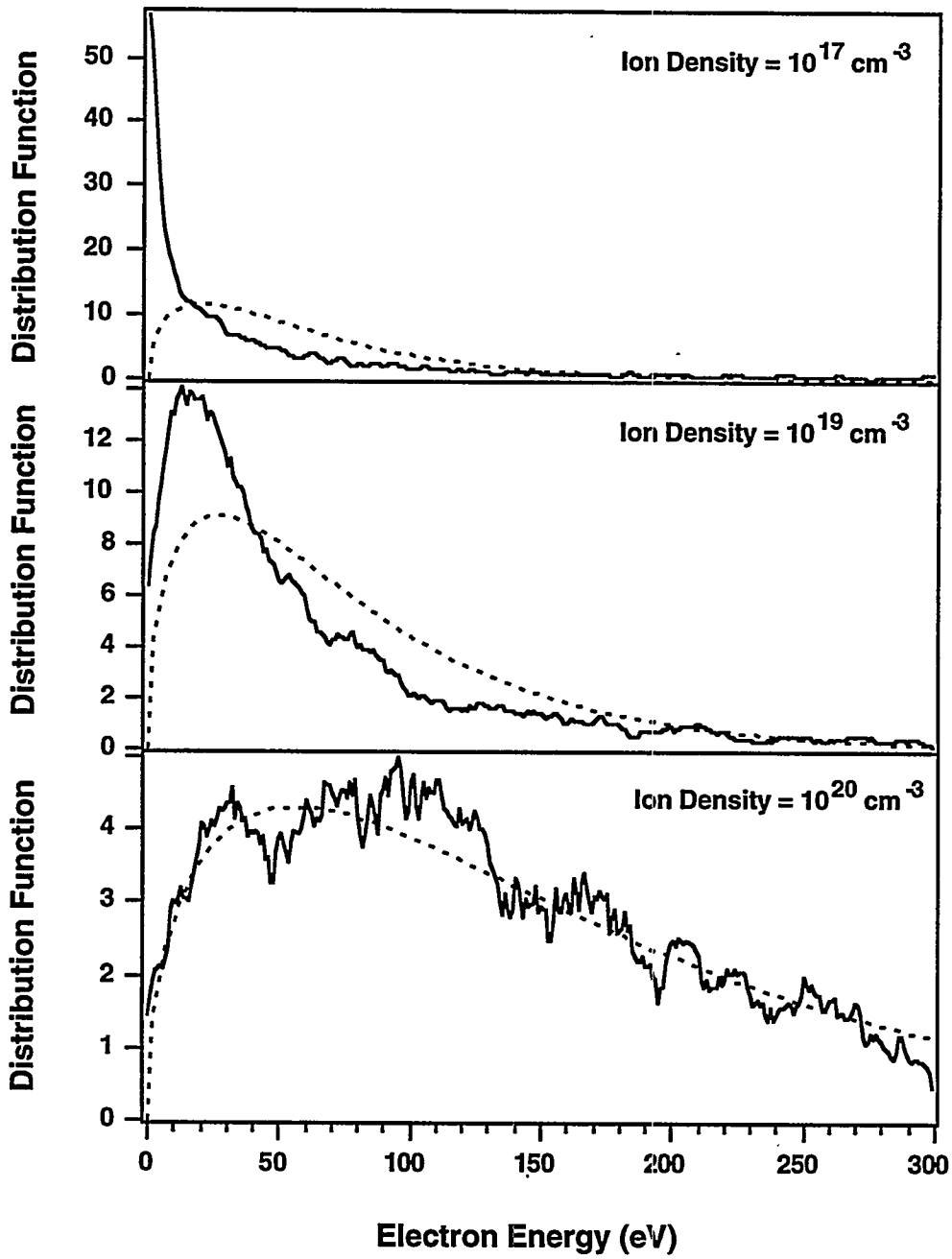

Figure III.25: Calculated electron energy distributions for densities of 10^{17}, 10^{19} and 10^{20} cm^{-3} for a helium plasma subject to an 800 nm, 100 fs pulse focused to 2 x 10^{16} W/cm^2. The solid line is the Monte Carlo calculation and the dashed line is a Maxwellian with the same average energy as the calculated distribution.

electron distribution evolves into a Maxwellian distribution at the highest density. This is a result of the fact that at the highest density, the distribution function is dominated by the collisions and not the ATI distribution. The evolution toward a Maxwellian at the highest density is also consistent with the predictions of Jones and Lee which indicate that the solution of the electron distribution function heated by inverse bremsstrahlung is that of a Maxwellian in the high field limit [85].

III.5 Conclusion

In this chapter, the theory of a variety of important laser-atom and laser-plasma interactions has been investigated. The physics behind high order harmonic generation by atoms subject to a strong laser field has been examined, and the theoretical limit on the wavelength range accessible with harmonic generation has been derived. The mechanism of plasma formation by tunnel ionization and the effects that the plasma formation has on the propagation of the laser were then explored. We presented data to confirm the validity of the tunnel ionization rate in He in low density gas and the onset of spectral blue shifting of the laser pulse in high density gas. A detailed examination of the three most important heating mechanisms in a tunnel ionized plasma followed: above threshold ionization, stimulated Raman scattering, and inverse bremsstrahlung. Calculations illustrated that plasma heating was not large in a low density plasma subject to irradiation by 100 fs pulses of intensity $<10^{17}$ W/cm^2. In general, we demonstrated that the plasma heating was predominately by single atom ATI and that a plasma with a temperature of < 50 eV was the usual result of the ionization of a low density gas by the short pulse laser.

Chapter IV

Studies and Characterization of Coherent X-Ray Production By High-Order Harmonic Generation

IV.1 Harmonic Generation: Overview of Experimental Aspects

IV.1.A Harmonics as a Source of Coherent X-rays

From the discussion of section III.2 the study of high order harmonic generation of a short, intense laser is of interest because it represents a direct pathway for coupling laser light into x-ray radiation. This is achieved through the nonlinear properties of atoms oscillating in the intense laser field. Harmonics have an additional feature that makes them very attractive: they are coherent. The generation of high order harmonics is a parametric process analogous to standard harmonic generation in a phase matched nonlinear crystal. Consequently the harmonics will exhibit the same coherence properties of the laser.

From the standpoint of applications, high-order harmonic generation is one of the potential sources of bright x-ray radiation for a host of future experiments in radiation-matter interaction physics [188]. When compared to other x-ray sources such as synchrotrons, and x-ray lasers, high order harmonic based sources exhibit a number of advantages. These include short pulse duration (40 fs - 100 ps), very high peak brightness ($>10^{23}$ photons mm^{-2} $mrad^{-2}$ sec^{-1}), good spatial coherence and broad spectral

tunability. For this reason, understanding the detailed properties of harmonic generation in the soft x-ray range is important.

In the past few years the emphasis has shifted from understanding the basic physics of high harmonic generation to the characterization of the harmonics for potential use in applications. These studies have included investigations of the spatial coherence of the harmonics, as well as the spectral and temporal characteristics [189, 43, 58]. The use of high order harmonics in applications has also begun to grow recently [9, 97]. Haight has utilized harmonics in an experiment that takes advantage of the harmonics' short pulse character by making time resolved measurements of surface states in semiconductors via photoelectron spectroscopy [77, 78]. Other applications include lifetime measurements of dipole transitions at XUV wavelengths [97]. In section IV.7 we describe an experiment that measured the relative photoionization cross section of various noble gases with harmonics.

As discussed in chapter III, the high order harmonics of visible radiation are generated when an intense, short pulse laser interacts with a gaseous medium of neutral atoms. The harmonics typically exhibit an initial drop in conversion with the first few orders, and then exhibit a plateau in conversion that can extend to very high orders, well into the x-ray wavelength range [102]. A characteristic spectrum of harmonics produced from a 600 fs, 1053 nm laser pulse laser focused into a gas jet of helium is shown in figure IV.1. The harmonic plateau is evident, with harmonics out to the 143rd order being generated, corresponding to a wavelength of 74 Å. From this data, it is clear that harmonics can be a means of converting laser radiation to coherent radiation with wavelengths below 100 Å.

As the laser intensity is increased, the yield of the harmonics typically grows nonlinearly. The harmonic yield with increasing laser intensity usually follows a characteristic curve [189]. An example of this dependence is illustrated in figure IV.2. The harmonic yield at low intensity initially rises rapidly with increasing intensity. This

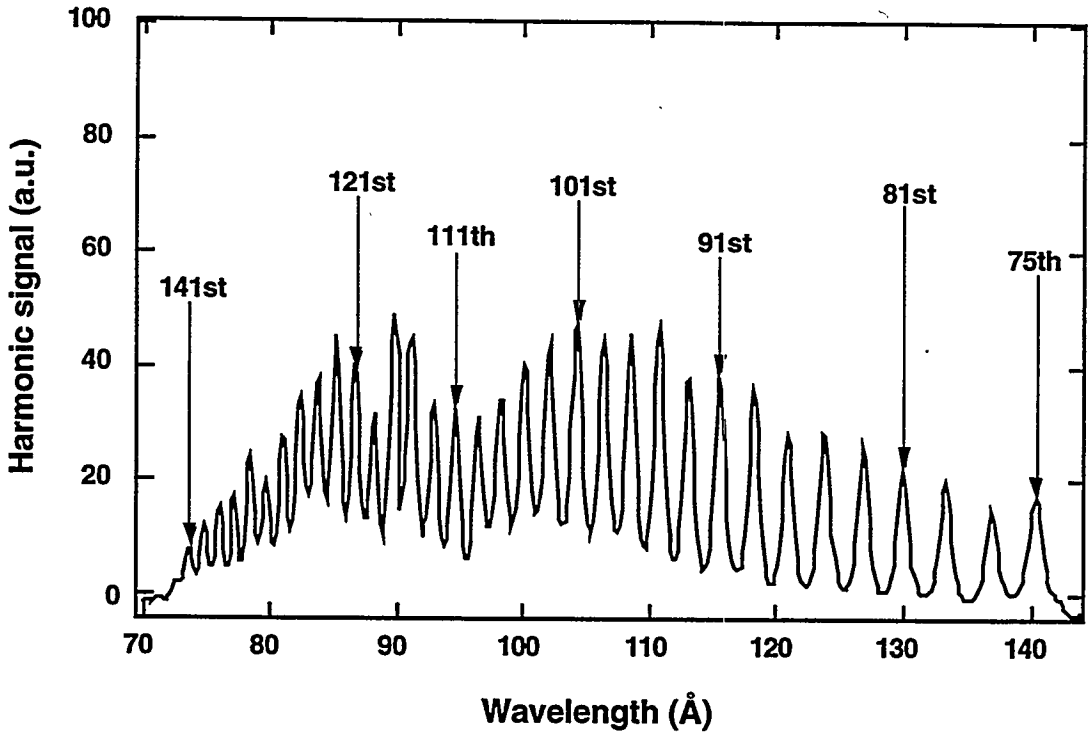

Figure IV.1: Spectrum of harmonics generated in helium by a 600 fs, 1053 nm glass laser focused to an intensity of 1 x 10^{16} W/cm^2 with an f/100 optic. (Data provided by J. K. Crane.)

corresponds to the intensity range in which the harmonic is in the cut-off of the spectrum. At higher intensity, the harmonic enters the plateau and exhibits a slower increase with laser intensity. When the laser intensity reaches a value sufficient to begin ionizing the atom with significant probability the yield begins to saturate and flatten out. This behavior is generally followed by all the high order harmonics in the tunneling regime.

IV.1.B Experimental Studies of Harmonic Generation.

In the experimental studies that are described in this chapter, harmonics from two different lasers were studied. The first is the Cr:LiSAF laser described in chapter II, and the second is a chirped pulse amplification laser system utilizing Nd:glass [141]. This second laser produces 600 fs pulses at a wavelength of 1052.7 nm with energies of up 8 J. Frequency doubling of this laser yields pulses at 526 nm with up to 3 J of energy.

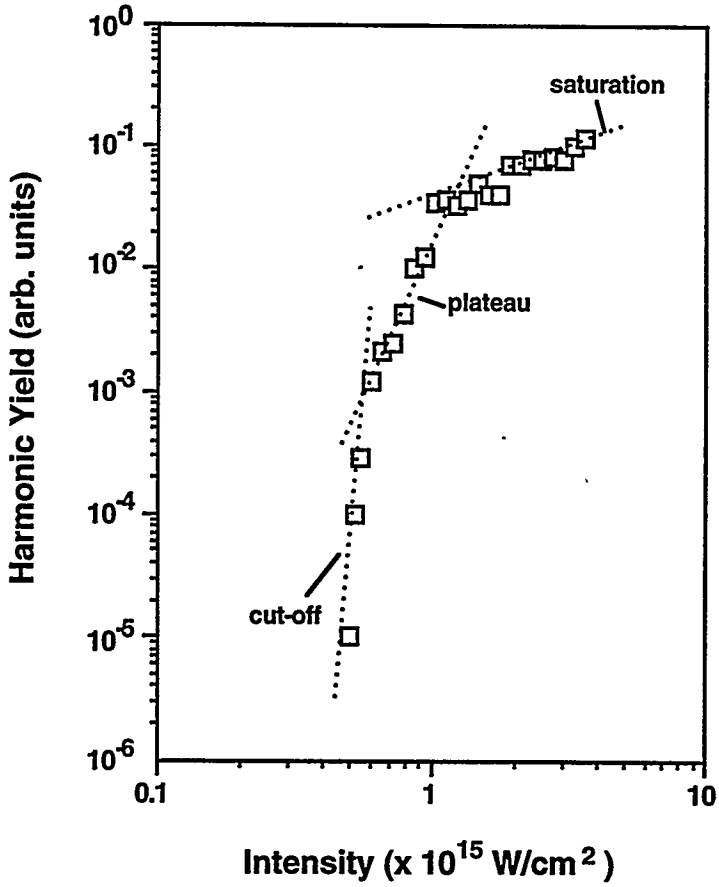

Figure IV.2: Measured yield of the 27th harmonic of the Cr:LiSAF laser in Ne as a function of increasing peak intensity.

For all the experimental studies the harmonics were generated in a gas medium produced by pulsing a gas jet into a vacuum chamber. The type of gas jet used varied for the different experiments, but all the jets employed produce gas density of 10^{17} to 10^{19} atoms/cm^3 depending on the actual jet utilized and the backing pressure used. To characterize the resulting harmonic radiation it is necessary to disperse the harmonic radiation to study the characteristics of the individual harmonics. A schematic illustrating the general layout of the spectrometers used in harmonic generation studies is shown in figure IV.3. The XUV and soft x-ray radiation is emitted from the jet on axis with the laser light. A grazing incidence grating then disperses the light. In all cases this grating is a variable line spaced gold grating operated at between 1 and 4° incidence depending on

the spectrometer. For some experiments, spectrometers were employed that utilized refocusing optics to increase the collection efficiency of the spectrometer. However, for most of the experiments, a flat grating was used without any refocusing in the plane transverse to the plane of wavelength dispersion. The harmonic radiation could be measured with a variety of detectors. These included a CsI coated micro-channel plate coupled to a phosphor screen, an electron multiplier, an x-ray streak camera with an image intensifier, and an x-ray CCD camera.

In this chapter experimental studies of the harmonic radiation produced under a variety of conditions are presented. The experiments were performed with an intent to characterize the harmonic radiation as a possible source of x-rays for applications. These studies include physical models to explain the behavior and to aid in the predictions of harmonic behavior under different conditions than those studied. The studies begin with an examination of the wavelength range achievable through harmonic generation. This is followed by a detailed study of the spatial profile qualities of the harmonics as well as a discussion of the effects of beam refraction on the harmonic spatial profiles. The spectral linewidth characteristics are also studied. These discussions are followed by a careful study of the energy yields and conversion efficiencies of the harmonics in the 350 to 170 Å range as well as a complete description of the conversion of harmonics in a numerical

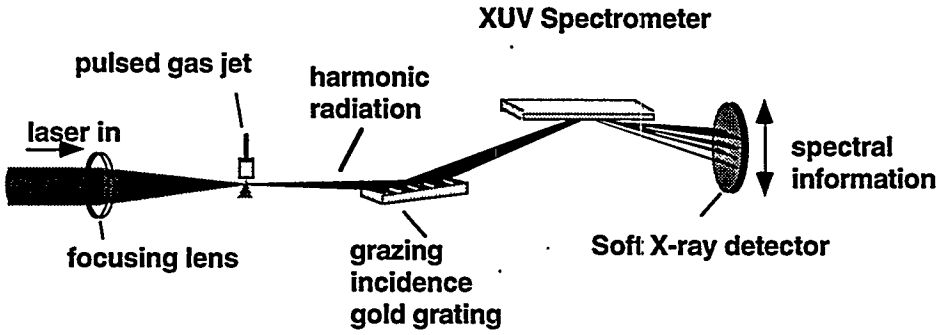

Figure IV.3: General experimental layout of high order harmonic generation experiments.

model. A demonstration experiment in which harmonics from the LiSAF laser are utilized in an application is then described. The chapter concludes with a discussion of an experiment that demonstrated the amplification of a harmonic in an x-ray laser amplifier performed at the Rutherford Appleton Laboratory in the United Kingdom.

IV.2 Accessible Wavelength Range With High Order Harmonics

Much of the recent research into harmonic generation to date has gone into determining the shortest wavelengths that are possible through harmonic generation [8, 101, 36]. Recalling the discussion of the last chapter, consideration of photon emission from a single atom suggests that harmonics can be generated out to the quasi-classical cut-off described by eq. (3.16) (from Krause et. al. [94]):

$$q\hbar\omega_0 \approx I_p + 3.2U_p \tag{4.1}$$

where, once again I_p is the atom ionization potential and U_p is the ponderomotive energy. As mentioned before, this formula suggests that shorter wavelength harmonics are attainable with a longer wavelength drive laser because of the λ^2 dependence of U_p. Furthermore, in the regime in which the peak focused intensity is comparable to or above the atom ionization intensity, the maximum value of U_p seen by the atoms will occur around this ionization intensity. Consequently, equation (4.1) predicts shorter wavelengths from the lighter noble gases such as neon and helium, which have higher ionization intensities (7.0×10^{14} W/cm^2 and 1.5×10^{15} W/cm^2 respectively for a 100 fs pulse).

A number of groups have experimentally explored the location of the high harmonic cutoff[8, 98, 119, 36, 93]. The 111th harmonic of 800 nm radiation has been observed by Macklin et. al. in neon [119]. The 135th harmonic of a 1ps, 1 μm glass laser

has been observed by L'Huillier et al. in neon [98]. We have observed up to the 85th harmonic of the 825 nm Cr:LiSAF laser in neon [45]. From equation (4.1), however, we expect that the shortest wavelengths are possible from helium with a long wavelength drive (preferably $\lambda > 1$ μm). In fact, the shortest wavelength achieved through harmonic generation in neutral atoms to date were generated, here, at LLNL, in helium by the 600 fs, 1053 nm glass laser focused to an intensity of 2×10^{15} W/cm^2 (figure IV.1, [45]). Harmonics extending to the 143rd order, a wavelength of 73 Å, were demonstrated. This cutoff wavelength falls somewhat below the prediction of equation (4.1), however, which predicts a cutoff harmonic near the 201st for these experimental conditions. This reduction in the cutoff wavelength at high intensity has been observed by others [101].

This reduction is due mainly to wave propagation phase matching effects [100]. As we mentioned in chapter III, when high conversion efficiency is desired, a focal geometry that minimizes the effects of the geometric phase mismatch from the focused laser beam is necessary. As we illustrated in chapter III, the qth harmonic has geometric coherence length given by $L_{coh} \approx \pi b / 2q$ where b is the focused laser confocal parameter. With weak focusing and a sufficiently long confocal parameter, it is possible to keep L_{coh} longer than the gas jet interaction length [113]. In this focusing regime, at high intensity the phase mismatch, Δk defined by $\Delta k = k_q - qk_0$, is dominated by the presence of a plasma. When the laser frequency is much less than the plasma frequency, the free electron phase mismatch is given approximately by:

$$\Delta k_e \cong \frac{e^2 n_e \lambda_q}{c^2 m_e}\left(1 - \frac{\lambda_0^{\,2}}{\lambda_q^{\,2}}\right) \tag{4.2}$$

Here n_e is the electron density and λ_q and λ_0 are the harmonic and laser wavelengths respectively. For a given drive wavelength, the phase mismatch increases with decreasing harmonic wavelength roughly like $\Delta k \sim \lambda_0 / \lambda_q$. Since the highest order harmonics are only produced at the highest intensities during the laser pulse, when the ionization rate is

significant, we, therefore, expect a significant reduction in efficiency for these higher orders due to the scaling of eq. (4.2).

We find that, in general, the cut-off predicted by eq. (4.1) tends to be more accurate for a shorter wavelength drive laser. The measured values of the harmonic plateau cut-off for three different laser wavelengths in three different target gases are tabulated in Table I. (Data from the 1 μm light was provided by J. K. Crane [34].) Here the measured value of the shortest wavelength harmonics are compared against the predictions of eq. (4.1) using ionization saturation intensities calculated from ADK tunnel ionization predictions [5]. The data at 1053 nm and 526 nm were from the fundamental and frequency doubled 600 fs Nd:glass laser respectively and the 825 nm data were from the Cr:LiSAF laser. All data were taken at comparable atom densities (~ 10^{18} atoms/cm^3) with a weak focus (confocal parameter much longer than the length of the 0.8 mm gas interaction length). The weak focus assures that the geometric coherence length for the cutoff harmonic was comparable to or greater than the gas jet length, minimizing the

Atom	Ionization Potential (eV)	λ_0 (nm)	Cut-off Order	Cut-off Energy (eV)	I_p+3.2U_p (eV)	γ
Ar	15.8	526 825 1053	13 33 47	30.7 49.7 55.5	29.1 60.5 68.5	3.6 2.5 2.4
Ne	21.6	526 825 1053	27 83 121	63.8 125.1 142.8	60.4 143.5 176.3	3.5 2.7 2.5
He	24.6	526 1053	35 141	82.7 166.4	97.3 314.3	2.5 1.6

Table IV.1: Comparison of the experimentally measured harmonic cut-off for various gases and laser wavelengths.

effects of the geometric phase mismatch. We have checked this by changing the confocal parameter but maintaining $L_{coh} > L_{jet}$, and confirming that the position of the cut-off is insensitive to focal geometry, (with the exception of the harmonics from the 1053 nm light in helium, where $L_{coh} \approx L_{jet}$ for the 141st harmonic). The peak intensity was approximately two to four times the saturation intensity for each gas assuring that the bulk of the atoms in the focal volume experienced an intensity above the saturation value.

We see that only the plateau produced by the 526 nm light in Ar and Ne extends to the prediction of eq. (4.1). The harmonics of the 825 nm and 1053 nm light consistently fall short of the $I_p + 3.2U_p$ prediction. We have also tabulated the value of γ which is defined by $E_{cutoff} = I_p + \gamma U_p$ for an experimentally observed cut-off. For all three gases, the value of γ falls with increasing drive wavelength. The value of γ is particularly small for the cutoff of the 1053 nm light in helium where it falls to 1.6. This can probably be attributed to the increased sensitivity of the free electron phase mismatch to the shorter wavelength harmonics. (This low value may also be attributable to an increase of the importance of the geometric phase mismatch for the extremely high orders, $q > 100$).

IV.3 Spatial Distribution Properties of the High-Order Harmonics

IV.3.A Studies of Harmonic Spatial Profiles at Intensity Around the Saturation Intensity

Another important aspect of characterizing harmonic generation is measuring the spatial divergence and profile of the harmonics. Knowledge of the harmonic spatial distribution yields some information on the spatial coherence of the harmonic source and determines the suitability of the source for refocusing in applications. A number of groups have investigated the spatial properties of the harmonics experimentally and numerically [167, 185, 99, 146, 136]. Tisch et. al. previously studied the spatial

properties of harmonics produced in He with a 1 ps, 1053 nm laser [185]. They observed a divergence that decreased with increasing harmonic order and found that the harmonics seemed to exhibit a large amount of structure, which they attributed to the effects of the free electron phase mismatch. Peatross et. al. studied low order harmonic distributions (q = 11 - 21) from a 1 ps, 1 μm laser at very low atom densities and found that the distributions contained a low divergence central lobe surrounded by broad wings [146].

- EXPERIMENTAL RESULTS

Since the use of the harmonics as a source demands high photon yields as well as a good spatial coherence properties, a knowledge of the spatial properties of harmonics produced in gas of higher density than used in these experiments is desirable. Consequently, we have examined the spatial properties of the harmonics produced by the LiSAF laser over a broad wavelength range in gases of density from 10^{18} to 10^{19} atoms/cm^3 [167]. These measurements were conducted prior to the installation of the 19 mm LiSAF amplifier in the system. The system also used both 9.5 mm amplifiers in a single pass configuration [49]. Though this configuration limited the laser energy to < 100 mJ, it permitted focusing to a smooth, 1.3 x diffraction limited Gaussian spot, which was optimal for the studies of the harmonic spatial coherence properties [49].

For these experiments, the laser was focused with an 85 cm focal length lens (f/17) to a round, 70 μm focal spot ($1/e^2$). The measured divergence of the focused beam was 62 mrad. The laser was focused into the plume of gas produced by a sonic, General-Valve pulsed gas jet. This jet provided density of $>10^{18}$ cm^{-3} when backing pressure above ~ 100 psi was used. The harmonics produced were collected by a flat field spectrometer consisting of a flat, variable line spaced, gold grating (1200 lines/mm) at grazing incidence ($\alpha = 3°$) and a single, flat, carbon folding mirror. A 25 mm diameter, CsI coated, dual micro-channel plate (MCP) detector was located at the image plane of the spectrometer, 59 cm from the source of the harmonics. A phosphorus screen coupled to

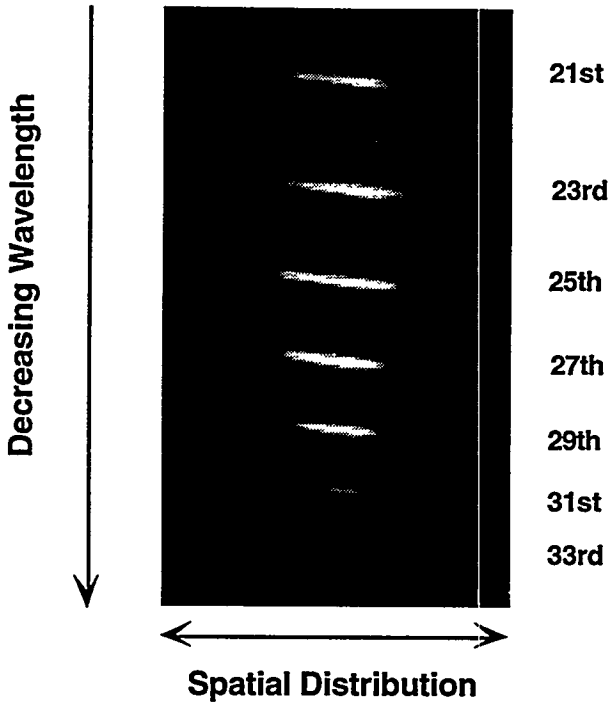

Figure IV.4: MCP image of harmonics produced in Ar by the LiSAF laser at an intensity of 4.0 x 10^{14} W/cm^2.

the MCP detector was read by an 8-bit CCD camera yielding simultaneous spectral and spatial information on each laser shot.

The experiments were conducted by averaging 5 laser shots in a 10% energy window. For intensities below the ionization saturation intensity, the images were extremely reproducible on a shot to shot basis. Figure IV.4 illustrates characteristic data. Here, the image of harmonics produced in Ar at an intensity of 4.0 x 10^{14} W/cm^2 are shown. The gas density for this data was about 1 x 10^{18} cm^{-3} Spectral information is contained in the vertical direction and spatial information is in the horizontal direction. Visible are the 19th through the 29th harmonics, (a wavelength range of 280 to 440 Å). At this peak intensity, which is comparable to the saturation intensity of the ionization in Ar, the profiles are smooth and structureless.

In figure IV.5, the line-outs of three harmonic profiles generated in argon at an intensity of 4.0 x 10^{14} W/cm^2 are shown. The 25th and the 29th harmonics represent harmonics in the plateau region of the spectrum and the 33rd harmonic is the highest order harmonic detectable in the cutoff with the MCP detector. The harmonic distributions exhibit near Gaussian profiles with little or no substructure. The harmonics' divergence, in general, decreases with increasing order. The divergence of the harmonics in argon range from 12 mrad for the orders around the 19th and the 21st down to 3 mrad for the 33rd harmonic. The predictions of the divergence on the basis of perturbation theory are also shown in figure IV.5. Perturbation theory predicts that, for a Gaussian laser profile, the divergence of the qth harmonic is given by

$$div.(q) \approx \frac{1}{\sqrt{q}} div.(laser) \tag{4.3}$$

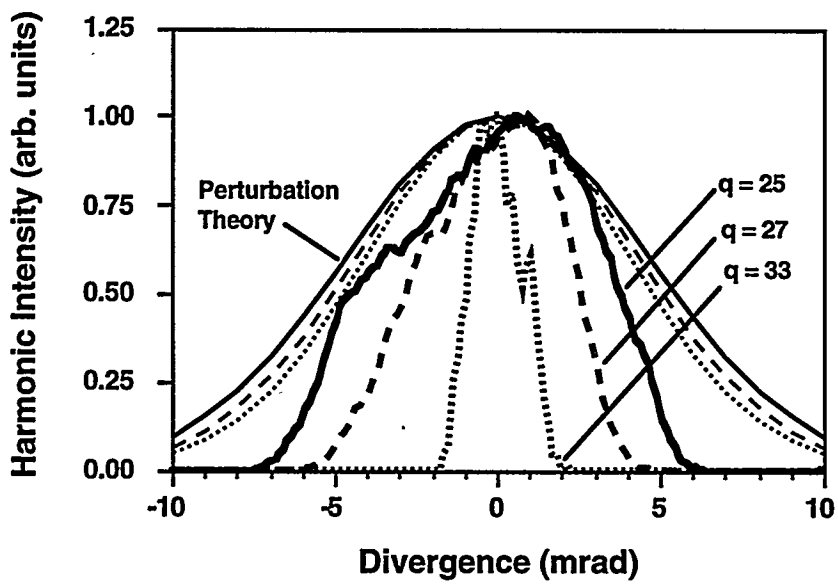

Figure IV.5: Integrated line-outs of harmonics produced in Ar (thick lines) for the 25th (solid line), the 27th (dashed line) and the 33rd (dotted line) harmonic. The perturbation theory predictions for these harmonics are shown as thin lines for comparison.

As can be seen in figure IV.5, the observed harmonic divergence is somewhat less than the predictions of lowest order perturbation theory.

Harmonics produced in neon show a similar behavior as those produced in argon. Data taken at an intensity of approximately the ionization saturation intensity, 7×10^{14} W/cm^2 is shown in figure IV.6. The 21st through the 43rd harmonics are visible in this image (191 to 392 Å). Like harmonics produced in argon, the distributions are smooth and without structure. Lineouts of the 29th, 35th and 41st harmonic are shown in figure IV.7. The neon harmonics exhibit a divergence that decreases from around 13 mrad for the lower orders down to 6 mrad for the 63rd harmonic. In general, as in Ar, we find that the harmonics in Ne exhibit a divergence that is slightly less than that predicted by lowest order perturbation theory.

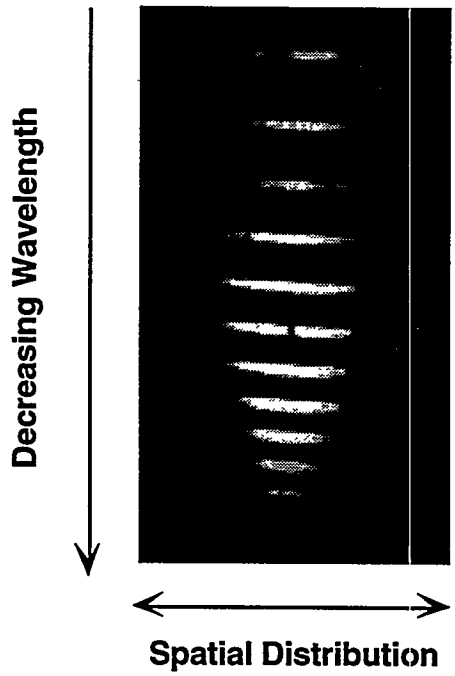

Figure IV.6: MCP image of harmonics produced in Ne by the LiSAF laser at an intensity of 7.0×10^{14} W/cm^2.

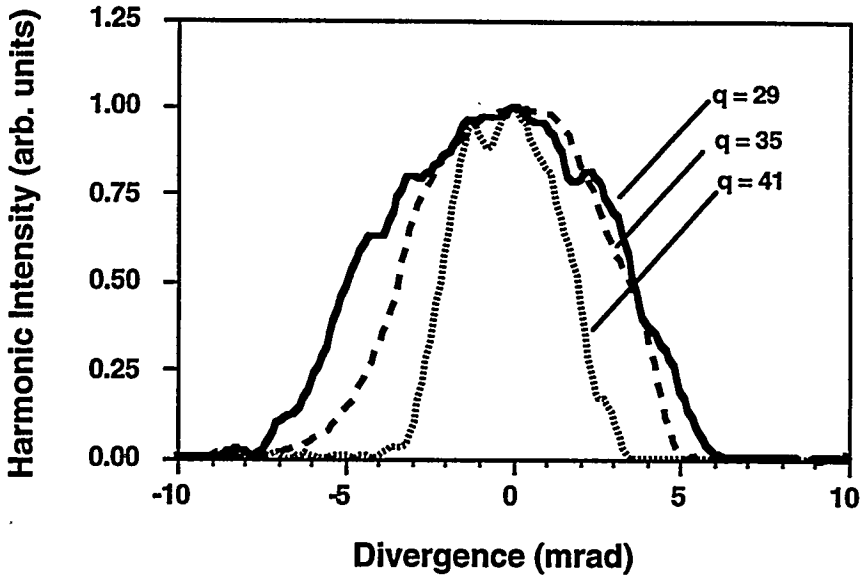

Figure IV.7: Integrated line-outs of harmonics produced in Ne (thick lines) for the 29th (solid line), the 35th (dashed line) and the 41st (dotted line) harmonic.

- PLANE WAVE, EFFECTIVE ORDER MODEL OF THE HARMONIC SPATIAL PROFILES

The narrow divergence can be explained by considering the fact that the yields of the high order harmonics scale with the laser intensity with an order that is typically less than the actual process order [102]. As discussed in chapter III, this behavior is characteristic of the strong field nature of the harmonic generation. We can make some simple approximations that permit us to devise a model accounting for the strong field response of the harmonics and more accurately predict their divergence in the weak focus limit.

We start with the fact that the yield of the high order harmonics in the plateau usually increases with increasing intensity with an effective order, p, that is typically less than the actual process order, q [102]. Second, we consider only the case of weak focusing, when the laser confocal parameter is much longer than the gas jet interaction length. As mentioned, this focal geometry is the case of greatest interest since it corresponds to the regime of highest conversion. The condition on weak focusing is

fulfilled in our experiment, since the confocal parameter was approximately 5 mm and the gas jet interaction length was of the order of 1 mm. When the condition of weak focusing is satisfied, it is a reasonable approximation to treat the laser field as a plane wave propagating through the medium.

With these two simplifying assumptions, the intensity distribution of the harmonic exiting the medium is approximately, in the absence of ionization, proportional to the pth power of the laser intensity. This implies that, if the laser has a Gaussian spatial profile at the focus, with a $1/e^2$ spot size of $\omega_0(1)$, then the qth harmonic's spot size is

$$\omega_0(q) \approx \frac{\omega_0(1)}{\sqrt{p}} \tag{4.4}$$

A Gaussian beam will then have a spot size that varies with z:

$$\omega(z) = \sqrt{1 + \frac{\lambda^2 z^2}{\pi^2 \omega_0^{\,2}}} \approx \frac{\lambda z}{\pi \omega_0} \tag{4.5}$$

The beam divergence is therefore

$$div. \sim \frac{\omega(z)}{z} \approx \frac{\lambda}{\pi \omega_0} \tag{4.6}$$

Coupled with the fact that $\lambda(q) = \lambda(1)/q$, this implies that

$$div.(q) \approx \frac{\sqrt{p}}{q} div.(laser) \tag{4.7}$$

This relation indicates that the divergence of the harmonics will, in general, be smaller than the prediction of eq. (4.3) due to the fact that p is less than q. Measurements of the effective nonlinear orders in Ar and Ne with the LiSAF laser for intensities corresponding to the plateau and the cut-off region for each harmonic are tabulated for selected harmonics in table IV.2. This data indicates that p varies from about 5 to 8 for plateau harmonics in Ar and varies from about 4 to 6 from harmonics in Ne.

Argon

Harmonic	Plateau	Cut-off
11th	5.0	11.1
21st	7.1	11.9
23rd	8.8	12.0
27th	7.0	13.0
31st	6.6	12.8

Neon

Harmonic	Plateau	Cut-off
21st	5.2	13.8
27th	6.2	11.1
31st	4.1	9.4
41st	5.8	11.8
51st	3.9	8.5

Table IV.2: Measured effective orders of harmonic signal increase with laser intensity for selected harmonics of the LiSAF laser in Ar and Ne.

To illustrate the use of eq. (4.7) , the measured divergence of harmonics in Ar are plotted as a function of order in figure IV.8. The lowest order perturbation theory predictions of eq. (4.3) are plotted as are the predictions of eq. (4.7) when an effective order of $p = 7$ is assumed. As can be seen here, the effective order predictions of the divergence are roughly comparable to the measured divergence in Ar. Though not exactly correct over the range of harmonics considered, the agreement is good considering the simple nature of the model and the assumptions made.

This picture does not account for the fact that the effective order of harmonic production, in fact, varies with intensity. A slightly more sophisticated approach to calculating the harmonic profiles is to use the actual measured dependence of the harmonic generation with increasing intensity to calculate the harmonic near field profile (i.e. at the focal spot). Thus the harmonic intensity at the focus is given by the relation:

$$I_q(r) = G\left[I_0 e^{-2r^2/w_0^2}\right] \tag{4.8}$$

where $G[I]$ is a function representing the harmonic yield as a function of intensity. It is derived from measurements similar to that illustrated in figure IV.2. The harmonic far field profile is calculated from the Fourier transform of eq. (4.8).

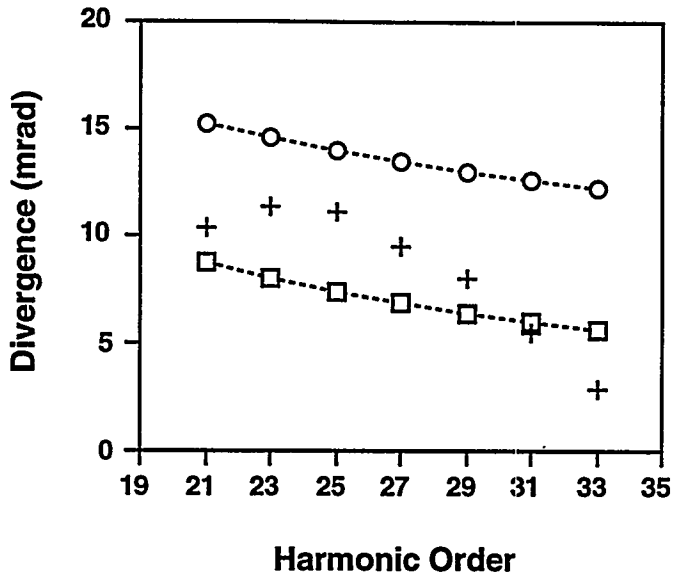

Figure IV.8: Measured divergence of harmonics in Ar with an intensity of 4 x 10^{14} W/cm^2 as a function of harmonic order (crosses). The predictions of perturbation theory are shown as circles, and the effective order predictions are shown as squares.

The divergence calculated in this manner tends to be larger than the prediction of eq. (4.7). At lower intensity, while the harmonic is still in the "cut-off" regime, the effective order is, in general larger (see table IV.2). Thus, the harmonic near field profile will tend to be truncated in radius in the lower intensity Gaussian wings at the laser focus. This will serve to make the effective near field size of the harmonic smaller than the simple I_0^p prediction and cause the harmonic divergence to be larger. This more sophisticated approach is compared to the measured harmonic divergence of the harmonics in Ne in figure IV.9. For comparison, the perturbation theory predictions of eq. (4.3) and the effective order model predictions of eq. (4.7) for a $p = 5$ (see table IV.2) are shown as well. The harmonics in neon exhibit a divergence that falls between the perturbation theory predictions and the plane wave model. The use of the general intensity dependence in Ne tends to more accurately predict the divergence than does the effective order model. Comparison of the predicted profiles of the 35th and 47th harmonics with the predicted far

field profiles of the plane wave model employing the actual, general intensity dependence of the harmonic are shown in figure IV.10 with the experimental values.

The simple theory outlined serves only as a guide for determining the harmonic divergence. In principle, a numerical integration of the wave equation, including the intensity dependent phase of the atomic dipole as well as the effects of ionization is required for a complete description of the harmonic profiles. Recent work by Salierès et. al. has investigated aspects of these results with such a model and found good agreement with experiment [168]. However, the essence of the physics of the harmonic generation is contained in this simple effective order analysis. The essential result of these measurements is that the harmonic radiation produced at an intensity near or below the ionization saturation intensity exhibit very clean, single transverse mode profiles. This suggests a high state of spatial coherence and is a promising result for applications.

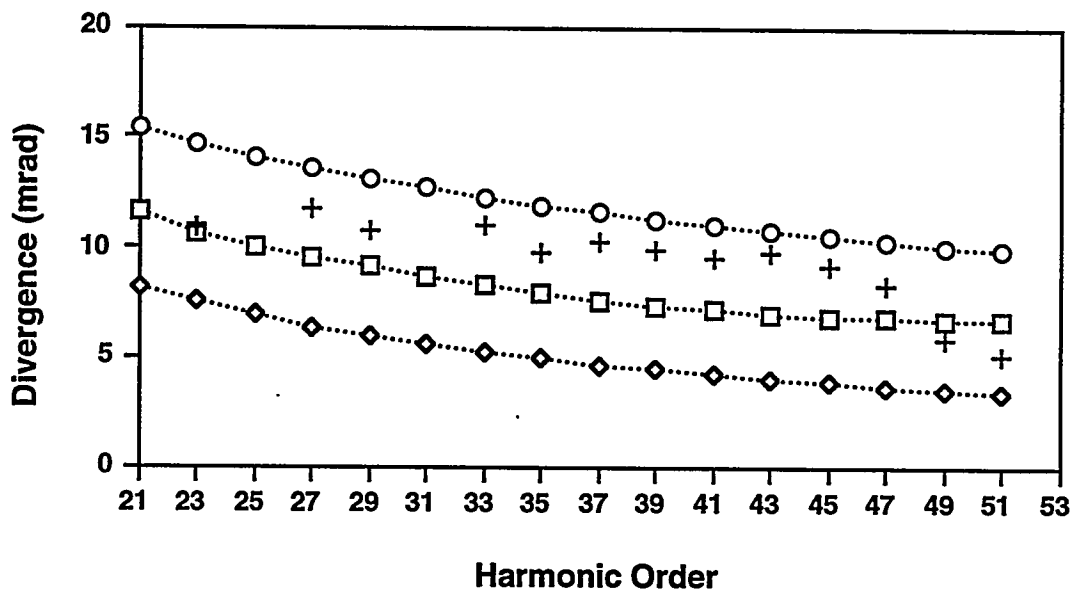

Figure IV.9: Measured divergence of harmonics in Ne with an intensity of 7 x 10^{14} W/cm^2 as a function of harmonic order (crosses). The predictions of perturbation theory are shown as circles, the effective order predictions are shown as diamonds, and the general plane wave model is shown a squares.

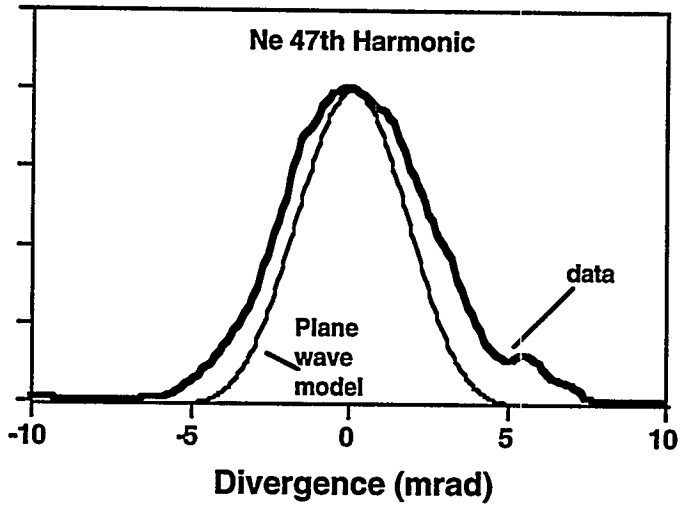

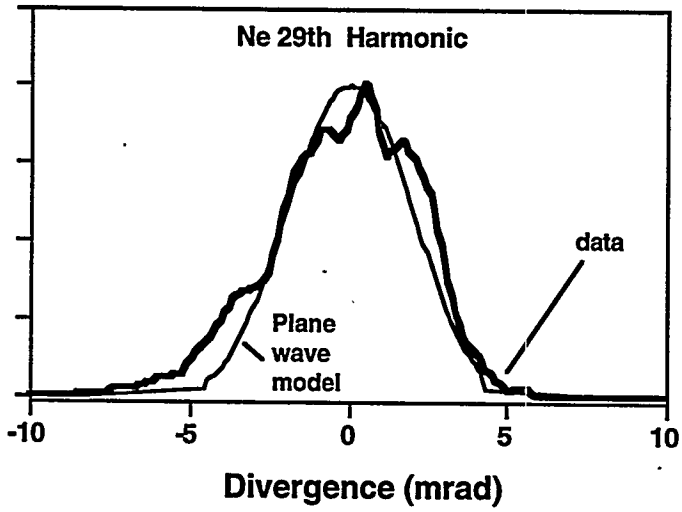

Figure IV.10: Measured harmonic profiles in Ne compared with the predicted profiles of perturbation theory and the general plane wave model.

IV.3.B The Effects of Plasma Formation on the Harmonic Spatial Distributions

At intensities above the ionization saturation intensity, this simple picture of the harmonic profiles is no longer true and the divergence can no longer be described by the effective order predictions of eq. (4.7) or even the general plane-wave model. Since the neutral atoms are destroyed by ionization at higher intensity, modeling the harmonic by a

simple monotonically increasing intensity dependence is no longer appropriate. Experimentally, at higher intensities just in the vicinity of the ionization saturation intensity, we see the harmonic divergence significantly increase above the estimates of eq. (4.7). Figures IV.11 a and IV.11b show the measured divergence of the 27th and 31st harmonics in Ar and the 37th and 43rd harmonics in Ne as a function of intensity. At an intensity above I_{sat} (indicated in the figure) the divergence begins to increase.

This behavior can be understood when the effects of plasma formation due to ionization during the harmonic generation are considered [45, 4]. As discussed in chapter III, the creation of a plasma gives rise to a temporally and spatially varying refractive index. The refraction of the harmonics resulting from the plasma formation is negligible due to their short wavelength. The refraction of the fundamental beam, however, can be quite severe under the experimental conditions in which we produce the harmonics

Recalling the result of section III.3.C, the refraction will result in a destruction of the single spatial mode character of the laser and effect the spatial character of the harmonics produced when the electron density on the propagation axis reaches the critical value defined in eq. (3.40). The gas density regime of interest for high harmonic conversion efficiency, ~ 10^{18} - 10^{19} atoms/cm^3, will cause this relation to be satisfied for 1 μm light focused to 100 μm when as little as 0.1% - 1% of the atoms have been ionized. We therefore expect significant refraction in our parameter range and subsequent effects on the spatial profiles of the harmonics.

Consequently, as the peak laser intensity is increased above the ionization threshold, the refraction of the fundamental begins to affect the harmonic profiles. To examine this effect, a series of experiments were performed at a higher density than in the studies of the previous section. For these studies, the target medium was produced by a gas jet equipped with a supersonic Laval nozzle. This jet produced a relatively uniform gas interaction region of ~0.8 mm in length [31] and an atom density of approximately

(a)

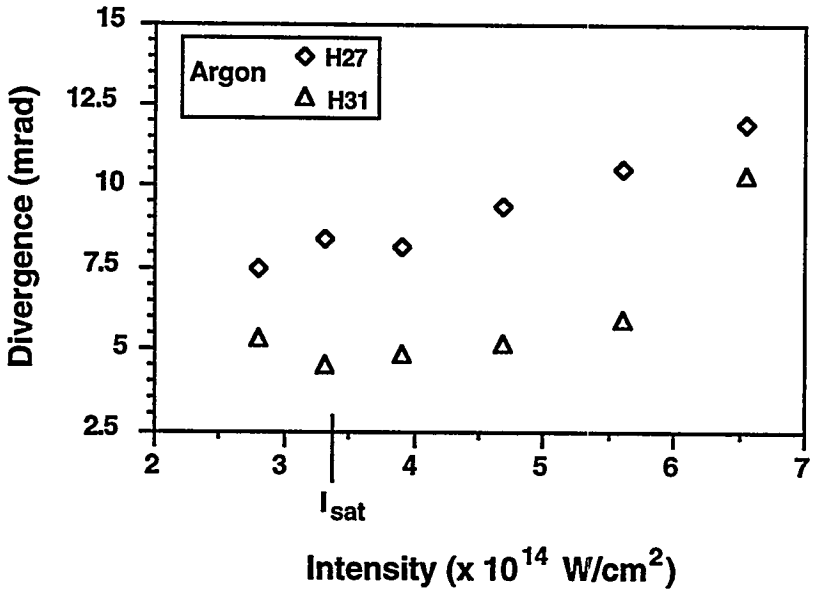

(b)

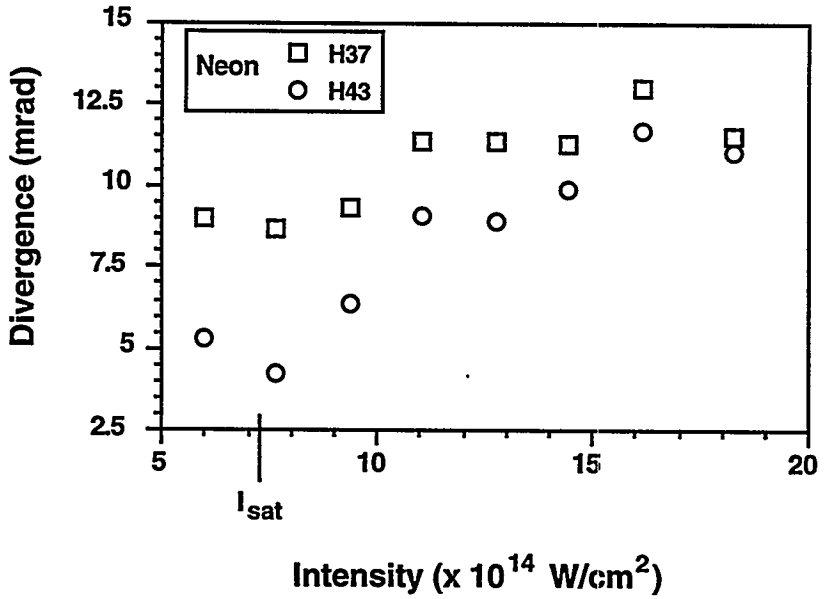

Figure IV.11: Measured divergence of harmonics of the LiSAF laser in a gas density of ~ 10^{18} cm^{-3} as a function of peak intensity for Ar **(a)** and Ne **(b)**.

5×10^{18} cm^{-3} [149]. We examined the profiles of harmonics produced with both the Cr:LiSAF laser as well as the frequency doubled Nd:glass laser at a focal speed of f/50. This was achieved with the LiSAF laser by focusing with a f = 1 m lens and aperturing the beam to a diameter of 2 cm and was achieved with the Nd:glass laser by aperturing the beam to 7 cm and focusing with an f = 3.5 m lens.

Figure IV.12 shows the profiles of harmonics produced in argon by the Cr:LiSAF laser at intensities corresponding to ~ I_{sat} (fig IV.12a) and an intensity ~2 x I_{sat} (fig IV.12b). In these images, the spectra are dispersed horizontally and the spatial distribution is in the vertical direction. The images are of the 19th through the 29th

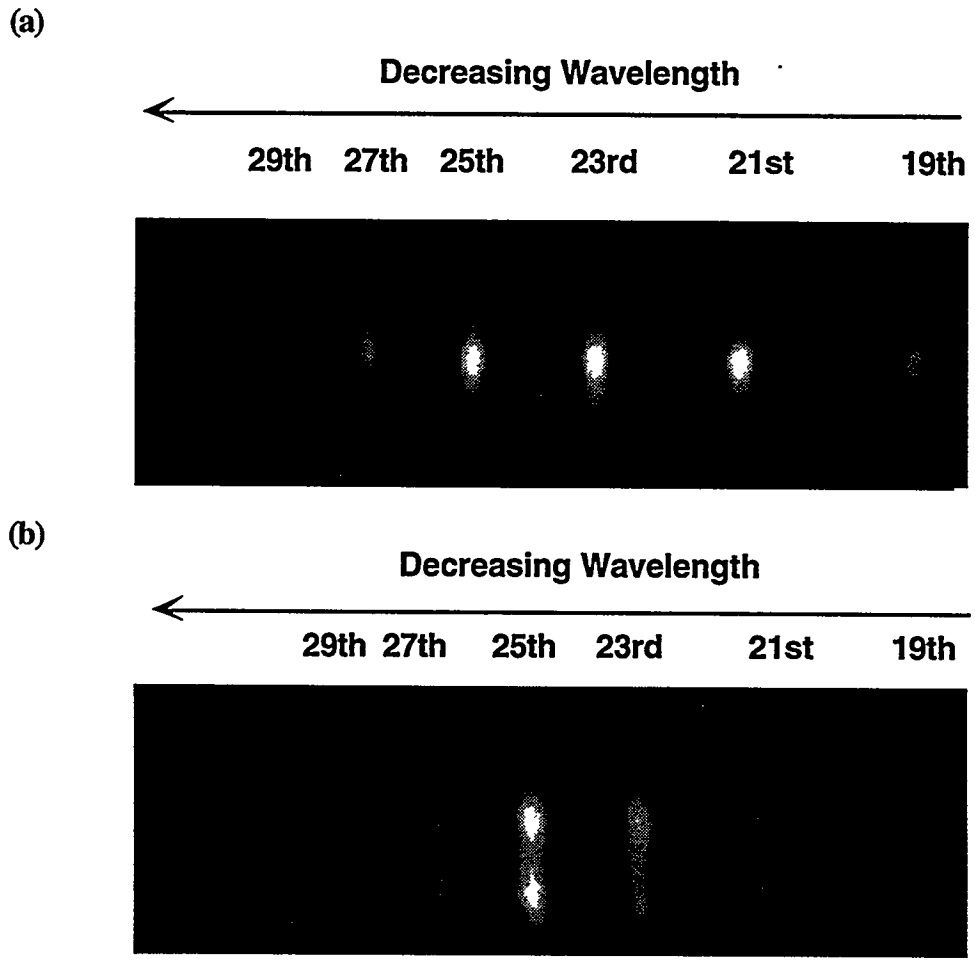

Figure IV.12: Harmonic profiles produced in a jet of Ar with a density of 5×10^{18} cm^{-3} with the LiSAF laser at a peak intensity of **(a)** 4×10^{14} W/cm^2 and **(b)** 1×10^{15} W/cm^2.

harmonic and were taken 75 cm from the laser focus. The divergence of the laser for this data was 43 mrad. At the lower intensity the profiles are very smooth and nearly Gaussian. However, at the higher intensity, the profiles exhibit some breakup from the refraction of the laser.

Even more dramatic is a consideration of the two dimensional images of the harmonics from a refracted laser. Figure IV.13 shows the images of harmonics produced from the frequency doubled Nd:glass laser in a helium jet . These images were taken on the laser axis with an x-ray CCD detector used for the conversion efficiency studies discussed in section IV.5. The detector was located 250 cm from the laser focus. A 7500 Å aluminum filter blocked the laser light and passed the soft x-ray radiation. The images are essentially a sum of the harmonic profiles of the harmonics that fall between the roll-over of the CCD detector on the long wavelength side at ~ 350 Å and the cutoff of the aluminum filter at 173 Å on the short wavelength side (i. e. the ~ 15th through the 31st harmonics.) The first image is of harmonics produced at 2×10^{15} W/cm^2 (i. e. $\sim I_{sat}$); the second and third images are at intensities of 5×10^{15} W/cm^2 and 8×10^{15} W/cm^2 respectively (i. e. $> I_{sat}$). The harmonics exhibit a clean, single mode Gaussian shape at the lower intensity but exhibit severe distortion at higher intensities.

It is this refraction that sets an upper limit on the useful conversion efficiency that is achievable with high order harmonic radiation. Though the harmonic yield scales as the square of the gas density implying that increasing the density is advantageous in achieving high yield, increasing the density and the laser intensity begin to cause a degradation in the harmonics profiles. This may be of concern for some applications. Equation (3.40) suggests that higher electron densities can be tolerated for a short wavelength laser. Therefore, the refraction effects will be more severe for the fundamental of a near IR laser at 800 or 1000 nm than for its second harmonic.

(a)

(b)

(c)

Figure IV.13: Two dimensional images of harmonics in the 350 to 170 Å wavelength window produced from the Nd:glass laser in helium. Density = 5×10^{18} atoms/cm^3 for **(a)** 2×10^{15} W/cm^2, **(b)** 5×10^{15} W/cm^2, and **(c)** 8×10^{15} W/cm^2.

IV.4 Linewidths and Blueshifting of the Harmonics

Another important parameter in the characterizing of the harmonics is the harmonics' bandwidth. Because the temporal duration of the harmonic is of the order of the drive laser pulse, the harmonics should be short pulse, and therefore, exhibit a rather broad bandwidth. Knowledge of the harmonics' bandwidth not only gives us some insight into the temporal nature of the harmonic, it is also important from the standpoint of applications. The harmonic bandwidth, for example, was a very important parameter in the experiment described in section IV.8 in which a harmonic was amplified in an x-ray laser [47].

The spectral distributions of selected high order harmonics produced by the Cr:LiSAF laser were measured using an imaging monochrometer, (described previously [189]). The monochrometer had an estimated resolution of 0.3 Å at a wavelength of 300 Å, and the spectral width of the laser for these experiments was 7.5 nm. Profiles of the 27th harmonic in argon and neon produced at intensities near the ionization saturation intensities for each atom are shown in figures IV.14a and IV.14b respectively. Accounting for the resolution of the spectrometer we find that the fractional bandwidth of the harmonics is $\Delta\lambda/\lambda \approx 1.7 \times 10^{-3}$ in argon and is slightly higher in neon with $\Delta\lambda/\lambda \approx 4.5 \times 10^{-3}$.

As the intensity increases above the saturation intensity, the bandwidth of the harmonic also increases. This is attributable to the onset of ionization induced self-phase modulation of the laser pulse. In particular, the laser undergoes a blue shift in parts of its spectrum. The details of this blue-shifting were described in chapter III. The distortion of the laser spectrum occurs at a time in the laser pulse when the tunnel ionization is important, and this occurs simultaneous to the production of the harmonics. The distortion of the laser spectrum can then affect the harmonics' spectra. This blue shifting of the

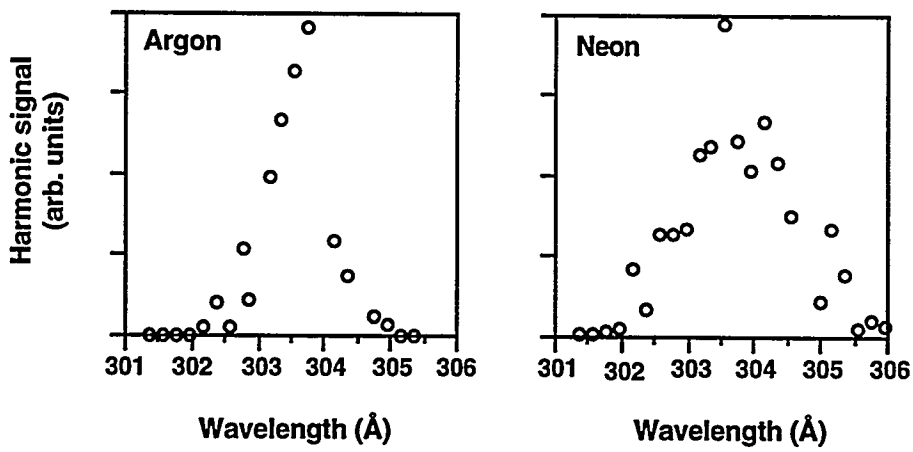

Figure IV.14: Spectral profile of the 27th harmonic produced near the saturation intensity **(a)** in argon at 4 x 10^{14} W/cm^2 and **(b)** in neon at 8 x 10^{14} W/cm^2.

harmonics in an ionizing medium has also been reported by Macklin et. al. [119] and Wahlström et. al. [189].

Figure IV.15 shows the measured harmonic line profile of the 27th harmonic of the 825 nm LiSAF laser produced in argon at two intensities, 4 x 10^{14} W/cm^2, (i. e. close to I_{sat}), and 7.5 x 10^{14} W/cm^2. The harmonic bandwidth at the lower intensity is in keeping with the estimates of lowest order perturbation theory for a Gaussian pulse if a correction is made for the effective order of variation of the harmonic generation with laser intensity. Performing an analysis in a manner similar as the one leading to that of eq. (4.7) we start by noting that, in the absence of ionization, the harmonics temporal profile is

$$I_q(t) \approx \left[I_o(t)\right]^p \tag{4.9}$$

If the laser profile is described by a transform limited Gaussian such that $I_0(t) = A_0 \exp\left[-t^2 / \tau^2\right]$ then its frequency bandwidth is

$$\Delta\omega_0 = \frac{1}{\tau} \tag{4.10}$$

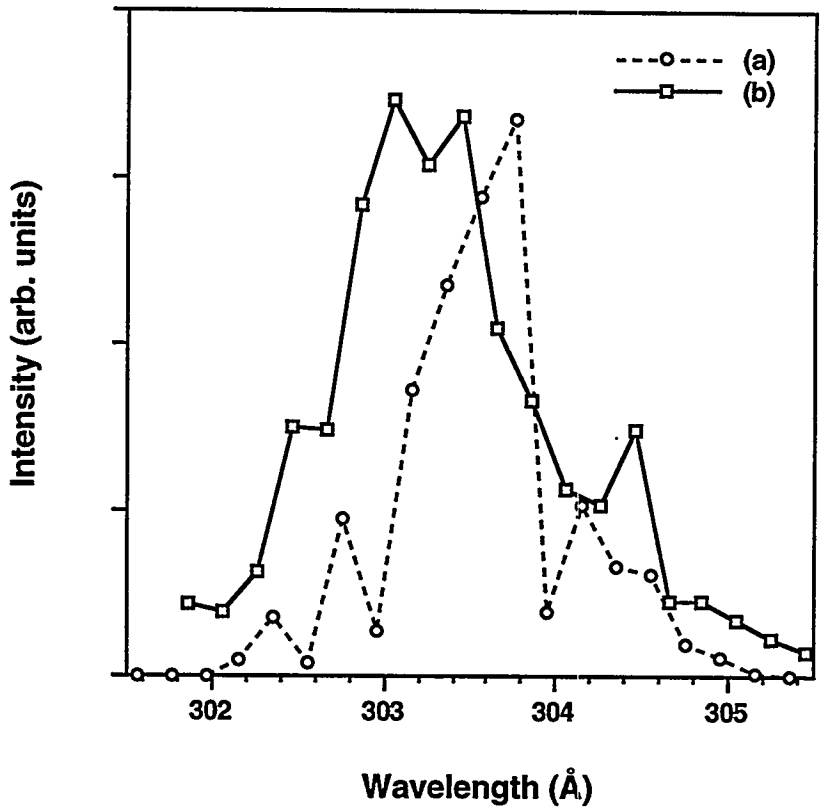

Figure IV.15: Harmonic line profiles of the 27th harmonic of the 825 nm LiSAF laser produced in argon **(a)** 4 x 10^{14} W/cm^2 and **(b)** 7.5 x 10^{14} W/cm^2.

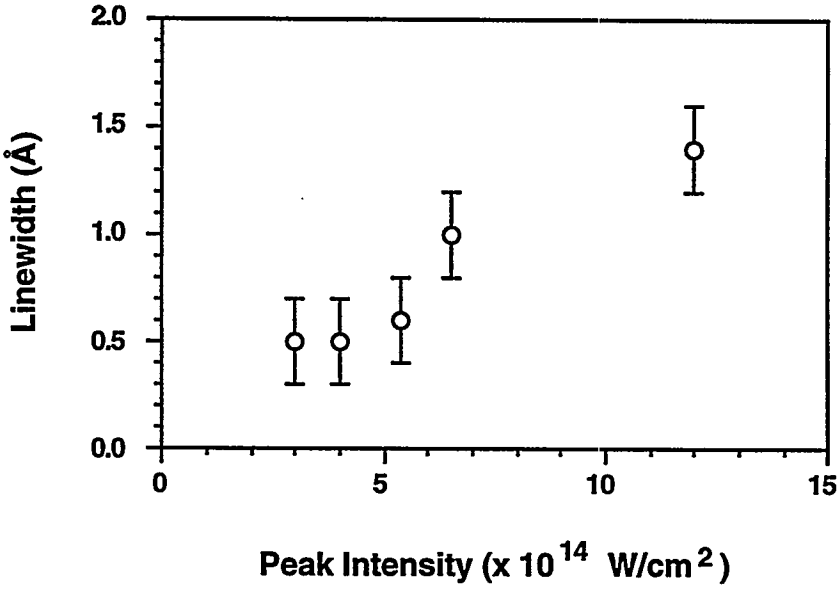

Figure IV.16: Measured linewidth of the 27th harmonic of the LiSAF laser produced in argon as a function of peak laser intensity.

and the harmonic bandwidth is

$$\Delta\omega_q = \frac{\sqrt{p}}{\tau} \tag{4.11}$$

Since $\lambda_q = \lambda_0 / q$ and $\Delta\lambda = \Delta\omega(\lambda / \omega)$ the qth harmonic bandwidth is given in terms of the laser bandwidth by:

$$\frac{\Delta\lambda_q}{\lambda_q} \approx \frac{\sqrt{p}}{q}\frac{\Delta\lambda_0}{\lambda_0} \tag{4.12}$$

Using the measured effective order of the 27th harmonic in Ar (table IV.2), eq. (4.12) predicts a fractional bandwidth for the 27th harmonic of $\approx 1 \times 10^{-3}$ approximating the measured value at low intensity.

At the higher intensity, which is above the ionization saturation in argon, the harmonic linewidth exhibits a distinct shift toward the blue and a broadening of the spectral width. The harmonic line width is approximately 0.9 Å. This is a fractional bandwidth of $\approx 3 \times 10^{-3}$, well above the prediction of equation (4.12) and nearly twice as broad as the line produced at low intensity. The line has also shifted nearly 0.5 Å toward the blue. The linewidth of the harmonic continues to increase with intensity since a larger focal volume undergoes ionization. The measured linewidth of the 27th harmonic as a function of laser intensity is shown in figure IV.16. The width increases from 0.5 Å to nearly 1.5 Å when the peak intensity increases above 10^{15} W/cm^2. As a larger portion of the focal volume experiences ionization the total harmonic linewidth increases. This spectral shift and broadening are also seen in the 27th harmonic in neon, though the lines tend to be slightly broader in neon as indicated in figure IV.14.

IV. 5 Energy Yield and Conversion Efficiency Measurement of Harmonics Produced by the 600 fs Nd:glass Laser

Though we have, up to this point concentrated on the characteristics of the harmonic radiation, such as spatial and spectral properties as well as the wavelength range accessible, the question still remains, how much energy can actually be produced in a harmonic? Though there have been preliminary studies[98], a complete measurement of the photon yields achievable with high order harmonics had not yet been undertaken until recently [44]. This aspect of harmonic generation is, perhaps the most important of all from the standpoint of using harmonics in applications. In this section a series of measurements of the absolute energy yields and conversion efficiencies of harmonics generated in the 310 to 170 Å wavelength range by the 600 fs Nd:glass under a variety of conditions are described.

IV.5.A Experimental Scheme for Harmonic Energy Yield Measurements

These experiments were performed using the 600 fs Nd:glass laser fundamental at 1052.7 nm as well as its second harmonic at 526 nm. The laser was focused into the plume of the pulsed, supersonic nozzle, gas jet described above. As mentioned, this jet produces localized atomic densities from 10^{18} to 5×10^{18} atoms/cm^3 and exhibits a roughly linear density dependence with gas jet backing pressure, verified by backward stimulated Raman scatter measurements [149]. The interaction length through the gas jet is 0.8 mm. Our measurements were conducted with an atom density of 5×10^{18} atoms/cm^3 $\pm$ 30%. The harmonic radiation is sampled by an astigmatic compensated, grazing incidence, XUV spectrometer. A calibrated aluminum foil filter prevented scattered laser light from reaching the detector. The experimental layout is shown in figure IV.17.

The harmonics were detected with an absolutely calibrated x-ray CCD detector

Configuration 1:
With Spectrometer to Separate Individual Harmonics

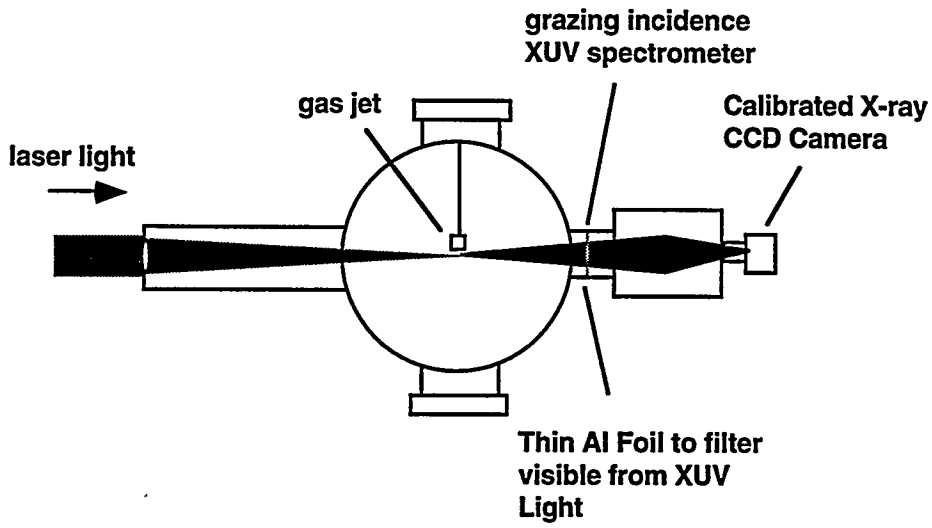

Configuration 2:
Without Spectrometer to Determine Total Detection System Through-put

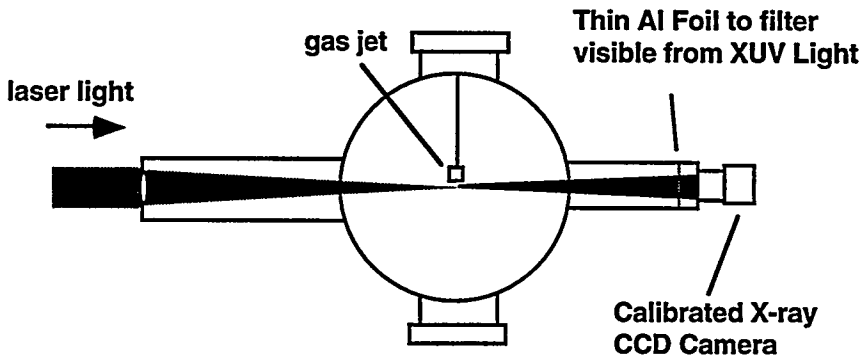

Figure IV.17: Experimental configurations for measuring the high harmonic energy yields from the Nd:glass laser.

(Princeton Instruments). This detector uses a thermo-electrically cooled Tektronix 1024B back illuminated CCD chip [84]. The quantum efficiency of the chip (which is lowered in the spectral region of interest by a thin layer of SiO_2 on the surface of the chip of approximately 5 to 10 nm thick) was calibrated at the Brookhaven National Synchrotron Light Source [39]. The quantum efficiency ranges from 0.7 for wavelengths between 200 and 100 Å and drops to below 0.2 at 300 Å. The response of this camera drops very quickly with wavelengths longer than 300 Å. The correlation factor between accumulated charge and detected counts on the camera was measured by exposing the CCD chip to single photon hits of $K\alpha$ emission from tin at a photon energy of 25 keV.

The throughput of the XUV spectrometer was measured by comparing signals of harmonics on the x-ray CCD produced under identical conditions with and without the spectrometer in the system (see figure IV.16). Data taken with the spectrometer yielded the relative energy in each harmonic while data taken without the spectrometer yielded the total integrated harmonic yield per laser shot. Two calibrated aluminum filters (8600 Å total thickness) were used to pass the harmonics and completely block all laser light for data taken without the spectrometer. Comparison of these shots with harmonics shots taken with the spectrometer at the same laser intensity yielded the spectrometer throughput of those harmonics between 300 Å and the aluminum L-edge at 170 Å. This measurement was repeated for a range of laser intensities and for four different laser focal configurations, f/25, f/35, f/50, and f/70 focusing. The f/25 and f/35 configurations were achieved by focusing with an f = 2 m spherical lens. The f/50 and f/70 geometries were achieved by using a 3.5 m lens and aperturing the beam to a 7 cm and a 5 cm diameter respectively.

IV.5.B Energy Yield Comparison Between 1053 nm and 526 nm Laser Light

Figure IV.18 shows the typical energy yields of harmonics produced in neon for drive wavelengths of 1053 nm and 526 nm. The error bars result from uncertainties in the

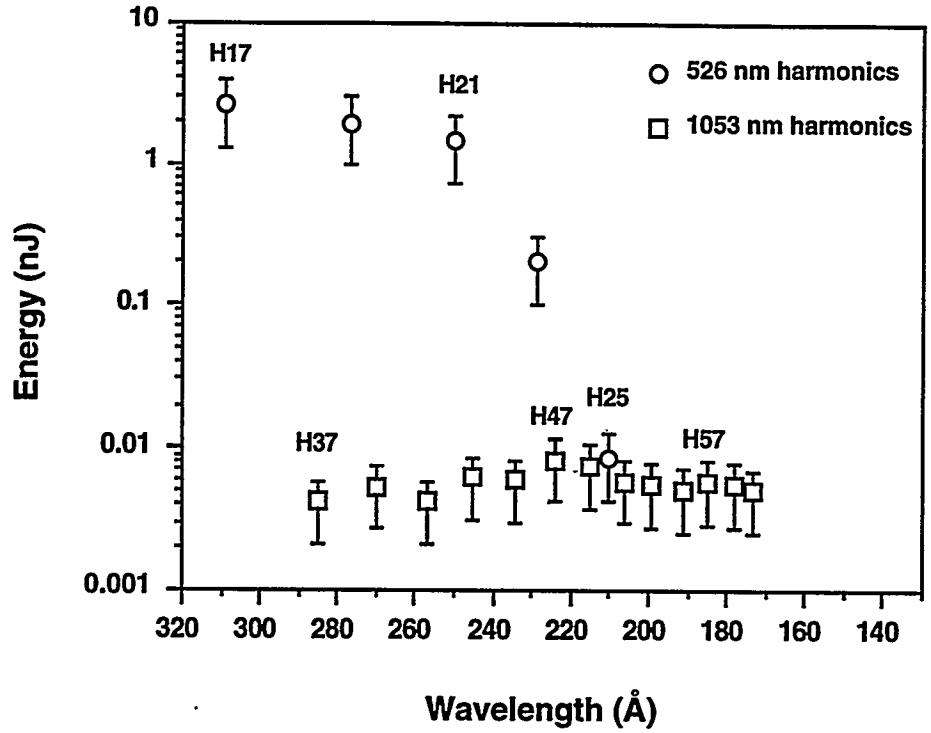

Figure IV.18: Energy yields of harmonics generated in neon by 526 nm light (circles) and harmonics generated by 1053 nm light (squares). The peak intensity was 1 x 10^{15} W/cm^2 and the confocal parameter was 2.5 cm.

spectrometer throughput measurement and in the CCD chip quantum efficiency. These shots were taken with the confocal parameter, *b*, held constant at a value of ~ 5 cm (which is much longer than the gas jet interaction length of 0.8 mm) and a constant peak intensity of 1 x 10^{15} W/cm^2. This intensity is above the ionization saturation intensity for neon (which is ≈ 5 x 10^{14} W/cm^2 for a 600 fs pulse). The harmonics of the 526 nm light were produced with 50 mJ focused by the f/50 geometry to a spot size of 140 μm (1/e^2 diameter), and the 1053 nm harmonics were produced with 90 mJ focused by the f/35 geometry to a spot size of 180 μm (1/e^2 diameter). The actual plateau of the 1053 nm harmonics extends well beyond the L-edge cutoff of the aluminum filter used for these measurements.

The harmonics in the 1053 nm plateau exhibit energies of between 6 and 8 pJ per

harmonic corresponding to a conversion efficiency of ~ 10^{-10}. The yields of the harmonics in the plateau of the 526 nm harmonics (the 17th through the 21st) have energies of 1 - 2 nJ. This dramatic difference in the conversion efficiency between the two colors has been reported previously [37], and can be explained on the basis of two factors; a single atom response and a phase matching term. Quantum mechanical calculations of Krause et. al. show that the single atom response favors the shorter wavelength driver [94]. This can be easily understood if one considers the quasi-classical model described in chapter III, in which the electron oscillates in a classical trajectory about the atom in the laser field. Whenever the electron returns to the atom during its oscillations it can emit a harmonic photon. Since the oscillation amplitude scales as λ_0^2, the electron spends more time in the vicinity of the atom with the shorter wavelength driver and, therefore, has a larger probability of emitting a harmonic photon per unit time.

The energy yield is also enhanced for the shorter wavelength by phase matching. It can be shown that if we assume the harmonic yield of the qth harmonic varies with the effective order p, the number of harmonic photons emitted in the laser pulse can be written as [102]:

$$N_q = \frac{\pi^2 b^3}{4\hbar} \tau_p n_0^2 |d(q\omega)|^2 |F_q|^2 \tag{4.13}$$

where b is the laser confocal parameter, τ_p is the integral of the pth power of the laser temporal envelope, n_0 is the atom density, and $d(q\omega)$ is the atomic dipole moment induced by the laser, representing the atomic contribution to the harmonic yield. Here, $|F_q|^2$ is the phase matching factor. This factor was derived in the weak field limit in eq. (3.19). We now consider the solution in the strong field case. In the weak focusing limit for a Gaussian beam focused through a uniform gas jet of length l, the phase matching factor can be written as

$$\left|F_q\right|^2 = \frac{q}{p}\frac{4l^2}{b^2}\left|\frac{\sin(\Delta kl/2 + ql/b - ql/pb)}{(\Delta kl/2 + ql/b - ql/pb)}\right|^2 \tag{4.14}$$

where Δk is the phase mismatch defined by $\Delta k = k_q - qk_0$. As we described before, when $I>I_{sat}$ the phase matching is dominated by free electrons. In this case the phase mismatch is given by eq. (4.2)

If $\lambda_0^2/\lambda_q^2 >> 1$ then the phase matching factor becomes

$$\left|F_q\right|^2 \approx \frac{q}{p}\frac{4l^2}{b^2}\left|\frac{\sin\left((2e^2 n_e \lambda_q / c^2 m_e)\lambda_0^2/\lambda_q^2\right)l/2}{\left((2e^2 n_e \lambda_q / c^2 m_e)\lambda_0^2/\lambda_q^2\right)l/2}\right|^2 \tag{4.15}$$

which means that the net harmonic yield at a given harmonic wavelength scales roughly like:

$$N_q \sim \frac{b n_0^2}{\lambda_0^4}. \tag{4.16}$$

This expression strongly favors the shorter wavelength drive. Our measurements were taken with a peak intensity that is well above the ionization saturation intensity so we expect significant ionization throughout the entire focal volume. Relation (4.16) largely explains the difference in our measured harmonic yields for the two drive wavelengths. A more detailed analysis of the free electron phase mismatch requires a solution of the wave equation, which will be discussed in the next section.

IV.5.C Energy Yield Comparison Between Harmonics Produced in Ne and He at 526 nm

The energy yields of harmonics produced in neon and helium generated by 250 mJ of 526 nm light focused with an f/50 geometry to an intensity of 6 x 10^{15} W/cm^2 are compared in figure IV.19. This intensity is well above the saturation intensity of both gases; (I_{sat} for He is 9 x 10^{14} W/cm^2 for a 600 fs pulse). The cutoff in He extends beyond that of Ne as predicted by the cutoff law of eq. (4.1), because of the greater

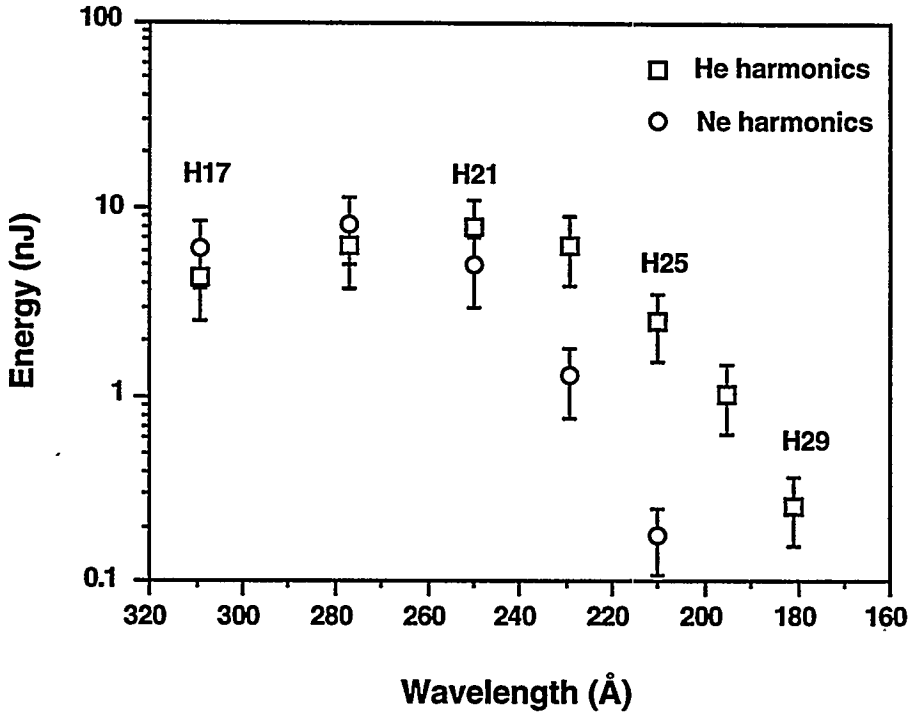

Figure IV.19: Energy yields of harmonics produced by 526 nm light in neon (circles) and in helium (squares). The peak intensity was 6 x 10^{15} W/cm^2 and the focal geometry was f/50 (b = 2.5 cm).

ionization potential of helium. The energy yields of harmonics in the plateau in both species, however, are approximately the same. Both gases exhibit harmonic yields of between 6 and 8 nJ in the plateau region. The yields drop to a few hundred pJ for the harmonics in the cut off, which occurs at the 25th in neon and at the 29th in helium.

Though earlier results found harmonic yields greater in neon than in helium [98], we find the conversion yields for both gases to be roughly the same. This can be understood when one considers that our measurements were taken with a peak intensity well above I_{sat} for both gases, so we expect ionization throughout the focal volume. Though neon is more polarizable than helium, implying higher photon yields, the helium survives to a higher intensity than does the neon during the pulse. Because of the high nonlinearity of the process, the majority of the harmonic photons are produced at an

intensity near I_{sat}; ionization prohibits harmonic generation at high intensities later in the pulse. The relative yields of the neon, N_q^{Ne}, and the helium, N_q^{He}, are therefore roughly described by the ratio:

$$\frac{N_q^{Ne}}{N_q^{He}} \sim \frac{|\chi_{Ne}(q\omega)|^2 \left(I_{sat}^{Ne}\right)^p}{|\chi_{He}(q\omega)|^2 \left(I_{sat}^{He}\right)^p}. \tag{4.17}$$

Data at intensities below I_{sat} indicate that $|\chi_{Ne}(q\omega)|/|\chi_{He}(q\omega)| \approx 3$ for harmonics of 526 nm laser light [36]. Using an effective order, p, of 6 implies that N_q^{Ne}/N_q^{He} is of the order of $3^2 \times (4.5 \times 10^{14}/7.0 \times 10^{14})^6 \approx .6$ for our conditions, consistent with our results. Thus, high conversion (> 10 nJ) is possible in both noble gases with the added advantage that shorter wavelengths are attainable in helium.

IV.5.D Energy Yield Variation with Focal Geometry

Eq. (4.16) also implies that higher yields are attainable by changing the focal geometry to increase the confocal parameter, b. Figure IV.20a shows energy yields of harmonics of 526 nm produced in helium at a constant intensity of 6×10^{15} W/cm^2 for three different f/# configurations. The harmonics were generated with 130 mJ at f/25, 280 mJ at f/50, and 460 mJ at f/70. The location of the cutoff is the same for all three focus speeds. The harmonic yield in the plateau, however, varies from roughly 1 nJ for the f/25 harmonics, to between 6 and 8 nJ for harmonics generated at f/50, and increases to better than 15 nJ per harmonic for those generated with f/70 focusing. The yield of the 21st harmonic (at 250 Å) is plotted in figure IV.20b as a function of the confocal parameter for an intensity of 6×10^{15} W/cm^2. The yield is linear with b, confirming the scaling predicted by eq. (4.16). The conversion efficiency, however, is constant with confocal parameter for any given intensity. Though the harmonic energy yield increases linearly with b, the confocal parameter is proportional to the focal spot area so a commensurate increase in laser energy is required to maintain a given peak intensity.

(a)

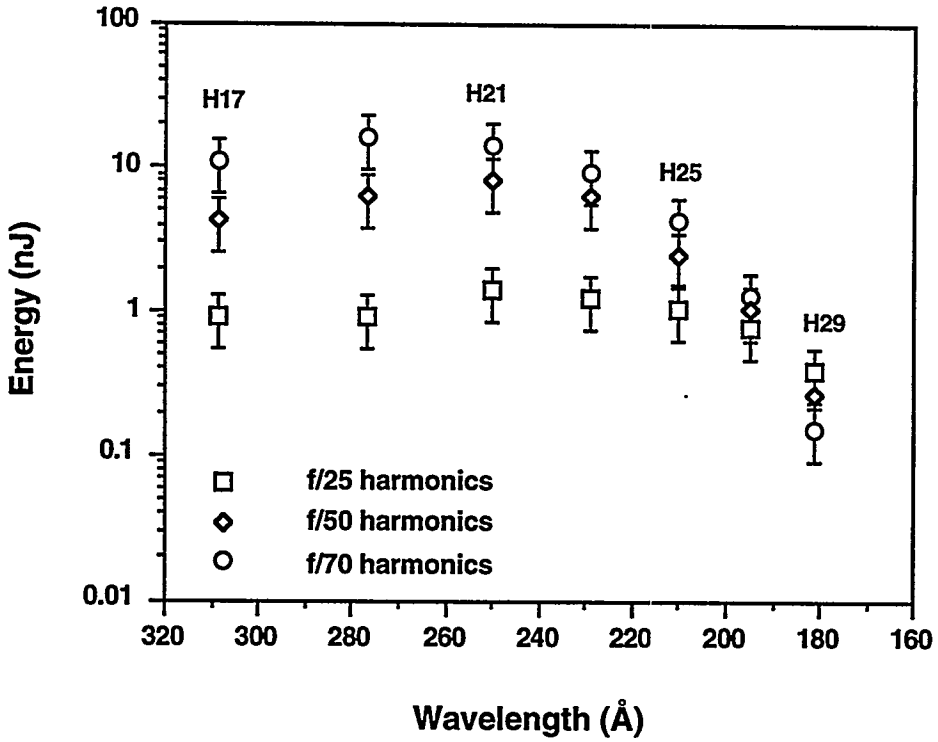

(b)

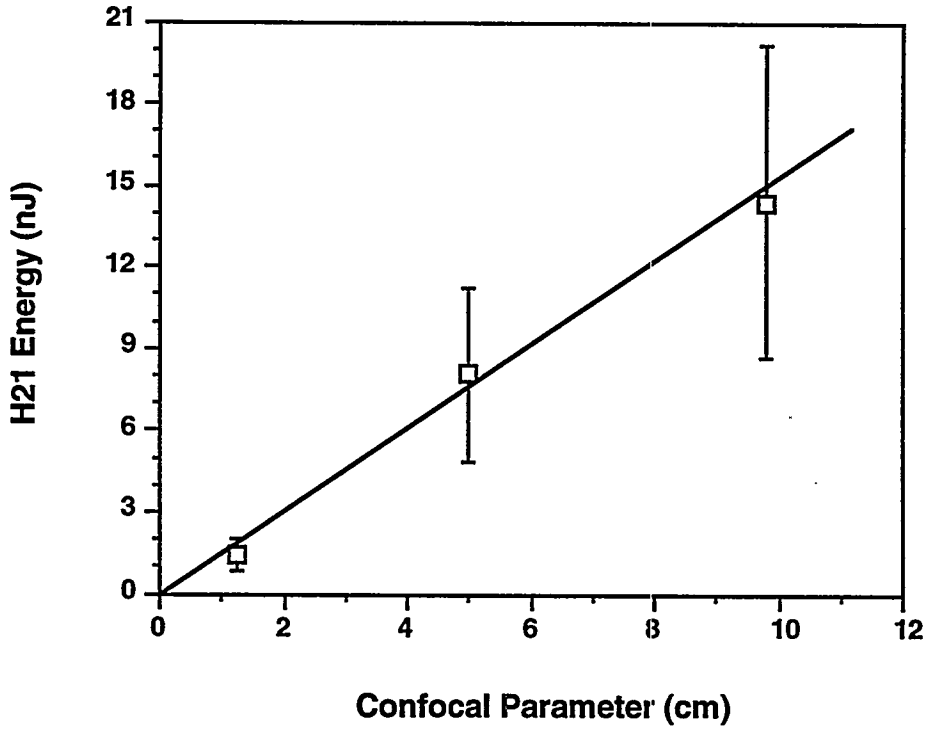

Figure IV.20: **(a)** Energy yields of harmonics produced by 526 nm light in He at a peak intensity of 6 x 10^{15} W/cm^2 for three different focal configurations. **(b)** Energy yield of the 21st harmonic as a function of confocal parameter.

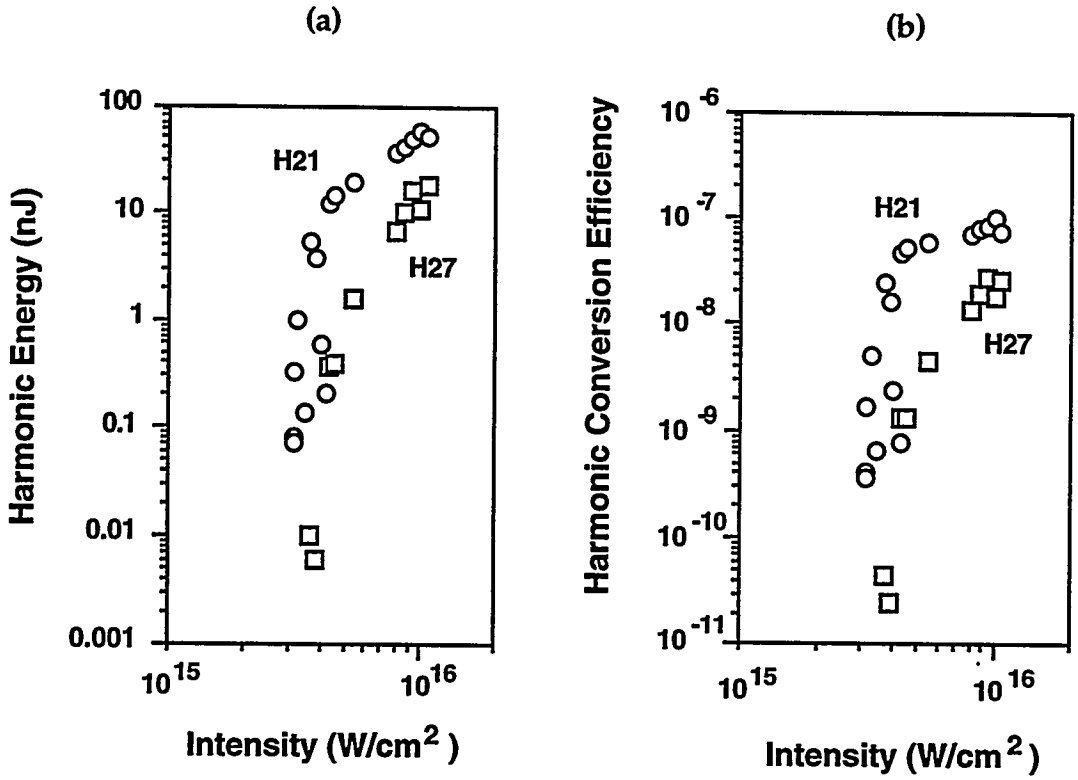

Figure IV.21: **(a)** Energy yields of the 21st harmonic (at 251 Å) and the 27th harmonic (at 195 Å) as a function of intensity. Harmonics were produced by 526 nm light in helium with f/50 focusing. **(b)** Harmonic conversion efficiencies of the 21st and 27th harmonics under the same conditions.

IV.5.E Energy Yields and Conversion Efficiency as a Function of Peak Intensity

We find that the best harmonic yields and conversion efficiencies are achieved with intensities well above the saturation intensity. Figure IV.21 shows the yields and conversion efficiency of the 21st harmonic of 526 nm light generated in helium as a function of peak laser intensity for f/50 focusing. For this focusing geometry we measured harmonic energies near 60 nJ at a peak intensity of 1.1 x 10^{16} W/cm^2 with a drive energy of 590 mJ. This corresponds to a conversion efficiency of $>10^{-7}$ from the laser into the harmonic at 250 Å. Similar yields (~ 40 nJ) were attainable at a lower intensity with f/70 focusing giving conversion efficiencies that are comparable to those generated at f/50. Harmonics generated in helium are also capable of generating harmonic

yields of nanojoules at wavelengths below 200 Å. The yields (figure IV.21a) and conversion efficiencies (figure IV.21b) of the 27th harmonic (at 195 Å) are shown for f/50 focusing. We measured harmonic energies of over 15 nJ at this wavelength at an intensity of 1.5×10^{16} W/cm^2. This corresponds to a conversion efficiency of 3×10^{-8}.

IV.6 Theoretical Calculations of Harmonic Energy Yields

To further quantify the energy yield measurements it is desirable to construct a model that directly calculates the energy yields using single atom dipole moments. Such a model will not only give us a tool to predict the yields of x-ray radiation from harmonics over a variety of conditions, but it will also give us insight into the harmonic generation process and allow us to explore the limitations of harmonic conversion efficiency. Furthermore, it provides a sensitive test of our understanding of the single atom dipole response as well as the propagation issues in harmonic generation by comparing the calculations with the experimental numbers presented in the last section. In this section we concentrate on calculations of the energy yields of harmonics produced in helium by the frequency doubled Nd:glass pulse. To perform the calculations of the harmonic energy yields we have constructed a model similar to that of L'Huillier et. al. [100] and applied it to calculations of absolute harmonic energy yields in the high focused intensity regime ($I > I_{sat}$). We have incorporated calculated dipole moments calculated by Ken Kulander for helium into a numerical solution of the wave equation for the harmonic field [42].

IV.6.A Harmonic Yield Model Description

To calculate the yield of the qth harmonic, we numerically integrate the wave

equation for the harmonic field propagating through the gas target. The wave equation for a field oscillating at a frequency ω_q is [22]

$$\nabla^2 A_q + \frac{n_q^{\,2}\omega_q^{\,2}}{c^2} A_q = -\frac{4\pi\omega_q^{\,2}}{c^2} P_q \tag{4.18}$$

where A_q is the field strength of the oscillating qth harmonic, n_q is the spatially and temporally varying refractive index of the media at ω_q, and P_q is the dipole moment induced by the laser field at a frequency w_q. Equation (4.18) ignores the group velocity dispersion of the harmonic pulse as well as the group velocity walk-off of the harmonic pulse with the laser pulse. Both of these effects are negligible for pulses of 100 fs or longer in a low density ($\leq 10^{19}$ atoms/cm^3) gas medium.

We can introduce the slowly varying envelopes for the harmonic field and the polarization into eq. (4.18). These are given by:

$$a_q(\overline{\mathrm{x}},t) = A_q(\overline{\mathrm{x}},t)\exp\left[-i\int_{-\infty}^{z}\left(qk_0(\overline{\mathrm{x}},t) + \Delta k(\overline{\mathrm{x}},t)\right)dz'\right] \tag{4.19a}$$

$$p_q(\overline{\mathrm{x}},t) = P_q(\overline{\mathrm{x}},t)\exp\left[-i\int_{-\infty}^{z} qk_0(\overline{\mathrm{x}},t)dz'\right] \tag{4.19b}$$

where k_0 is the wave number of the fundamental laser field, and the phase mismatch of the harmonic with the laser field is defined as, $\Delta k \equiv k_q - qk_0$. Using the slowly varying envelope approximation in eq. (4.18) we arrive at the paraxial wave equation for the qth harmonic:

$$\nabla_\perp^{\,2} a_q + 2ik_q\frac{\partial a_q}{\partial z} - 2k_q\Delta k a_q + ik_q N\sigma_{abs}a_q = -\frac{4\pi\omega_q^{\,2}}{c^2}p_q \tag{4.20}$$

To derive this we have explicitly separated the real and imaginary part of the harmonic wave number, where k_q is the real part of the harmonic wave number, σ_{abs} is the absorption cross section for harmonic photons, and N is the gas density. We assume that the phase mismatch is dominated by the presence of free electrons from ionization induced

plasma formation during the harmonic generation and ignore the small contribution of the neutral atoms to the phase mismatch [102]. If the electron density, n_e, is much lower than the critical density for both the harmonic and the fundamental field, this phase mismatch can be approximated by eq. (4.2)

In deriving eq. (4.20) we have ignored all terms that vary as $\nabla_\perp k_q$; this is equivalent to saying that

$$\frac{\partial n_q}{\partial x} = \frac{\partial n_q}{\partial y} \approx 0 \tag{4.21}$$

In doing this we have ignored any refraction of the harmonic field by a spatially varying refractive index arising from the plasma formation. This is a very good approximation since short wavelength radiation will be very resistant to refraction by plasmas because of the large critical density associated with soft x-ray radiation [161]. This refraction, however, may have an effect on the spatial profile of the laser fundamental and consequently affect the harmonic as we have seen in section IV.3.B. These calculations, however, do not account for refraction of the laser by ionization. Though the refraction of the fundamental has effects on the far field profile of the harmonic, it has less of an effect on the energy yields since the majority of the harmonic radiation is produced in regions where there is only a small amount of ionization (see figure IV.23), and the fundamental beam undergoes very little spreading within the short length of the gas medium [134]. In other words, though the ionization induced refractive index change affects the phase of the laser field in the focus, which manifests itself as modulation in the far field, it has only a small effect on the amplitude profile of the near field, at least for media of sufficiently short length.

We treat the focused fundamental laser beam as a Gaussian spatial profile. Though our experimental results were taken with a flat-top profile focused into the gas medium, resulting in Lommel function profiles at the focus [20], the use of a Gaussian is a reasonable approximation when the confocal parameter is much longer than the

interaction region, a condition satisfied by all of our experiments. Consequently, we take the laser intensity as

$$I(\bar{\mathrm{x}},t) = I_0 \frac{1}{1+4z^2/k_0^2 w_0^4} \exp\left[-\frac{2\left(x^2+y^2\right)}{w_0^2\left(1+4z^2/k_0^2 w_0^4\right)}\right] \exp\left[-4\ln 2t^2/\tau_{FWHM}^2\right] \quad (4.22)$$

where w_0 is the $1/e^2$ radius of the laser at best focus. The spatially and temporally varying harmonic polarization is then given by

$$p_q(\bar{\mathrm{x}},t) \cong 2N(\bar{\mathrm{x}},t)\left|d_q(I(\bar{\mathrm{x}},t))\right| \exp\left[-iq\tan^{-1}\left[2z/k_0 w_0^2\right] - iq\frac{2k_0(x^2+y^2)z}{k_0^2 w_0^4+4z^2}\right] \quad (4.23)$$

where $\left|d_q(I(\bar{\mathrm{x}},t))\right|$ is the intensity dependent dipole moment oscillating at a frequency q. For our calculations we use values for $\left|d_q(I(\bar{\mathrm{x}},t))\right|$ that have been calculated by Krause, Schafer, and Kulander by numerical integration of the Schrödinger equation for helium irradiated by 526 nm laser light [94]. We ignore the intensity dependence of the phase of the dipole, $d_q(I(\bar{\mathrm{x}},t))$, which has been shown to be important in affecting the far - field spatial profiles of harmonics in the 400 to 100 Å range [168, 145]. This is a good approximation for our calculations since we consider only weak focusing, in which the laser intensity varies very little in the z direction over the length of the medium and, therefore, has very little effect on the phase matching.

Finally, the time dependent density of the neutral atoms and the free electrons is calculated by simultaneously solving the ionization rate equation in a manner similar to that described in chapter III:

$$\frac{dN(\bar{\mathrm{x}},t)}{dt} = -W_{ti}(I(\bar{\mathrm{x}},t))N(\bar{\mathrm{x}},t) \quad (4.24)$$

for the density of helium atoms. W_{ti} is the tunnel ionization rate which we take to be given by the rate ADK rate, eq. (3.26). We assume that there is no harmonic generation from the singly ionized helium.

The computer algorithm solves eq. (4.20) for a_q on a three dimensional (x,y,z) grid for each time slice in the laser pulse. The grid is 128 x 128 x 100 points. Eq. (4.20) is solved using the split operator method of Feit and Fleck [62]. The incident laser pulse is assumed to be a Gaussian with a 600 fs full width at half maximum, focused at the center of the medium. We solve eq. (4.20) for independent time slices separated by 25 fs. The harmonic field is calculated assuming an initial neutral atom medium that is 800 μm long and uniform along the entire length. The output harmonic energy, E_q, exiting the medium is then found from

$$E_q = \frac{c}{8\pi}\int \left|a_q(\bar{\mathrm{x}},t)\right|^2 dx\,dy\,dt \tag{4.25}$$

All of our calculations and measurements were conducted for situations of weak focusing. An example of the harmonic field calculated exiting the helium medium illustrating the importance of ionization in calculating the harmonic yield is shown in figure IV.22. Here we show the intensity distribution of the 21st harmonic of 526 nm light exiting the gas medium calculated for two points in the laser pulse, 450 fs before the peak and right at the peak for a focal spot diameter of 160 μm ($1/e^2$) and a focused peak intensity of 3 x 10^{15} W/cm^2. The gas density was taken to be 4 x 10^{18} atoms/cm^3. Because the peak intensity is approximately four times the ionization saturation intensity for the helium, the medium begins to ionize at the peak of the focus at approximately 400 fs before the pulse peak. As the intensity increases later in the pulse the radial extent of the ionization increases. Consequently, the harmonics produced in the pulse before the onset of ionization (figure IV.22a) exhibit a Gaussian profile.

After ionization, however, the harmonics are produced in a small annulus limited on the inside by ionization and falling off rapidly on the outside due to the highly nonlinear dependence of the polarization with laser intensity (figure IV.21b). The size of this annulus expands later in the pulse as the intensity at the focus increases. Previously, L' Huillier et. al. [100] found that the harmonic field produced from a tightly focused laser

(a)

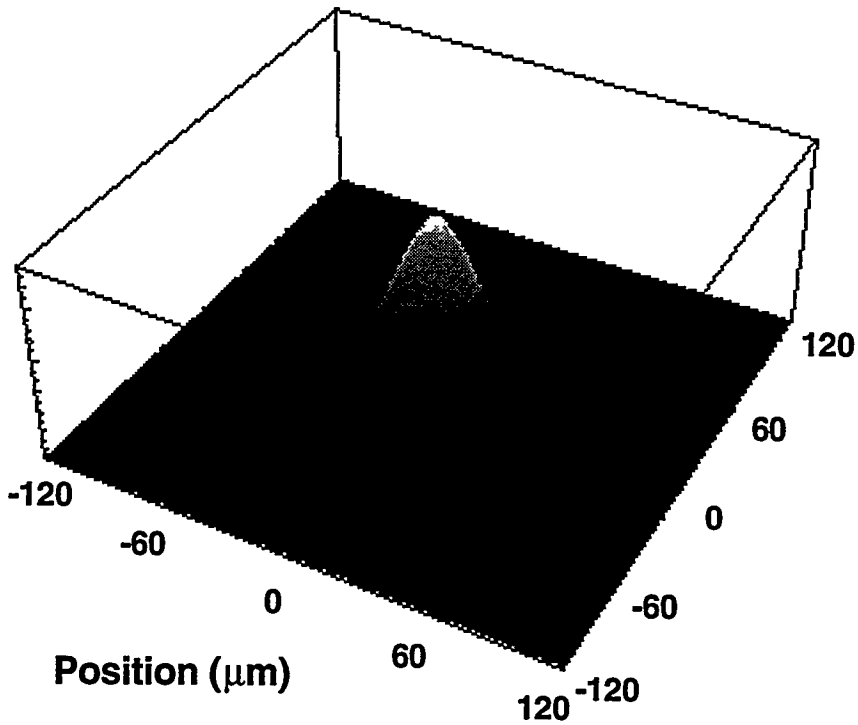

(b)

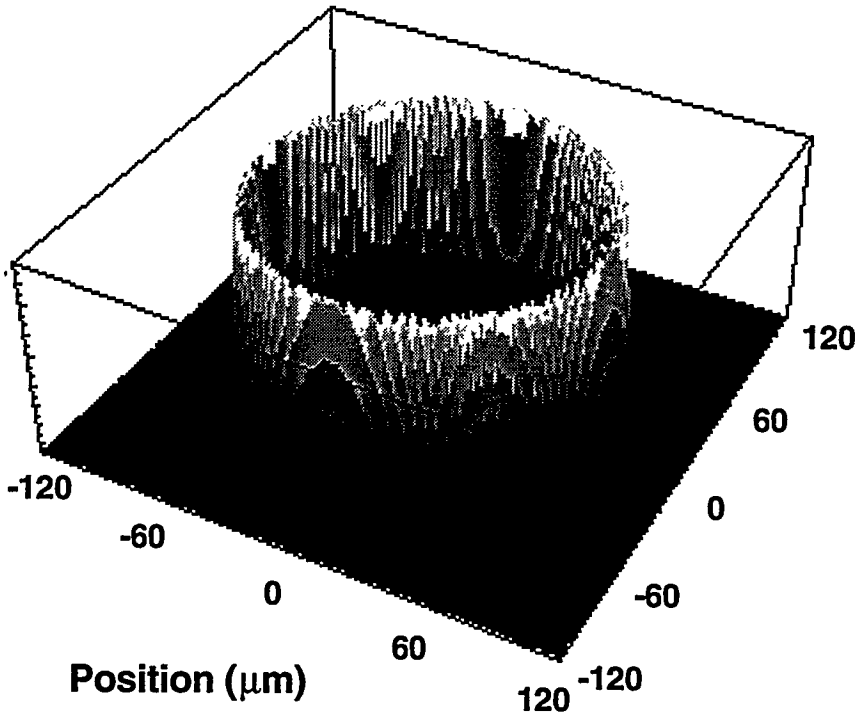

Figure IV.22: Calculated intensity of the 21st harmonic exiting the gas jet at: **(a)** 450 fs before the pulse peak and **(b)** at the pulse peak. Focal spot = 160 μm. Intensity = 3 x 10^{15} W/cm^2.

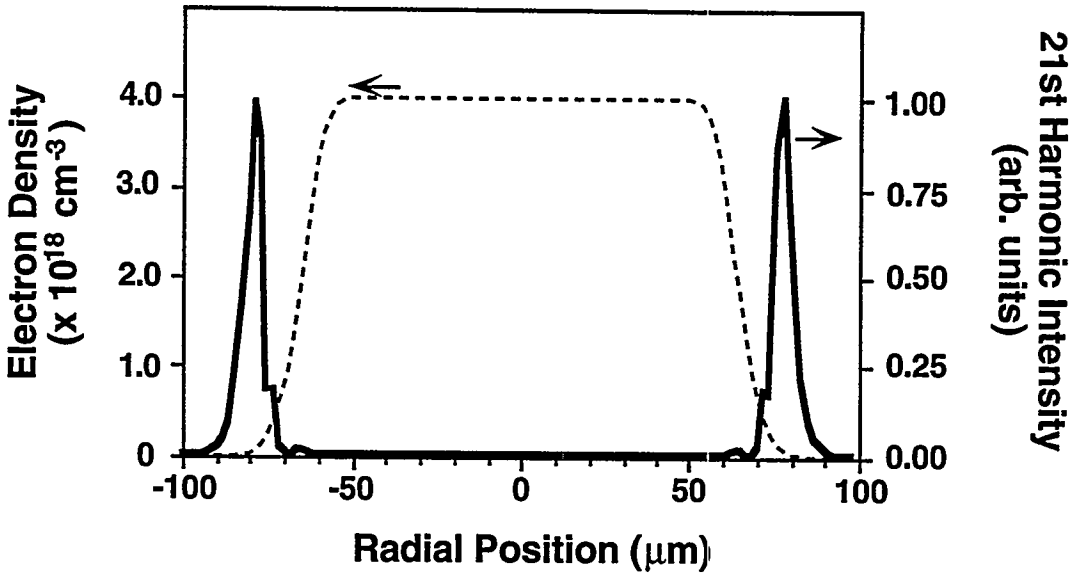

Figure IV.23: A slice through the harmonic profile at the peak of the laser pulse from the calculation of figure IV.22 compared with the radial dependence of the electron density at $z = 0$.

(i. e. when the confocal parameter is comparable to the gas jet interaction length) exhibited a ring structure. These were due to the geometric phase mismatch. The ring structure we see in figure IV.22b is not due to this geometric phase interference, which is negligible since we are considering a case in which the laser focus is weak, but is instead due to the free electron production and neutral atom depletion on axis from ionization. A slice through the harmonic profile at the peak of the laser pulse is compared with the radial dependence of the electron density at $z = 0$ in figure IV.23. From this we see that the majority of the harmonic radiation is produced in the annular spatial region just outside the region of complete neutral atom depletion where there is some ionization and free electrons.

IV.6.B Comparison of the Harmonic Yield Calculations with the Energy Measurements

In figure IV.24 we show energy yields of the 17th through the 29th harmonics of

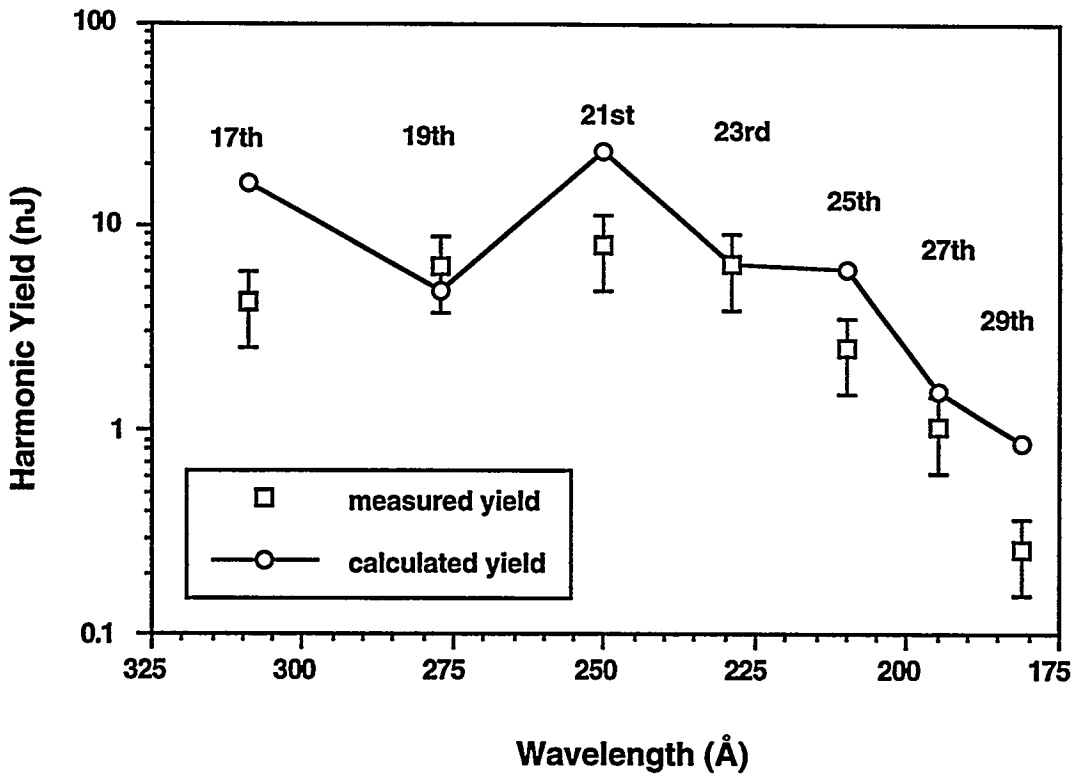

Figure IV.24: Calculated and measured energy yields of the 17th through the 29th harmonics of 526 nm produced in helium with a peak focused intensity of 3 x 10^{15} W/cm^2.

526 nm produced in helium with a peak focused intensity of 3 x 10^{15} W/cm^2 found by averaging five shots in a ±10% peak intensity bin around 3 x 10^{15} W/cm^2. The calculated yield under these conditions is shown in figure IV.24 for comparison. The calculations predict energy yields of between 15 and 20 nJ in the plateau, falling to ~ 1 nJ for the 29th harmonic. The calculated yields fall to within a factor of two to four of the measured yields. This close agreement between calculation and measurement is quite remarkable since the calculation is based on a first principle solution of the Schrödinger equation for the single atom response and the solution of the wave equation for the energy yield with no fitting parameters. The location of the cutoff is at the 27th harmonic, a wavelength of 195 Å (photon energy of 64 eV). This is also mirrored in the energy yield calculation.

The fall-off in the harmonic energy above the 27th is in part due to the calculated single atom response of the helium since the 27th harmonic is near the single atom cut-off for helium with a 526 nm drive. The dramatic drop in energy yield is also due, in large part, to the increased importance of the free electron phase mismatch for the shorter wavelength harmonics. The experimental consequences of this effect were considered in section IV.2.

Figure IV.25 compares the energy yield of the 21st harmonic of 526 nm light at a constant intensity of 3 x 10^{15} W/cm^2 for three different f/# (f/25, f/50 and f/70) configurations with the calculated yield as a function of confocal parameter ranging from 1 to 12 cm. Though the calculated yield is somewhat higher, it is close to the measured values and its linear increase with increasing *b* follows the experimental data.

In figure IV.26 is shown the calculated yield of the 21st harmonic for f/50

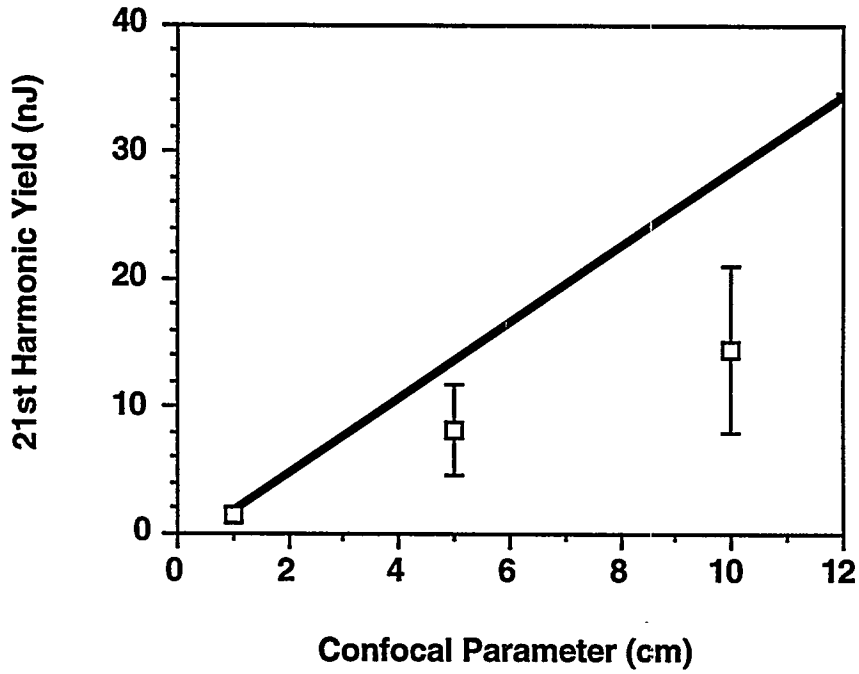

Figure IV.25: Calculated and measured energy yields of the 21st harmonic of 526 nm light at a constant intensity of 3 x 10^{15} W/cm^2 as a function of confocal parameter, $k_0\omega_0^2$.

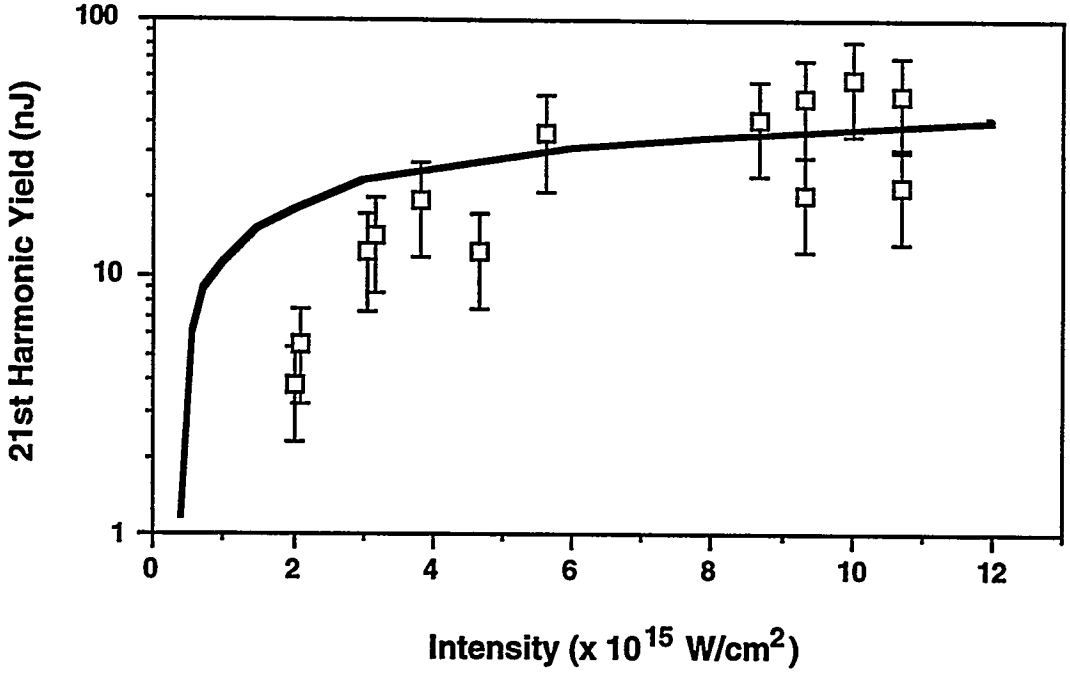

Figure IV.26: Calculated and measured energy yields of the 21st harmonic of 526 nm light generated in helium as a function of peak laser intensity for f/50 focusing.

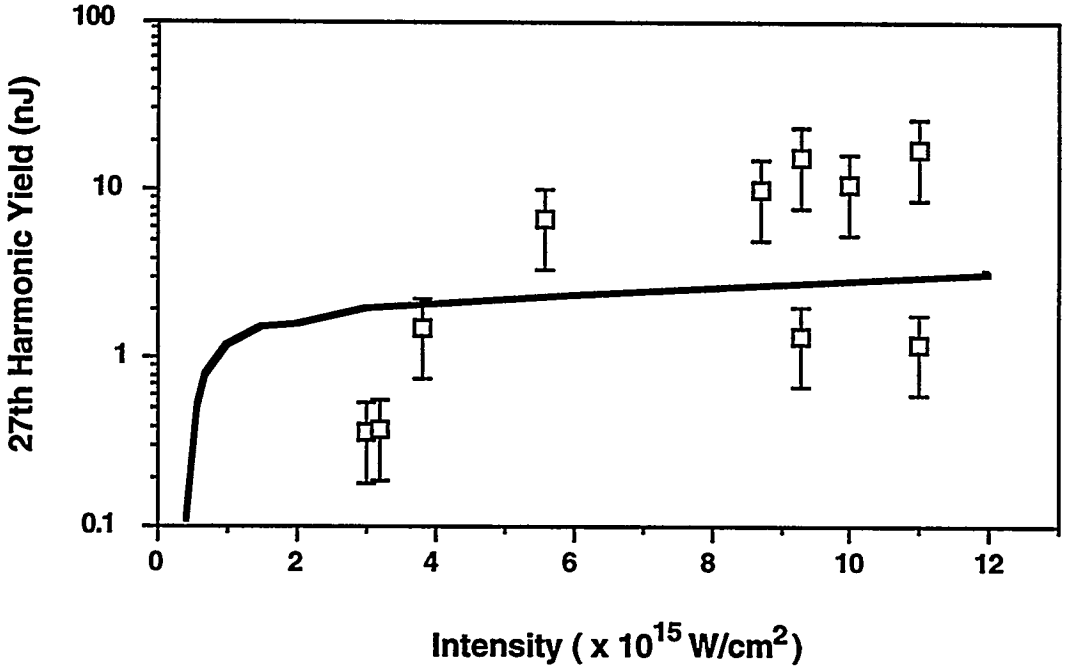

Figure IV.27: Calculated and measured energy yields of the 27th harmonic of 526 nm light generated in helium as a function of peak laser intensity for f/50 focusing.

focusing as a function of energy compared with the measured energy yield. The agreement between the calculated energies and the measured energy is quite reasonable. The calculated yield is within a factor of three of the measured yield over nearly the entire measured range of peak intensities above the ionization saturation. We also find good agreement with the shorter wavelength harmonics in the cutoff of the harmonics spectrum. The yields of the 27th harmonic (at 195 Å) are shown in figure IV.27 for f/50 focusing with the calculated yield shown on this plot as a solid line. This illustrates the validity of our calculations for harmonics in the cut-off as well as the plateau.

IV. 7 Harmonics in Applications: High Order Harmonics Used in Photoionization Studies

From the above consideration it is clear that the high order harmonics are a potentially valuable source of short wavelength photons for use in applications. Using the parameters from the previous section we can summarize the characteristics of a high order harmonic based source using currently available laser technology. This summary is contained in table IV.3. In principle, a source with an average power of 10 μW at $\lambda <$ 100 Å should be attainable in the near future with the development of >100 W short pulse lasers. The next logical step is to demonstrate the use of the harmonics in applications experiments.

Along these lines we have, in collaboration with the group at Saclay, France, utilized the harmonics generated by the LiSAF laser in measuring the relative photoionization cross sections of various gases [9]. The experimental set-up for these experiments is shown in figure IV.28. The general idea of these experiments is to reimage a given harmonic from one gas jet into a second gas jet. By simultaneously measuring the harmonic yield and the number of ions produced by photo ionization in the second gas jet,

Wavelength Range	70 - 10,000 Å
Photon Energy Range	1-180 eV
Tunability	Continuous
Energy/pulse in each Harmonic	1 - 100 nJ
Pulse Width	40 - 1000 fs
Repetition Rate	10 - 100 Hz
Peak Power per Harmonic	> 1 MW
Average Power per Harmonic	1 - 10 mW
Angular Divergence	< 10 mrad
$\Delta\lambda/\lambda$	$< 10^{-3}$ at 200 Å
Peak Brightness per Harmonic	10^{22} mm^{-2} $mrad^{-2}$ s^{-1}

Table IV.3: Summary of the capabilities of a high order harmonics based soft X-ray source based on the measurements of this chapter.

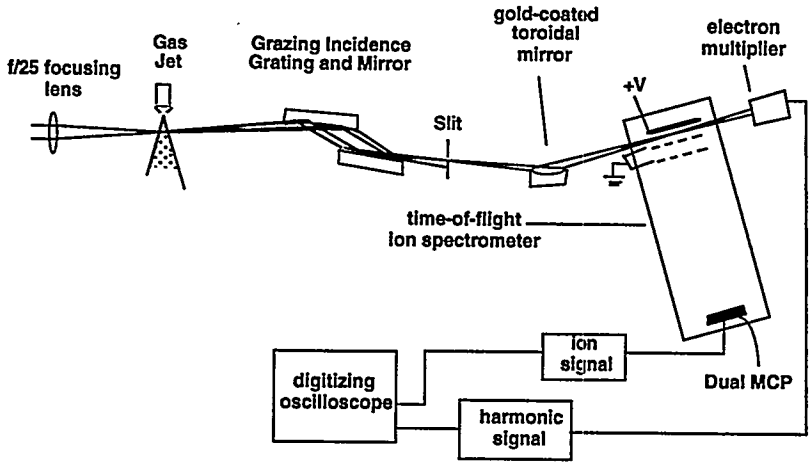

Figure IV.28: Experimental layout for the harmonics photo-ionization studies.

the relative value of the ionization cross section at the harmonic wavelength is derived. This method takes advantage of the fact that a wide range of wavelengths are attainable through the use of different individual harmonics.

For these experiments the laser is focused into a pulsed gas jet which produced an atomic density at the laser focus of roughly 10^{17} atoms/cm^3. To maximize the total harmonic yield, the focal volume was increased by aperturing the beam so as to produce a weak focus, (f/50 focal geometry for the experiments described here, yielding a focal spot of roughly 150 μm in diameter.) The harmonics produced at the laser focus are dispersed by a variable line spaced grating from the Saclay spectrometer (see figure IV.27) and reimaged by a toroidal mirror. A 100 μm slit at the first image plane selects a single harmonic from the harmonic spectrum. This harmonic is then reimaged by a second toroidal mirror to a point between the extraction plates of the time-of-flight apparatus (figure IV.27).

A second pulsed valve gas jet is situated between the acceleration plates of the time-of-flight apparatus and provides the target for the harmonic photons. This jet produces gas densities of roughly 10^{17} atoms/cm^3 at the backing pressures used for these

experiments. An electron multiplier tube collects the harmonic photons immediately beyond the interaction region to give a shot by shot harmonic photon yield. The ions produced in the interaction region are extracted by 600 V applied across the time-of-flight plates. A micro-channel plate detector located at the end of a 1 m drift tube detects all ions extracted from the photoionization region with single ion detection efficiency.

The noble gas used as the target gas for the focused laser light was chosen depending on the XUV spectral range desired in each experiment. Using xenon, krypton, or argon as the harmonic producing gas gave high yields of lower harmonic orders, (the shortest wavelength produced being limited by the harmonic cutoff in each gas). The use of neon as the target gas permitted harmonic production to very high orders (with lower photon yield) and allowed production of photon energies in excess of 100 eV.

The relative photoionization cross section at each harmonic wavelength was determined measuring the ion yield of the singly ionized species as a function of the harmonic photon flux. The slope of this dependence is proportional to the photoionization cross section. A representative example of such a measurement is shown in figure IV.29. In this case the photoionization cross section of neon at a photon energy of 83 eV is measured from the 55th harmonic of 825 nm produced in neon. The horizontal axis represents harmonic photon yield and the vertical axis the ion yield. Each point represents a 4% bin in the harmonic yield and is the average of at least 20 shots. The line is a least squares fit to the experimental points and it is from the slope of this line that the relative photo-ionization cross section is extracted.

A scan of the photoionization cross section as a function of photon energy in neon was conducted for harmonics from the 9th harmonic (13.6 eV) to the 69th harmonic (104 eV) with neon as the gas producing the harmonics. The results of that measurement are shown in figure IV.30. The points represent photoionization cross sections measured by use of the harmonics. Because of uncertainties in the absolute harmonic yield, the total throughput of the spectrometer, and the length of the interaction region only the relative

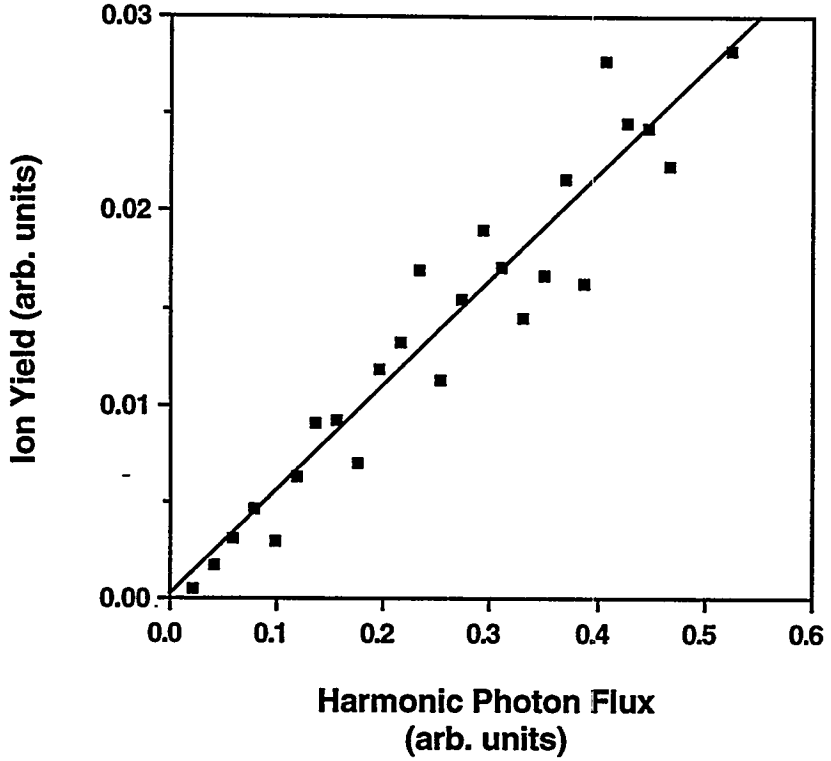

Figure IV.29: Representative measurement of the photo-ionization cross section in neon at 83 eV by using the 55th harmonic of the LiSAF laser. The slope of the signal is proportional to the photo-ionization cross section.

cross sections are obtained. For comparison with previous measurements, the cross sections obtained from the harmonics are scaled to known values and compared to the cross sections measured in ref. [28] (shown as a solid line in figure IV.30). The agreement of the measurement using harmonics with that of ref. [28] is good. This measurement represents the first use of high order harmonic radiation with photon energies in excess of 100 eV for experimental studies.

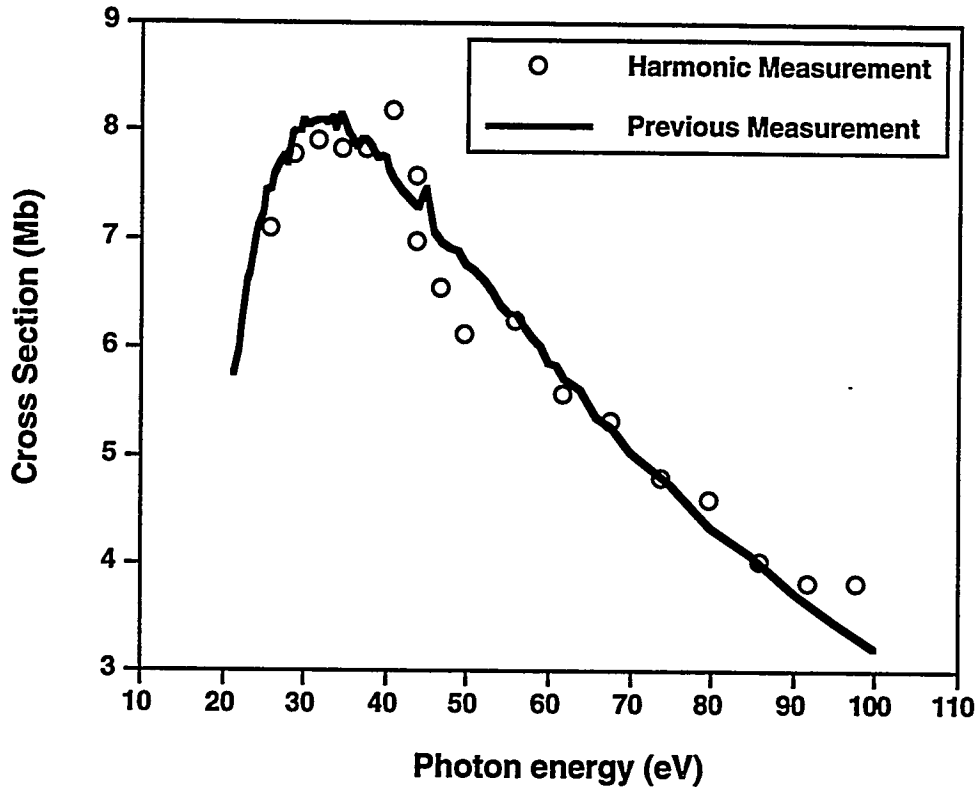

Figure IV.30: Photo-ionization cross section of Ne as a function of photon energy measured with the high order harmonics of the LiSAF laser. A previously measured curve of the cross section is shown for comparison.

IV. 8 Amplification of a Harmonic in a Ga X-Ray Laser

Though an ability to produce 10 -100 nJ of energy per harmonic has been demonstrated, the fundamental limitation on the use of harmonics as a source of soft X-rays remains the low conversion efficiency. One possible mechanism for increasing the energy of a harmonic is to amplify it in an x-ray laser amplifier, a device with an efficiency of better than an order of magnitude greater than that of harmonic generation. As a first step toward this possibility, we participated in an experiment in collaboration with groups from Imperial College in London, Queens University in Belfast, Oxford University, and Rutherford Appleton Laboratory in the UK in which the 21st harmonic from a 1 ps, frequency doubled, glass laser was amplified in a Ga collisionally pumped x-ray amplifier at 251 Å [47].

IV.8.A X-Ray Lasers as Amplifiers for Harmonics

As we described in the introduction, the availability of kilojoule, nanosecond laser pulses has made it possible to create soft x-ray lasers based on electron collisionally pumped laser schemes [124]. These lasers operate by amplification of spontaneous emission, and the plasmas are produced from solid slab , thin foil and fiber targets. Used as sources of ASE with no cavity, these lasers typically exhibit low spatial and temporal coherence. By using a collisionally pumped laser plasma as an amplifier for high order harmonic radiation, high energy soft X-ray pulses with a duration determined by the harmonic pulse can be achieved, in principle. With this motivation we conducted an experiment in which we amplified a high order harmonic in a collisionally pumped x-ray laser amplifier. This was achieved by injecting harmonic radiation from a frequency doubled Nd:glass CPA laser into a neon-like gallium plasma. To do this, the 21st harmonic of the Nd:glass laser was tuned to give a spectral overlap with the J = 2-1 transition of GaXXII at a wavelength of 251.1 Å.

IV.8.B Experimental Set-Up

For these experiments, the high energy Vulcan laser at the Rutherford Appleton Laboratory was configured to operate with one arm in the short pulse CPA mode for the generation of harmonics and with three arms providing long pulse pumping beams for the x-ray laser amplifier. The experimental set up is shown in figure IV.31. An 850 fs pulse from a Nd:LMA oscillator was stretched, amplified to 10-30 J in one arm of the Vulcan Nd:glass laser chain, and then recompressed to a final pulse length of 1.3 ps (FWHM). The beam was then frequency doubled in a 4 mm thick KD*P crystal with a conversion efficiency of 30% giving up to 5 J of second harmonic light in a 7 cm diameter beam This was focused with an f = 3.5 m lens (f/50) to an approximately 4 x diffraction limited spot giving a peak intensity of ~ 5 x 10^{15} W/cm^2. The confocal parameter was approximately 10 mm. This focal geometry was chosen as an optimum compromise between maintaining good harmonic conversion efficiency based on our conversion efficiency measurements which suggested that a large focal spot size was optimal, and reasonable spatial overlap of the harmonic and the 100 μm Ga gain region which demanded a small focal spot size. The 527 nm beam was focused into our supersonic gas nozzle.

For success, we needed to match the wavelength of the 21st harmonic with that of the 251.1 Å gain line of the soft x-ray amplifier, implying that the fundamental of the harmonic producing beam needed to be tuned to 1054.6 nm. The short pulse Nd:LMA laser oscillator used to seed the CPA arm of Vulcan operated at a center wavelength of 1055.4 nm and a bandwidth of 1.4 nm. Light entering the amplifier chain was tuned by spectral windowing using a knife edge placed in the Fourier plane of the stretcher. This, in combination with the gain spectral profile in the glass amplifier chain, determined the output spectrum of the amplified pulse.

The Ga laser amplifier was pumped by three 1054 nm beams, each providing 200 J in an 800 ps pulse to pump the soft x-ray laser amplifier. Ga was chosen as the x-ray laser amplifier because of the very close overlap of one of the J = 2-1 lines with the 21st

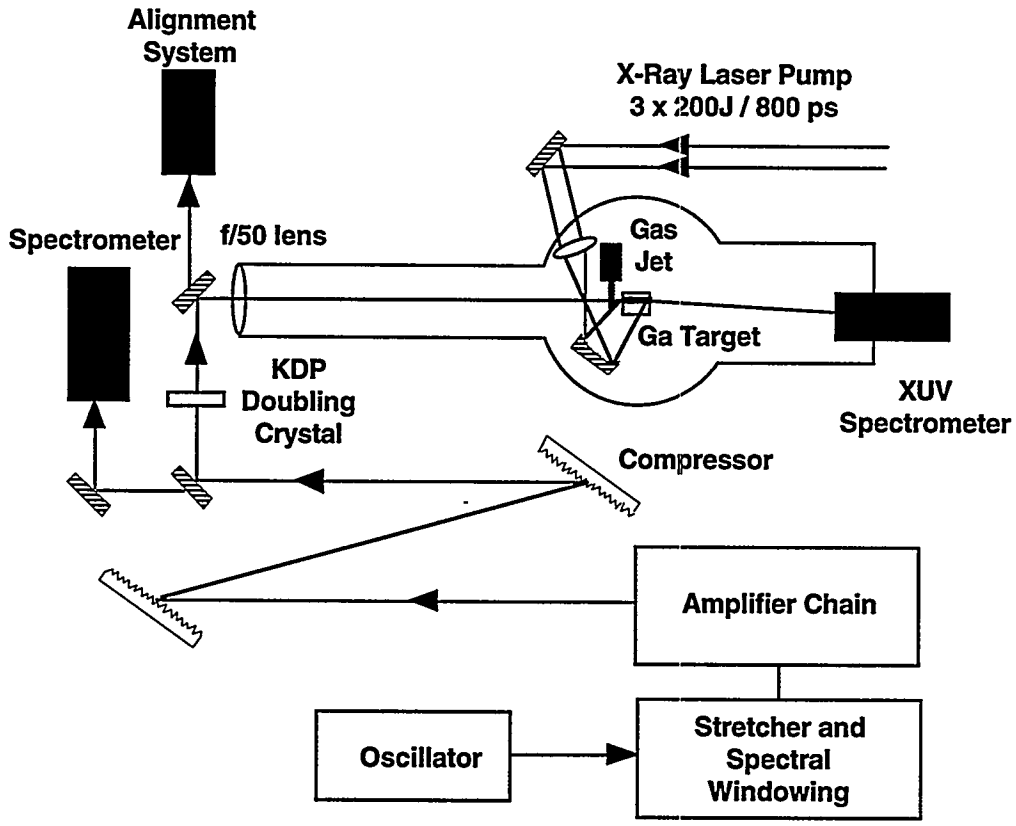

Figure IV.31: Experimental set up for the injection of high harmonics into a neon - like Ga XXII plasma.

harmonic of the frequency doubled Nd:glass laser. The target was a vacuum evaporated strip of Ga on a glass substrate. The stripe was 600 nm thick, 200 μm wide and up to 18 mm long. This target was irradiated from one side with three overlapped line foci produced by an off-axis lens/mirror system [164]. The separation of the gas jet and the entrance to the gallium amplifier was 20 mm which is comparable to the Rayleigh range of the harmonic beam. This allowed for good coupling of the harmonics into the approximately 80 μm diameter gain region of the laser plasma, while being sufficiently far removed to avoid preionization of the gas jet by thermal XUV radiation from the plasma.

The radiation from the harmonic beam was analyzed with an axial x-ray spectrometer placed 2 m from the gas jet. Spectra were recorded with either a time integrated x-ray CCD camera similar to the one used for the harmonic conversion efficiency measurements, or an x-ray streak camera with a low density CsI photocathode. For x-ray laser or amplified harmonics shots, the instrument was shifted slightly off axis to allow for refraction by the density gradient in the gallium plasma. For the 18 mm plasma lengths used in the experiment we expected this shift to be on the order of 5 mrad. All stray light from the laser and emission from the plasma at wavelengths below 173 Å was rejected by a combination of a 400 nm thick aluminum filter and-reflections from a pair of 8° grazing incidence gold mirrors placed at the spectrometer input.

Lasing in GaXXII has only been observed in one previous experiment [107] with few details and no gain coefficient reported. We expected, however, that neon-like gallium would exhibit similar properties to the germanium XXIII system, its neighbor in the periodic table. The Ge system has been extensively studied experimentally and computationally [139]. We, therefore, expected that the 800 ps pump pulse would produce gain on the two gallium J=2-1 laser lines for approximately 400-600 ps allowing relatively straightforward timing of the harmonic beam to the x-ray laser pump pulse.

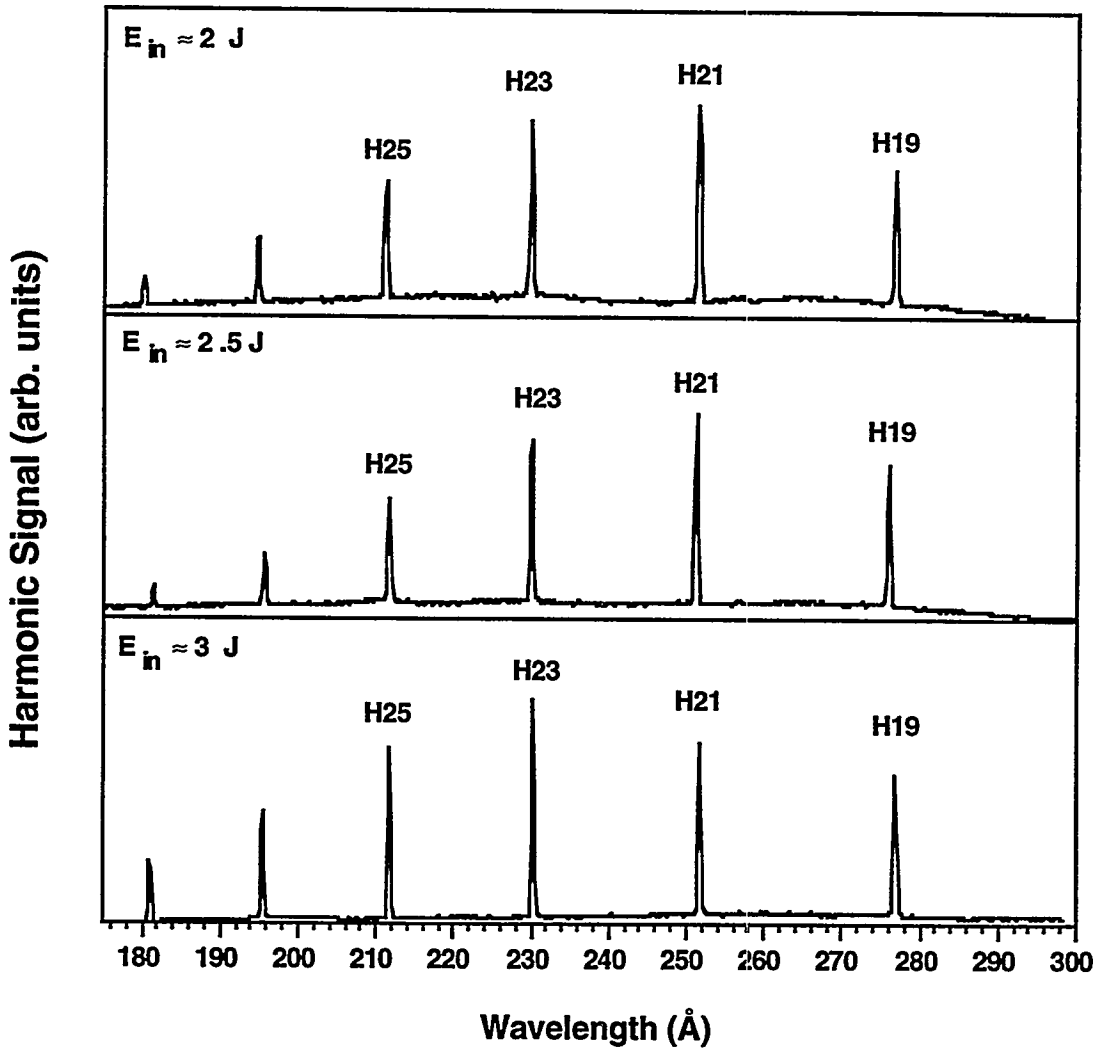

Figure IV.32: Time integrated harmonics spectra from He gas targets at an intensity of 1 - 1.5 x 10^{15} W/cm^2 showing little shot-to-shot variation in the relative size of the 19th, 21st, and 23rd harmonics.

IV.8.C Harmonic Amplification Experimental Results

The spectrum of the harmonics produced in helium at a focused intensity of 1 - 2 x 10^{15} W/cm^2 is shown in figure IV.32. The measured energy of the 21st harmonic at 251 Å was between 0.5 and 2nJ. The efficiency of harmonic production is estimated to be ~ 10^{-9}, which is substantially less than the measurements taken under similar conditions described in section IV.5. We attribute this difference to the 4 x diffraction limited

character of the Vulcan CPA beam which reduced the coherent power to 1/16th of the total and, therefore, reduced the conversion efficiency relative to that for a Gaussian beam. The maximum shot to shot variation of the ratio of the 21st harmonic to the 19th and 23rd harmonics was on the order of ~ 20%. This allowed us to use this ratio as a relative intensity calibration of the 21st harmonic.

The gain of the Ga laser was measured using the axial spectrometer to determine the length dependence of the two gallium J = 2-1 laser lines at 251.1 and 247 Å for plasmas up to 18 mm. Figure IV.33a shows the nonlinear growth in the 251 Å and 247 Å lines when the length of the Ga plasma was increased from 9 to 18 mm. Figure IV.33b shows the 251.1 Å line intensity as a function of plasma length, fitted to the gain formula of Linford et. al. [112] with a gain coefficient of approximately 3 cm^{-1}. The time integrated output of the 251.1 Å line for an 18 mm long plasma was estimated to be between 10 and 20 nJ. With the harmonic beam injected, time integrated spectra of combined harmonic and plasma emission (for a 9 mm target) clearly shows the harmonic radiation visible above the continuum emission. On these shots there was spatial break up of the harmonic radiation into two lobes which suggests that some of the harmonic radiation is being refracted by the plasma. A CCD image exhibiting this two lobe harmonic signal is shown in figure IV.34. Here we compare it to a spectrum image generated by harmonics alone to show the location of each harmonic over the background emission from the Ga plasma.

In order to distinguish the amplified 21st harmonic radiation from the longer lived background plasma emission, we used a streak camera to time resolve the spectra. Figure IV.35 shows the time evolution of signal at 251 Å from an 18 mm Ga target shot with a clearly visible intensity spike at early time from the injection of the 21st harmonic into the plasma 150 ps before the peak of the plasma emission. The time resolution of this data is ~ 50 ps.

In figure IV.36, we compare time resolved spectra from a harmonic shot with no

(a)

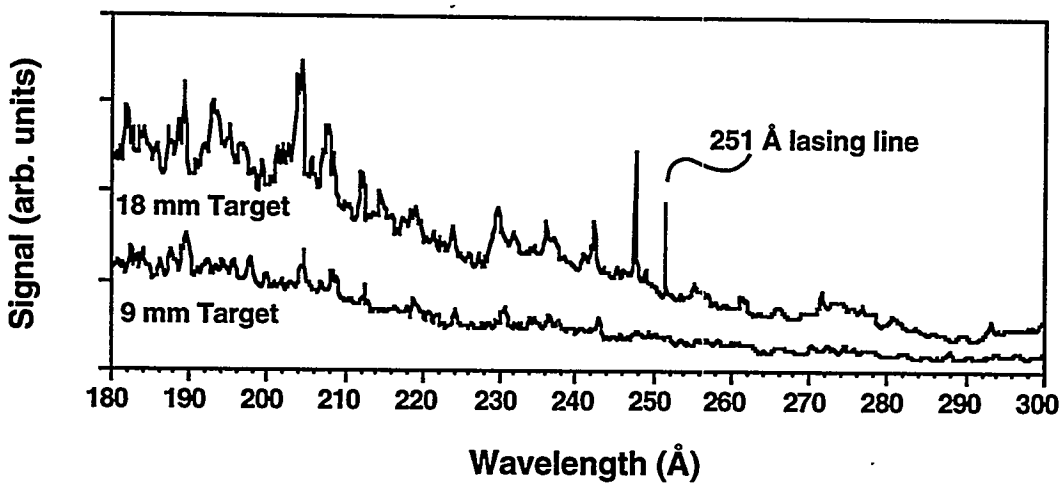

(b)

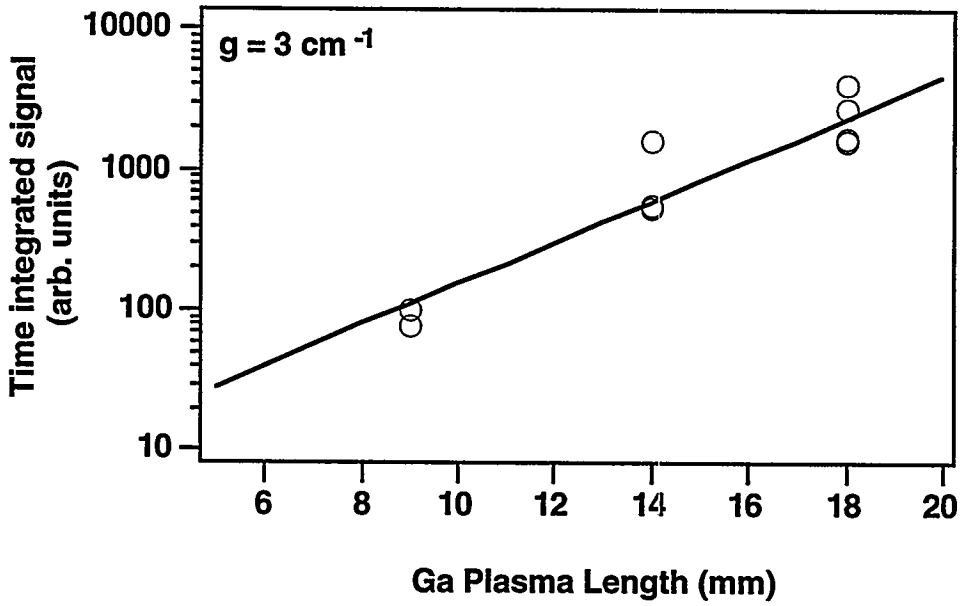

Figure IV.33: **(a)** Time integrated spectra of axial emission from the Ga plasma for two target lengths, 9 mm and 18 mm, Illustrating the nonlinear growth of the 247 Å and 251 Å lasing lines with respect to the background emission. **(b)** Neon-like gallium J=2-1 251 Å line intensity as a function of plasma length fitted to a Linford gain curve with a gain coefficient of ~ 3 cm^{-1}.

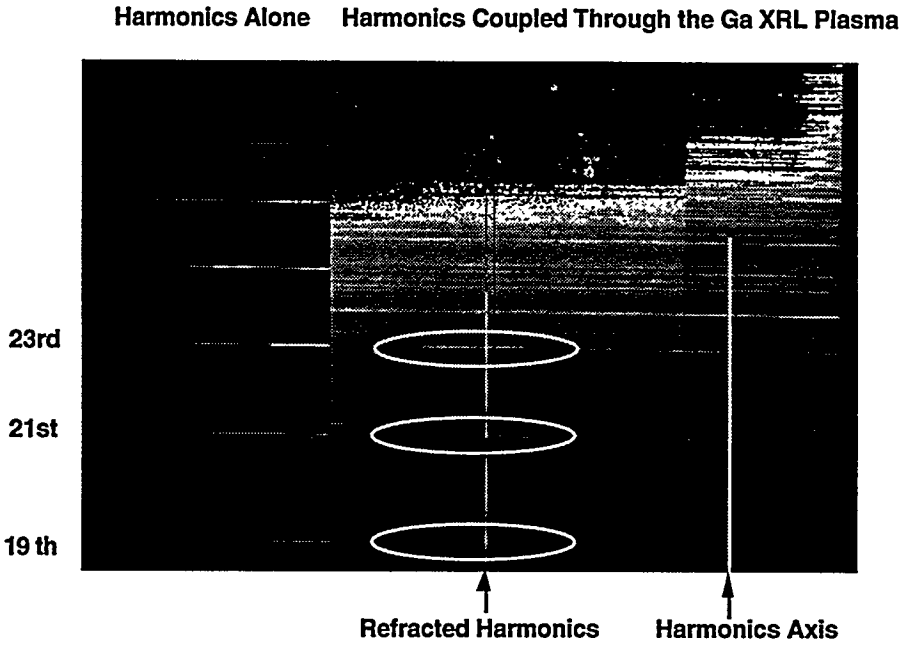

Figure IV.34: X-ray CCD image angularly resolving the harmonic emission after passage through the Ga plasma. The left image is a pure harmonics spectrum without a Ga plasma to show the positions of the harmonics. Two lobes are visible in the profile of the harmonics that passed through the X-ray laser plasma implying refraction of the harmonic radiation by the plasma density gradients of the Ga plasma.

plasma present, and a harmonic spectrum after traversing an 18 mm Ga plasma. This data represents the shot exhibiting the highest gain on the 21st harmonic. For this data, the streak camera was off-set from the harmonic axis to account for the refraction of the harmonics by the Ga plasma and to sample only the harmonics that had traversed the Ga gain region. The harmonic was tuned to give optimum spectral overlap with the 251.1 Å laser line. These two lineouts were averaged over a 30 ps time window, the resolution of the streak camera. The instrument and filter response have been deconvolved and the background, found from averaging 50 ps intervals on either side of the harmonic signal, has been subtracted. There is a clear enhancement of approximately a factor of three on the 21st harmonic relative to the 19th and 23rd harmonics in the case where the harmonic propagates through the amplifying plasma.

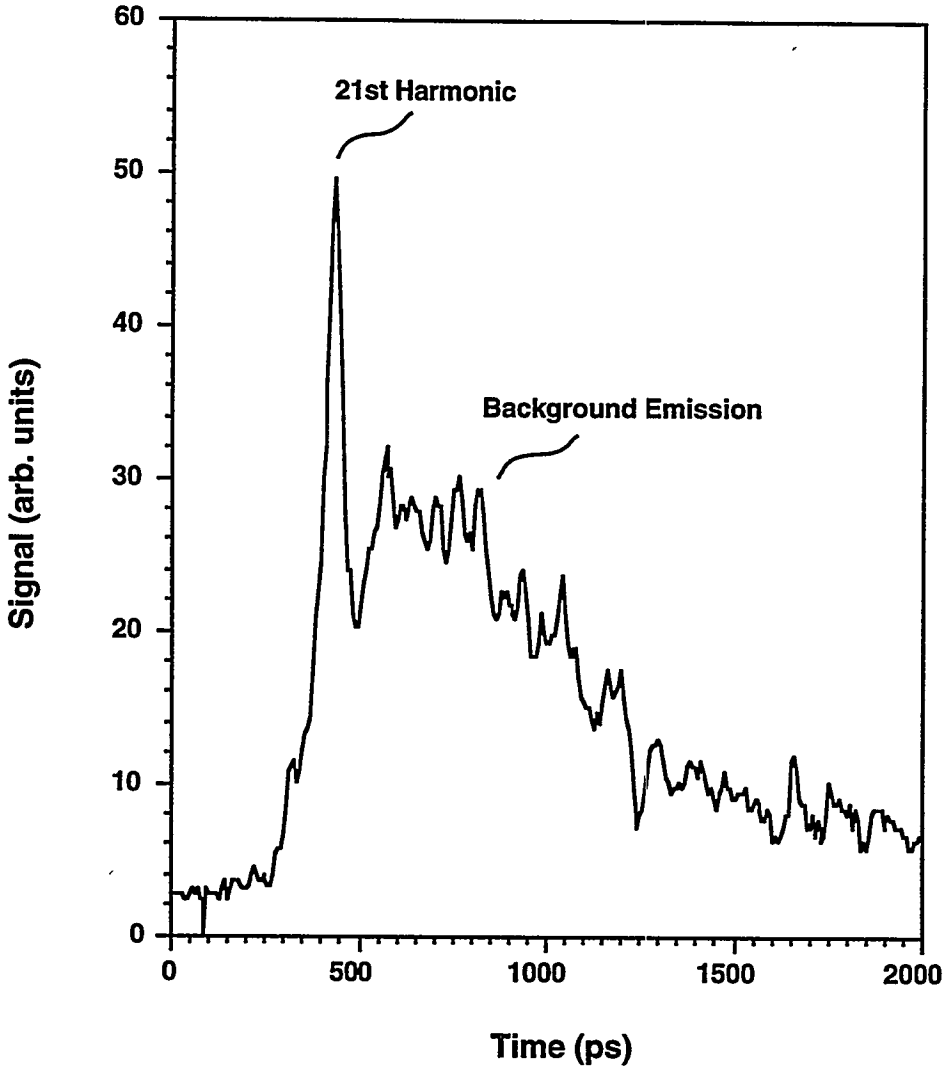

Figure IV.35: Time evolution of the background plasma emission at 251.1 Å from an 18 mm Ga target, showing the amplified 21st harmonic signal at early time.

IV.8.D Harmonic Gain Analysis

We can estimate the expected gain for the 21st harmonic based on the measured 3 cm^{-1} gain coefficient for the 251.1 Å GaXXII laser line and the coupling efficiency between the harmonic and the plasma amplifier. For complete coupling between the harmonic and the 18 mm x-ray amplifier, we would expect a small signal gain of $\exp[\alpha l] \approx 220$. However, this will be reduced by both the spectral and spatial overlap of the

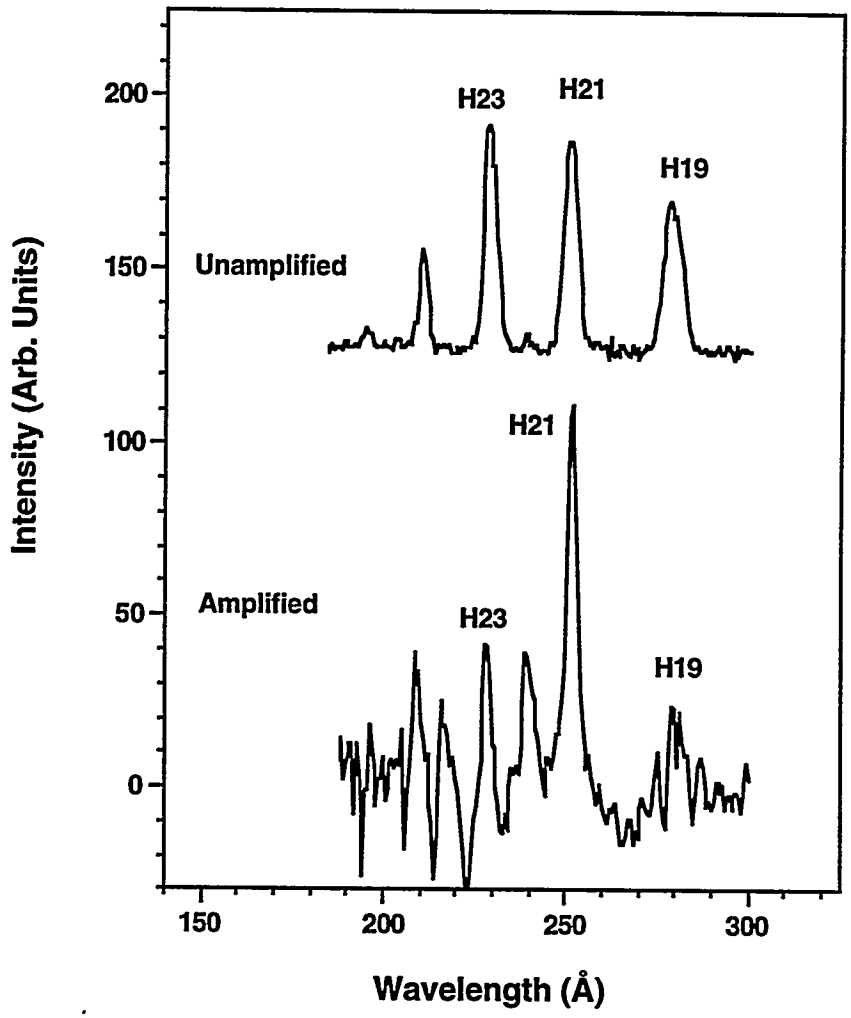

Figure IV.36. Comparison of (background subtracted) harmonic spectra with and without a Ga XXII plasma present. Spectral data is integrated over a 50 ps time window and the unamplified spectrum is off-set in intensity for ease of comparison.

harmonic with the gain region of the plasma. Based on our measurements of the harmonic linewidths for the LiSAF laser and scaling of eq. (4.12) and figure IV.16 we estimate the linewidth of the 21st harmonic to be ~ 0.1 Å (FWHM) which is well below the resolving power of the spectrometer. Measurements of the linewidths of similar collisionally pumped neon-like x-ray lasers can be used to infer the line width of the similar Ga laser [92]. From this work we estimate that the linewidth of the Ga XXII, J=2-1 transition is ~0.05 Å. Thus, with optimum spectral overlap of the harmonic to the laser line, we calculate that the line integrated gain will be ~ 25% that of the peak gain assuming a convolution of Gaussian spectral profiles. This lowers the maximum harmonic gain to ~ 50. The observable harmonic gain is further reduced because only a fraction of the harmonic energy is coupled into the plasma since the spatial extent of the harmonic exceeds that of the gain region. We estimate from far field measurements that the beam waist of the harmonics at the plasma is ~ 300 μm while the diameter of the gain region is only ~ 80 μm. This further reduces the observable gain to ~ 3.5. This is in good agreement with the observed value of gain on the 21st harmonic. This experiment demonstrates the feasibility of amplifying a high order harmonic in an x-ray laser amplifier. Further optimization of the experiment could conceivably lead to amplification on a harmonic by as much as two orders of magnitude.

IV.9 Conclusion

In this chapter we have presented a series of measurements that describe the generation of coherent soft x-ray radiation by efficient high order harmonic conversion at high laser intensity. We have presented measurements that indicate the wavelengths that are attainable. We have shown that a wavelength as short as 70 Å is possible with a 1 μm laser driver, and have also shown that harmonic energies in the 350 - 170 Å range exhibit

yields approaching 100 nJ with conversion efficiencies above 10^{-7} under optimum conditions with a 526 nm laser driver. We have shown that these energy yield measurements are in good agreement with calculated harmonic yields based on a numerical solution to the wave equation for the harmonics.

The coherence properties of the harmonics have also been investigated. We find that at a peak intensity near and below the saturation intensity, the harmonic spatial profiles are smooth, structureless Gaussian profiles. This is consistent with the assertion that the harmonics exhibit a high degree of spatial coherence. At higher intensity, however, the refraction of the fundamental accompanying plasma production by tunnel ionization can lead to a distortion of the harmonics far-field spatial profiles. We also presented measurements of the harmonics' spectral bandwidths. We found that the temporally varying plasma density phase modulates the fundamental pulse with a resulting blue shift and broadening of the harmonic line profile.

Finally we demonstrated the feasibility of using harmonics in the x-ray region in application. We presented experimental results in which the photoionization cross section of neon was measured with harmonics out to a photon energy of 100 eV. After that, an experiment demonstrating the first amplification of a high order harmonic in an x-ray laser amplifier was presented. The investigations of the harmonics' properties coupled with the demonstration of high order harmonics in application suggest that high order harmonics produced by small scale, terawatt class lasers may offer a very unique and economical source of x-rays for a variety of uses in the future.

Chapter V

Strong X-Ray Emission from Plasmas Produced By the Intense Irradiation of Atomic Clusters

V.1 Introduction and Background

In the previous chapter we examined the production of soft x-ray radiation with a short pulse laser in a gas through high order harmonic radiation. Though this mechanism holds great potential as a source of coherent x-rays it clearly exhibits a number of limitations. As the studies in section IV.2 illustrated, the wavelength range accessible with harmonics is essentially limited to longer than 100 Å. But the most obvious limitation stems from the low conversion efficiency from laser light to x-ray radiation. It is sometimes desirable to generate much higher photon yield efficiencies at the expense of the coherence of the light. To do this requires a target material that exhibits higher laser energy absorption than a low density gas. The most straightforward solution is to utilize a solid, high Z target for the laser [138, 29].

Unlike gases, solid targets often exhibit very large laser energy absorption. The use of solids as targets for intense lasers has successfully produced both photons and particles with energies up to the MeV range [90, 64]. Because of the strong absorption mechanisms in a solid density plasma, such as collisional heating, resonance absorption, and various plasma instabilities [95] significant fractions of the laser pulse energy (>10%)

can be deposited into the plasma [138, 159]. The hot plasmas that result can emit copious amounts of x-rays. Conversion efficiency of nearly 1% of laser light into x-rays in the 1 keV photon energy range has been demonstrated [73, 180]. This conversion efficiency can be increased to 10% when the surface of the target is coated with a layer of porous Au-black, which is composed of individual 100Å clusters of Au [138, 73]. This Au-black was shown to be much more efficient at absorbing the incident laser energy than conventional flat gold targets due to the large surface to volume ratio of the clusters.

The results with Au-black suggest that an alternate approach to increasing the laser absorption is to choose a target material that consists not of single isolated atoms, as is the case in a low density gas, nor of a single macroscopic object such as a solid metallic object, but that consists of some microscopic collections of atoms. The enhanced absorption exhibited by the Au-black indicate that it might be possible to construct an object that is optimum for absorbing laser energy. Small molecules, which ionize and then dissociate upon illumination by an intense laser, do not offer any significant advantages over single atoms. Large molecules, or atomic clusters, with many atoms (> 1000 atoms) however, may provide a potential medium for significant laser energy absorption.

High pressure gas jets, in fact, produce such a unique target source under certain conditions [128]. Solid density clusters can form in the jet, resulting from the cooling associated with the adiabatic expansion of the gas into vacuum [76]. This cooling causes the gas to supersaturate and nucleate. Under appropriate conditions, when the gas jet backing pressure exceeds a few atmospheres, the clusters formed in the expanding jet can be quite large ($>10^4$ atoms per cluster) for gases such as Ar, Kr, N_2 and Xe. Recently, McPherson et. al. observed anomalous x-ray line emission from high Kr and Xe charge states when a high intensity ($0.5 - 80 \times 10^{17}$ W/cm^2), 248 nm laser was focused into a jet of these gases [127, 129]. They suggested that this emission was the result of inner shell vacancies produced by collisions of laser driven electrons with atoms in small (~2-100

atom) clusters, and that the observed emission was prompt (~ 100 - 1000 fs) after excitation by the laser. Recently, however, we have observed similar strong x-ray emission from a gas jet containing clusters, but we find that the emission from these interactions is long lived (~ 1 ns), contrary to the hypothesis of McPherson et. al. [46]. In our experiments the vast majority of the x-rays emitted from the laser cluster interaction do not come from the cluster itself, contrary to the claims of McPherson et. al., but that the clusters serve only to absorb the laser energy with the bulk of the x-ray emission occurring after the cluster has expanded.

In this chapter, we examine the interaction of femtosecond laser pulses with large clusters in detail. We find that the atomic clusters are very efficient at absorbing laser energy, with the coupling of the laser energy into the cluster being predominately by collisional heating of electrons. This large heating within the cluster results in rapid production of high ion charge states, followed by long lived (~ ns) x-ray emission from these charge states by the hot, underdense plasma that results after the clusters have expanded. First we shall examine the physics that is involved in the laser/cluster interactions and we present a numerical model that incorporates this physics to make some predictions about the cluster plasma. We then present a model of the underdense plasma that results after the clusters expand. This model allows us to compare the numerical predictions with the experimental data. Finally, we present a detailed experimental study of the interaction of pulses from the LiSAF laser with atomic clusters, and we show that these clusters are, indeed, a very good target for efficient x-ray generation.

V.2 Cluster Formation in a Gas Jet

When high pressure gas flows into vacuum through an orifice, the expansion is isentropic; the random thermal energy is converted into directed kinetic energy resulting in a decrease in temperature. For certain gases, when the backing pressure is high (>10 psi for typical gas jets), the gas can become supersaturated and solid density droplets will form [76]. These droplets, which are held together by van der Waals forces, can become quite large under appropriate conditions. Very extensive studies of these process have been carried out and these allow accurate predictions of the threshold and size of clusters that can be produced under a variety of experimental conditions.

Hagena found that the onset of clustering in gas jets and size variation of the clusters produced can be characterized by an empirical parameter that varies with the experimental conditions of the gas jet [76, 75]. This Hagena parameter is given by

$$\Gamma^* = k\frac{(d / \tan\alpha)^{0.85} p_0}{T_0^{2.29}} \tag{5.1}$$

where d is the jet throat diameter in mm, α is the jet expansion half angle (which is 45° for a sonic expansion, but smaller for a supersonic expansion), p_0 is the backing pressure in mbar, T_0 is the initial gas temperature and k is a constant that depends on the atomic species ($k \approx 2900$ for Kr, 1700 for Ar, 180 for Ne, and 4 for He[194]). Most studies have shown that clustering begins when this parameter exceeds ~300 with the average size of clusters produced increasing roughly as $\sim(\Gamma^*)^{2.0-2.5}$ [76, 59]. These studies show that large clusters (>10^4 atoms/cluster) predominate when $\Gamma^* > 5 \times 10^4$ [194]. This scaling indicates, first, that clustering is more significant for the heavier noble gases such as Kr and Ar than for Ne and He. For a typical gas jet throat of ~1 mm, backing pressures as low as 300 psi are sufficient for producing large clusters at room temperature in Kr or Ar, while >2000 psi is required for the onset of any clustering at all in helium. The scaling of

eq. (5.1) also suggests that clustering is enhanced when the jet flow expansion angle is restricted by a shaped nozzle downstream from the jet throat. The increase of clustering with a supersonic nozzle has been confirmed for a wide variety of gases [1].

These characteristics point toward the use of heavier gases for the formation of large clusters. Though small clusters of Ne and He have been observed under certain conditions [76], the scaling of (5.1) suggests that Ar, Kr, N_2, and Xe are most favorable for the production of large clusters. We can estimate the size of clusters that will be desirable for illumination by a short pulse laser, if we require that the time it takes for the cluster to disassemble is comparable to or longer than the laser pulse. As will be discussed below, the predominate expansion mechanism for the clusters of interest is hydrodynamic expansion of the cluster plasma sphere after the electrons have been heated by the laser pulse. We can estimate the time of this expansion if we assume sonic expansion and require the density to drop from the solid cluster density to the surrounding ambient gas density. The resulting cluster expansion time is approximately

$$\tau_{ex} \approx r_0 \sqrt{\frac{m_i}{ZkT_e}} \left(\frac{n_0}{n_s}\right)^{1/3} \tag{5.2}$$

where r_0 is the initial cluster radius, kT_e is the cluster electron temperature and m_i is the ion mass. For an argon cluster (which has an initial lattice spacing of approximately 3.8Å [23]) with an initial electron temperature of 1 keV, a $Z \approx 8$, and a surrounding bulk plasma with a density of 10^{18} atoms/cm^3, the expansion time will be longer than approximately 1 ps if the initial cluster is larger than about 100Å in diameter. This corresponds to about 10^5 atoms per cluster. We expect, therefore, that 100 fs laser pulses will interact with the clusters over the majority of the laser pulse if the clusters are of the order of 100 Å. Pulses longer than ~ 1 ps, however, will only interact with the cluster over a section of the pulse.

Illumination of a gas jet with these large clusters with sufficiently short pulses will, therefore, deposit laser energy in a manner that is quite different than a low density gas without clusters. Most importantly, the collisionality of the atoms is greatly enhanced by their close proximity to each other in the cluster. This collisionality results in significant electron heating during the laser pulse. As we illustrated in chapter III, the temperature of low density gases illuminated by 100 fs pulses at intensities below 10^{17} W/cm^2 is usually quite low, typically around 10 to 50 eV. Only when high density clusters are present in the gas will the absorption deviate significantly from this picture. When clusters are present in the gas, collisional processes, such as inverse bremsstrahlung and collisional ionization will become dominant because of the much higher density within the cluster.

V.3 The Theory of Short Pulse Laser Interactions with Clusters

We treat the interaction of the laser pulse with the cluster as that of the laser interacting with a small ball of high density plasma. We shall assume that the collisionality inside the cluster is high enough and the spatial size of the cluster is small enough that no thermal gradients exist within the cluster. Thus, we can assume that the temperature is uniform and the electron velocity distribution is isotropic and described by a Maxwellian. This will be true when the electron thermalization time is small on the time scale of the laser interaction. Strictly speaking, this picture of the cluster as a small plasma ball is only valid when the cluster dimension is significantly larger than a Debeye length $\lambda_d = \sqrt{kT_e / 4\pi n_e e^2}$, which is equal to ~5 Å for a solid density, 1000 eV plasma. Therefore, it is a good description for the large clusters (~100 Å) considered here.

We shall also assume that the density within the cluster is uniform during the expansion and heating by the laser. The ionization rate will be a combination of field

ionization and collisional ionization rates. The heating is predominately by inverse bremsstrahlung. The expansion of the cluster will be by a combination of hydrodynamic expansion and a coulomb explosion that results when a significant charge has accumulated on the cluster. This second mechanism requires a knowledge of the rate at which electrons "free-stream" out of the cluster and to what degree they are retained by space charge. Before calculating this free streaming or the heating rate, we require knowledge of the ionization rate to determine the electron density in the cluster.

V.3.A Ionization Mechanisms within the Cluster

There are three ionization mechanisms which can be important in the interaction of the laser with the atoms of the cluster. The first mechanism is direct optical ionization of the atoms. This mechanism is most important in the early stages of the laser pulse interaction with the cluster since it produces the initial electrons that form the plasma. This rate can be calculated using the cycle averaged ADK tunnel ionization rate, described by the formula in eq. (3.26).

The second ionization mechanism in the cluster turns out to be the most important for conditions of interest. This is ionization that occurs from inelastic collisions between electrons and ions. Once a few electrons are produced by optical ionization the production of higher charge states is dominated by collisional ionization as a result of the high density in the cluster. To calculate this rate in our model we use the empirically determined collisional ionization rate formula of Lotz [114]. This rate per ion averaged over a Maxwellian electron distribution is

$$W_{kT} = n_e \frac{a_i q_i}{I_p (kT_e)^{1/2}} \int_{I_p/kT_e}^{\infty} \frac{e^{-x}}{x} dx \tag{5.3}$$

where n_e is the electron density, I_p is the ionization potential in eV, a_i is an empirical constant = 4.5 x 10^{-14} eV^2 cm^{-3} [114], and q_i is the number of electrons in the outer shell

of the ion. For the conditions that prevail in the cluster, this rate can be quite high. For example, in a solid density cluster with eight times ionized Ar (Z=8), $n_e = 2 \times 10^{23}$ cm^{-3}, so at a temperature of 1 keV the rate for ionization of the argon to Ar^{9+} from Ar^{8+} (I_p = 422 eV) is 0.4 fs^{-1}. Therefore this ionization mechanism can be responsible for the production of high charge states well below the intensity threshold for tunnel ionization in the cluster if sufficient heating occurs inside the cluster. (Note, for example, that the tunnel ionization mechanism to Ar^{9+} only becomes significant when the laser intensity reaches $>10^{18}$ W/cm^2).

The ionization rate in eq. (5.3) accounts only for the collisional ionization by electrons with thermal energy sufficient to ionize the ion. The electrons in the cluster also have a velocity associated with their oscillations in the field. In general, the rate of collisional ionization by electrons driven by a laser in a dense plasma is a difficult problem due to the large number of coulomb collisions that the electrons undergo which randomize their sinusoidal oscillation velocity. Nonetheless, we can estimate the magnitude of this ionization mechanism rate by considering electrons with pure sinusoidal velocity. This treatment will, in general, overestimate the collision ionization rate since we allow the electrons to have larger peak oscillation velocities then they will really acquire due to randomization of the velocity by coulomb collisions.

To calculate this rate we use the collision ionization cross section of Lotz and treat the electron velocity as sinusoidal. The ionization rate per ion is

$$W_{las}(t) = n_e \sigma_i \frac{eE}{m_e \omega} \sin \omega t \tag{5.4}$$

where σ_i is the velocity dependent cross section for ionization. It is convenient to determine the cycle averaged rate of ionization for comparison to the other ionization rates. We find this by averaging eq. (5.4) over the part of the laser cycle in which the driven

electron has enough kinetic energy, K_e to ionize the ion (i.e. $K_e > I_p$). The cycle averaged rate is

$$\begin{aligned} W_{las} &= \langle W_{las}(t) \rangle \\ &= \frac{n_e}{\pi} \int_{\phi_{\min}}^{\pi} \sigma_i \frac{eE}{m_e \omega} \sin\phi d\phi \end{aligned} \tag{5.5}$$

The Lotz cross section for the ionization is [114]

$$\sigma_i = a_i q_i \frac{\ln(K_e / I_p)}{K_e I_p} \tag{5.6}$$

Using the fact that $\sin\phi\, d\phi = (4U_p)^{-1}(1 - K_e / 2U_p)^{-1/2} dK_e$, the cycle averaged ionization rate can be written:

$$W_{las} = n_e \frac{a_i q_i}{\pi I_p} \sqrt{\frac{1}{m_e U_p}} \int_{I_p}^{2U_p} \frac{\ln(K_e / I_p)}{2K_e} \frac{1}{\sqrt{1 - K_e / 2U_p}} dK_e \tag{5.7}$$

Eq. (5.7) cannot be integrated directly but if we concern ourselves with the electrons of energies around the ionization potential where the ionization rate is highest [114] we can expand the logarithm around the small parameter $1 - I_p / K_e$ and write

$$\ln(K_e / I_p) \approx 3/2 - 2\frac{I_p}{K_e} + \frac{I_p^2}{2K_e^2} \tag{5.8}$$

This approximation turns out to be a good one not only for electron kinetic energies close to I_p but for energies somewhat above I_p as well (up to about $K_e \sim 2I_p$). With this approximation, the cycle averaged laser driven collisional ionization rate then becomes

$$\begin{aligned} W_{las} \approx\ & n_e \frac{a_i q_i}{2\pi I_p m_e^{1/2} U_p^{1/2}} \times \\ & \left[\left(3 + \frac{I_p}{U_p} + \frac{3}{32}\left(\frac{I_p}{U_p}\right)^2 \right) \ln\left[\frac{1 + \sqrt{1 - I_p / 2U_p}}{1 - \sqrt{1 - I_p / 2U_p}} \right] - \left(\frac{7}{2} + \frac{3I_p}{8U_p} \right) \sqrt{1 - I_p / 2U_p} \right] \end{aligned} \tag{5.9}$$

This rate is plotted in figure V.1 as a function of U_p / I_p for an electron density of 1 x 10^{23} cm^{-3}. This rate is compared with the thermal ionization rate of eq. (5.3) as a function of kT_e / I_p. From this comparison we see that these two rates are of comparable magnitude if the temperature of the plasma is comparable to the ponderomotive energy of the laser field inside the cluster (a situation that will prevail in a highly collisional plasma).

V.3.B Cluster Heating Mechanisms

We shall now consider the heating of the cluster sphere. Since we assume no temperature gradients in the cluster we treat the heating from the laser as uniform over the cluster volume. First we shall consider the general heating of a dielectric sphere by a time

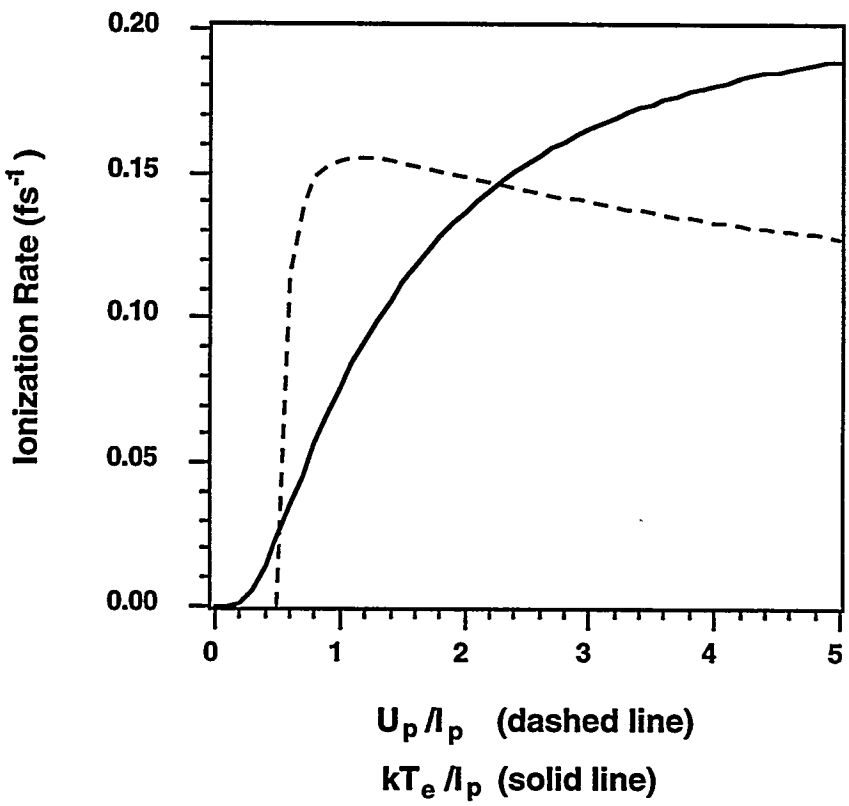

Figure V.1: Calculated ionization rate for Ar^{8+} ions in a plasma with an electron density of 10^{23} cm^{-3} from thermal electrons (solid line) and laser driven electrons (dashed line).

varying electric field. The energy deposited per unit volume in the cluster is given by [103]:

$$\frac{\partial U}{\partial t} = \frac{1}{4\pi}\mathbf{E} \bullet \frac{\partial \mathbf{D}}{\partial t} \tag{5.10}$$

The laser field inside the cluster is $\mathbf{E} = \frac{1}{2}\hat{\mathbf{x}}\left(Ee^{i\omega t} + c.c.\right)$ and $\mathbf{D} = \varepsilon\mathbf{E}$. The heating rate then becomes upon time averaging:

$$\frac{\partial U}{\partial t} = \frac{\omega}{8\pi}\mathrm{Im}[\varepsilon]|E|^2 \tag{5.11}$$

Since the diameter of the clusters considered in our study are, in general, much smaller than the wavelength of the laser light, we can approximate the field inside the cluster by assuming that it is given by the solution for the field inside a dielectric sphere surrounded by a constant, uniform field. The solution for the field inside of a uniform sphere is [83]

$$E = \frac{3}{|\varepsilon + 2|}E_0 \tag{5.12}$$

where E_0 is the strength of the laser field in vacuum, outside the cluster. The heating rate inside the cluster becomes

$$\frac{\partial U}{\partial t} = \frac{9\omega}{8\pi}\frac{\mathrm{Im}[\varepsilon]}{|\varepsilon + 2|^2}|E_0|^2 \tag{5.13}$$

We use a simple Drude model for the plasma dielectric constant:

$$\varepsilon = 1 - \frac{\omega_p{}^2}{\omega(\omega + i\nu)} \tag{5.14}$$

where ν is the electron-ion collision frequency. The heating rate per unit volume in the cluster becomes

$$\frac{\partial U}{\partial t} = \frac{9\omega^2\omega_p{}^2\nu}{8\pi}\frac{1}{9\omega^2\left(\omega^2 + \nu^2\right) + \omega_p{}^2\left(\omega_p{}^2 - 6\omega^2\right)}|E_0|^2 \tag{5.15}$$

Note that when the electron density inside the cluster sphere is high, i. e. when $n_e / n_{crit} >> 3$, then the field inside the cluster given by eq. (5.12) is smaller than the field surrounding the cluster in vacuum. This results in a decrease of the heating rate since the laser electric field energy density is shielded from the cluster interior. However, when $n_e / n_{crit} = 3$, then $|\varepsilon + 2|$ goes through a minimum and the field, and, therefore, the heating rate, inside the cluster is enhanced. The relative height and width of this resonance is determined by the value of the collision frequency, ν. The functional form of the heating rate from eq. (5.15) as a function of n_e for a fixed values of the collision frequency ν, is shown in figure V.2. As the electron density in the cluster increases, the heating rate peaks and then falls below the vacuum heating rate when $n_e / n_{crit} >\sim 5$.

The electron-ion collision frequency can be described by the standard coulomb formulas of Silin [175]. These frequencies have analytic formulas for the extreme cases in

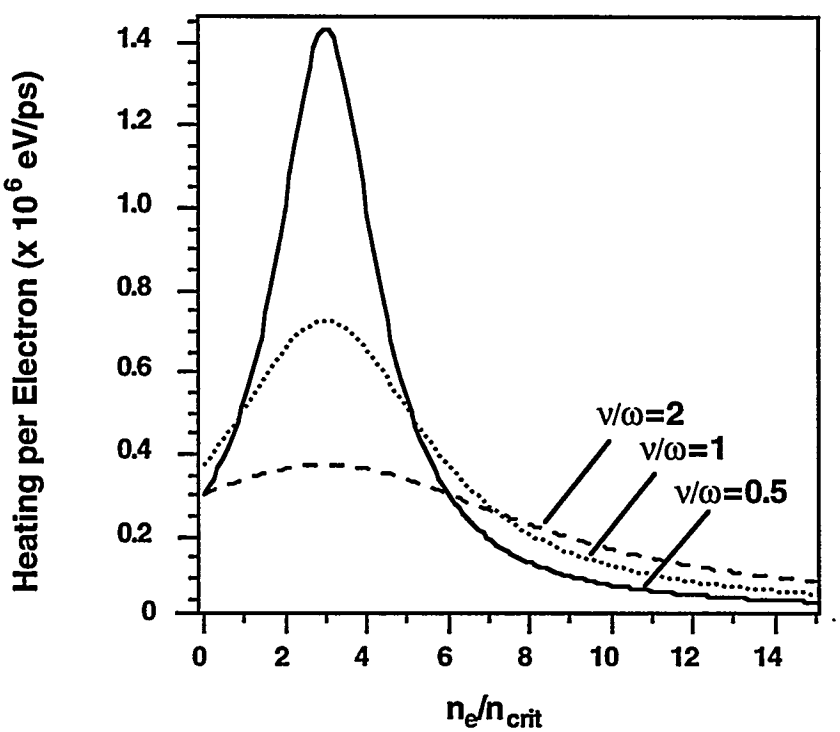

Figure V.2: Calculated heating rate in a cluster by an 825 nm laser pulse with a peak intensity of 10^{16} W/cm^2 as a function of n_e for three values of the collision frequency, ν.

which $v_{osc} << v_{kT}$ and when $v_{osc} >> v_{kT}$. When the oscillation velocity is small the collision frequency is given by

$$\nu = \frac{4}{9}\sqrt{\frac{2\pi}{3}}\frac{Z^2 e^4 n_i}{m_e^{1/2}(kT_e)^{3/2}}\ln\Lambda \qquad v_{osc} << v_{kT} \qquad (5.16)$$

while the opposite case is described by

$$\nu = \frac{16Z^2 e n_i m_e \omega^3}{E_0^{\,3}}\left(\ln\left[\frac{eE_0}{2m_e\omega v_e}\right]+1\right)\ln\Lambda \qquad v_{osc} >> v_{kT} \qquad (5.17)$$

To find the collision frequency for the intermediate case when $v_{osc} \approx v_{kT}$ we numerically integrate the general equation describing the collision frequency in ref. [175].

At high densities, however, the equations of Silin predict collision frequencies that are physically too high (i.e. $\nu >> \omega$). It is, therefore, necessary to clamp ν at some reasonable value. For our calculations we use a harmonic average of the Silin frequency with some suitably chosen maximum collision frequency:

$$\frac{1}{\nu} = \frac{1}{\nu_{coul}} + \frac{1}{\nu_{max}} \qquad (5.18)$$

We take $1/\nu_{max}$ to be equal to the minimum time it would take for an electron driven by the laser field to traverse the distance between two ions a distance $n_i^{-1/3}$ apart. This maximum collision frequency is given by

$$\nu_{max} \cong \frac{2eEn_i^{1/3}}{\pi m_e \omega} \qquad (5.19)$$

where E is the field inside the cluster (given by eq. (5.12)). This maximum collision frequency is typically on the order of the laser frequency ω for solid density plasma. For example, in a plasma with a density of 10^{22} cm^{-3} in a field corresponding to an intensity of 10^{15} W/cm^2, the maximum collision frequency for an 800 nm laser is $\nu_{max} \sim 4\omega$. From eq. (5.15) and figure V.2 it is clear that the collisional heating of the cluster can be

quite high. Solid density will only be maintained for a short time, however, since the cluster will begin to expand once it begins to be heated.

V.3.C Cluster Expansion Mechanisms

There are two forces which act on the cluster causing it to expand during and after the laser pulse. The first is the pressure associated with the hot electrons. The heated electrons expand and pull the cold, heavy ions outward with them. The characteristic speed for this expansion is the plasma sound speed:

$$v_{expand} \sim \sqrt{\frac{ZkT_e}{m_i}} \tag{5.20}$$

The other force acting on the cluster results from a charge buildup on the cluster. The hottest electrons in the cluster will have a mean free path large enough that they can free stream directly out of the cluster, and, if the electrons' energy is large enough to overcome the space-charge build-up on the cluster, they will leave the cluster altogether. If the charge build-up is sufficiently large, the cluster will undergo a coulomb explosion in a manner analogous to the photo-ionization of molecules.

We can calculate the rate of expansion by the cluster by considering the conservation of energy of an expanding fluid sphere that maintains a uniform (but decreasing) density throughout the sphere during the expansion [79]:

$$P4\pi r^2 \frac{\partial r}{\partial t} = \frac{\partial K_c}{\partial t} \tag{5.21}$$

Here P is the total pressure associated with the surface of the sphere. If we ignore the pressure of the cold ions, P can be broken down into a hydrodynamic term from the electron pressure and a suitably chosen pressure from the coulomb force:

$$P = P_e + P_{coul} \tag{5.22}$$

The equation for the radius of the cluster becomes

$$\frac{\partial^2 r}{\partial t^2} = 3\frac{P_e + P_{coul}}{n_i m_i}\frac{1}{r} \tag{5.23}$$

The hydrodynamic contribution to the expansion corresponds to a conversion of electron thermal energy to directed kinetic energy. The effects that the expansion has on the electron temperature can be calculated by equating the rate of change of radial kinetic energy from the thermal contribution with the rate of change of thermal energy within the cluster:

$$P_e 4\pi r^2 \frac{\partial r}{\partial t} = -\tfrac{3}{2}\left(\tfrac{4}{3}\pi r^3\right) n_e k \frac{\partial T_e}{\partial t} + \frac{\partial U_{coll}}{\partial t} \tag{5.24}$$

where $\partial U_{coll}/\partial t$ is the energy deposition due to the collisional heating. Since the electron pressure is given by

$$P_e = n_e k T_e \tag{5.25}$$

the rate of temperature drop from the cluster expansion is

$$\left.\frac{\partial T_e}{\partial t}\right|_{exp} = -2\frac{T_e}{r}\frac{\partial r}{\partial t} \tag{5.26}$$

To estimate the force of expansion due to a charge build-up we shall treat the cluster plasma sphere as a perfect conductor and assume that the accumulated charge, Qe, on the cluster resides on the surface. The stored energy of the spherical "capacitor" is

$$E_{Qe} = \frac{Q^2 e^2}{2r} \tag{5.27}$$

which implies that the force per unit area on the surface of the cluster is

$$P_{coul} = \frac{Q^2 e^2}{8\pi r^4} \tag{5.28}$$

From the $1/r^4$ scaling in eq. (5.28) we see that the coulomb force becomes most important for small clusters. It is informative to compare the relative contributions of these forces on the cluster for parameters of interest to determine which will be dominant. Comparing eqs. (5.25) and (5.28) we see that for a 100 Å cluster with an electron density of 10^{23} cm^{-3} the coulomb pressure will become comparable to the hydrodynamic pressure when $Q \approx 10^5$. This corresponds to ~ 20% of the electrons having exited the cluster volume (for Z = 8). This is a significant, but not unreasonable number. We, therefore, expect that both expansion terms may play a role in calculating the dynamics of the cluster expansion. Once the cluster expands, however, the hydrodynamic force will begin to dominate since the hydrodynamic pressure scales as $1/r^3$ (through n_e) while the coulomb force scales as $1/r^4$.

To accurately calculate the time dependent coulomb pressure it is necessary to calculate the rate at which electrons leave the cluster volume. This rate needs to account for the collisionality of the plasma and the shape and size of the cluster. Instead of imposing an arbitrary flux limiter as is customary, we estimate the rate accounting for the geometry of the cluster and relative size of the electron mean free path within the cluster. To account for the collisionality of the cluster plasma we shall assume, first, that to leave the cluster volume, the electron needs to traverse less than one mean free path, λ_e, to reach the surface of the cluster sphere. To account for the space-charge build-up on the cluster we assume an electron can escape the cluster only if its kinetic energy exceeds the coulomb potential energy at the cluster surface.

The rate of electrons exiting the cluster can then be written as

$$W_{fs} = \int \mathrm{v} f(\mathrm{v}) dA d\mathrm{v} \tag{5.29}$$

where $f(\mathrm{v})$ is the velocity distribution function of the electrons in the cluster which we take to be Maxwellian:

$$f(\mathrm{v}) = 4\pi n_e \left(\frac{m_e}{2\pi k T_e}\right)^{3/2} \mathrm{v}^2 \exp\left[\frac{-m_e \mathrm{v}^2}{2kT_e}\right] \tag{5.30}$$

The integral in eq. (5.29) over velocity is constrained to include only those velocities that are high enough to escape the coulomb attraction of the cluster. The integration over the cluster surface is constrained to include only those electrons whose path is within one mean free path of the cluster surface. Accounting for the volume of the cluster encompassed by this constraint, the integral in eq. (5.29) can be written

$$W_{fs} = 4\pi r^2 \int_{v_{esc}}^{\infty} \int_{\rho_{min}}^{r} \int_{0}^{2\pi} \int_{\cos\psi_{max}}^{\cos\psi_{min}} \mathrm{v} f(\mathrm{v}) \frac{3\rho^2}{4\pi r^3} d\cos\psi \, d\phi \, d\rho \, d\mathrm{v} \tag{5.31}$$

The geometry of the integral is shown in figure V.3. The free streaming constraints can be written as

$$x < \lambda_e \tag{5.32a}$$

$$\cos\psi_{max} = -1$$

$$\cos\psi_{min} = \frac{\rho^2 + \lambda_e^{\,2} - r^2}{2\rho\lambda_e} \tag{5.32b}$$

$$\rho_{min} = r - \lambda_e \tag{5.32c}$$

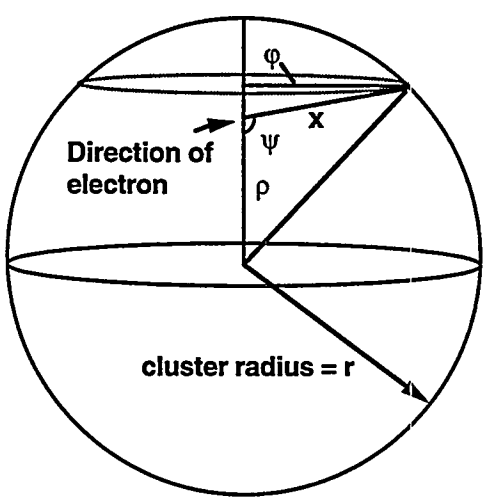

Figure V.3: Geometry of the free streaming rate integral, eq. (5.31).

Evaluation of eq. (5.31) with these constraints yields for the free streaming rate:

$$W_{fs} = n_e \frac{2\sqrt{2\pi}}{m_e^{1/2}(kT_e)^{1/2}}(K_{esc} + kT_e)\exp\left[-\frac{K_{esc}}{kT_e}\right] \times \begin{cases} \frac{\lambda_e}{4r}(12r^2 - \lambda_e^2) & \lambda_e < 2r \\ 4r^2 & \lambda_e > 2r \end{cases} \tag{5.33}$$

Note that when $\lambda_e > 2r$ and $K_{esc} = 0$ this formula reduces to the classical free streaming rate of electrons from a uniform sphere. For the electron mean free path in the cluster plasma we use the standard Spitzer formula [178]:

$$\lambda_e = \frac{(kT_e)^2}{4\pi n_e (Z+1)e^4 \ln\Lambda} \tag{5.34}$$

To estimate the electron escape energy we exploit our assumption that the cluster sphere is a perfect conductor and that any built up charge, therefore, resides on the surface of the sphere. The electron escape kinetic energy is, therefore, set equal to the coulomb potential energy of the electron at the cluster sphere surface

$$K_{esc} = \frac{(Q+1)e^2}{r} \tag{5.35}$$

This model assumes that the electron energy distribution function is Maxwellian at all times. This is not strictly correct since the majority of the free streaming electrons will come from the hot tail of the Maxwellian. It will take a finite time for the energy distribution to thermalize and repopulate the distribution with the most energetic electrons. Consequently, our treatment will overestimate the rate of free streaming. However, we find that the charge buildup on the cluster is not very important in determining the expansion dynamics of large clusters. Only when small clusters (< 50 Å) are considered does the free streaming become important.

Whether the expansion is through hydrodynamic forces or coulomb forces, the expansion of the cluster will be quite rapid once significant heating has taken place. It is clear from this analysis, however, that large clusters will expand more slowly than small

clusters. Thus larger clusters, in general, are superior for absorption since they will hold together longer during heating by the laser pulse.

V.3.D Electron-Ion Thermalization in the Cluster

The laser energy is deposited primarily into the electrons in the cluster. This energy can be coupled to the cluster ions in two ways. The hydrodynamic expansion discussed above accelerates the ions radially. At the same time, coulomb collisions of the electrons will transfer thermal energy to the ions. This equilibration rate can be written as [178]

$$\left.\frac{\partial T_e}{\partial t}\right|_{eq} = -\frac{T_e - T_i}{\tau_{eq}} \tag{5.36}$$

The electron-ion equilibration time is given by [178]

$$\tau_{eq} = \frac{3 m_e m_i}{8\sqrt{2\pi} n_i Z^2 e^4 \ln\Lambda}\left(\frac{kT_e}{m_e} + \frac{kT_i}{m_i}\right)^{3/2} \tag{5.37}$$

For a cluster with Z = 8 and an electron temperature of 1 keV, (with cold ions) this equilibration time is approximately 30 ps. Therefore, this is relatively unimportant on the time scale of the cluster heating by the laser pulse. The predominate mechanism for coupling energy from the electrons to the ions is through the radial expansion.

V.4 Numerical Modeling of the Laser-Cluster Interaction

To explore the interplay of the various processes described in the previous section a numerical code that solves for the cluster parameters subject to these processes has been developed. This code self consistently solves the time dependence of the ionization stages

of the cluster atoms and the respective electron and ion densities by numerically integrating the ionization rates of eqs. (3.26), (5.3) and (5.9). These processes are calculated by assuming that the electric field inside the cluster is shielded according to eq. (5.12). The cluster radius is found using eq. (5.23). The heat deposition of the laser into the cluster is found using equation (5.15) with appropriately chosen collision frequencies as a function of cluster plasma conditions. The electron temperature is calculated using this heat deposition rate, the electron cooling associated with the cluster expansion, given by eq. (5.26), and the transfer of energy to the ions, given by eq. (5.36). Finally, the time dependence of the charge build-up on the cluster is found from eq. (5.33) and the pressure used in eq. (5.23) is adjusted accordingly.

Since the experimental data are largely dependent on the electron temperature of the underdense plasma that results after the clusters have expanded, we calculate the electron temperature by including not only the random thermal energy the electrons retain with respect to the spherical cluster after expansion, but we also include the average of the radial expansion velocity. We assume that after expansion, the electrons interact with the electrons from other clusters and the directed radial velocity of the electrons is reconverted into random thermal energy through electron-electron collisions in the underdense bulk plasma. Thus, we calculate the cluster parameters until the density of the ions in the cluster has dropped by expansion of the cluster to a value that is characteristic of the bulk underdense plasma. Since we have assumed a uniform expansion by the cluster, the electron radial velocity linearly increases from zero as the radial position increases in the cluster. The electron energy is therefore found by averaging over the cluster sphere and is given by

$$\langle K \rangle = \frac{3}{2} kT_e + \frac{3}{10} m_e \, \mathrm{v}_{expand}{}^2 \tag{5.38}$$

An example of cluster parameters for one calculation is shown in figure V.4. This calculation is for a 100 Å diameter Ar cluster (initial density = 1.8 x 10^{22} cm^{-3}) irradiated

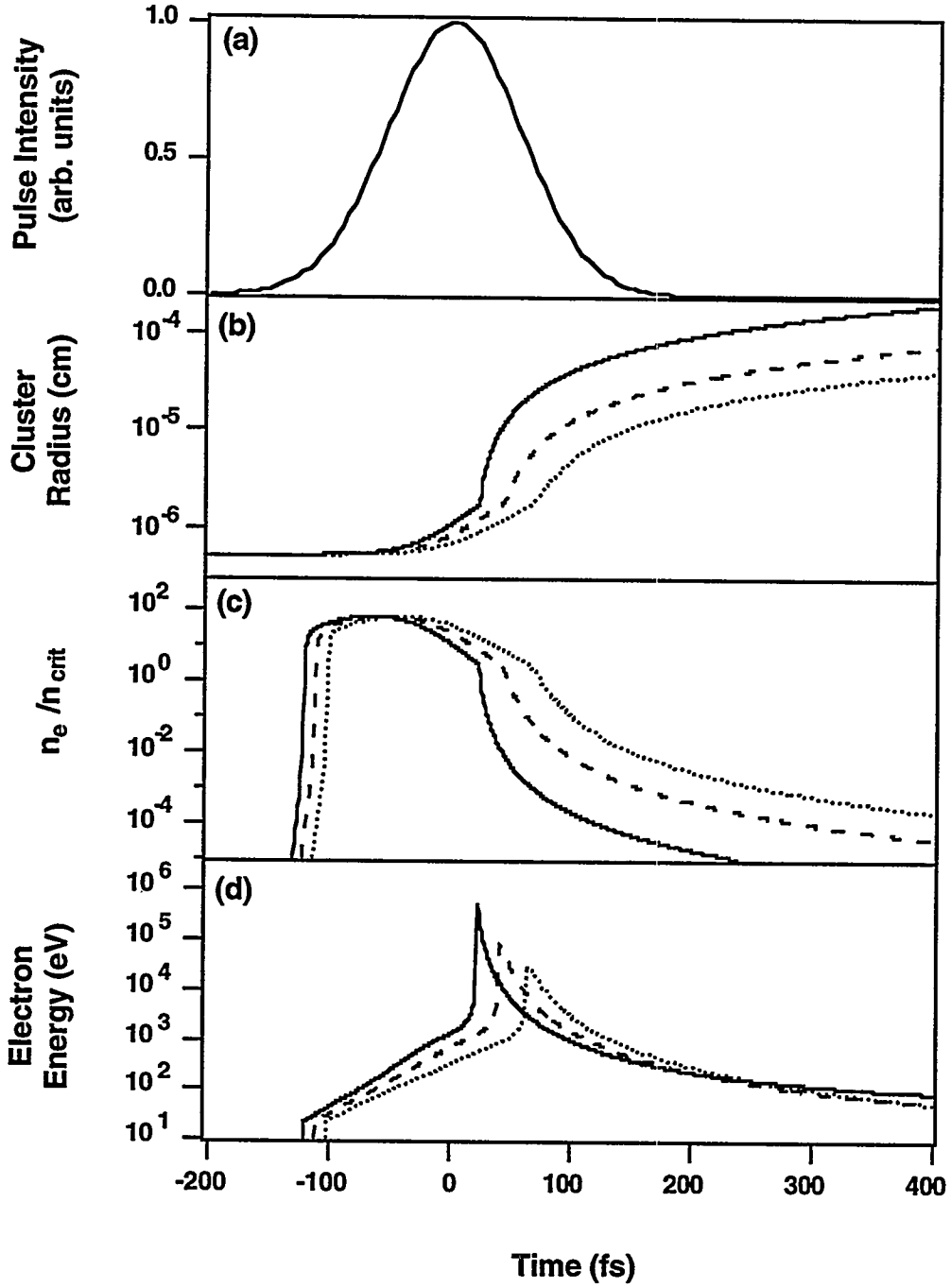

Figure V.4: Simulation results for a 100 Å Ar cluster subject to a 130 fs, 825 nm laser pulse with three different peak intensities, 0.5 x 10^{16} W/cm^2 (dotted line), 1.0 x 10^{16} W/cm^2 (dashed line), and 2.0 x 10^{16} W/cm^2 (solid line). **(a)** Pulse intensity profile. **(b)** Cluster radius. **(c)** Cluster electron density. **(d)** Electron energy.

by a 130 fs pulse (FWHM) with a wavelength of 825 nm and peak intensities of 0.5, 1.0, and 2.0 x 10^{16} W/cm^2. Figure V.4a shows the laser pulse profile. Figure V.4b shows the radius of the cluster as a function of time, figure V.4c shows the electron density and figure V.4d shows the average electron energy (defined by eq. (5.38)) as a function of time.

Initially the electron density rises rapidly from zero during the leading edge of the laser pulse due to the onset of tunnel ionization. This occurs early in the laser pulse when the intensity is approximately 2 x 10^{14} W/cm^2. This rate is then quenched since the electric field is shielded by the formation of a high density plasma in the cluster. The plasma begins to slowly heat and expand. At this point, the dominant ionization mechanism becomes the collisional ionization. The electron temperature rises to a few hundred eV accelerating the cluster expansion rate. When the electron density has dropped due to expansion to a value such that $n_e / n_{crit} = 3$, the field is enhanced and the electron energy jumps. This gives rise to the "spikes" in the electron temperature seen in figure V.4d. The rapid increase in temperature is followed by an accelerated rate of expansion and the electron energy drops as the electrons give some of their energy to the much more massive ions in the expansion process. After the pulse has passed the electrons retain about 500-2000 eV of energy.

This calculation illustrates the importance of the cluster expansion and the electric field enhancement in determining the cluster electron heating. The phenomena of increased laser energy absorption when $n_e / n_{crit} = 3$ is essentially equivalent to the well known fact that the laser absorption, when a laser illuminates a solid, occurs predominately at the point in the electron density profile where $n_e \sim n_{crit}$ [95]. With an electron density higher than n_{crit} the field is shielded, lowering the net heating rate. This is exactly the case in the cluster, however, the exact location of the resonance has shifted to $3n_{crit}$ due to the geometry of the plasma. From this analysis we see that the cluster expansion is actually quite important in determining the electron temperatures attainable

since it is the passage of the cluster density through the region of $n_e \sim 3n_{crit}$ that produces the majority of laser energy deposition.

We also note that under the conditions considered in figure V.4, the coulomb expansion force does not play a significant role in the cluster dynamics. Figure V.5a compares the calculated radius of the cluster as a function of time for the case when coulomb expansion effects are included with the case when they are neglected (laser intensity = 10^{16} W/cm^2). There is only a slight difference (less than a factor of two) between the cluster radii of the two cases. Figure V.5b shows the ratio of the coulomb pressure, eq. (5.28), to that of the electron thermal pressure, eq. (5.25), as a function of time. This quantity never exceeds 0.1 indicating that it is the hydrodynamic pressure which is most important in determining the cluster expansion rate. The calculated fraction of electrons that have left the cluster by free streaming is plotted in figure V.5c. In the early stages of the cluster heating this fraction remains below 10%. Only after the rapid heating resulting from the passage of the cluster resonance does the free streaming rate become significant, with the fraction of electrons exited rising to 25%. By this time, however, the cluster has expanded significantly and the coulomb expansion term remains unimportant.

The situation is somewhat different for smaller clusters. When the cluster is smaller (<50 Å) the free streaming rate is more important (due to the higher surface to volume ratio) and the contribution to the expansion by the coulomb expansion is the dominant term. In a sense, this means that small clusters expand like large molecules in an intense laser field, by a coulomb explosion, while large clusters behave in a manner characteristic of a plasma.

The most striking aspect of these calculations is that they indicate that electron temperatures > 1000 eV are achievable when large clusters are illuminated by pulses with peak intensity >10^{16} W/cm^2. Figure V.6 shows the calculated electron temperature (defined as 2/3 x eq. (5.38)) as a function of peak laser intensity for a 130 fs, 825 nm

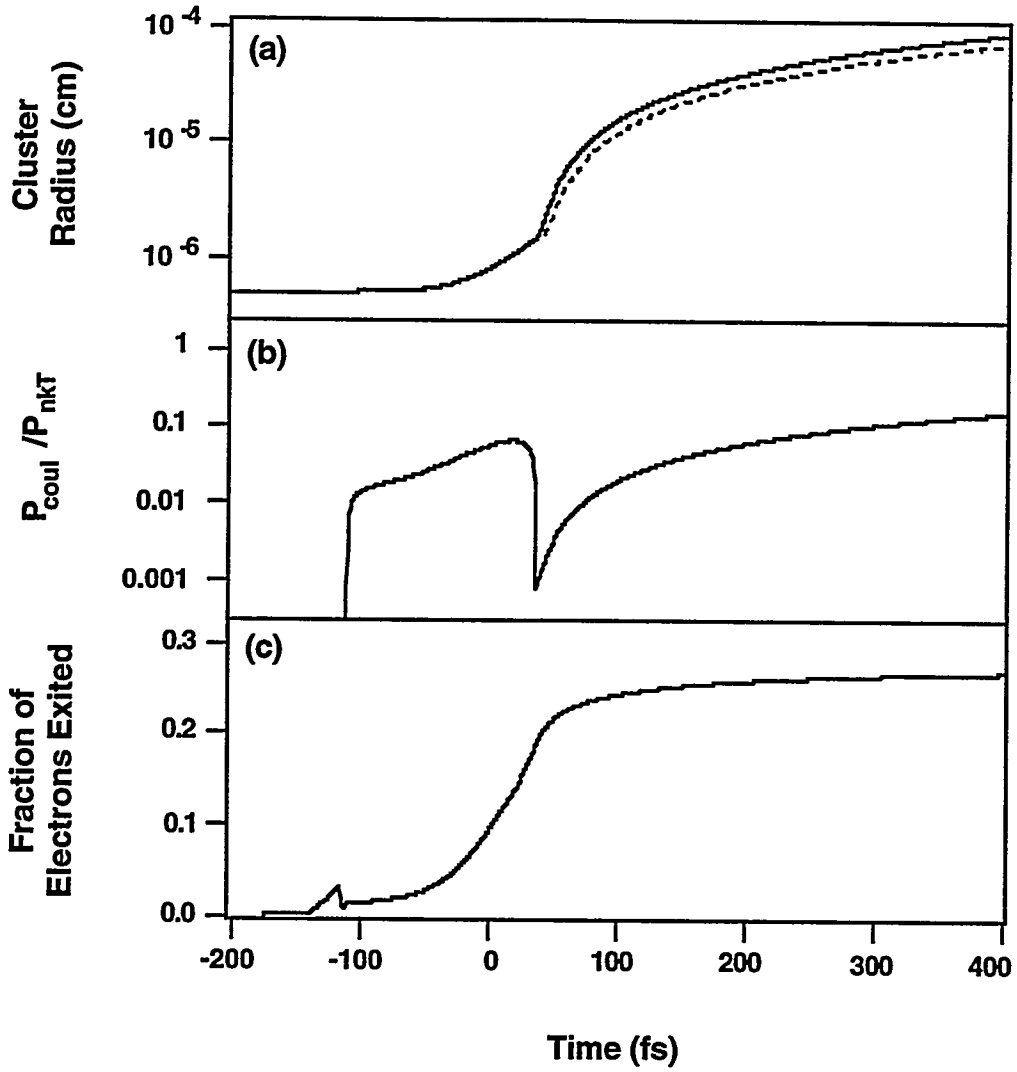

Figure V.5: Simulation results for a 100 Å Ar cluster subject to a 130 fs, 825 nm laser pulse with a peak intensity, 1.0 x 10^{16} W/cm^2. **(a)** Cluster radius without a coulomb expansion force (dashed line) and with the coulomb expansion force (solid line). **(b)** Ratio of the coulomb expansion pressure to the hydrodynamic expansion pressure. **(c)** Fraction of cluster electrons exited the cluster sphere by free streaming.

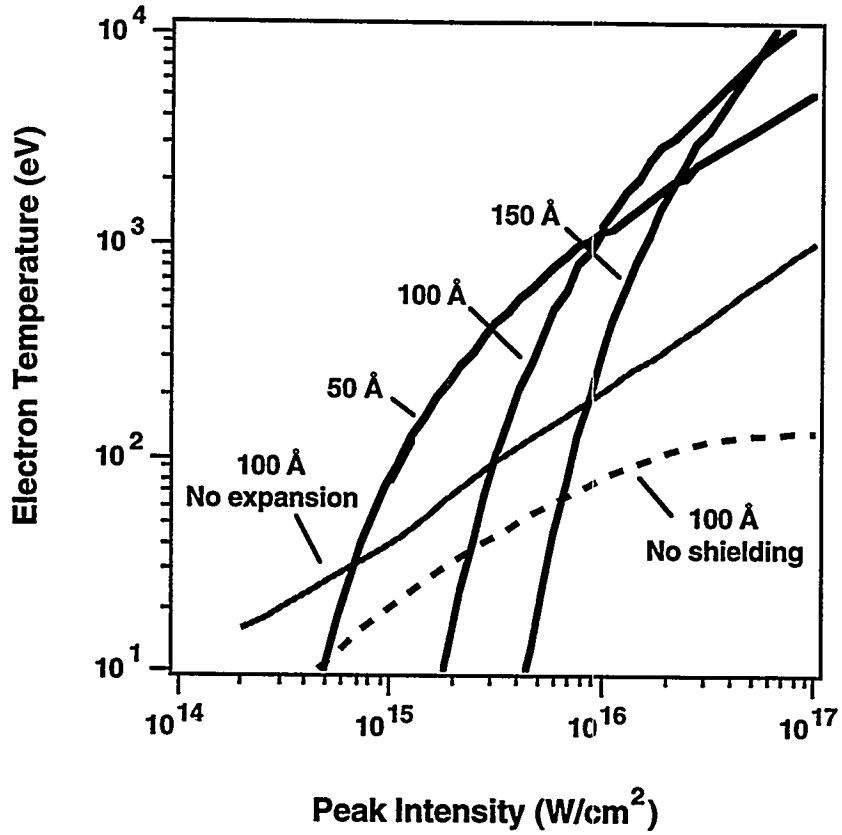

Figure V.6: Calculated electron temperature of electrons in Ar clusters heated by a 130 fs, 825 nm laser after the clusters have expanded as a function of laser peak intensity for a variety of initial cluster diameters.

pulse illuminating an Ar cluster. (The calculated temperatures of clusters of other species are comparable.) The calculated temperature for three different cluster sizes, 50 Å, 100 Å, and 150 Å, is shown. In all cases the electron temperature exceeds 1 keV when the laser pulse intensity is $>10^{16}$ W/cm^2. For comparison, the electron temperature has been calculated for the case when a 100 Å Ar cluster is heated but not allowed to expand. Also shown is the calculation for the case in which the cluster expands but the field inside the cluster is set equal to the field outside the cluster at all times during the laser pulse (no shielding). At the high intensities, these calculated temperatures are significantly lower than for the full calculation. This is because the passage of the cluster through the field

resonance enhances the electron temperature but this phenomena is absent when expansion or shielding is ignored.

At the low intensities, however, the temperature of the cluster is quite low compared to the case in which expansion is ignored. This is because the initial ionization and heating of the clusters is late in the pulse and the cluster does not expand through the field resonance until after the pulse has passed. This trend can be seen in figure 6d where the spike in the electron temperature comes later and is smaller as the intensity is decreased. Note that the smaller cluster size (50 Å) actually exhibits higher temperatures at lower intensity then does the larger clusters. This is due to the more rapid expansion rate of the smaller cluster which brings the cluster plasma into resonance during the laser pulse at a lower intensity.

This analysis suggests that an optimum cluster size might exist for optimum heating. The calculated electron temperature after expansion of Ar clusters as a function of initial cluster diameter is shown in figure V.7 for two intensities, 5×10^{15} and 1×10^{16} W/cm^2. The electron temperature exhibits a broad maximum and peaks at around 70 Å for 1×10^{16} W/cm^2. Small clusters remain relatively cold due to their rapid expansion which moves the cluster plasma through resonance rapidly. Large clusters, on the other hand, do not expand rapidly enough to come into resonance during the 130 fs laser pulse.

The high electron temperatures that are achieved in the cluster during the laser pulse also give rise to rapid electron collisional ionization. Consequently, high charge states can be created in the cluster before it disassembles. Figure V.8a shows the calculated fractional populations of Ar ions from Ar^{5+} to Ar^{11+} as a function of time in a 100 Å Ar cluster irradiated by a pulse with an intensity of 1×10^{16} W/cm^2. Under these conditions it is the thermal ionization that dominates the ionization dynamics. The threshold for significant tunnel ionization for these charge species (defined as the peak intensity at which $\int W_{tun} dt = 1$) is 6×10^{15}, 9×10^{15}, 2×10^{16}, 3×10^{16}, 1×10^{18}, 2×10^{18}, and 3×10^{18} W/cm^2 respectively. As can be seen in figure V.8, the dominate

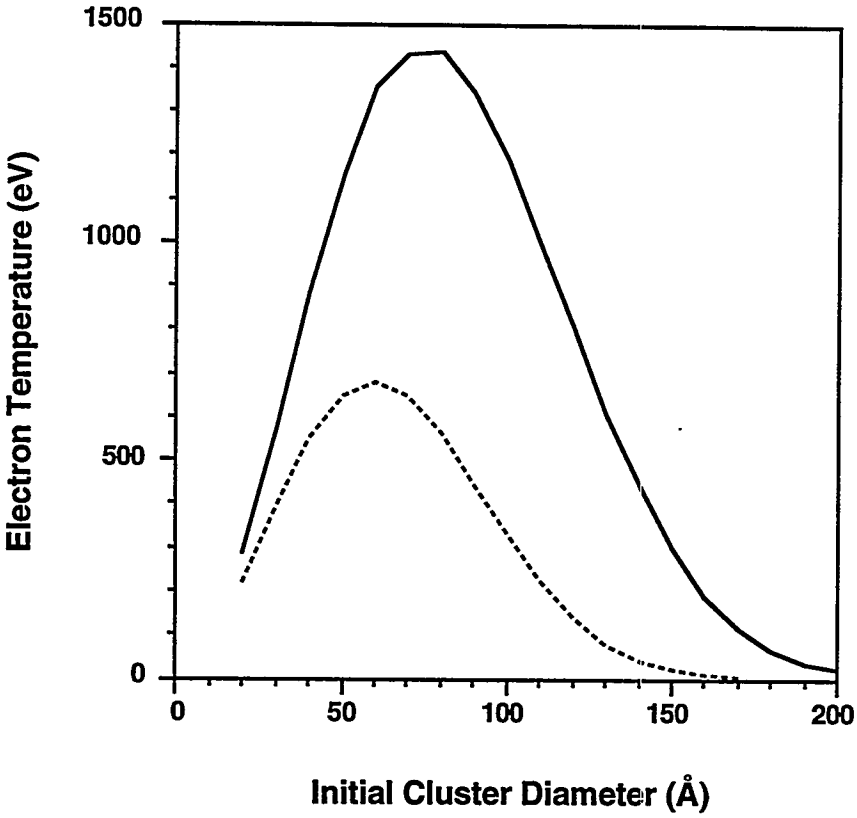

Figure V.7: Calculated electron temperature of electrons in Ar clusters heated by a 130 fs 825 nm laser with a peak intensity of 5.0 x 10^{15} W/cm^2 (dashed line), and 1.0 x 10^{16} W/cm^2 (solid line) after the clusters have expanded, as a function of the initial cluster size.

charge species created in the cluster plasma are Ar^{8+}, Ar^{9+}, and Ar^{10+}. A peak intensity of 100 times higher than used in the simulation would be required to access these charge states by tunnel ionization. Due to the rapid drop in density as the cluster expands the ionization rate drops and these charge states are effectively "frozen-in" in the underdense plasma that results after the clusters expand. Calculations of krypton exhibit similar behavior with somewhat higher charge states accessed under similar conditions. Figure V.8b shows the ionization fraction time histories for Kr^{8+} to Kr^{14+} for a 100 Å Kr cluster illuminated by a an intensity of 1 x 10^{16} W/cm^2. Here the dominate charge states created are Kr^{11+}, Kr^{12+}, Kr^{13+}, and Kr^{14+}. To tunnel ionize to these charge states requires 3 x 10^{17}, 5 x 10^{17}, 6 x 10^{17}, and 8 x 10^{17} W/cm^2 respectively. Furthermore, the high charge

(a)

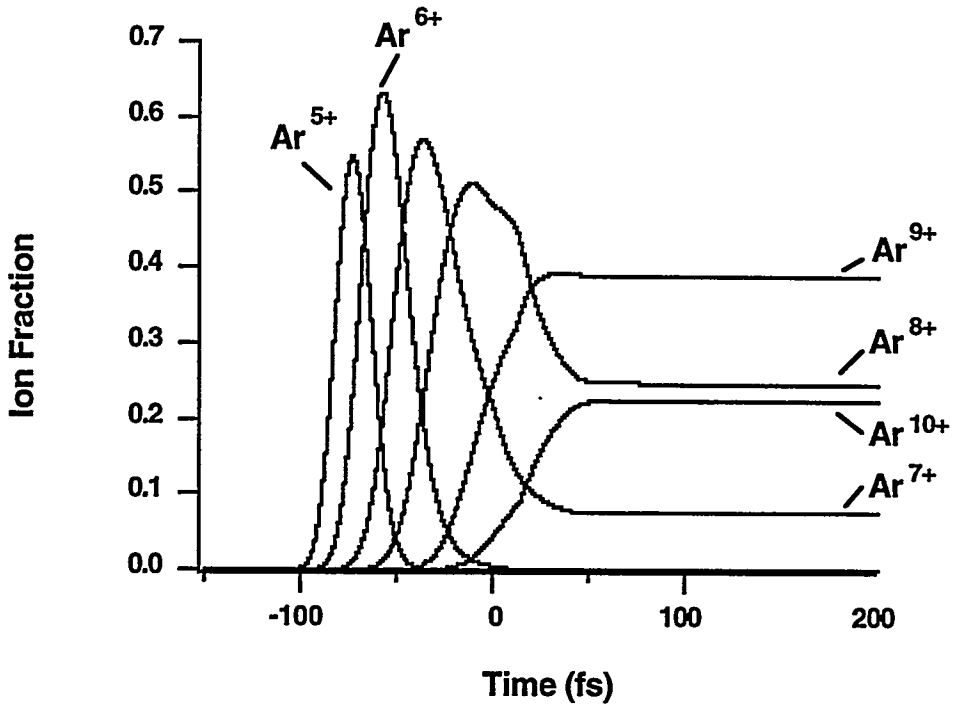

(b)

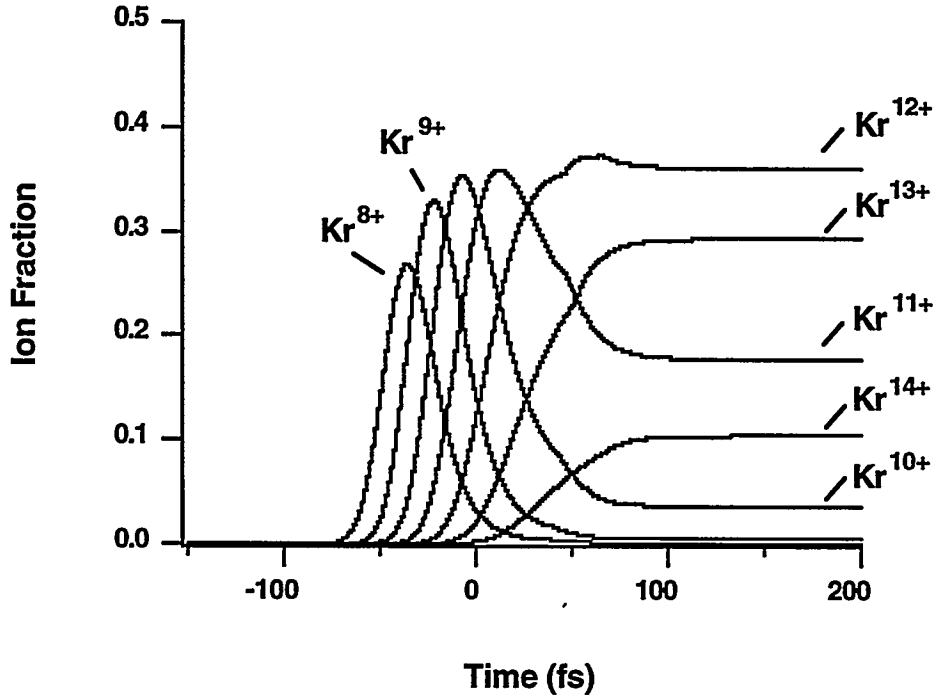

Figure V.8: Calculated fractional populations of **(a)** Ar ions from Ar^{5+} to Ar^{11+} and **(b)** Kr ions from Kr^{8+} to Kr^{14+} as a function of time in a 100 Å clusters irradiated by a pulse with an intensity of 1.0×10^{16} W/cm^2.

states produced in the cluster, with ionization potentials > 200 eV, can be produced at relatively low intensity.

In light of these computational results it is interesting to consider the heating of clusters when compared to heating of solids. The primary difference between the heating of the clusters considered in this work and the heating of a solid target by an intense laser pulse is that the heating of a solid is accompanied by conductive cooling of the hot plasma into the cold, bulk substrate by conductive and free streaming cooling [137]. Heating of the cluster is not hindered by this cooling and might, therefore, be expected to reach temperatures in excess of that for solid targets under similar conditions. As mentioned, the heating in a solid is predominantly at the critical surface. The expansion of the small clusters serves to bring the electron density into a region around the critical density for all the electrons in the plasma for a brief period of time. Consequently, the absorption of the laser light by the clusters should be comparable if not superior to that of a sold for these reasons. Experimental investigation described below confirms this.

The experimental investigations, however, typically observe x-ray emission from the plasma on a time scale longer than we have considered in these calculations (≥ 10 ps). Consequently, we also need to consider the dynamics of the underdense plasma to derive information about the temperature and charge state production in the clusters from the experimental data.

V.5 Properties of an Underdense Plasma Heated by Laser Irradiation of Clusters

After the clusters expand, the properties of the plasma are quite different. The plasma that is created by the passage of the laser pulse through the gas jet will cool and decay on a time scale that is much longer than the expansion time scale of the clusters. If

the laser confocal parameter is longer than the width of the gas jet flow, the resulting plasma is roughly cylindrical with a radial dimension that is roughly that of the laser focus (typically ~ 25 - 50 μm). To compare the calculations to experiments and to evaluate the cluster plasma as a potential source of soft x-rays, it is necessary to evaluate the mechanisms for x-ray production and cooling of the hot, low density plasma.

V.5.A X-Ray Emission Mechanisms

The characteristics of the gaseous plasma that results after the irradiation of the clusters include a high state of ionization (Z > 8 for Ar, Z > 10 for Kr) and high electron temperatures (100 - 1000 eV). The plasma emission will be dominated by line emission from the resonance lines of the ions. The excited states of these ions can populated in two ways. First, collisional excitation of the hot electrons can excite the transitions in these ions provided that the electron temperature is sufficiently high for this to be important. Second, recombination of free electrons into the upper states of the ions will be followed by a collisional-radiative cascade into the upper levels of strong radiative transitions[70]. This will be important after the plasma has cooled from its initial hot state by expansion and conductive cooling.

The collisional excitation of the resonance transitions in most ions can be estimated from the simple formula[55]

$$W_{nn'} = \frac{1.6\times10^{-5} f_{nn'}\langle\bar{g}\rangle}{\Delta E\sqrt{kT_e}}\exp[-\Delta E / kT_e] \qquad (\mathrm{cm^3 s^{-1}}) \qquad (5.39)$$

where $f_{nn'}$ is the transition oscillator strength, $\langle\bar{g}\rangle$ is the Gaunt factor (≈ 0.2 for ions[55]), and ΔE is the transition energy (in eV). From this relation we see that this excitation rate is significant only when $kT_e \sim \Delta E$. For the transitions of energies that are comparable to the initial temperature, this excitation mechanism will only be significant in the early stages of the plasma decay before the plasma has cooled significantly. After the

plasma has cooled, three body recombination becomes important. The rate of recombination can be estimated from the simple formula[197]:

$$W_{recom} = n_e \frac{4\pi\sqrt{2\pi}}{9} \frac{Z^3 e^{10}}{m_e^{1/2}(kT_e)^{9/2}} \ln\Lambda \tag{5.40}$$

This rate strongly favors colder plasma because of its strong $(kT_e)^{-9/2}$ scaling.

V.5.B Plasma Cooling Mechanisms

To calculate the time scale for the x-ray emission from a plasma that has been heated by the presence of clusters we have developed a code that calculates the cooling and expansion of the cylindrical plasma. This calculation includes the effects of both adiabatic expansion by the plasma as well as the conductive cooling of the hot plasma at the center of the laser focus to the colder plasma surrounding the center. The hydrodynamics of the plasma are determined by solving the ion fluid equations subject to electron fluid pressure gradients:

$$\frac{\partial n_i}{\partial t} = -u\frac{\partial n_i}{\partial r} - \frac{n_i u}{r} - n_i \frac{\partial u}{\partial r} \tag{5.41}$$

$$\frac{\partial u}{\partial t} = -u\frac{\partial u}{\partial r} - \frac{ZkT_e}{n_e m_i}\frac{\partial n_e}{\partial r} - \frac{Z}{m_i}k\frac{\partial T_e}{\partial r} \tag{5.42}$$

where u is the radial ion fluid velocity.

The cooling of the electrons in the plasma is determined by the adiabatic expansion as well as the magnitude of the heat flow from conduction, q. The electron temperature, which is a function of both r and t, in the plasma cylinder is therefore found from the equation:

$$\frac{\partial T_e}{\partial t} = -\frac{4T_e}{3r}u + \frac{2}{3n_e}\left(\frac{q}{r} + \frac{\partial q}{\partial r}\right) \tag{5.43}$$

The heat flow, q, is found by using the nonlocal heat flow formula of Luciani et. al. [115]. A nonlocal treatment of the heat flow is required since the classical Spitzer heat flow [177] can exceed the physical heat flux limit of free streaming, $q_{fs} = n_e kT_e \mathrm{v}_{kT}$ when the temperature gradients become large. We use the same simplification to the formula of Luciani et. al. [115] for cylindrical coordinates as used by Djaoui and Offenberger [52]. The heat flow q, is then given by the formula

$$q(r) = \int \frac{1}{64\lambda(r')} q_{Spitz}(r') \exp\left[-\frac{1}{32 n_e(r')\lambda(r')} \int_{-\infty}^{\infty} n_e(r'')dr'' \right] \max(1, r'/r) dr' \quad (5.44)$$

Here $q_{Spitz} = -\kappa \nabla(kT_e)$ is the classical Spitzer heat flow (κ is the classical thermal conductivity for a plasma.) [177]. Djaoui and Offenberger found that the use of this formula in the calculation of underdense plasma temperatures heated by a 12 ps KrF laser was in good agreement with experimental measurements of the temperature.

In general, we find that the conductive cooling of the plasmas produced by the irradiation of clusters is important in the early stages of the cooling since high temperatures (~ 1000 eV) can be generated at the laser pulse peak. After this initial cooling, however, the time scale for cooling is dominated by the hydrodynamic expansion of the plasma. To illustrate this we show the temperature and electron density radial profiles for an Ar gas that has been heated by the irradiation clusters in figure V.9. The initial ion density is taken to be 1 x 10^{18} cm^{-3}. The initial temperature and electron density profile are found by assuming a focused spot of 100 μm in diameter ($1/e^2$) and using the calculation of the electron temperature and ionization state as a function of laser intensity for 100 Å Ar clusters detailed in the previous section. A peak temperature of 1 keV is assumed (corresponding to a peak intensity of about 10^{16} W/cm^2). As can be seen from figure V.9, the center of the temperature distribution drops rapidly between the passage of the laser pulse (t = 0) and 500 ps. After this time, the temperature cools from the expansion of the plasma on a longer time scale (> 1 ns). This calculation suggests that

(a)

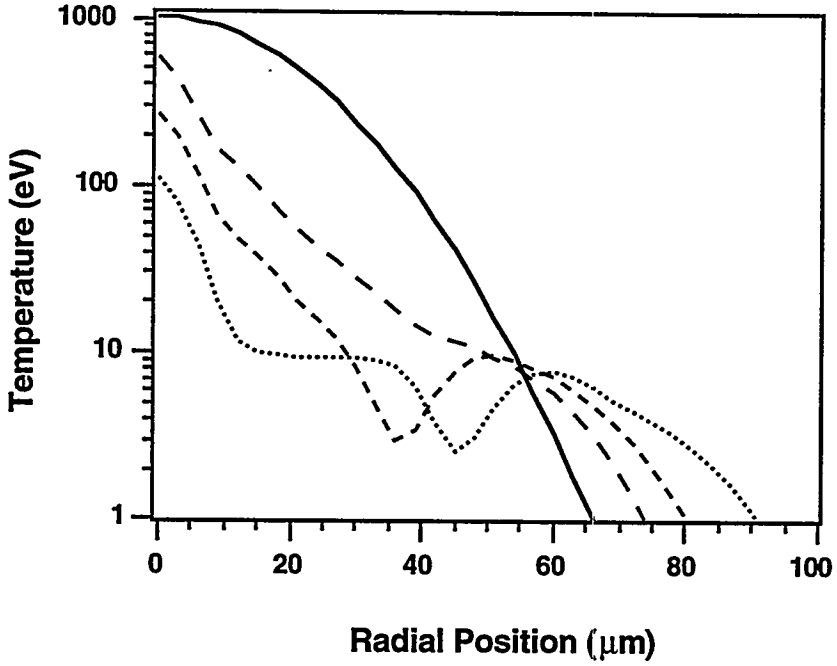

(b)

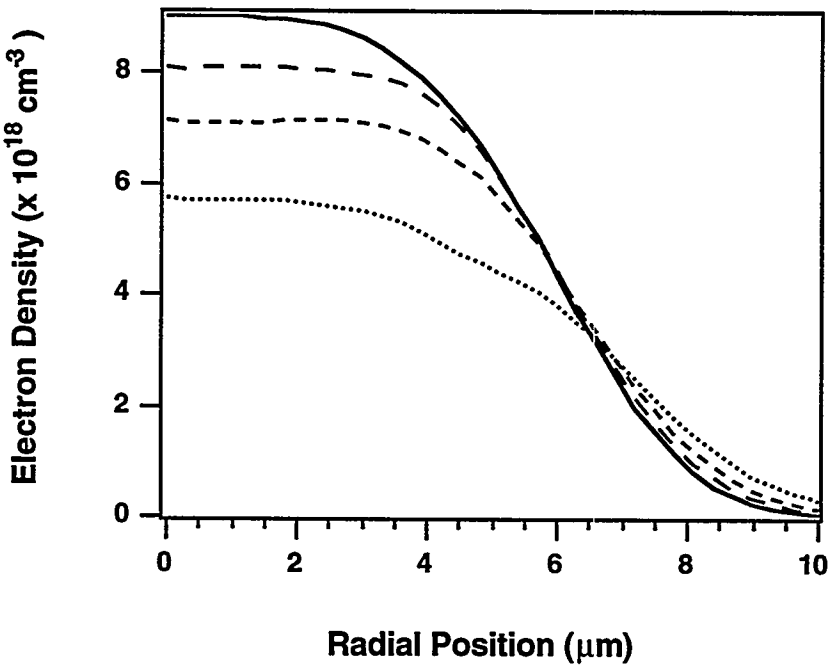

Figure V.9: Calculated temperature **(a)** and electron density **(b)** radial profiles for an underdense Ar gas of initial ion density 1 x 10^{18} cm^{-3} that has been heated by the irradiation of clusters. The times are t = 0 (solid line), t = 500 ps (long dashed line), t = 1 ns (short dashed line), and t = 2 ns (dotted line).

"warm" plasmas (>100 eV) persist in the plasma for many ns (> 1-2 ns). This is due primarily to the slow rate of cooling associated with the low density plasma. This is in direct contrast to the time scales of short pulse heated solid target plasmas which typically cool in a < 10 ps time scale by conduction. The plasma heated by clusters can emit x-rays for many ns after the laser has passed.

To determine the actual histories of the ion charge states, it is necessary to solve for the kinetics of the plasma. We do this by using the plasma kinetics code, FLY, of R. W. Lee [106]. This code solves for the time dependent populations of levels and charge states in the plasma by solving rate equations. The time history of the temperature and density from the hydrodynamics of the plasma is utilized in this code to estimate the actual yields and time history of the x-ray emission from a plasma heated by illumination of the clusters. The results of these calculations will be discussed in the context of the experimental results below.

V.6 Experimental Apparatus

We have detailed the theory of the interaction of an intense, 100 fs laser with atomic clusters in a gas jet and shown how these interactions can give rise to high charge state production, hot plasmas, and short wavelength generation. To explore these predictions we have conducted a number of experiments. In these experiments, the 130 fs laser pulse from the LiSAF laser is focused into the plume of the gas jet and the plasma produced is characterized by performing spectroscopy on the resulting x-ray emission. The laser pulses are focused into a vacuum chamber with an f/25 MgF_2 lens (f = 100 cm). The focal spot of this lens contains roughly half of the energy in a 30 μm x 50 μm spot. The remainder of the energy is surrounds the central spot in a disk of approximately 120 μm in diameter. The spot can be roughly approximated for purposes of modeling by a

100 μm diameter $1/e^2$ spot (see figure II.21). The peak intensity is roughly 10^{17} W/cm^2 with 0.5 J of energy focused into the chamber.

The laser is focused into the output of a supersonic gas jet nozzle. The gas jet used in these experiments is our supersonic Laval nozzle that produces atom densities of 0.5 to 5 x 10^{18} atoms/cm^3 for backing pressures of 100 to 900 psi [149]. For all experiments the laser was focused ~ 1mm from the nozzle output, which is 1.4 cm downstream from the jet throat. This jet was chosen because it is predicted to produce large clusters in the heavier noble gases for the backing pressures with which we operate (100-700 psi). We can estimate the expected cluster size by calculating the Hagena parameter, eq. (5.1) for our experimental conditions. The jet throat diameter is 150 μm, α is ~ 5° for our jet nozzle, and T_0 was room temperature (~ 300 K). This parameter varied from ~ 1 x 10^4 to 1 x 10^5 for Ar and ~ 2 x 10^4 to 2 x 10^5 for Kr backing the gas jet with 100 to 600 psi respectively. It never exceeded 5000 for Ne and He in our experiments.

A schematic of the set-up used to diagnose the plasmas formed from the irradiation

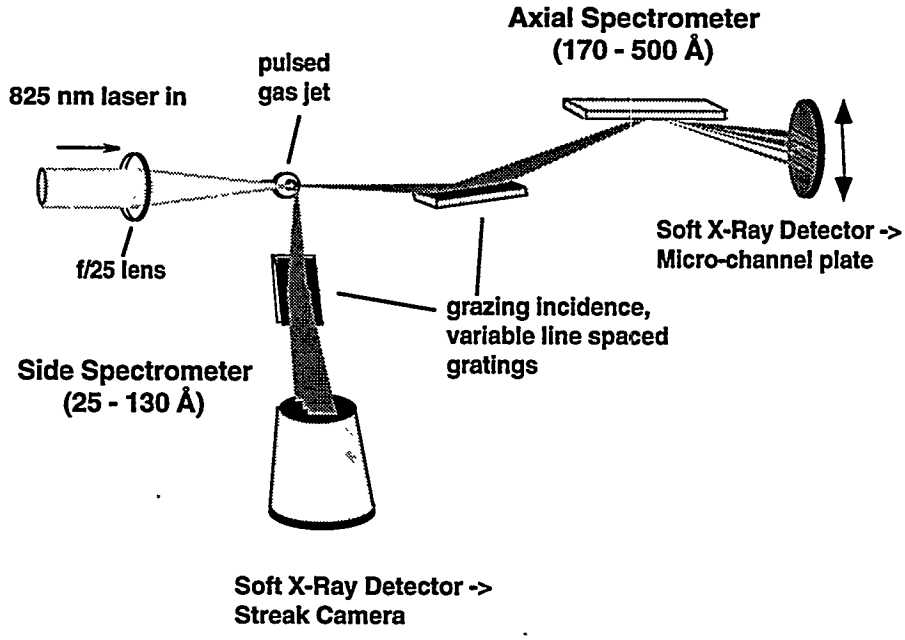

Figure V.10: Schematic of the experimental set-up showing the soft x-ray diagnostics.

of gas from our jet is shown in figure V.10. Through the use of two spectrometers, we were able to monitor the soft x-ray emission from 500 Å down to 25 Å on each shot. Both spectrometers utilize variable line spaced gold gratings with a grove density of 1200 lines/mm. One spectrometer monitored x-ray emission along the laser axis in the 500 - 170 Å spectral region. A 2000 Å Al filter blocked the direct laser light for this spectrometer. The second spectrometer monitored emission from 170 Å down to 25 Å in a direction perpendicular to the laser propagation. The spectral resolution of both spectrometers was roughly $\Delta\lambda/\lambda \sim 10^{-2}$. Either spectrometer could be mounted with either a CsI coated, 45 mm micro-channel plate detector, which yielded simultaneous information on the spectrum and the angular distribution of the radiation on each shot, (similar to the harmonics data of chapter IV), or a Kentech x-ray streak camera, which permitted simultaneous measurement of the spectrum and the time history of the x-ray radiation. The temporal resolution of the streak camera was limited to approximately 10 ps.

An example of data characteristic of the illumination with a laser intensity of $\sim 10^{16}$ W/cm^2 of the gas jet when it is backed with 300 psi of Ar is shown in figure V.11. Figure V.11a shows the time integrated emission of the x-rays in the 500 - 170 Å wavelength range in the axial direction. Very strong line emission is observed from the plasma over the entire spectral region. The high order harmonics generated by the laser are easily distinguishable from the plasma emission, which emits into all directions. A time resolved measurement under the same experimental conditions is shown in figure V.11b. The 23rd, 25th, and 27th harmonics are clearly visible as temporal spikes at the time the laser traverses the gas. The line emission over the entire spectral range, on the other hand, lasts for many ns after the laser produces the plasma.

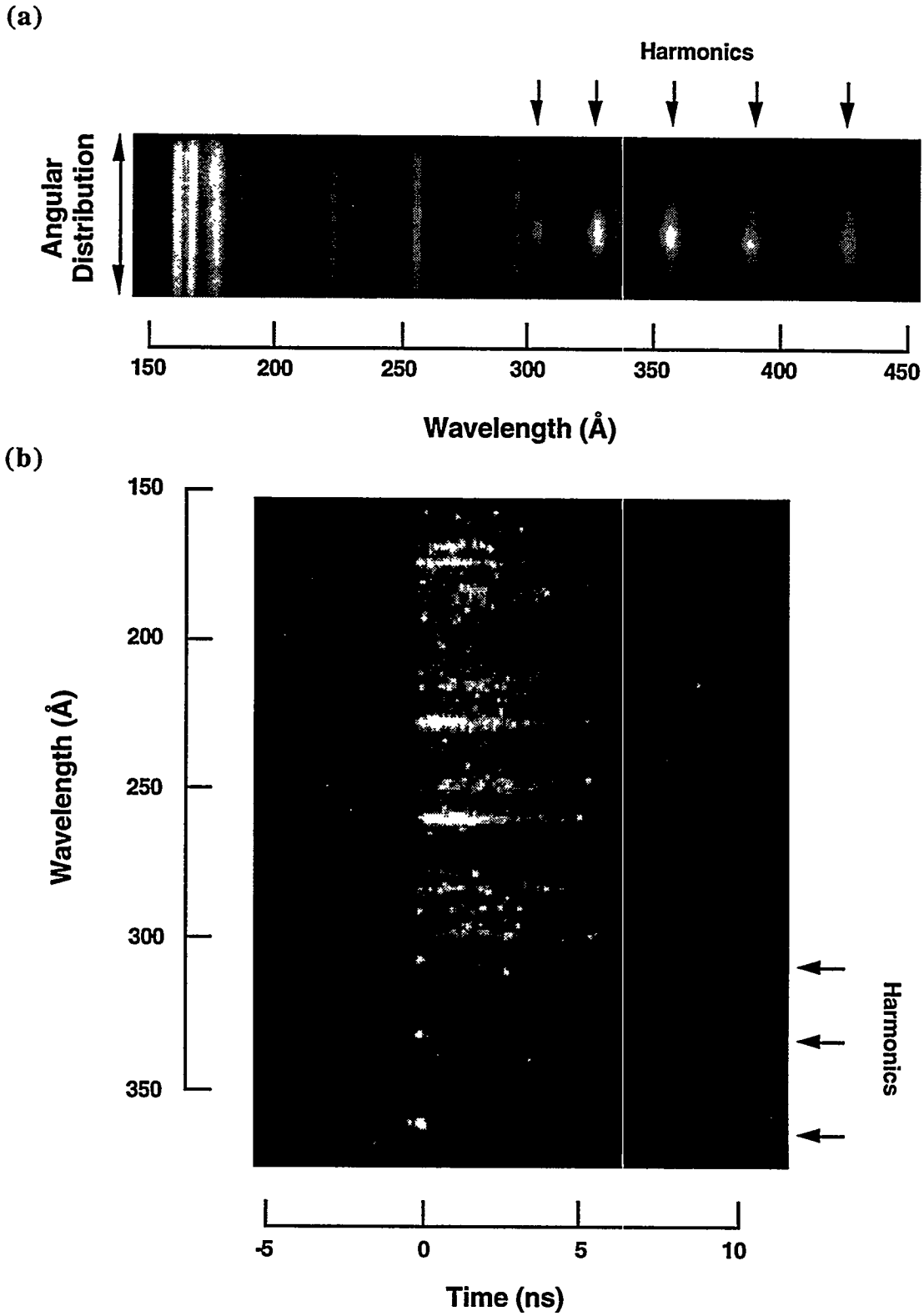

Figure V.11: Raw data in the 150 - 400 Å range with the gas jet backed with 300 psi of Ar and a intensity of ~10^{16} W/cm^2. **(a)** Spatially resolved spectra. **(b)** Time resolved spectra.

V.7 Cluster Condensation Onset and Size Measurement By Rayleigh Scattering

V.7.A Experimental Set-Up

To experimentally confirm the presence of large clusters in our gas jet we used a technique of Rayleigh scattering [2, 89]. The experimental set-up for these measurements is shown in figure V.12. To do this, the gas jet was probed with light from the LiSAF laser that had been frequency doubled in a 3 mm thick crystal of KDP. The second harmonic was used because of the strong dependence of the Rayleigh scattering cross section with decreasing wavelength. The gas at the output of the jet nozzle was irradiated with approximately 1 mJ of 412 nm light. The centerline of the 1 mm diameter flow was probed with a beam of approximately 400 μm in diameter. The 90° scattered light was collected with a lens and imaged onto the face of a photomultiplier tube.

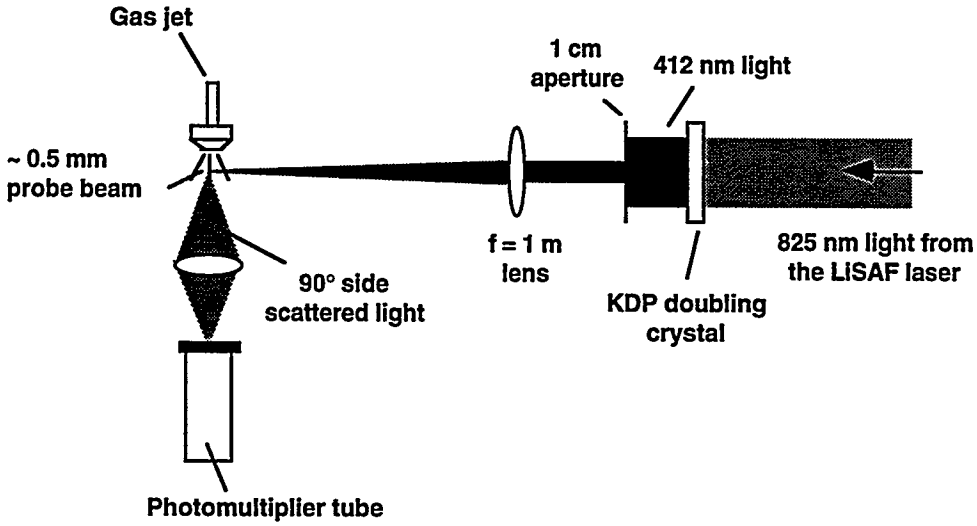

Figure V.12: Experimental set-up for Rayleigh scatter measurements of cluster condensation in the gas jet.

V.7.B Rayleigh Scattering Results in the Mach 8 Gas Jet

Figure V.13a shows the scattered light signal as a function of backing pressure for He, Ne, Ar, and Kr. No significant light scattering above the noise level is observed from either Ne or He over the range of backing pressures studied. The scattered light signal from the expansion of Ar and Kr, however, exhibits nonlinear growth with backing pressure, rising above the noise with as little as 150 psi backing the gas jet. This measurement qualitatively confirms our assertion that large clusters are formed in our gas jet when it is backed with Ar or Kr, and that neither He or Ne cluster to any significant degree in the jet.

The nonlinear dependence of the scattered signal is consistent with accepted scaling for the cluster size with backing pressure. Previous measurements of clustering in Ar have shown that the mean number of atoms per cluster, N_C, scales roughly like, $N_c \sim p^2$ [59]. Since the scattering cross section is given by the classical Rayleigh scattering cross section formula:

$$\frac{d\sigma}{d\Omega} = 2\pi \frac{r^6}{\lambda^4}\left(\frac{n^2-1}{n^2+2}\right) \tag{5.45}$$

then we can say that the observed scattered signal should scale as $S \sim n_{clust} N_c^2$ where n_{clust} is the density of clusters in the gas jet. In the regime of large cluster formation (i. e. when $\Gamma^* > 1000$) we can assume that 100% of the atoms have condensed into clusters [16]. This implies that if n_0 is the average gas density, which is presumably linear with backing pressure, then $n_{clust} = n_0 / N_c$. Thus, the scattered signal at the highest backing pressures should scale as $S \sim p^3$. This is in good agreement with the rise in the Ar data which scales as $S_{Ar} \sim p^{3.3}$, as well as the Kr data which grows as $S_{Kr} \sim p^{3.5}$.

We can make a quantitative estimate for the cluster size based on the scattered light levels. Using eq. (5.45) and an extrapolation estimate for the refractive index of the cluster, the signal levels at the highest backing pressure (600 psi) suggest that the mean cluster size is 2 - 10 x 10^4 atoms for Ar and 1 - 5 x 10^5 atoms for Kr. Based on the

(a)

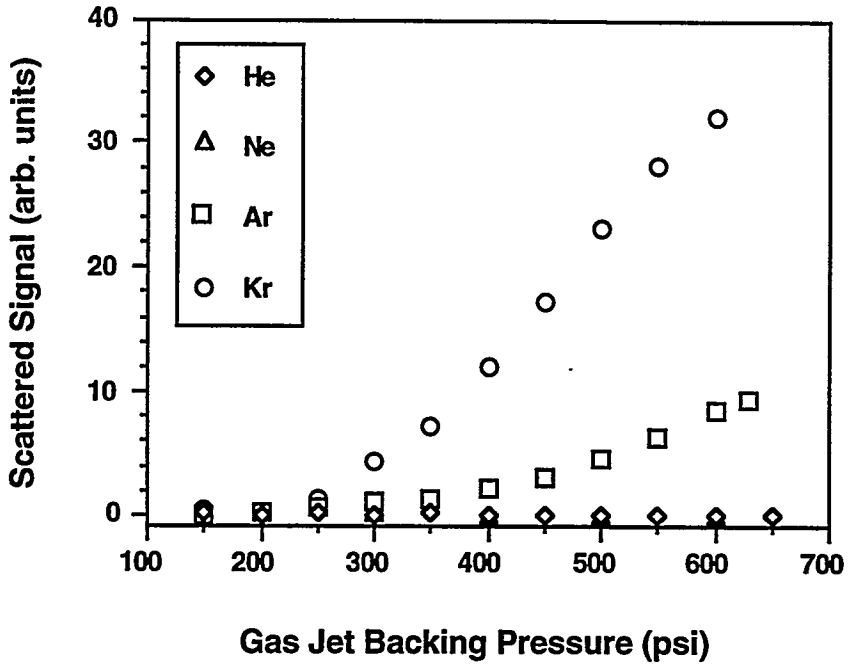

(b)

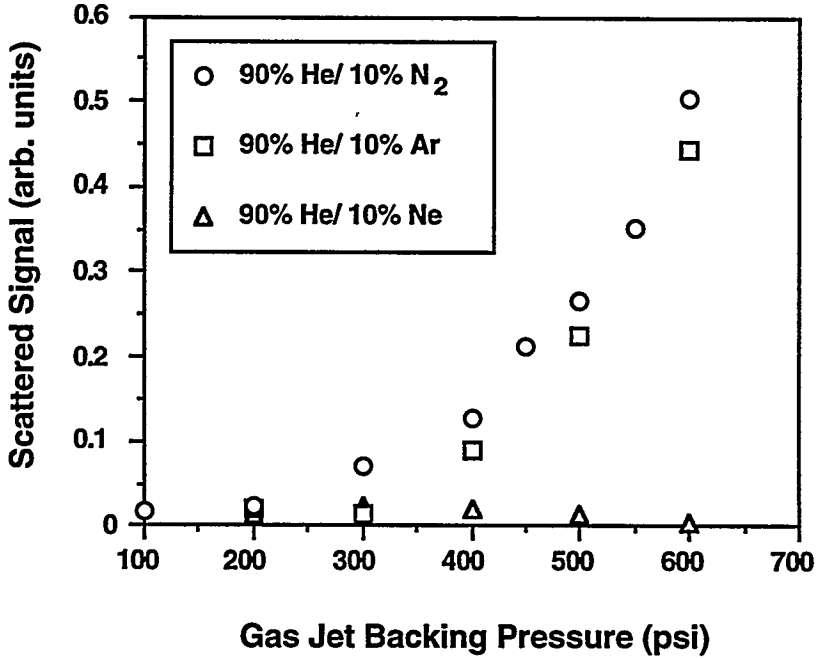

Figure V.13: Measured Rayleigh scattered light signal as a function of backing pressure for **(a)** pure He, Ne, Ar, and Kr, and **(b)** 10% mixtures of Ar, N_2 and Ne with He.

experiment noise level we can put an approximate upper bound on the size of Ne or He clusters of < 3000 atoms per cluster, if clusters exist at all in the gas jet. Estimates for the Hagena parameter for helium, suggest that no clusters should form for the backing pressures studied. The size of the possible error in these estimates is large due to a lack of detailed knowledge about the average gas density as well as possible errors in estimating the throughput of our scattered light detection set-up. Nonetheless, this corresponds to an accuracy in estimating the cluster diameter of better then ±40%.

For experiments to be described below, we wished to form clusters of the heavier gases while mixed with helium. It is well known that the use of He as a carrier gas will significantly enhance the formation of clusters of heavier atoms in a gas expansion, while the He does not itself undergo clustering [195]. We confirmed the presence of clusters in small fractional mixtures of a heavy gas (fraction ≤ 0.1) with a majority of He. Even though the partial pressure for the clustering gases was low, we observe cluster formation in mixtures that contain a heavier gas, as shown in figure V.13b. In this data, the 10% mixtures of Ar and N_2 exhibit nonlinear growth in the scattered Rayleigh signal while a 10% mixture of Ne with He shows no evidence for cluster formation.

V.8 Soft X-Ray Emission Characteristics of the Various Gases

With a confirmation of the presence of large clusters in our experiments we can examine the nature of the x-ray emission from the various gases upon irradiation of the laser. Figure V.14 compares the time integrated soft x-ray emission from Ne, N_2, Ar, and Kr. In all cases the gas jet was backed with 500 psi of pressure and the incident peak laser intensity was 2×10^{16} W/cm^2. The only signal in Ne comes from very weak harmonics. The signal from the other gases, all gases forming large clusters, exhibit

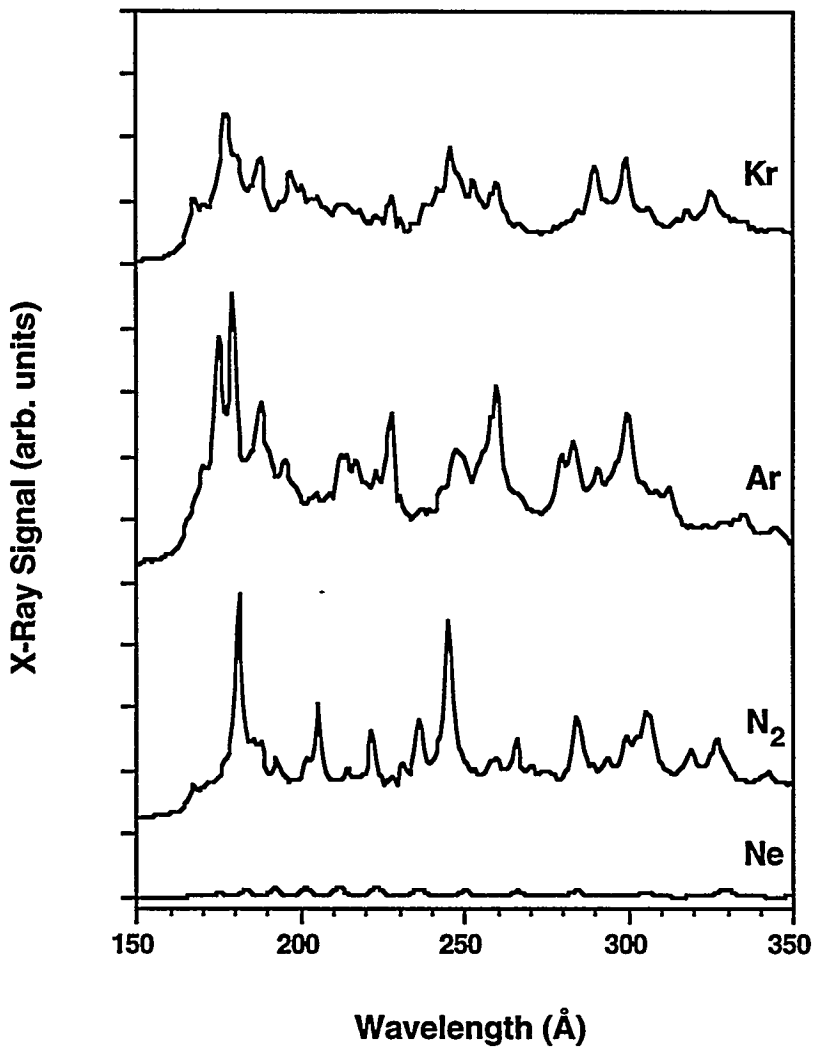

Figure V.14: Time integrated soft x-ray emission from Ne, N_2, Ar, and Kr with a peak laser intensity of 2×10^{16} W/cm^2 and a gas jet backing pressure of 500 psi.

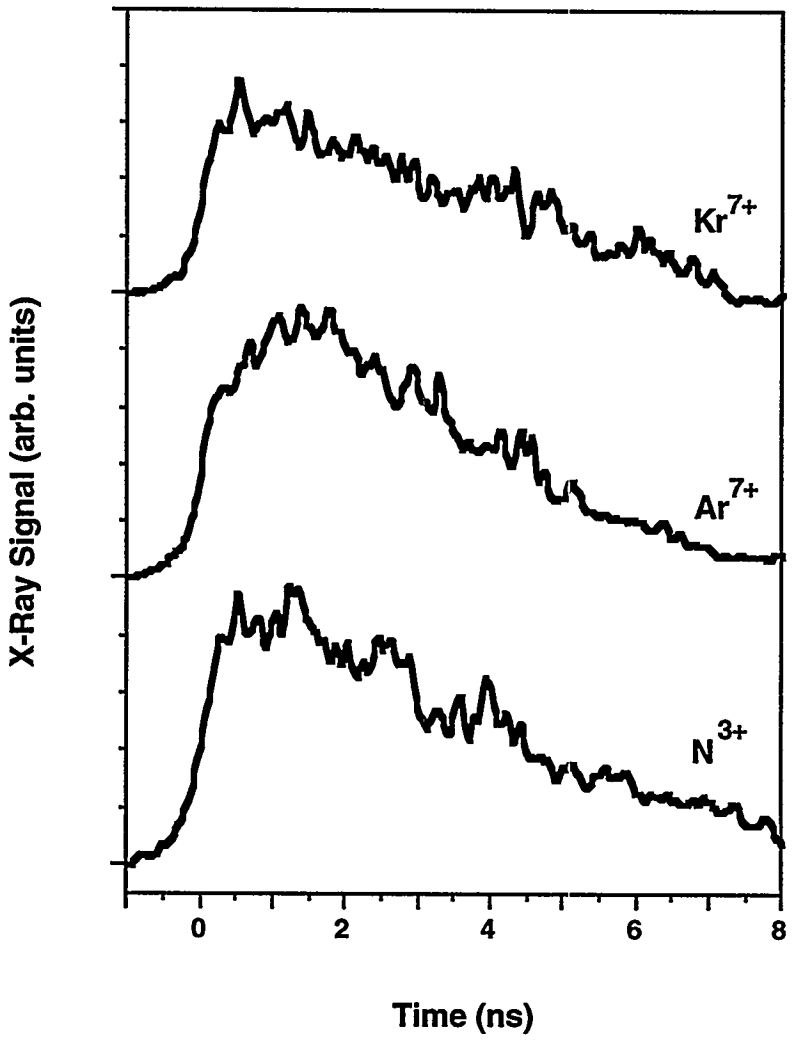

Figure V.15: Time histories of select lines from around 180 Å from the spectral data of figure V.14.

strong line emission across the spectrum. The lines in N_2 originate predominately from N^{3+}, N^{4+}, N^{5+}, the lines in Ar originate from Ar^{5+}, Ar^{6+}, and Ar^{7+}, and the lines in Kr are largely from Kr^{5+}, Kr^{6+}, and Kr^{7+} [88]. In general the signal levels from these three gases is roughly equivalent in this range.

The time histories of select lines from these gases under identical conditions are compared in figure V.15. Here we compare the N^{3+} 4p->2s line at 189 Å, the Ar^{7+} 4d->3p line at 179 Å, and the strong feature in Kr at around 175 Å which probably arises from Kr^{7+}. The time resolution of this data is approximately 280 ps. For all three gases the emission starts promptly after the passage of the laser through the plasma and the decay times are roughly the same for all three species, between 6 and 8 ns. This behavior is qualitatively consistent with our supposition that these high charge states are produced during the laser pulse in the cluster. The long decay time is also consistent with the production of a reasonably hot plasma. For example, if we assume that the temperature of the plasma is given by the ATI calculation of figure III.15 ($kT_e \sim 10$ eV), the three-body recombination time for Ar^{7+} according to eq. (5.40) is ~ 100 ps. This is a much faster decay than is observed. These time scales are more consistent with the plasma temperature decay time predicted by the calculations detailed in section V.3.

A more quantitative comparison of the soft-x-ray data can be made by comparing the ratio of the various charge states in the plasma as a function of time. Figure V.16 shows the spectra of the Ar plasma at intervals of 1 ns integrated over a time window of 500 ps in each case. Initially, the strongest emission comes the Ar^{7+} lines. Later, the Ar^{6+} and Ar^{5+} lines come up relative to the Ar^{7+} emission. This confirms the calculation of the cluster ionization under these conditions which indicated that the argon was ionized past the lower charge states with a predominance of Ar charge states of 7+ and higher. The strong emission from the Ar^{7+} at the later times probably comes from the recombination of Ar^{8+} as the plasma cools.

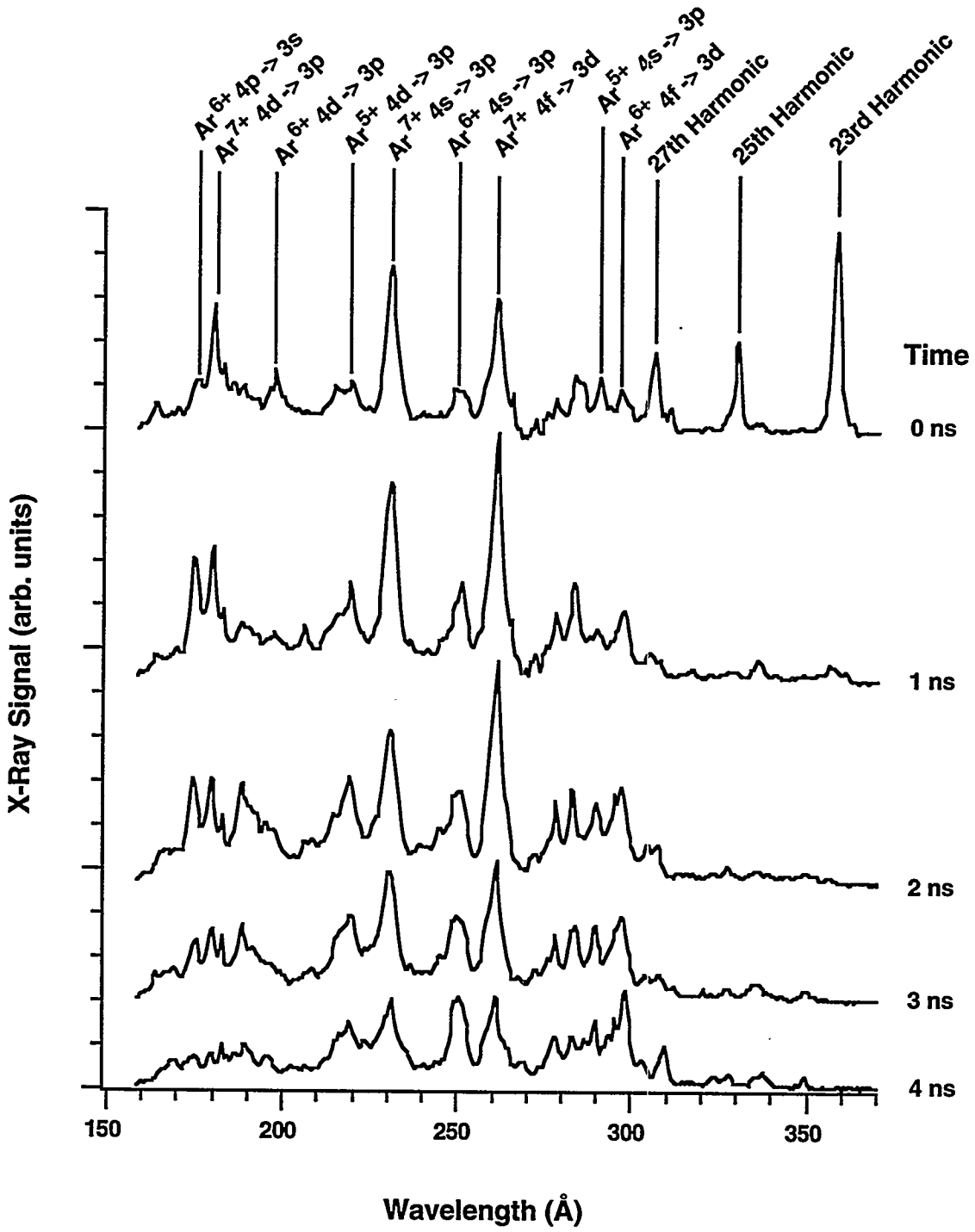

Figure V.16: Spectra of the Ar plasma at intervals of 1 ns integrated over a time window of 500 ps with a peak intensity of 1 x 10^{16} W/cm^2.

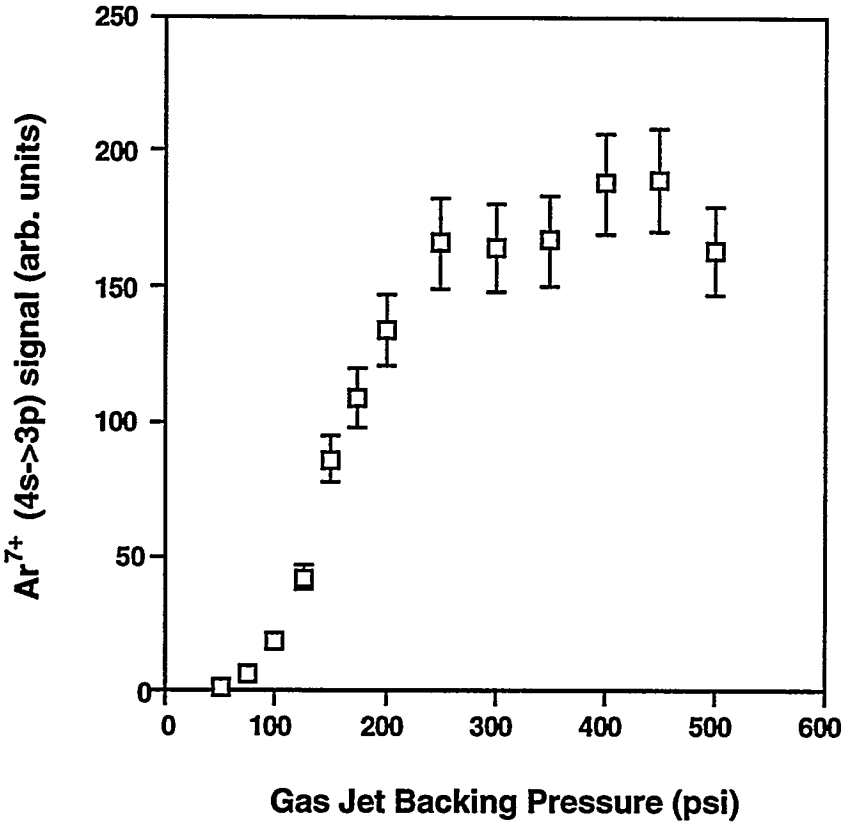

Figure V.17: Measured backing pressure dependence of the Ar^{7+} 4s->3p line at a peak intensity of 10^{16} W/cm^2.

The measured backing pressure dependence of the Ar^{7+} 4s->3p line is shown at a peak intensity of 10^{16} W/cm^2 in figure V.17. The line appears at backing pressures above about 100 psi, coinciding with the observed onset of large cluster formation in argon by the Rayleigh scattering measurements. The signal rises rapidly at first and then rolls over at about 250 psi. This roll-over point corresponds to an estimated cluster diameter of 60-80 Å based on the estimates of the previous section and the measured scattered signal at 250 psi. This may correspond to the optimum size for heating the cluster (see figure V.6) and may explain this roll-over. It is also possible that ionization induced refraction may be clamping the intensity. However, if refraction were the cause, we would not expect such an abrupt change in the signal dependence with backing pressure. The behavior in figure

V.17 seems to be more consistent with a change in the heating conditions of the clusters due to the nonlinear increase in cluster size with increasing backing pressure.

V.9 Helium/Cluster Mixture Emission Characteristics

To more carefully investigate the production of heated electrons by the illumination of the clusters, we have conducted a series of experiments in which a small fraction (0.01 - 0.1) of a gas known to cluster is mixed with He and passed through the gas jet. Since the He does not itself cluster, observation of the intensity of the Lyman series transitions in He^+ allowed us to study the dynamics of the bulk plasma without concern for intra-cluster effects. The presence of the clusters served to absorb laser energy which resulted in a thermal plasma which can then collisionally excite the He levels in the low density "warm" plasma that results after the clusters expand.

V.9.A Lyman α Enhancement with Clusters

Figure V.18 compares the emission spectra of helium for two conditions. The dashed line shows the spectrum when helium alone backs the gas jet. Here the peak intensity is about 3×10^{16} W/cm^2. The intensity required to optically ionize He to He^{2+} is approximately 1.5×10^{16} W/cm^2 with a 130 fs laser pulse. Above this intensity Ly α light will be emitted due to the recombination of electrons into the upper levels of the doubly ionized He. Since no clusters are present a small amount of signal is observed on the He Ly α line resulting from this recombination. The solid line in figure V.18, however, shows the spectrum of the helium when the backing gas contained 1% Ar mixed with the helium. Though the peak intensity is only 3×10^{15} W/cm^2, below the threshold for optically ionizing the helium to the required charge state for recombination, the spectrum exhibits strong emission on the Ly α line as well as the n = 3->1 and n = 4->1

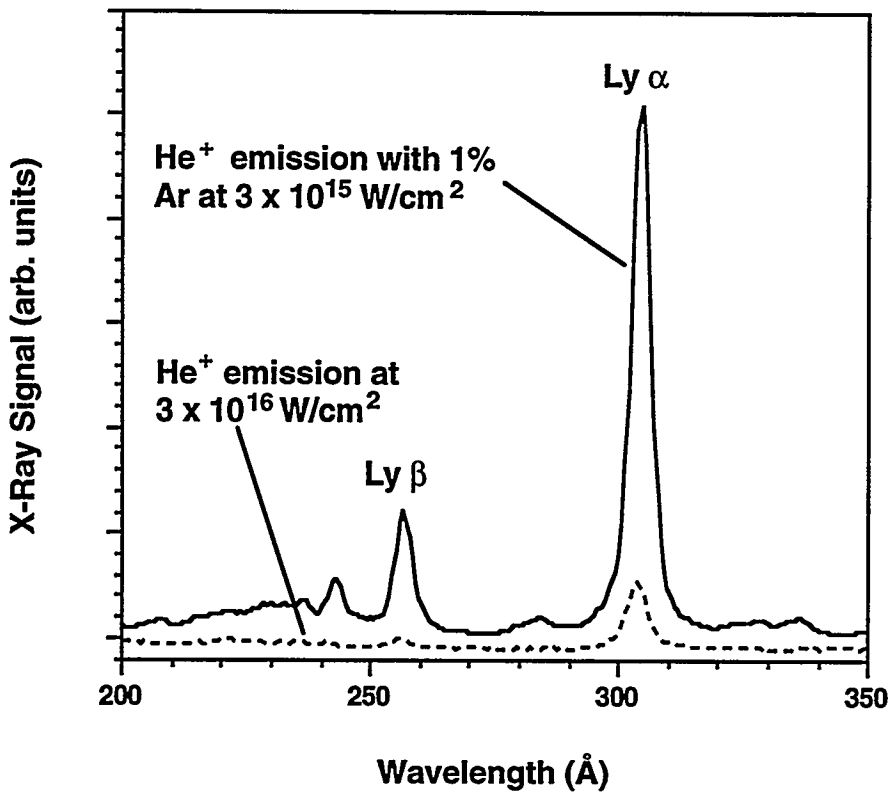

Figure V.18: Emission spectrum with a peak irradiance of 3x 10^{16} W/cm^2 in pure helium (dashed line) compared with the emission spectrum from a 1% Ar/ 99% He mixture irradiated with an intensity of 3x 10^{15} W/cm^2.

transitions. This represents evidence for the presence of plasma temperatures that are sufficient to collisionally ionize the helium to the doubly ionized state.

In figure V.19 the integrated yield on the Ly α line in He is plotted as a function of intensity for a variety of gas mixtures. When a plasma is formed from 100% pure helium we observe a small amount of Ly α light at peak intensities above which the tunneling ionization to He^{2+} begins. Addition of a small fraction of Ne does not significantly change the observed Ly α signal. This is consistent with the fact that large clusters are absent in the He and He/Ne expansions and the small observed signal is due only to direct strong-field ionization by the laser. When a small amount (10%) of Ar, Kr, or N_2 is mixed with the helium, all gases with a strong propensity for forming large clusters, the magnitude of the He Ly α signal is significantly enhanced exceeding the signal of the pure

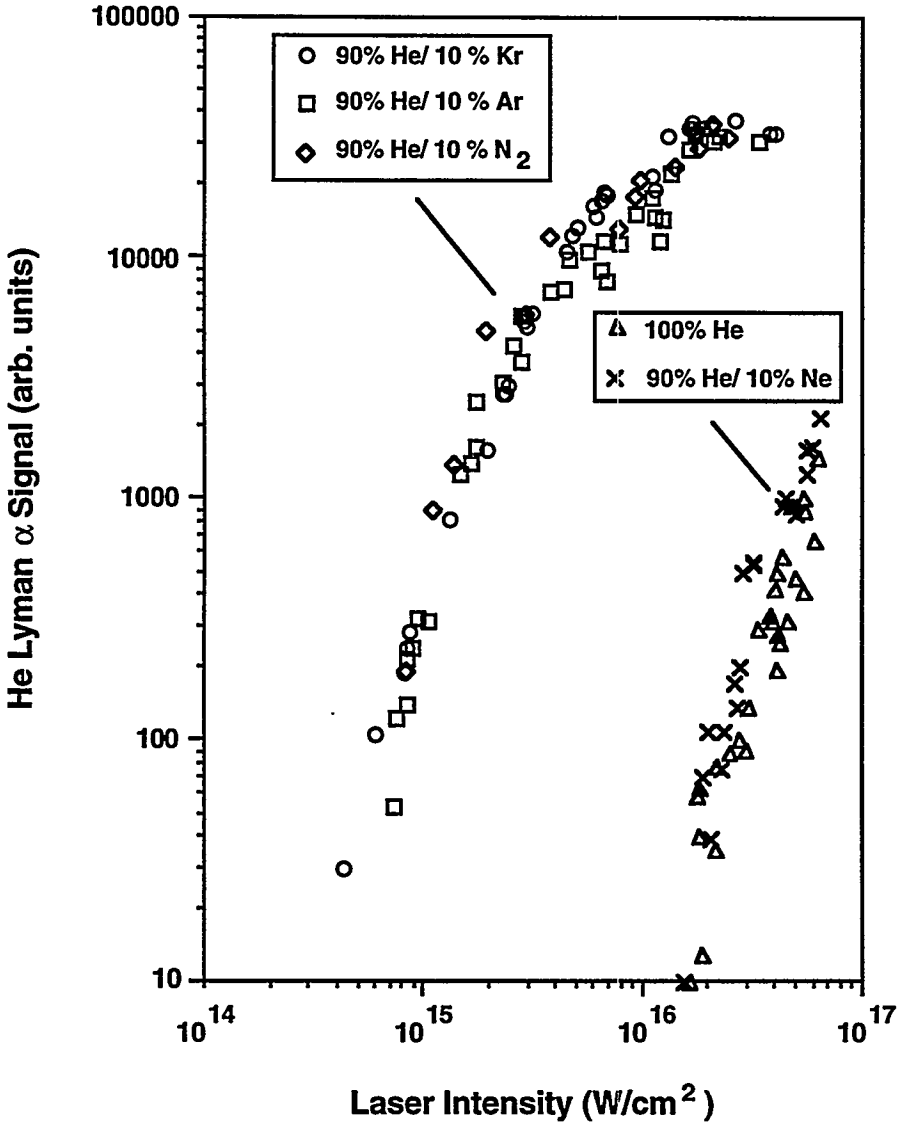

Figure V.19: Integrated yield on the Ly α line at 304 Å in He plotted as a function of intensity for a variety of gas mixtures.

helium by nearly a factor of 100 at the highest intensities. Furthermore, the Ly α signal appears at an intensity that is 20 times lower than the threshold for the production of He^{2+} predicted by tunneling ionization.

V.9.B Lyman α Backing Pressure Dependence

The importance of the clusters is confirmed when we compare the Ly α signal dependencies with gas jet backing pressure for the situations when a dopant gas is added to the helium and when impurity is absent. The Ly α signal emitted as a function of backing pressure for an intensity of 3×10^{16} W/cm^2 when no clustering impurity gas is present in the helium is plotted in figure V.20a, illustrating the linear increase in signal that is expected due to the linear increase in the number of emitters in the focal volume. The Ly α signal exhibits a nonlinear increase when 1% Ar is present in the helium jet that is irradiated by a peak intensity of 3×10^{15} W/cm^2. The signal increases roughly like $\sim p^{3.2}$. This nonlinear increase in signal is probably due to two factors. The production of the Ly α radiation is by collisional mechanisms, and is therefore nonlinearly dependent on the density of the underdense gas. This is contrary to the production of the charge states in the clusters themselves where the collisional mechanisms occur within the solid density of the cluster, a density which, of course, is independent of backing pressure. The rapid rise in Ly α may also be due to the increase of absorption efficiency of the Ar clusters as they grow in size with increasing backing pressure.

V.9.C Lyman α Time History

The difference in the plasma temperature between the optically ionized (pure He) case and the cluster heated case is most dramatically evident in the comparison of the Ly α time decay dynamics. The measured time histories over the first 50 ns after the laser pulse for both cases are shown in figure V.21. (The time the laser passes through though the gas jet can be determined by the appearance time of the harmonics.) These plots represent

(a)

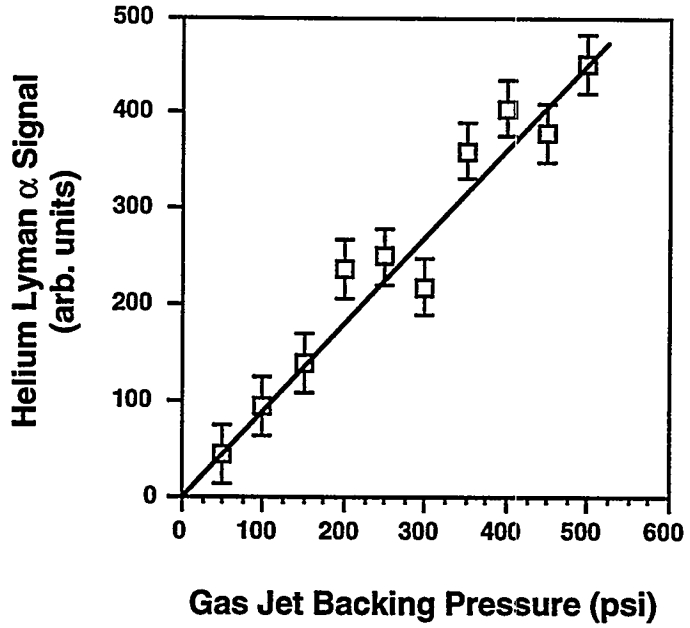

(b)

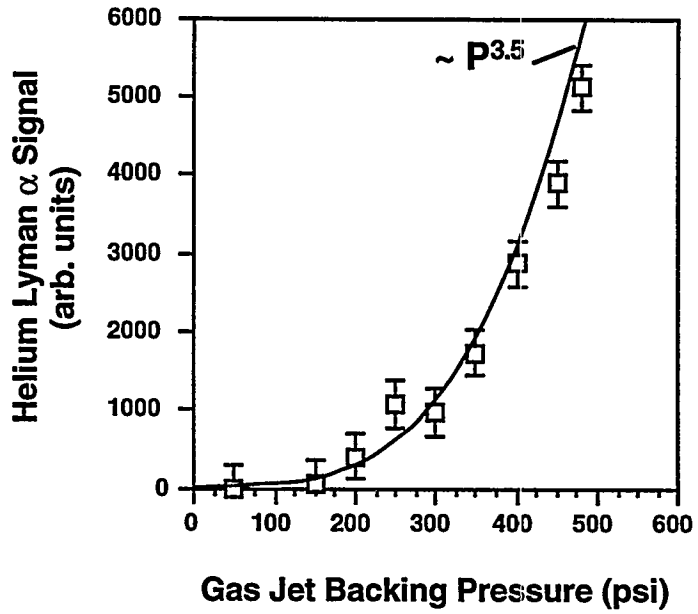

Figure V.20: Ly α signal emitted as a function of backing pressure for **(a)** an intensity of 3 x 10^{16} W/cm^2 in pure He, and **(b)** an intensity of 3 x 10^{15} W/cm^2 in a mixture of 1% Ar and 99% He.

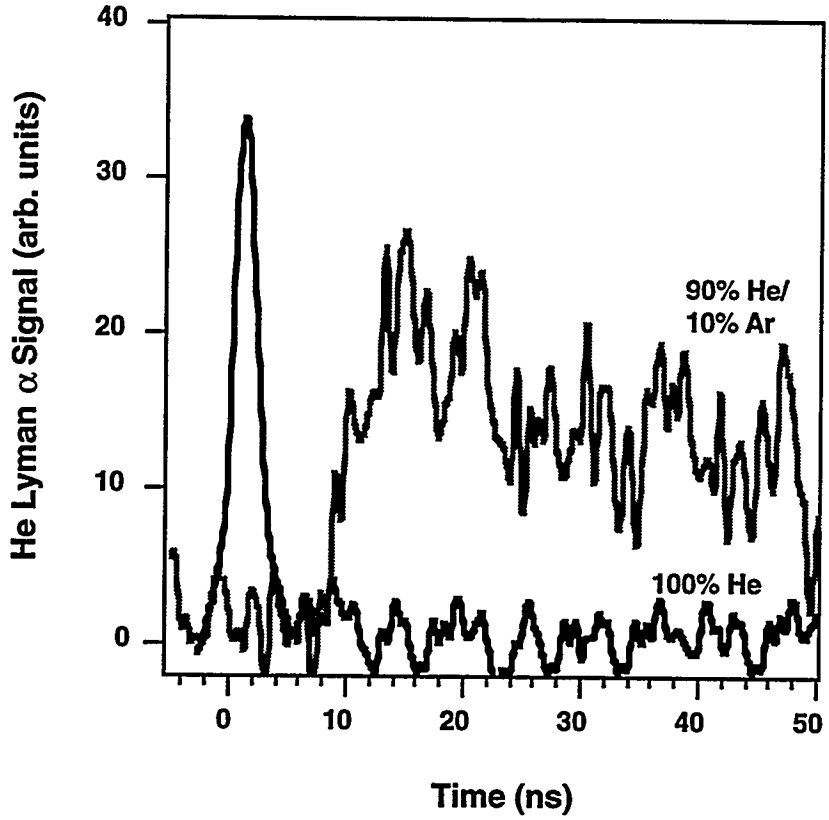

Figure V.21: He Lyman α time history for an intensity of 7 x 10^{16} W/cm^2 in pure He (black line), and an intensity of 6 x 10^{15} W/cm^2 in a mixture of 10% Ar and 90% He (gray line).

an average over ten laser shots. The time history of the helium extends out to >150 ns after the laser. The optically ionized helium (100% He, I = 7 x 10^{16} W/cm^2) exhibits emission immediately (< 1 ns) after creation by the laser followed by a fast (~ 2 ns) fall. The plasma heated by the presence of clusters (10% Ar, I = 6 x 10^{15} W/cm^2) shows no Ly α signal immediately after the laser, due to the fact that the intensity of the laser is sufficient to ionize to He^+ only. The hot electrons from the clusters, however, serve to collisionally ionize the He on a long (~ 10 ns) time scale resulting in Ly α emission on a ~ 100 ns time scale. The slow turn-on of the He line is because of the slow rate of collisional ionization to He^{2+} in the relatively low density of the plasma.

A calculation of the time scale for the population of the n = 2 state in He^+ using the calculated hydrodynamic temperature history in FLY is shown in figure V.22 for the first

15 ns. The solid curve assumes the ATI prediction for the plasma temperature of 40 eV and an initial population of He^{2+} from optical ionization. The calculation reproduces the observed time scale of decay for this case. The dashed line in figure V.22 shows the n=2 population for a plasma with an initial temperature of 250 eV. The calculation shows that the time scale for population of this level is roughly 10 ns, in excellent agreement with the observed data. The population of this level in helium in this case is predominately by collisional ionization of the He^{+} followed by three body recombination. Since the Ar clusters contribute only ~ 30% of the electrons in the plasma, this modeling indicates that the cluster electrons probably have an initial temperature of the order of 500-1000 eV.

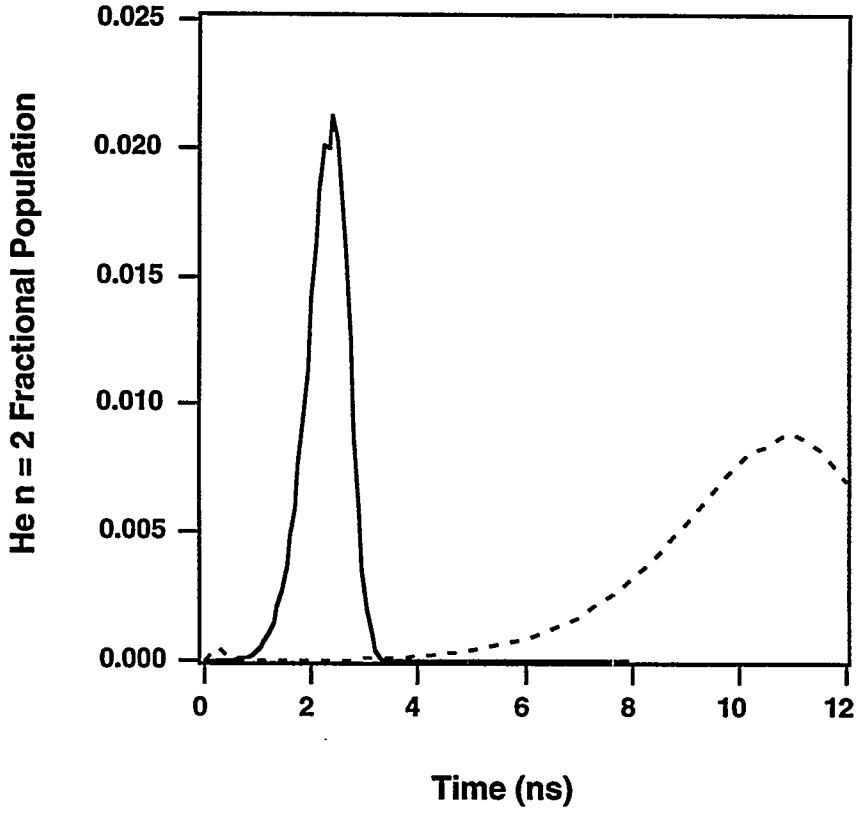

Figure V.22: Calculation of the time scale for the population of the n=2 state in He^{+} for **(a)** an ATI heated plasma (35 eV) an initial stripped He^{2+} ions, and **(b)** a cluster heated plasma (250 eV) with He initially stripped to He^{+}.

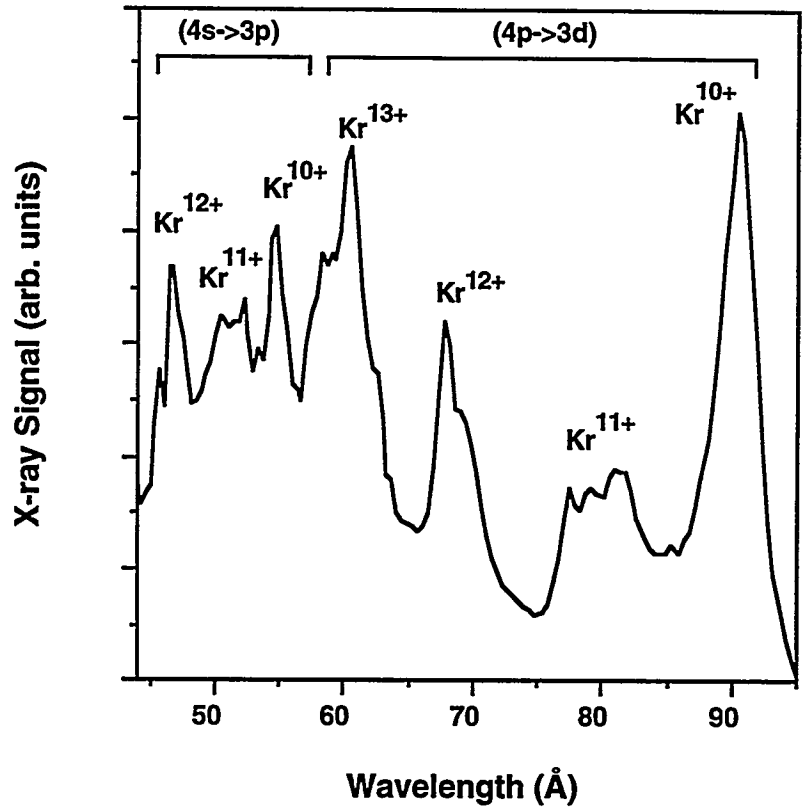

Figure V.23: Time integrated spectrum in Kr with an intensity of 1.5 x 10^{16} W/ cm^2 into the gas jet backed by 500 psi.

V.10 50 - 100 Å Emission in Krypton

The enhanced absorption by clusters also suggests that short wavelength (< 100 Å) x-rays may be produced at relatively modest laser intensity. Figure V.23 shows the time integrated spectrum between 40 and 100Å produced by the laser focused to an intensity of approximately 1.5 x 10^{16} W/cm^2 into the gas jet backed by 500 psi of pure Kr. The spectrum exhibits strong emission from the 4p->3d, and 4s->3p arrays of Kr^{10+}, Kr^{11+}, Kr^{12+}, and Kr^{13+} [17, 60]. Tunnel ionization predicts that intensities of 3, 4, 6 and 8 x10^{17} W/cm^2 respectively are required to produce these states by optical ionization, over an order of magnitude in excess of the actual laser intensity used here.

The observed charge states in Kr agree very well with the predicted ionization stages of the cluster calculations of figure V.8b which shows that under these intensities, ionization in the cluster should produce Kr ionized to 11 - 14+.

Similar to the softer x-ray emission of Kr when large clusters are present in the gas jet target, the emission from these lines is long lived. The time history of the Kr^{10+} 4p->3d line is shown in figure V.24; the streak camera temporal resolution of this data is approximately 280 ps. The radiation from this line is emitted for nearly 3 ns after the laser produces the plasma. The long lifetime is consistent with the long lived emission of the hot, underdense bulk plasma. The actual lifetime of these lines is insensitive to the gas jet backing pressure. The measured decay time of the Kr^{10+} 4p->3d line (defined as the time for the signal to fall to 1/e of its peak value) is plotted as a function of backing pressure for

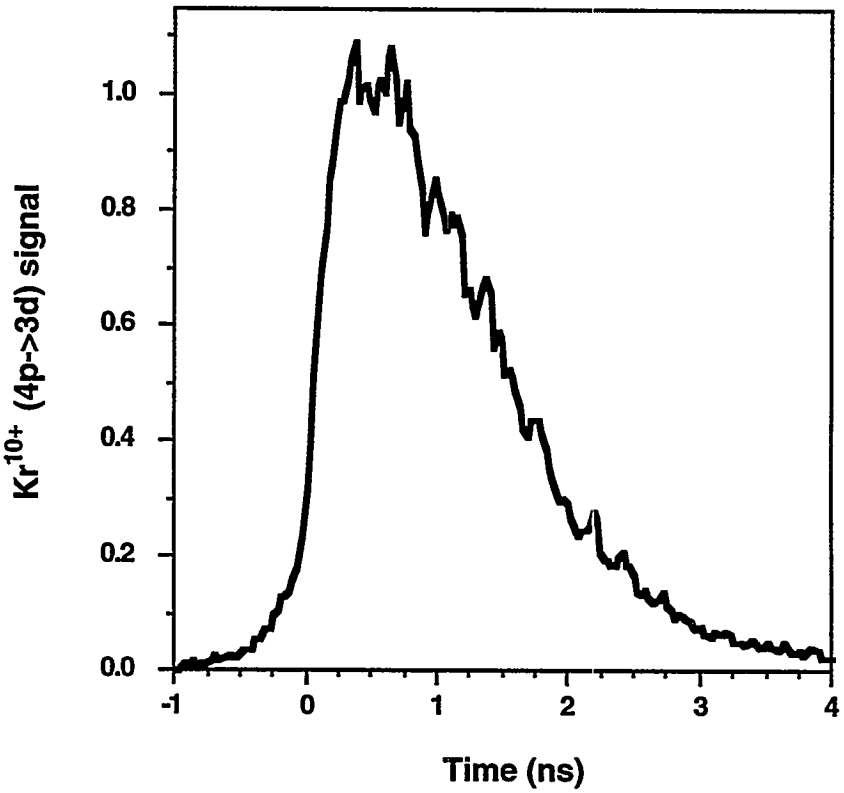

Figure V.24: Time history of the Kr^{10+} 4p->3d line. Streak camera resolution is 280 ps.

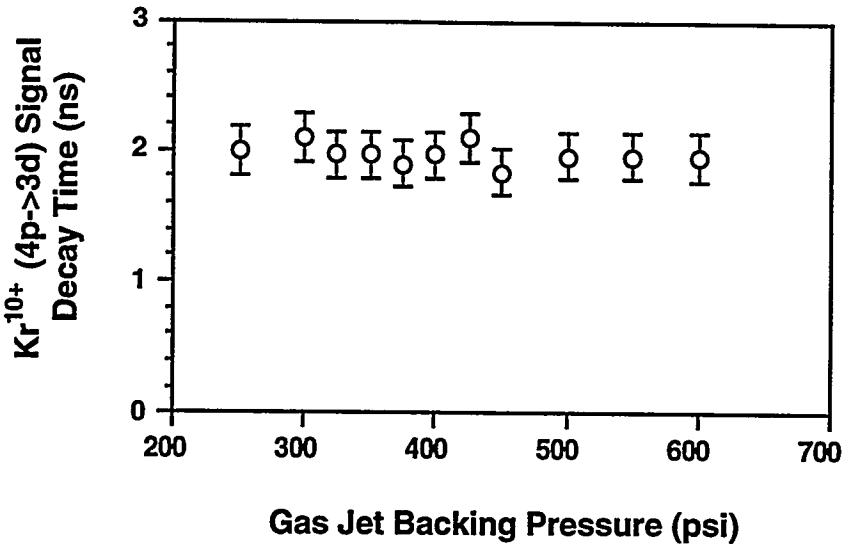

Figure V.25: Measured decay time of the Kr^{10+} 4p->3d line is plotted as a function of backing pressure for a peak intensity of 1 x 10^{16} W/cm^2.

a peak intensity of 1 x 10^{16} W/cm^2 in figure V.25. The decay time is roughly 2 ns over the range of backing pressures from 200 to 700 psi. This data suggests that the dominate mechanism for the production of this radiation is collisional excitation. The time scale for collisional excitation will be set by the cooling rate of the plasma which is largely determined by the speed of expansion. This speed, roughly given by the sound speed of the plasma, is independent of the gas density. If the time scale were set by the rate of recombination, eq. (5.40), the decay time would be strongly dependent on the gas density.

Evidence for the interaction of the laser with solid density clusters is found when the time history of the Kr emission is observed over the first 100 ps. Data showing the streaked spectrum of Kr is shown in figure V.26a. The time resolution of this data is roughly 20 ps. Figure V.26b shows a lineout illustrating the time history of the Kr^{10+} 90 Å line for the first 100 ps after illumination by the laser (here the time resolution has been decreased to 10 ps). We observe an initial spike in the emission of the Kr^{10+} line, faster

(a)

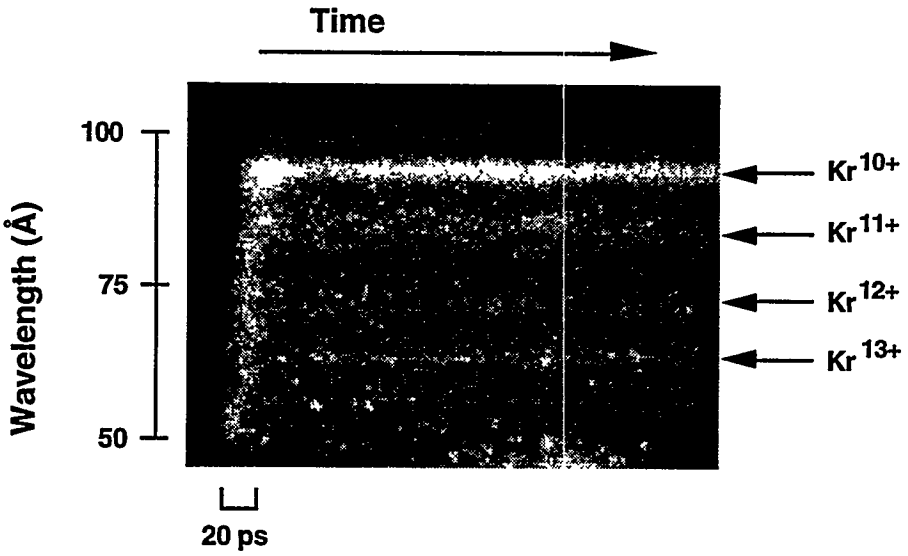

(b)

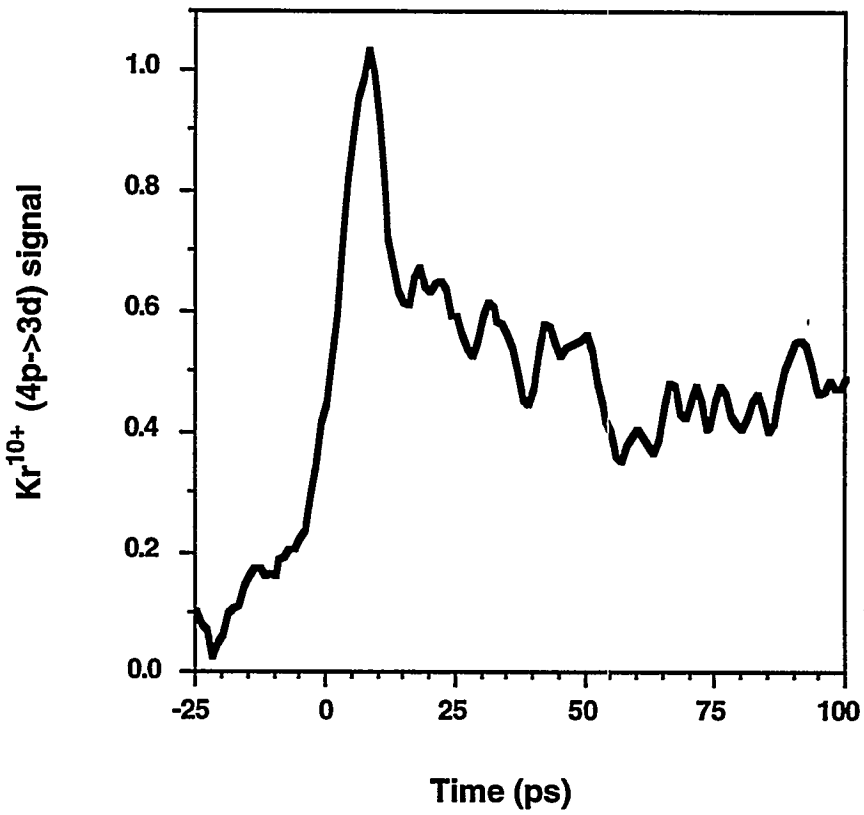

Figure V.26: **(a)** Streaked spectrum of Kr with a time resolution of 20 ps. **(b)** Time history of the Kr^{10+} 90Å line for the first 100 ps (with ~10 ps time resolution).

than the time resolution of the streak camera, followed by the long lived emission demonstrated in fig. V.24. A similar spike is seen on all the charge states' lines as well as in the background continuum emission. This initial spike is indicative of intense x-ray emission by the dense cluster micro-plasmas immediately after heating by the laser. The fast (< 1 ps) expansion of the cluster is then followed by lower intensity emission by the lower density bulk plasma on a long (3 ns) time scale. The fast rise time of the emission from the high charge states indicates that rapid ionization (< 1 ps) occurs to Kr^{10+} - Kr^{13+} within the cluster, consistent with our calculations. Though the number of photons contained within this spike is much less than the total number of photons that are emitted by the plasma, the relative brightness is higher than the long lived emission. If the emission is only a few hundred fs in duration, as our model suggests, then the relative brightness of the spike would be two orders of magnitude above that of the underdense plasma emission.

V.11 Short Wavelength Emission in Argon

Short wavelength emission is observed under similar conditions in Ar as well. A time integrated spectrum of Ar emission from 20 to 140 Å is shown in figure V.27. The gas jet backing pressure was 450 psi and the laser was focused to 8×10^{15} W/cm^2. The most dramatic aspect of this spectrum is the observation of strong emission from lines at wavelengths below 50 Å in neon-like Ar (Ar^{8+}) [61]. This signal is very strong; we estimate that the photon yield on these lines indicates that up to 1 - 5% of the laser energy is converted to x-rays in this wavelength range. To produce this charge state by tunnel ionization would require a focused intensity of $>1.5 \times 10^{18}$ W/cm^2, more than two orders of magnitude higher than that used in the experiment. In fact, the appearance intensity of this charge state is consistent with the predictions of the calculation illustrated in figure

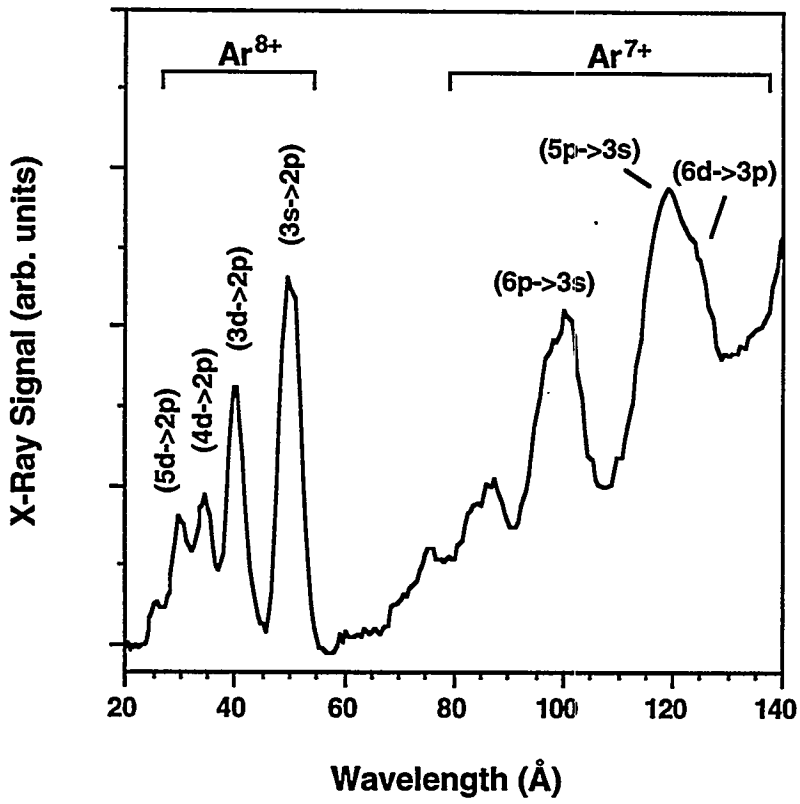

Figure V.27: Time integrated spectrum of Ar emission from 20 to 140 Å with a gas jet backing pressure of 450 psi and an intensity of 8×10^{15} W/cm^2.

V.8. The measured signal of the Ar^{8+} 3s->2p line and the Ar^{7+} 4d->3p line are plotted versus intensity in figure V.28. The appearance of these lines at an intensity of 2×10^{15} W/cm^2 for the Ar^{7+} and 3×10^{15} W/cm^2 for the Ar^{8+} signal agree very well with the calculation of Ar ionization in the cluster.

The time history of the neon-like Ar emission is of a duration that is comparable to the Kr emission. Figure V.29 illustrates the characteristic emission history of the Ar^{8+} 3s->2p line at 49 Å. The signal exhibits a ~ 1ns drop followed by a longer (~ 4 ns) tail. We have modeled the dynamics of the Ar emission in detail to describe this history. Figure V.30 shows the calculated time histories of the temperature at various radial points, (as before, we have used the calculated temperature as a function of intensity to determine the

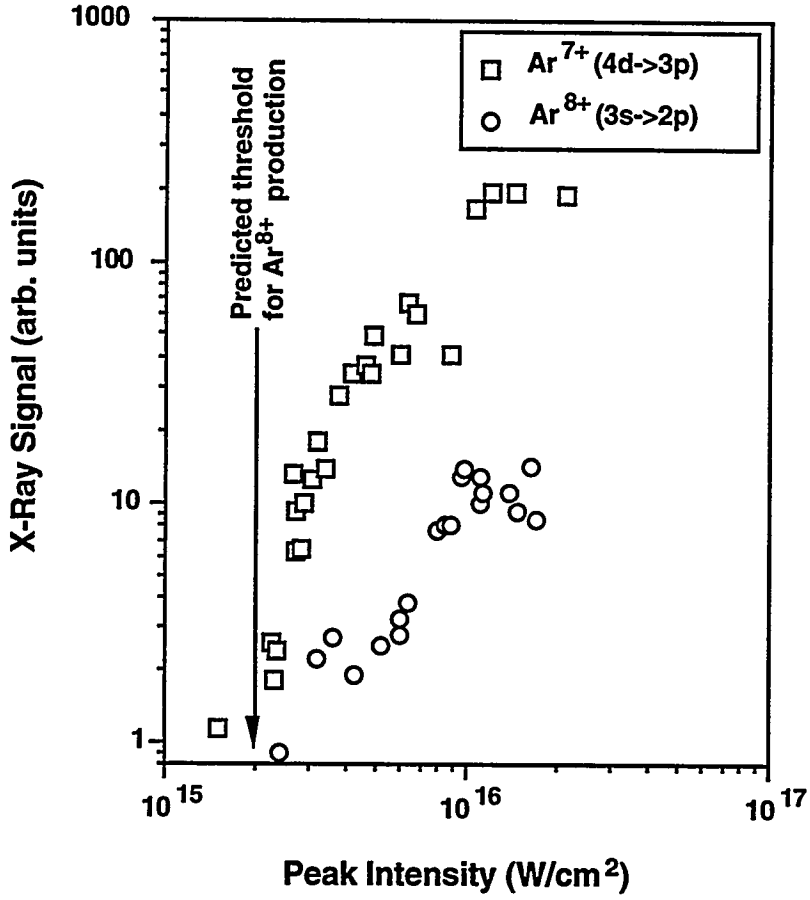

Figure V.28: Measured signal of the Ar^{8+} 3s->2p line and the Ar^{7+} 4d->3p line as a function of intensity.

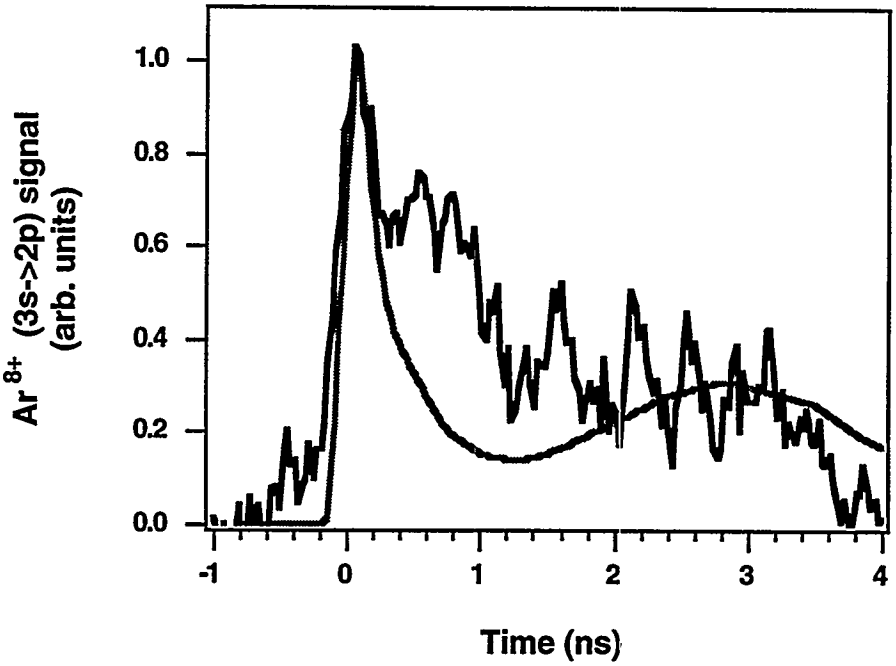

Figure V.29: Measured (solid line) and calculated (gray line) emission history of the Ar^{8+} 3s->2p line at 49Å.

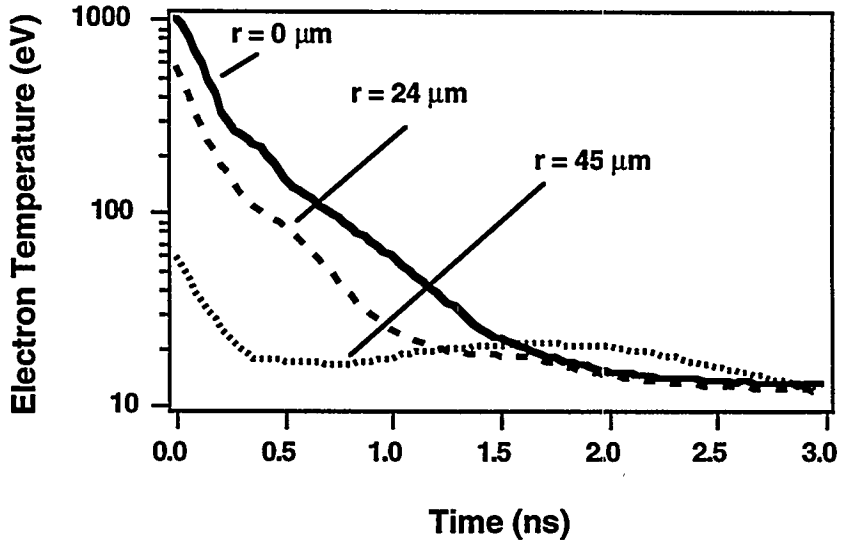

Figure V.30: Calculated time history of the temperature in an Ar plasma at various radial points in the laser focus (assuming a 100 μm diameter Gaussian focus).

initial temperature profile.) We have assumed that the peak initial temperature is 1000 eV. The temperature drops rapidly at first due to the free streaming cooling of the hot center to the cold surrounding plasma. This is followed by a slower decay from 100 - 200 eV by hydrodynamic expansion. To calculate the Ar emission time history we have calculated the charge state time histories at four radial points using FLY and weighted the emission by the volume at each radius.

The population of the 3s->2p transition was estimated by assuming pumping by collisional excitation in the Ar^{8+} ions and recombination pumping from Ar^{9+}. The collisional excitation rates of Mohan et. al. were used to calculate the magnitude of the collisional pumping mechanism [133]. The recombination rate of eq. (5.40) was used to determine the rate that the upper levels of Ar^{9+} are filled. We then assume that these electron cascade through the lower levels and populate the n = 3 levels by their statistical weights. The calculated time history of the Ar 3s->2p emission is shown as a gray line in figure V.29. The strong initial signal over the first ~ 1 ns results from collisional excitation. The long tail comes from the recombination. The combination of these mechanisms seems to adequately explain the emission time history. The fall of the collisional contribution to the signal is faster compared to the Kr time history due to the higher energy of the transition and the faster expansion rate (since the Kr ions are more massive than the Ar ions and therefore expand more slowly).

V.12 Prepulse Experiments

Since the clusters expand rapidly after heating by the laser, the presence of a laser prepulse of sufficient energy to ionize the cluster should be sufficient to destroy the clusters. To explore this effect we examined the yields and time history of a cluster plasma with and without a laser prepulse. In the first experiment we generated a prepulse

by placing a fused silica blank in the beam with hole removed in the center of the beam. The part of the beam that passed though the hole preceded the main part of the beam by roughly 35 ps. The intensity of this pulse was about 30% of the main pulse.

V.12.A Fast Time History of Kr Emission With and Without a Prepulse

The fast time history of the Kr^{10+} emission for a peak intensity of 2×10^{16} W/cm^2 is shown in figure V.31 (dark line) compared to the case when the prepulse was allowed into the chamber (gray line) with the same intensity. The case in which both pulses were focused into the gas exhibit only one spike in the x-ray emission, though two pulses traversed the jet. Furthermore, the x-ray yield of the case with the prepulse is approximately 0.3 times that of the case in which only the main pulse was focused into the jet. When the prepulse was present, the signal is reduced because only the prepulse energy is absorbed. The main pulse traverses underdense plasma only and does not deposit any substantial energy in the plasma. No spike in x-rays is observed coincident with the main pulse in this case.

V.12.B Cluster Emission Control with a 14 ns Prepulse

To more accurately determine the intensity at which the clusters disassemble, a second experiment was performed in which a small prepulse 14 ns before the main pulse is generated by allowing some pulse energy to leak out of the regenerative amplifier cavity. Tuning the timing of the Pockels cell in the cavity permitted control over the amplitude of the prepulse which was monitored on the fast photodiode and a sampling scope. Figure V.32 illustrates the dramatic difference in the x-ray spectrum between the case when Ar is irradiated with an intensity of 2×10^{16} W/cm^2 and no prepulse is present and when a prepulse of approximately 8×10^{14} W/cm^2 precedes the main pulse. The strong line and continuum emission that results from single pulse irradiation of Ar in the

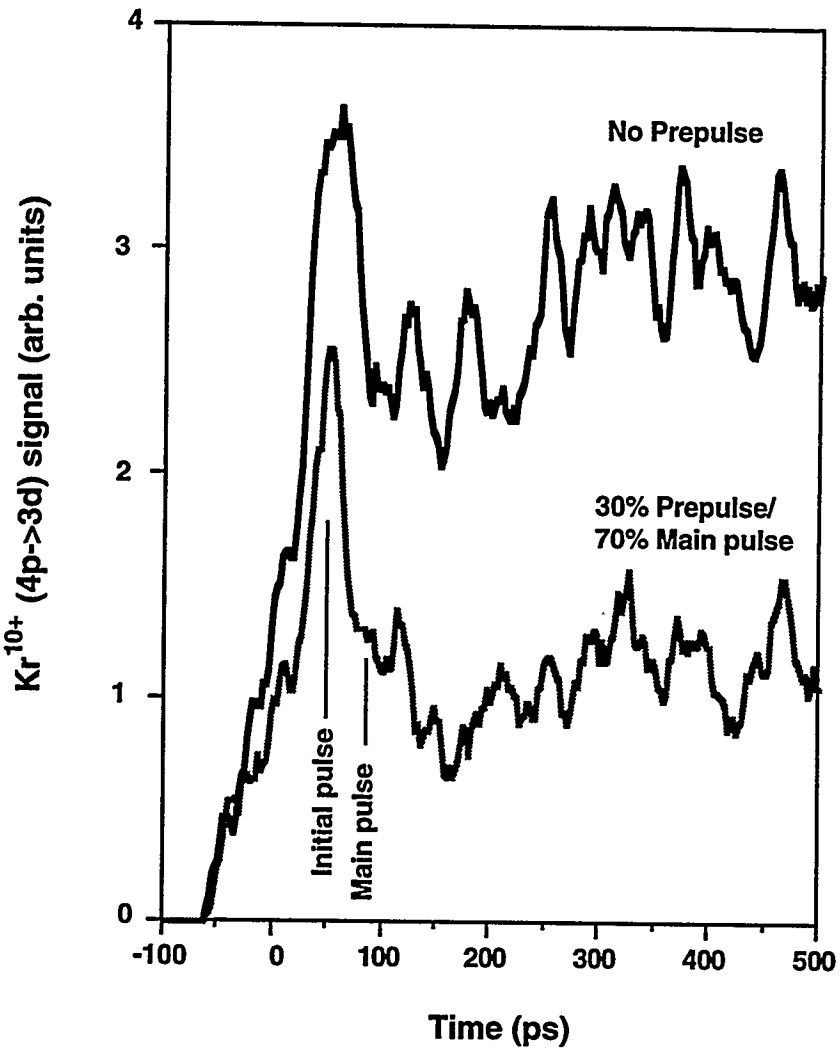

Figure V.31: Fast time history of the Kr^{10+} emission for a peak intensity of 2×10^{16} W/cm^2 when no prepulse is used (dark line) compared to the case when a 30% prepulse was allowed into the chamber 35 ps before the main pulse (gray line).

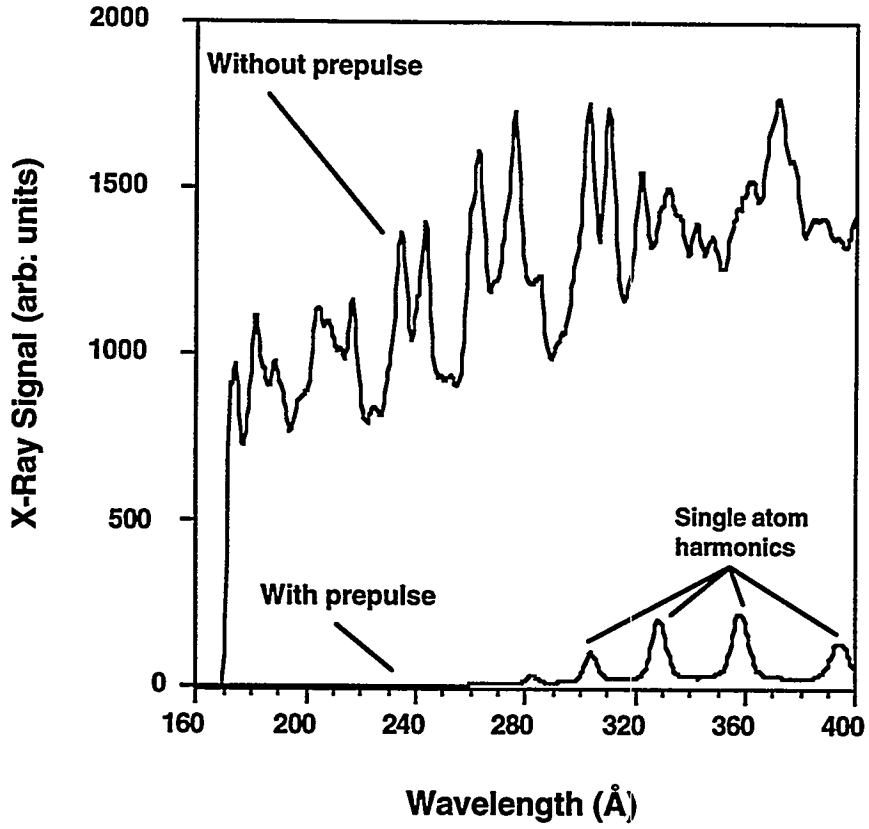

Figure V.32: Comparison of time integrated emission from Ar when irradiated with an intensity of 2 x 10^{16} W/cm^2 and no prepulse is present and when a prepulse of approximately 8 x 10^{14} W/cm^2 precedes the main pulse by 14 ns.

gas jet disappears completely when a prepulse is used. Only the harmonics, which are generated by individual atoms, are observable when the prepulse is added.

A similar effect can be seen when a mixture of He and 10% Ar is irradiated. Figure V.33 shows the helium spectrum with a peak intensity of 7 x 10^{15} W/cm^2 in the main pulse. Addition of a prepulse of 1 x 10^{15} W/cm^2 effectively lowers the Ly α emission to unobservable levels. This indicates that at an intensity of ~ 1 x 10^{15} W/cm^2 the cluster sees sufficient intensity to undergo some ionization to cause it to disassemble,

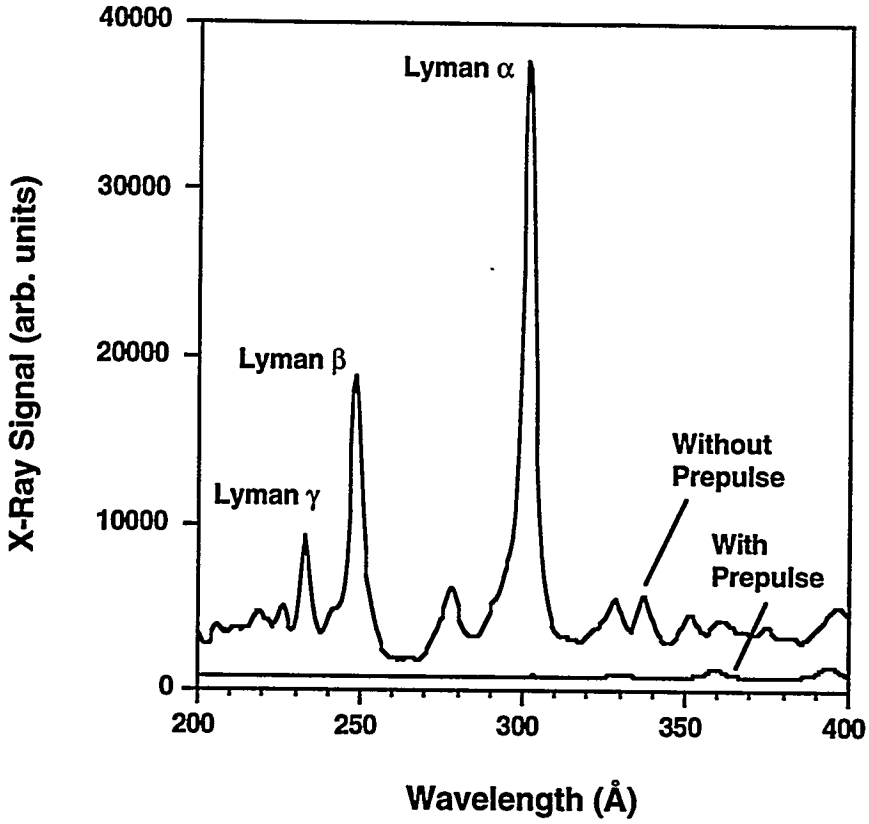

Figure V.33: Helium emission spectrum with a 10% Ar mixture with a peak intensity of 7 x 10^{15} W/cm^2 in the main pulse with and without a 14 ns prepulse of 1x 10^{15} W/cm^2.

however, it does not acquire any significant amount of heat, and therefore, does not excite any emission in the surrounding underdense He plasma. The threshold for the disassembly of the clusters begins abruptly with increasing prepulse intensity. The He Ly α yield for a fixed main pulse intensity of 7 x 10^{15} W/cm^2 is shown as a function of prepulse intensity in figure V.34. The helium signal drops rapidly for prepulse intensities above about 4 x 10^{14} W/cm^2. This sharp drop is probably due to the nonlinear nature of the tunnel ionization rate for the Ar atoms in the cluster.

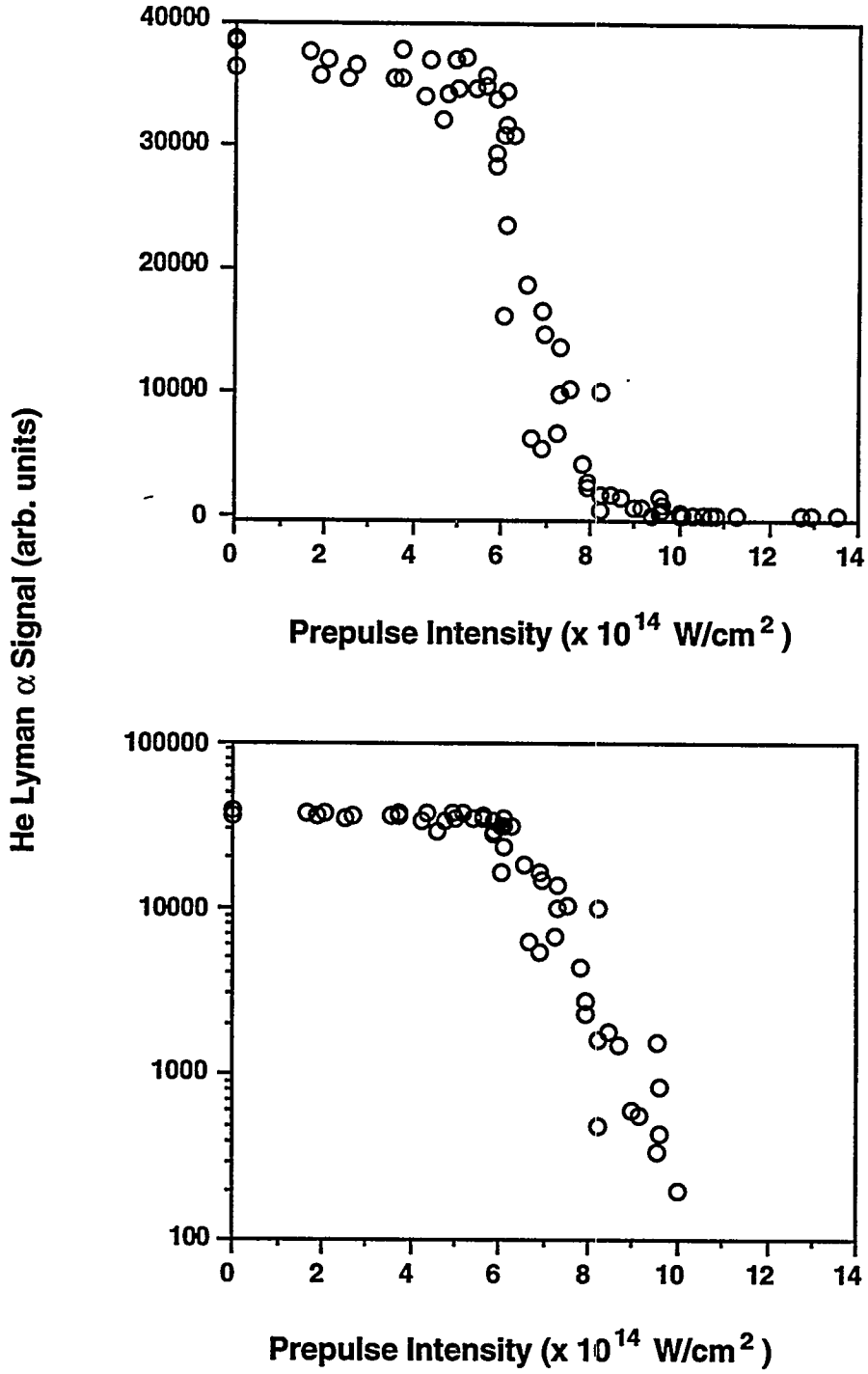

Figure V.34: He Ly α yield with a 10% Ar mixture for a fixed main pulse intensity of 7×10^{15} W/cm^2 as a function of 14 ns prepulse intensity.

V.13 X-ray yields for Long and Short Pulses

The dramatic effect of a prepulse on the plasma emission from a gas containing clusters suggests that there should be a very large difference in the x-ray yields between when a long (~ 1 ns) and a short (~ 100 fs) pulse is used. Since the clusters disassemble on a < 1 ps time scale, the short pulse sees the solid density particles. The long pulse, however, essentially sees only underdense plasma through the majority of the pulse.

To illustrate this point, we measured the x-ray yield in Ar in the wavelength band between 300 and 170 Å for cases of short pulse and long pulse illumination (figure V.35). We estimated the x-ray yield by comparing the signal level with harmonics yields under known conversion efficiency conditions. We also estimated the yield from the known throughput of the spectrometer and the gain of the micro-channel plate to confirm that this was consistent with the numbers arrived at through comparison with the harmonics. The long pulse for this experiment was derived by simply focusing the uncompressed LiSAF pulse, which has a 400 ps width, into the chamber. The x-ray conversion efficiency is plotted for the long and short pulse cases in figure V.35. For the case of the long pulse, >0.25 J of energy was required ($I \sim 3 \times 10^{13}$ W/cm^2) to achieve any significant signal in this wavelength range. The conversion efficiency for this case reached just above 1% for approximately 0.5 J of energy. The short pulse, however, exhibited a much greater conversion efficiency at a much more modest energy. The conversion efficiency increased into the 10% range for 30-40 mJ of laser energy. Saturation of the MCP prevented us from increasing the energy still further.

This sort of conversion efficiency is comparable to x-ray conversion efficiencies attainable with flat solid targets [73]. Thus, the use of clusters increases the coupling efficiency of the laser light into the target material to point that is comparable to a solid target. In principle, using an extended source of clusters, such as a gas jet with a slit nozzle, even higher conversion efficiencies may be possible.

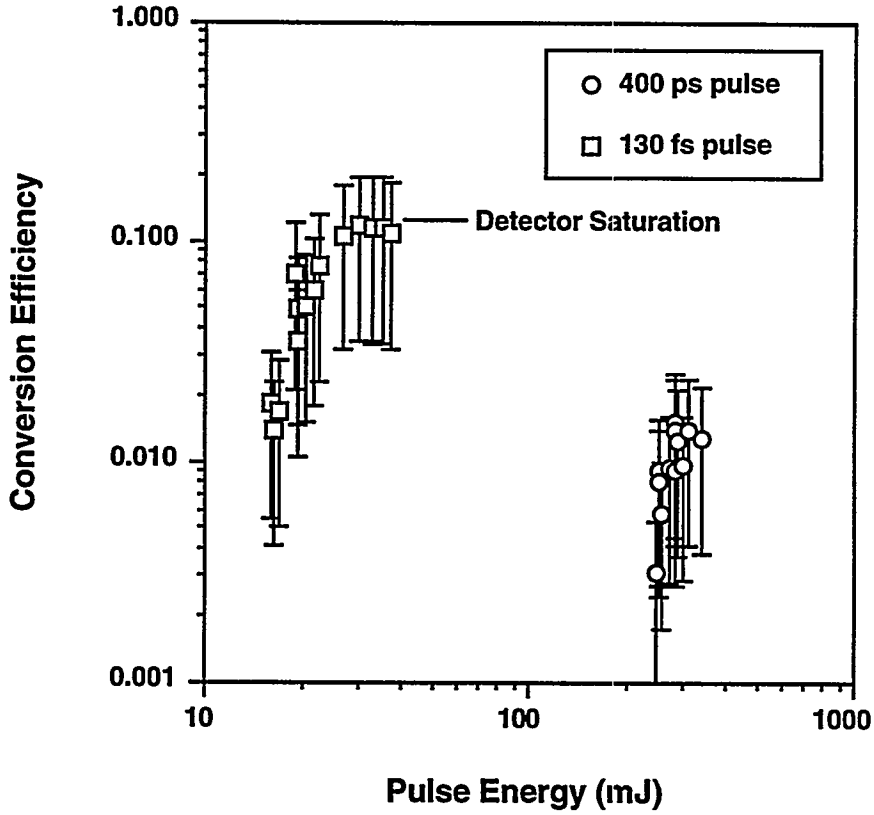

Figure V.35: X-ray yield in Ar in the wavelength band between 300 and 170 Å for cases of short pulse (130 fs) and long pulse (400 ps) illumination.

V.14 Conclusion

In conclusion, we have shown that large clusters produced in expanding gas jets can be used to produce hot, moderate density plasmas with intense, short pulse lasers. We find that the thermal plasmas produced by the illumination of clusters by femtosecond pulses of 10^{16} to 10^{17} W/cm^2 dominate the plasma kinetics, producing emission from high charge states that can last for many nanoseconds. These experimental results are in good agreement with modeling of the laser-cluster interaction and the dynamics of the underdense plasma that results after the heated clusters expand. These novel plasmas exhibit dramatically enhanced absorption of the laser light relative to pure gases, with plasma temperatures well in excess of that expected from the illumination of a low density gas alone. Furthermore, the x-ray yields are comparable to those that can be achieved with solid targets. These cluster heated plasmas have the potential for providing a source of strong, x-ray radiation with the modest irradiance (10^{15} to 10^{17} W/cm^2) produced by small-scale short-pulse lasers through a unique combination of the advantages inherent to both solid and gas targets.

Chapter VI

Conclusion and Future Directions

VI.1 Summary

The goal of this work has been to experimentally investigate the physics of soft x-ray generation in gases with a short pulse laser. These investigations have centered around two different mechanisms leading to radiation generation in the 500-20 Å wavelength range. Though both mechanisms are quite different in their details, they both exploit the interaction of electrons oscillating in an intense field with charged ions to produce short wavelength photons. The primary emphasis of this thesis has been to understand the physics of the laser interaction with gas from a gas jet. This work has tried to go beyond this initial understanding, however, and has attempted to present a complete characterization the radiation that results with an eye toward the possible use of either mechanism for generating soft x-rays for applications.

Before conducting these investigations, it was necessary to develop a suitable laser with sufficient intensity to access the physics leading to soft x-ray generation. I have described the design and performance of a Cr:LiSAF laser that is capable of producing 130 fs pulses with a peak power above 8 TW. I have shown that flashlamp pumped LiSAF presents an important alternative to more traditional Nd:YAG pumped Ti:sapphire for use in CPA lasers with compressed pulse widths of 100 fs or shorter. LiSAF's greatest advantage is its ability to be flashlamp pumped which permits easy scaling of the

power amplifiers to aperture > 1 cm. Weak focusing of this laser system described in this work yields peak intensity of > $2x10^{17}$ W/cm^2.

The first method of soft x-ray generation that was explored was the process of high order harmonic generation. The physics behind this process was motivated in chapter III and then a detailed experimental investigation of the properties of harmonics in the 500-100 Å range was presented. These investigations included studies of the harmonic spatial and spectral profiles as well as energy yields and conversion efficiencies under a variety of conditions. The measurements presented in this work illustrate that the harmonics represent a source of light in the XUV with good spatial qualities and with relatively high conversion efficiency (~10^{-7}) into each harmonic. These measurements are in reasonable agreement with models describing the harmonic generation. The energy yield measurements, in particular, are in good agreement with a full, 2-dimensional numerical integration of the wave equation for the harmonic production in an ionizing gas. The experimental investigation of the harmonics was concluded with a description of two experiments illustrating the use of harmonics in applications. The first illustrated the use of harmonics in photo-ionization spectroscopy of rare gases, and the second demonstrated the amplification of a harmonic at 251 Å in an x-ray laser amplifier.

Finally, experimental and computational investigations of x-rays produced in the hot plasmas generated during the interaction of an intense laser pulse with the atomic clusters present in an expanding gas jet were presented. These studies showed that the laser energy absorbed by the gas was greatly enhanced by the presence of large clusters in the gas. The clusters enhance the collisionality of the plasma and significantly increase the laser absorption over that of a low density gas. Plasma with electron temperature of many hundreds of eV can be created during the laser pulse. These hot plasmas emit copious amounts of x-rays. Strong emission was observed at wavelengths as short as 20 Å in Ar^{8+} and Kr^{13+}, charge states that would require focused intensity 10 to 100 times higher than that used to produce them by tunnel ionization. Most importantly from the stand

point of possible applications, we found that the conversion efficiency of laser light into x-rays with the cluster target is comparable to that of solid targets.

VI.2 Future Directions

The experiments describe in this thesis point toward a number of future directions that warrant further efforts. I have alluded to the fact that the primary motivation of these studies has been the potential development of table-top, laser driven soft x-ray sources. Taking additional steps to make this a reality are directions that this work suggests. Though a full survey of possible future directions is beyond the scope of this chapter, I would like to describe three specific examples of possible future work suggested by this thesis. This will give a flavor of the many directions that one could take.

VI.2.A High Average Power Short Pulse Lasers

From the standpoint of laser development, one of the next major challenges will be to scale the terawatt peak power systems to higher repetition rate and, therefore, to higher average power. To make a viable table top x-ray source, higher average powers of x-rays are necessary. It is, therefore, desirable to develop a CPA laser with average power > 100 W and ultimately > 1 kW. Such lasers will become possible in the near future with the advancement of diode pumped solid state lasers [12]. With average power operation, pumping schemes more efficient than flashlamp pumping are desirable since the heat load on the laser material becomes considerable. The natural approach is to use laser diodes to pump the solid state gain medium.

LiSAF can be directly diode pumped. In fact, diode pumped, femtosecond, mode-locked LiSAF oscillators have been demonstrated [69]. Diode pumped LiSAF offers one potential avenue to a high average power terawatt class laser. Another possible avenue

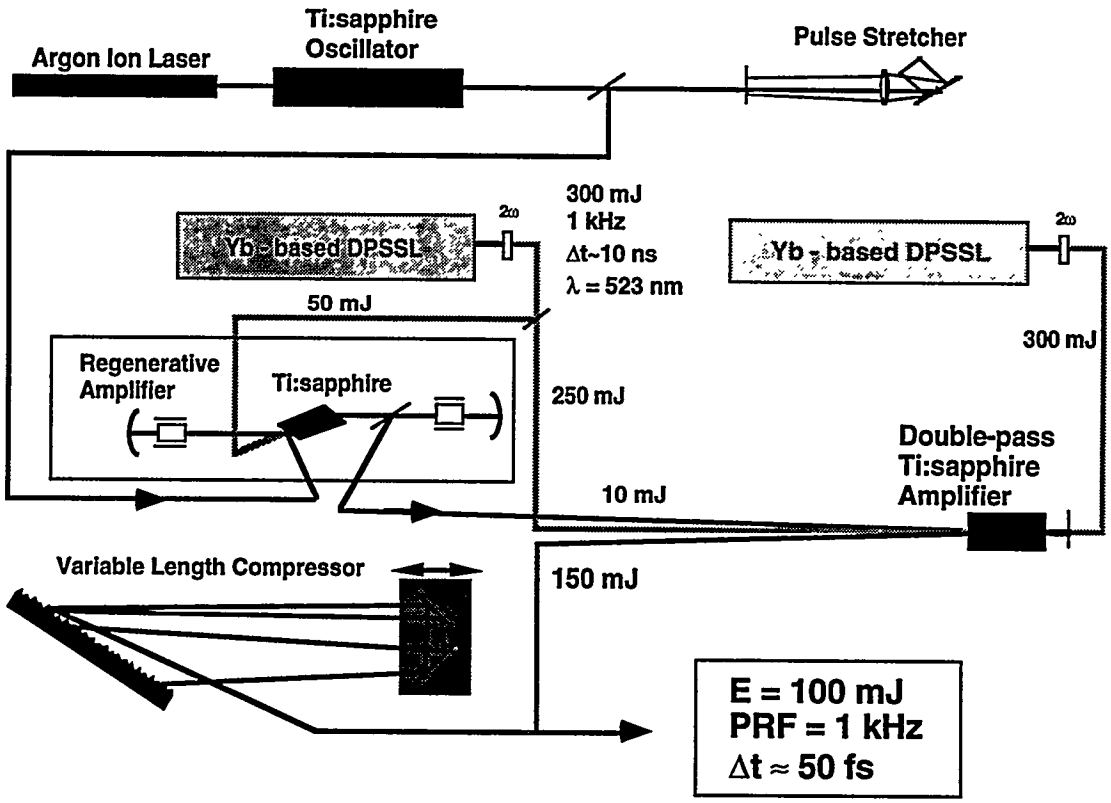

Figure VI.1: Conceptual design of a 100 W, terawatt class, Ti:sapphire laser. (Note: DPSSL = "diode pumped solid state laser".)

exploits currently developed, diode pumped q-switched laser technology to develop a high average power terawatt system. This approach utilizes a high average power, diode pumped, q-switched laser operating at a wavelength of 1 μm which can be frequency doubled to pump Ti:sapphire at a high repetition rate. The conceptual design of such a laser is shown in figure VI.1. In this case, two diode pumped lasers, based on a Yb-doped crystal [41], are frequency doubled to pump two Ti:sapphire amplifiers. Lasers with a capability of producing > 300 W of green pump power will soon be available [11]. Such a system should be able to produce > 100 W of average power of sub-100 fs pulses. The system would operate at a repetition rate of 1 kHz with each pulse exhibiting a peak power of > 1 TW.

VI.2.B Time Resolved Probing of Plasma Kinetics with Harmonics

Future directions in high harmonic research will almost certainly be directed into the use of harmonics in applications. One possible use of the soft x-rays produced with high harmonic generation is to probe laser plasmas and core level transitions in highly charged ions. Such experiments take advantage of the low angular divergence of the harmonics allowing one to probe selected spatial regions of an inhomogeneous plasma. They also take advantage of the harmonics' short pulse character which permits pump-probe experiments to be performed with time resolution as short as the pulse length of the laser.

One such example of a potential plasma probing experiment using harmonics would be to probe the recombination dynamics of a cold, optically ionized plasma. In such an experiment, a harmonic is tuned to the resonance transition of a particular charge state of an atom in a recombining plasma. The soft x-ray harmonic radiation is then focused (with a multi-layer mirror, for example) through the plasma and detected after the harmonics have traversed the plasma. The relative population of the lower level of the transition can be probed by determining the absorption undergone by the harmonic

passing through the plasma. By varying the time delay between the ionizing pulse and the harmonic producing pulse, the time dynamics of the lower level population can be probed. Such a technique would allow direct probing of the dynamics of a recombining plasma. By tuning a specific harmonic to a line in the plasma, the absorption of the harmonic will be an indicator of the presence of the ion that possesses that line. Therefore, the lifetime of that particular ion in the recombining plasma can be determined with a time resolution of the order of the harmonics' pulse width (~ 50 fs).

To demonstrate the feasibility of such an experiment I have conducted a simple calculation in which the 27th harmonic of an 825 nm laser traverses an optically ionized He plasma. The harmonic is tuned so as to be resonant with the 304 Å Lyman α line in He. It is assumed that the harmonic exhibits a Gaussian linewidth of 1.2 Å (based on the measurements of chapter IV), and that the stark broadened He^+ line can be approximated by a Lorentzian line with FWHM of .5 Å (calculated using the formulation of Griem [74]). The calculated transmission fraction for the 27th harmonic tuned to the 304 Å line is shown in figure VI.2. From this plot, we see that the absorption of the harmonic is a very sensitive function of the ground state population. This calculation suggests that pump probe experiments of this kind can be a very sensitive way to examine recombination dynamics with a time resolution never before demonstrated in the history of plasma spectroscopy.

VI.2.C High Average Power Cluster Based Soft X-Ray Source

The third direction in which this thesis points is toward high average power x-ray sources. As we demonstrated in chapter IV, conversion efficiency of > 10^{-7} of laser energy into a single high harmonic at a wavelength below 300 Å is possible. Conversion of better than 1% into incoherent light in the water window was demonstrated from an argon plasma heated by the illumination of clusters in chapter V. These results suggest that the next logical step is to combine these capabilities with a high average drive laser

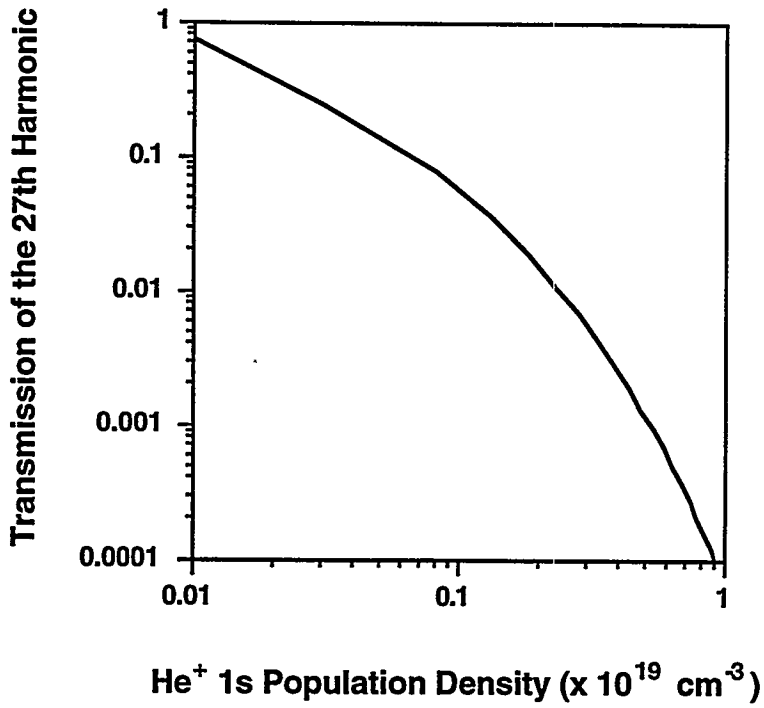

Figure VI.2: Calculated transmission fraction for the 27th harmonic of a 100 fs laser tuned to the 304 Å line in helium as a function of the population density of the 1s state (assuming negligible population of the 2p state) for an optically ionized He plasma of initial density 10^{19} cm^{-3} and a length of 1 mm.

like that proposed in section VI.2.A. Such a laser used to shoot a cluster gas jet target could produce as much as 1 - 10 W of average power in incoherent x-ray radiation. The laser could also be used to produce 10 - 100 μW of average power in a coherent, harmonic generated beam.

The use of a cluster based incoherent source has a number of advantages over the more conventional use of solid targets to produce x-rays with laser pulses. Most importantly, the use of a gas target does not generate debris like a solid target does. This is very important for an application such as proximity projection lithography where it is desirable to have the x-ray generating plasma close to the lithography mask. A solid generates enough debris to cause damage to the mask over a long time scale. Use of a gas

target avoids this problem. Using a gas target is also practically more useful than a solid since it can be repetitively used; a solid target requires some form of rastering so that each laser pulse strikes a clean surface. This advantage will be most important at very high repetition rate (> 1 kHz).

The use of clusters, however, demands the use of short pulses for generating the x-rays. Since the cluster disassembles on a fast time scale (<1 ps), efficient energy generation is possible only with a short laser pulse. This fact was demonstrated in figure V.35. This possible application is a strong impetus for the development of high average power short pulse lasers.

VI.3 Conclusion

It is clear, by the wealth of papers published each month, that the physics of intense short pulse interactions with matter is a vibrant field. Though interesting in itself, the possible use of this physics for bright, soft x-ray generation adds a dimension to this field by opening a door to possible applications in other fields. From the first experiments in second harmonic generation, the generation of short wavelength radiation with intense laser pulses has come a long way. The next decade will most likely see an exponential growth in the uses of these soft x-ray sources in scientific and commercial applications. Only time will tell, however, if the x-ray sources being developed now will gain wide acceptance in the same manner that visible wavelength lasers have in the past.

References

1. O. Abraham, J.H. Binn, B.G. Deboer, and G.D. Stein, "Gasdynamics of Very Small Laval Nozzles," Phys. Fluids **24**, 1017 (1981).

2. O. Abraham, S.-S. Kim, and G.D. Stein, "Homogeneous Nucleation of Sulfur Hexaflouride Clusters in Laval Nozzle Molecular Beams," J. Chem. Phys. **75**, 402 (1981).

3. P. Agostini, F. Fabre, G. Mainfray, G. Petite, and N.K. Rahman, "Free-Free Transitions Following Six-Photon Ionization of Xenon Atoms," Phys. Rev. Lett. **42**, 1127 (1979).

4. C. Altucci, N.A. Ansari, R. Bruzzese, C.d. Lisio, S. Solimeno, and R.B. Kay, "Distortion of the Laser Beam Induced by the Electron Plasma in Harmonic Generation Experiements," J. Phys. B: At. Mol. Opt. Phys. **26**, 1761 (1993).

5. M.V. Ammosov, N.B. Delone, and V.P. Krainov, "Tunnel Ionization of Complex Atoms and of Atomic Ions in an Alternating Electromagnetic Field," Sov. Phys. JETP **64**, 1191 (1986).

6. S. Augst, D.D. Meyerhofer, D. Strickland, and S.L. Chin, "Laser Ionization of Noble Gases by Coulomb-Barrier Suppression," J. Opt. Soc. B **8**, 858 (1991).

7. P.V. Avizonis and R.L. Grotbeck, "Experimental and Theoretical Ruby Laser Amplifier Dynamics," J. Appl. Phys. **37**, 687 (1966).

8. P. Balcou, C. Cornaggia, A.S.L. Gomes, L.A. Lompré, and A. L'Huillier, "Optimizing High-Order Harmonic Generation in Strong Fields," (1992).

9. P. Balcou, P. Salières, K.S. Budil, T. Ditmire, M.D. Perry, and A. L'Huillier, "The Application of High-Order Harmonic Radiation to Photoionization Spectroscopy," Z. Phys. D to be published. (1995).

10. C.P.J. Barty, C.L.G. III, and B.E. Lemoff, "Multiterawatt 30-fs Ti:sapphire Laser System," Opt. Lett. **19**, 1442 (1994).

11. R. Beach, "Proposed DPSSL Development Plan for AVLIS," Internal Memo, Laser Program, Lawrence Livermore National Laboratory (1995).

12. R.J. Beach, M.A. Emanuel, W.J. Benett, B.L. Freitas, D. Ciarlo, N.W. Carlson, S.B. Sutton, J.A. Skidmore, and R.W. Solarz, "Improved Performance of High

Average Power Semiconductor Arrays for Applications in Diode Pumped Solid State Lasers," in *Laser Diode Technology and Applications VI*, (SPIE, 1994), Vol. 2148, p. 13

13. P. Beaud, E. Miesak, Y.-F. Chen, B.H.T. Chai, and M.C. Richardson, "110 fsec Fourier-Transform Limited Gaussian Pulses from a Cr:LiSAF Regenerative Amplifier," Opt. Comm. **95**, 46 (1993).

14. P. Beaud, M.C. Richardson, Y.-F. Chen, and B.H.T. Chai, "Optical Amplification Characteristics of Cr:LiSAF and Cr:LiCAF under Flashlamp-Pumping," IEEE J. Quant. Elec. **QE-30**, 1259 (1994).

15. P. Beaud, M.C. Richardson, E.J. Miesak, and B.H.T. Chai, "8-TW 90-fs Cr:LiSAF Laser," Opt. Lett. **18**, 1550 (1993).

16. H.P. Birkhofer, H. Haberland, M. Winterer, and D.R. Worsnop, "Penning, Photo and Electron Impact Ionization of Argon Clusters," Ber. Bunsenges. Phys. Chem. **88**, 207 (1984).

17. R.D. Bleach, "XUV Spectra from Kr XI-XIV," J. Opt. Soc. Am. **70**, 861 (1980).

18. W.J. Blyth, S.G. Preston, A.A. Offenberger, M.H. Key, J.S. Wark, Z. Najmudin, A. Modena, A. Djaoui, and A.E. Dangor, "Plasma Temperature in Optical Field Ionization of Gases by Intense Ultrashort Pulses of Ultraviolet Radiation," Phys. Rev. Lett. **74**, 554 (1995).

19. J. Bokor, P.H. Buckbaum, and R.R. Freeman, "Generation of 35.5 nm Coherent Radiation," Opt. Lett. **8**, 217 (1983).

20. M. Born and E. Wolf, *Principles of Optics: Electromagnetic Theory of Propagation, Interference, and Diffraction of Light*, (Oxford: Pergamon, 1989).

21. R.D. Boyd, J. Britten, D. Decker, B. Shore, M.D. Perry, and L. Li, "High-Efficiency Metallic Diffraction Gratings for Laser Applications," Appl. Opt. **34**, 1697 (1995).

22. R.W. Boyd, *Nonlinear Optics*, (Boston: Academic Press, 1992).

23. C.L. Briant and J.J. Burton, "Molecular Dynamics Study of the Structure and Thermodynamic Properties of Argon Microclusters," J. Chem. Phys. **63**, 2045 (1975).

24. K.S. Budil, P. Salières, A. L'Huillier, T. Ditmire, and M.D. Perry, "Influence of Ellipticity on Harmonic Generation," Phys. Rev. A **48**, R3437 (1993).

25. N.H. Burnett and P.B. Corkum, "Cold-Plasma Production for Recombination Extreme-Ultraviolet Lasers by Optical-Field-Induced Ionization," J. Opt. Soc. Am. B **6**, 1195 (1989).

26. N.H. Burnett, C. Kan, and P.B. Corkum, "Ellipticity and Polarization Effects in Harmonic Generation in Ionizing Neon," Phys. Rev. A **51**, R3418 (1995).

27. B. Chai, Center for Research in Lasers and Electro-Optics, Orlando, FL (1992), personal communication.

28. W.F. Chan, G. Cooper, X. Guo, and C.E. Brion, Phys. Rev. A **45**, 1420 (1992).

29. C.Y. Chien, J.S. Coe, G. Mourou, J.C. Kieffer, M. Chaker, Y. Beaudoin, O. Peyrusse, and D. Gilles, "Production of a High-Density and High-Temperature Plasma with an Intense High-Contrast Subpicosecond Laser," Opt. Lett. **18**, 1535 (1993).

30. Y. Chuang, L. Zheng, and D.D. Meyerhofer, "Propagation of Light Pulses in a Chirped-Pulse Amplification Laser," IEEE. J. Quant. Elec. **QE-29**, 270 (1993).

31. C.E. Clayton and M.J. Everett, "Measurements of the Transverse and Longitudinal Density Profiles an a Pulsed Supersonic Nitrogen Gas Jet," Rev. Sci. Instrum. to be published (1995).

32. P.B. Corkum, "Plasma Perspective on Strong-Field Multiphoton Ionization," Phys. Rev. Lett. **71**, 1994 (1993).

33. C.A. Coverdale, C.B. Darrow, C.D. Decker, W.B. Mori, K.-C. Tzeng, K.A. Marsh, C.E. Clayton, and C. Joshi, "Propagation of Intense Subpicosecond Laser Pulses Through Underdense Plasma," Phys. Rev. Lett. **74**, 4659 (1995).

34. J.K. Crane, Lawrence Livermore National Laboratory, Livermore, CA 94550 (1993), personal communication.

35. J.K. Crane, H. Nguyen, T. Ditmire, C. Coverdale, T.E. Glover, M.D. Perry, and Y. Zakharenkov, "Strong Anomalous Emission from He- and H- Like Neon in Short-Pulse Laser Driven Plasmas," J. Opt. Soc. Am. B to be published (1995).

36. J.K. Crane, M.D. Perry, S. Herman, and R.W. Falcone, "High-Field Harmonic Generation in Helium," Opt. Lett. **17**, 1256 (1992).

37. J.K. Crane, M.D. Perry, D. Strickland, S. Herman, and R.W. Falcone, "Coherent and Incoherent XUV Emission in Helium and Neon, Laser-Driven Plasma," IEEE Trans. Plasma Sci. **21**, 82 (1993).

38. C.B. Darrow, C. Coverdale, M.D. Perry, W.B. Mori, C. Clayton, K. Marsh, and C. Joshi, "Strongly Coupled Stimulated Raman Backscatter from Subpicosecond Laser-Plasma Interactions," Phys. Rev. Lett. **69**, 442 (1992).

39. L.B. DaSilva, Lawrence Livermore National Laboratory, Livermore, CA 94550 (1994), personal communication.

40. L.B. DaSilva, B.J. MacGowan, S. Mrowka, J.A. Koch, R.A. London, D.L. Matthews, and J.H. Underwood, "Power Measurements of a Saturated Yttrium X-Ray Laser," Opt. Lett. **18**, 1174 (1993).

41. L.D. DeLoach, S.A. Payne, L.L. Chase, L.K. Smith, W.L. Kway, and W.F. Krupke, "Evaluation of Absorption and Emission properties of Yb^{3+} Doped Crystals for Laser Applications," IEEE J. Quant. Elec. **QE-29**, 1179 (1993).

42. T. Ditmire, K. Kulander, H. Nguyen, J. K. Crane, M. D. Perry, "Calculation and Measurement of High Order Harmonic Energy Yields in Helium," J. Opt. Soc. Am. B to be published (1995).

43. T. Ditmire, J.K. Crane, K.S. Budil, M.D. Perry, P. Salières, and A. L'Huillier, "Coherence Properties of High Order Harmonic Radiation," in *Conference on Ultrafast Phenomena IX*, ed. P.F. Barbara, *et al.*, (Springer-Verlag: Berlin, 1994), Vol. 60, p. 228-232.

44. T. Ditmire, J.K. Crane, H. Nguyen, L.B. DaSilva, and M.D. Perry, "Energy-Yield and Conversion-Efficiency Measurements of High-Order Harmonic Radiation," Phys. Rev. A **51**, R902 (1995).

45. T. Ditmire, J.K. Crane, H. Nguyen, and M.D. Perry, "Plasma Effects on High-Order Harmonic Generation," J. of Nonlinear Opt. Phys. and Mat. **4**, (1995).

46. T. Ditmire, T. Donnelly, R.W. Falcone, and M.D. Perry, "Strong X-ray Emission from Hot Plasmas Produced by Intense Irradiation of Clusters," Phys. Rev. Lett. **75**, 3122 (1995).

47. T. Ditmire, M.H.R. Hutchinson, M.H. Key, C.L.S. Lewis, A. MacPhee, I.P. Mercer, D. Neely, M.D. Perry, R.A. Smith, J.S. Wark, and M. Zepf, "Amplification of XUV Harmonic Radiation in a Gallium Amplifier," Phys. Rev. A **51**, R4337 (1995).

48. T. Ditmire, H. Nguyen, and M.D. Perry, "Amplification of Femtosecond Pulses to 1J in Cr:LiSrAlF$_6$," Opt. Lett. **20**, 1142 (1995).

49. T. Ditmire, H. Nguyen, and M.D. Perry, "Design and Performance of a Multiterawatt Cr:LiSrAlF$_6$ Laser System," J. Opt. Soc. Am. B **11**, 580 (1994).

50. T. Ditmire, A. M. Rubenchik, and M.D. Perry, "Monte Carlo Simulation of Laser Plasma Heating in Tunnel Ionized Gas," Phys. Rev. E in preparation for submittal (1995).

51. T. Ditmire and M.D. Perry, "Terawatt Cr:LiSrAlF$_6$ Laser System," Opt. Lett. **18**, 426 (1993).

52. A. Djaoui and A.A. Offenberger, "Heating of Underdense Plasmas by Intense Short-Pulse Lasers," Phys. Rev. E **50**, 4961 (1994).

53. J.F. Drake, P.K. Kaw, Y.C. Lee, G. Schmidt, C.S. Liu, and M.N. Rosenbluth, "Parametric Instabilities of Electromagnetic Waves in Plasmas," Phys. Fluids **17**, 778 (1974).

54. J.H. Eberly and J. Javanainen, "Above-Threshold Ionization," Eur. J. Phys. **9**, 265 (1988).

55. R.C. Elton, "Atomic Processes," in *Plasma Physics,* ed. H.R. Griem and R.H. Lovberg, (New York: Academic Press, 1970),

56. R.C. Elton, *X-Ray Lasers*, (Boston: Academic Press, 1990).

57. J.M. Evans, D.E. Spence, W. Sibbett, B.H.T. Chai, and A. Miller, "50-fs Pulse Generation from a Self-Mode-Locked CrLiSrAlF6 Laser," Opt. Lett. **17**, 1447 (1992).

58. M.E. Faldon, M.H.R. Hutchinson, J.P. Marangos, J.E. Muffett, R.A. Smith, J.W.G. Tisch, and C.G. Wahlstrom, "Studies of Time-Resolved Harmonic Generation in Intense Laser Fields in Xenon," J. Opt. Soc. B **9**, 2094 (1992).

59. J. Farges, M.F.d. Feraudy, B. Raoult, and G. Torchet, "Noncrystalline Structure of Argon Clusters II: Multilayer Icosahedral Structure of Ar_N Clusters 50<N<750," J. Chem. Phys. **84**, 3491 (1986).

60. B.C. Fawcett and A.H. Gabriel, "Resonance Lines of Argon XI and XII and Krypton IX and X," Proc. Phys. Soc. **84**, 1038 (1964).

61. B.C. Fawcett, A.H. Gabriel, B.B. Jones, and N.J. Peacock, "Grazing Incidence Spectra of Highly Ionized Atoms from Laboratory Plasmas," Proc. Phys. Soc. **84**, 257 (1964).

62. M.D. Feit and J.A. Fleck, "Solution of the Schrodinger Equation by a Spectral Method," J. Comp. Phys. **47**, 412 (1982).

63. M. Ferray, A. L'Huillier, X.F. Li, L.A. Lompré, G. Mainfray, and C. Manus, "Multiple-Harmonic Conversion of 1064 nm Radiation in Rare Gases," J. Phys. B: At. Mol. Opt. Phys. **21**, L31 (1988).

64. A.P. Fews, P.A. Norreys, F.N. Beg, A.R. Bell, A.E. Dangor, C.N. Danson, p. Lee, and S.J. Rose, "Plasma Ion Emission from High Intensity Picosecond Laser Pulse Interactions with Solid Targets," Phys. Rev. Lett. **73**, 1801 (1994).

65. D.W. Forslund, J.M. Kindel, and E.L. Lindman, "Theory of Stimulated Scattering Processes in Laser-Irradiated Plasmas," Phys. Fluids **18**, 1002 (1975).

66. P.A. Franken, A.E. Hill, C.W. Peters, and G. Weinreich, "Generation of Optical Harmonics," Phys. Rev. Lett. **7**, 118 (1961).

67. L.M. Frantz and J.S. Nodvick, "Theory of Pulse Propagation in a Laser Amplifier," J. Appl. Phys. **34**, 2346 (1963).

68. R.R. Freeman and P.H. Bucksbaum, "Investigations of Above-Threshold Ionization Using Subpicosecond Laser Pulses," J. Phys. B: At. Mol. Opt. Phys. **24**, 325 (1991).

69. P.M.W. French, R. Mellish, J.R. Taylor, P.J. Delfyett, and L.T. Florez, "Mode-Locked All-Solid-State Diode-Pumped Cr:LiSAF Laser," Opt. Lett. **18**, 1934 (1993).

70. T.E. Glover, J.K. Crane, M.D. Perry, R.W. Lee, and R.W. Falcone, "Measurement of Velocity Distributions and Recombination Kinetics in Tunnel-Ionized Helium Plasmas," Phys. Rev. Lett. **75**, 445 (1995).

71. T.E. Glover, T.D. Donnelly, E.A. Lipman, A. Sullivan, and R.W. Falcone, "Subpicosecond Thomson Scattering Measurements of Optically Ionized Helium Plasmas," Phys. Rev. Lett. **73**, 78 (1994).

72. H. Goldstein, *Classical Mechanics*, (Reading, MA: Addison-Wesley, 1980).

73. S.P. Gordon, T. Donnelly, A. Sullivan, H. Hamster, and R.W. Falcone, "X-Rays from Microstructured Targets Heated by Femtosecond Lasers," Opt. Lett. **19**, 484 (1994).

74. H.R. Griem, *Plasma Spectroscopy*, (New York: McGraw-Hill, 1964).

75. O.F. Hagena, "Cluster Ion Sources," Rev. Sci. Instrum. **63**, 2374 (1992).

76. O.F. Hagena and W. Obert, "Cluster Formation in Expandion Supersonic Jets: Effect of Pressure, Temperature, Nozzle Size, and Test Gas," J. Chem. Phys. **56**, 1793 (1972).

77. R. Haight and D.R. Peale, "Tunable Photoemission with Harmonics of Subpicosecond Lasers," Phys. Rev. Lett. **70**, 3979 (1993).

78. R. Haight and D.R. Peale, "Tunable Photoemission with Harmonics of Subpicosecond Lasers," Rev. Sci. Instr. **65**, 1853 (1994).

79. A.F. Haught and D.H. Polk, "Formation and Heating of Laser Irradiated Solid Particle Plasmas," Phys. Fluids **13**, 2825 (1970).

80. J.R. Houliston, M.H. Key, and I.N. Ross, "Modeling of Saturated Chirped Pulse Amplification and Recompression," Opt. Comm. **108**, 111 (1994).

81. J.T. Hunt, J.A. Glaze, W.W. Simmons, and P.A. Renard, "Suppression of Self-Focusing Through Low-Pass Spatial Filtering and Relay Imaging," Appl. Opt. **17**, 2053 (1978).

82. E.P. Ippen, C.V. Shank, and T.K. Gustafson, "Self-Phase Modulation of Picosecond Pulses in Optical Fibers," App. Phys. Lett. **24**, 190 (1974).

83. J.D. Jackson, *Classical Electrodynamics*, (New York: John Wiley & Sons, 1975).

84. J.R. Janesick, T. Elliott, H.H. Marsh, S. Collins, J.K. McCarthy, and M. Blouke, "Potential of CCDs for UV and X-Ray Plasma Diagnostics," Rev. Sci. Instrum. **56**, 796 (1985).

85. R.D. Jones and K. Lee, "Kinetic Theory, Transport, and Hydrodynamics of a High-Z Plasma in the Presence of an Intense Laser Field," Phys. Fluids **25**, 2307 (1982).

86. L.V. Keldysh, "Ionization in the Field of a Strong Electromagnetic Wave," Sov. Phys. JETP **20**, 1307 (1965).

87. J.H. Kelly, D.C. Brown, and K. Teegarden, "Time Resolved Spectroscopy of Large Bore Xe Flashlamps for Use in Large Aperture Amplifiers," App.Opt. **19**, 3817 (1980).

88. R.L. Kelly, *Atomic and Ionic Spectrum Lines Below 2000 Angstroms: Hydrogen through Krypton*, Vol. 1, (Washington, D. C.: American Chemical Society, 1987).

89. R. Klingelhöfer and H.O. Moser, "Production of Large Hydrogen Clusters in Condensed Molecular Beams," J. Appl. Phys. **43**, 4575 (1972).

90. J.D. Kmetec, C.L.G. III, J.J. Macklin, B.E. Lemoff, G.S. Brown, and S.E. Harris, "MeV X-Ray Generation with a Femtosecond Laser," Phys. Rev. Lett **68**, 1527 (1992).

91. J.D. Kmetec, J.J. Macklin, and J.F. Young, "0.5-TW, 125-fs Ti:Sapphire Laser," Opt. Lett. **16**, 1001 (1991).

92. J.A. Koch, B.J. MacGowan, L.B. DaSilva, D.L. Matthews, J.H. Underwood, P.J. Batson, R.W. Lee, R.A. London, and S. Mrowka, "Experimental and Theoretical Investigation of Neonlike Selenium X-Ray Laser Spectral Linewidths and Their Variation with Amplification," Phys. Rev. A **50**, 1877 (1994).

93. K. Kondo, T. Tamida, Y. Nabekawa, and S. Watanabe, "High-Order Harmonic Generation and Ionization Using Ultrashort KrF and Ti:sapphire Lasers," Phys. Rev. A **49**, 3881 (1994).

94. J.L. Krause, K.J. Schafer, and K.C. Kulander, "High-Order Harmonic Generation from Atoms and Ions in the High Intensity Regime," Phys. Rev. Lett. **68**, 3535 (1992).

95. W.L. Kruer, *The Physics of Laser Plasma Interactions*, (Redwood City: Addison-Wesley, 1988).

96. K.C. Kulander and K.J. Schafer, "Limits on High-Order Harmonic Generation from Single-Atom Calculations," in *Multiphoton Processes,* ed. D.K. Evans and S.L. Chin, (Singapore: World Scientific, 1994), pp. 391-396.

97. A. L'Huillier, T. Auguste, P. Balcou, B. Carré, P. Monot, P. Salières, C. Altucci, M.B. Gaarde, J. Larsson, E. Mevel, T. Starczewski, S. Svanberg, C. Wahlström, R. Zerne, K.S. Budil, T. Ditmire, and M.D. Perry, "High Order Harmonics: A Coherent Source in the XUV Range," J. of Nonlinear Opt. Phys. and Mat. **4**, (1995).

98. A. L'Huillier and P. Balcou, "High-Order Harmonic Generation in Rare Gases with a 1-ps, 1053 nm Laser," Phys. Rev. Lett. **70**, 774 (1993).

99. A. L'Huillier and P. Balcou, "Recent Advances in Strong-Field Harmonic Generation," Las. Phys. **3**, 654 (1993).

100. A. L'Huillier, P. Balcou, S. Candel, K.J. Schafer, and K.C. Kulander, "Calculations of High-Order Harmonic Generation Processes in Xenon at 1064 nm," Phys. Rev. A **46**, 2778 (1992).

101. A. L'Huillier, M. Lewenstein, P. Salières, P. Balcou, M.Y. Ivanov, J. Larsson, and C.G. Wahlström, "High-Order Harmonic Generation Cutoff," Phys. Rev. A **48**, R3433 (1993).

102. A. L'Huillier, L. Lompré, G. Mainfray, and C. Manus, "High-Order Harmonic Generation in Rare Gases," in *Atoms in Intense Laser Fields,* ed. M. Gavrila, (Boston: Academic Press, 1992), pp. 139-202.

103. L.D. Landau and E.M. Lifshitz, *Electrodynamics of Continuous Media*, (Oxford: Pergamon Press, 1984).

104. L.D. Landau and E.M. Lifshitz, *Quantum Mechanics*, (New York: Pergamon, 1965).

105. S.P. LeBlanc, R. Sauerbrey, S.C. Rae, and K. Burnett, "Spectral Blue Shifting of a Femtosecond Laser Pulse Propagating Through a High-Pressure Gas," J. Opt. Soc. Am. B **10**, 1801 (1993).

106. R.W. Lee, "User Manuel to FLY," (1995).

107. T.N. Lee, E.A. McLean, J.A. Stamper, H.R. Griem, and C.K. Manka, "Laser-Driven Soft X-Ray Laser Experiments at NRL," Thirtieth Bull. Am. Phys. Soc. **33**, 1920 (1988).

108. W.P. Leemans, C.E. Clayton, W.B. Mori, K.A. Marsh, P.K. Kaw, A. Dyson, C. Joshi, and J.M. Wallace, "Experiments and Simulations of Tunnel-Ionized Plasmas," Phys. Rev. A **46**, 1091 (1992).

109. B.E. Lemoff and C.P.J. Barty, "Quintic-Phase-Limited, Spatially Uniform Expansion and Recompression of Ultrashort Optical Pulses," Opt. Lett. **18**, 1651 (1993).

110. B.E. Lemoff, G.Y. Yin, C.L.G. III, C.P.J. Barty, and S.E. Harris, "Demonstration of a 10-Hz Femtosecond-Pulse-Driven XUV Laser at 41.8nm in Xe IX," Phys. Rev. Lett. **74**, 1574 (1995).

111. X.F. Li, A. L'Huillier, M. Ferray, L.A. Lompre, and G. Mainfray, "Multiple-Harmonic Generation in Rare Gases at High Laser Intensity," Phys. Rev. A **39**, 5751 (1989).

112. G.J. Linford, E.R. Peressini, W.R. Sooy, and M.L. Spaeth, "Very Long Lasers," Appl. Opt. **13**, 379 (1974).

113. L.A. Lompré, A. L'Huillier, M. Ferray, P. Monot, G. Mainfray, and C. Manus, "High Order Harmonic Generation in Xenon: Intensity and Propagation Effects," J. Opt. Soc. B **7**, 754 (1990).

114. W. Lotz, "Electron-Impact Ionization Cross-Sections and Ionization Rate Coefficients for Atoms and Ions from Hydrogen to Calcium," Z. Phys. **216**, 241 (1968).

115. J.F. Luciani, P. Mora, and J. Virmont, "Nonlocal Heat Transport Due to Steep Temperature Gradients," Phys. Rev. Lett. **51**, 1664 (1983).

116. T.S. Luk, A. McPherson, K. Boyer, and C.K. Rhodes, "Mechanisms of Short Wavelength Generation," in *Atoms in Intense Laser Fields,* ed. M. Gavrila, (Boston: Academic Press, 1992), pp. 207-246.

117. B. MacGowan, S. Maxon, P.L. Hagelstein, C.J. Keane, R.A. London, D.L. Matthews, M.D. Rosen, J.H. Scofield, and D.A. Whelan, "Demonstration of Soft X-Ray Amplification in Nickel-like Ions," Phys. Rev. Lett. **59**, 2157 (1987).

118. B.J. MacGowan, S. Maxon, L.B.D. Silva, D.J. Fields, C.J. Keane, D.L. Matthews, A.L. Osterheld, J.H. Scofield, G. Shimkaveg, and G.F. Stone, "Demonstration of X-Ray Amplifiers Near the Carbon K Edge," Phys. Rev. Lett. **65**, 420 (1990).

119. J.J. Macklin, J.D. Kmetec, and I. C. L. Gordon, "High-Order Harmonic Generation Using Intense Femtosecond Pulses," Phys. Rev. Lett. **70**, 766 (1993).

120. T.H. Maiman, "Stimulated Optical Radiation in Ruby," Nature **187**, 493 (1960).

121. P. Maine, D. Strickland, P. Bado, M. Pessot, and G. Mourou, "Generation of Ultrahigh Peak Power Pulses by Chirped Pulse Amplification," IEEE J. Quant. Elec. **25**, 398 (1988).

122. J.P. Markiewicz and J.L. Emmett, "Design of Flashlamp Driving Circuits," IEEE J. Quant. Elec. **QE-2**, 707 (1966).

123. O.E. Martinez, "3000 Times Grating Compressor with Positive Group Velocity Dispersion: Application to Fiber Compensation in the 1.3-1.6 mm Region," IEEE J. of Quant. Elec. **QE-23**, 454 (1987).

124. D. Matthews, P. Hagelstein, M. Rosen, M. Eckart, N. Ceglio, A. Hazi, H. Medecki, B. MacGowan, J. Trebes, B. Whitten, L. Pleasance, G. Rambach, J. Scofield, G. Stone, and T. Weaver., "Demonstration of a Soft X-Ray Amplifier," Phys. Rev. Lett. **54**, 110 (1985).

125. T.J. McIlrath, P.H. Bucksbaum, R.R. Freeman, and M. Bashansky, "Above Threshold Ionization Processes in Xenon and Krypton," Phys. Rev. A **35**, 4611 (1987).

126. A. McPherson, G. Gibson, H. Jara, U. Johann, T.S. Luk, I.A. McIntyre, K. Boyer, and C.K. Rhodes, "Studies of Multiphoton Production of Vacuum-Ultraviolet Radiation in the Rare Gases," J. Opt. Soc. B **4**, 595 (1987).

127. A. McPherson, T.S. Luk, B.D. Thompson, A.B. Borisov, O.B. Shiryaev, X. Chen, K. Boyer, and C.K. Rhodes, "Multiphoton Induced X-Ray Emission from Kr Clusters on M-Shell and L-Shell Transitions," Phys. Rev. Lett. **72**, 1810 (1994).

128. A. McPherson, T.S. Luk, B.D. Thompson, K. Boyer, and C.K. Rhodes, "Multiphoton-Induced X-Ray Emission and Amplification from Clusters," App. Phys. B **57**, 337 (1993).

129. A. McPherson, B.D. Thompson, A.B. Borisov, K. Boyer, and C.K. Rhodes, "Multiphoton-induced X-Ray Emission at 4-5 keV from Xe Atoms with Multiple Core Vacancies," Nature **370**, 631 (1994).

130. I.P. Mercer, "Ultra Short Pulse Generation For High Intensity Laser Application," Ph.D. Thesis, Department of Physics, Imperial College of Science, Technology, and Medicine, London, UK (1993)

131. E. Mevel, P. Breger, R. Trainham, G. Petite, P. Agostini, A. Migus, J.-P. Chamberet, and A. Antonetti, "Atoms in Strong Optical Fields: Evolution from Mutiphoton to Tunnel Ionization," Phys. Rev. Lett. **70**, 406 (1993).

132. A. Migus, C.V. Shank, E.P. Ippen, and R.L. Fork, "Amplification of Subpicosecond Optical Pulses: Theory and Experiment," IEEE J. Quant. Elec. **QE-18**, 101 (1982).

133. M. Mohan, M.L. Dourneuf, and A. Hibbert, "Electron Impact Excitation of Ar^{8+} From its Ground State," J. Phys. B: At. Mol. Opt. Phys. **24**, 299 (1991).

134. P. Monot, T. Auguste, L.A. Lompré, G. Mainfray, and C. Manus, "Focusing Limits of a Terawatt Laser in an Underdense Plasma," J. Opt. Soc. Am. B **9**, 1579 (1992).

135. P.F. Moulton, "Spectroscopic and Laser Characteristics of Ti:Al_2O_3," J. Opt. Soc. Am. B **3**, 125 (1986).

136. J.E. Muffett, C.-G. Wahlström, and M.H.R. Hutchinson, "Numerical Modelling of the Spatial Profiles of High-Order Harmonics," J. Phys. B **27**, 5693 (1994).

137. M.M. Murnane, H.C. Kapteyn, and R.W. Falcone, "High-Density Plasmas Produced by Ultrafast Laser Pulses," Phys. Rev. Lett. **62**, 155 (1989).

138. M.M. Murnane, H.C. Kapteyn, S.P. Gordon, J. Bokor, E.N. Glytsis, and R.W. Falcone, "Efficient Coupling of High-Intensity Subpicosecond Laser Pulses into Solids," Appl. Phys. Lett. **62**, 1068 (1993).

139. D.M. O'Neill, C.L.S. Lewis, D. Neely, J. Uhomoibhi, M.H. Key, A. MacPhee, G.J. Tallents, S.A. Ramsden, A. Rogoyski, E.A. McLean, and G.J. Pert, "Characterisation of Soft X-Ray Amplification Observed in Ne-Like Germanium," Opt. Comm. **75**, 406 (1990).

140. F.G. Patterson, R. Gonzales, and M.D. Perry, "Compact 10-TW, 800-fs Nd:Glass Laser," Opt. Lett. **16**, 1107 (1991).

141. F.G. Patterson, M.D. Perry, and J.T. Hunt, "Design and Performance of a Multiterawatt, Subpicosecond Neodymium: Glass Laser," J. Opt. Soc. Am. B **8**, 2384 (1991).

142. S. Payne, Lawrence Livermore National Laboratory, Livermore, CA 94550 (1992), personal communication.

143. S.A. Payne, L.L. Chase, L.K. Smith, W.L. Kway, and H.W. Newkirk, "Laser Performance of $LiSrAlF_6$:Cr^{3+}," J. Appl. Phys. **66**, 1051 (1989).

144. S.A. Payne, L.K. Smith, R.J. Beach, B.H.T. Chai, J.H. Tassano, L.D. DeLoach, W.L. Kway, R.W. Solarz, and W.F. Krupke, "Properties of Cr:$LiSrAlF_6$ Crystals for Laser Operation," App. Opt. **33**, 5526 (1994).

145. J. Peatross, M.V. Fedorov, and K.C. Kulander, "Intensity-Dependant Phase-Matching Effects in Harmonic Generation," J. Opt. Soc. Am. B **12**, 863 (1995).

146. J. Peatross and D.D. Meyerhofer, "Angular Distribution of High-Order Harmonics Emitted from Rare Gases at Low Intensity," Phys. Rev. A **51**, R946 (1995).

147. B.M. Penetrante and J.N. Bardsley, "Residual Energy in Plasmas Produced by Intense Subpicosecond Lasers," Phys. Rev. A **43**, 3100 (1991).

148. M.D. Perry, "High-Order Multiphoton Ionization of the Noble Gases," Ph.D. Thesis, University of California, Berkeley, CA, UCRL-53852 (1987).

149. M.D. Perry, C. Darrow, C. Coverdale, and J.K. Crane, "Measurement of the Local Electron Density by Means of Stimulated Raman Scattering in a Laser-Produced Gas Jet Plasma," Opt. Lett. **17**, 523 (1992).

150. M.D. Perry, T. Ditmire, and B.C. Stuart, "Self-Phase Modulation in Chirped-Pulse Amplification," Opt. Lett. **19**, 2149 (1994).

151. M.D. Perry, O.L. Landen, J. Weston, and R. Ettlebrick, "Design and Performance of a High-Power, Synchronized Nd:YAG-Dye Lase System," Opt. Lett. **14**, 42 (1989).

152. M.D. Perry and G. Mourou, "Terawatt to Petawatt Subpicosecond Lasers," Science **264**, 917 (1994).

153. M.D. Perry, F.G. Patterson, and J. Weston, "Spectral Shaping in Chirped-Pulse Amplification," Opt. Lett. **15**, 381 (1990).

154. M.D. Perry, D. Strickland, T. Ditmire, and F.G. Patterson, "Cr:$LiSrAlF_6$ Regenerative Amplifier," Opt. Lett. **17**, 604 (1992).

155. G.J. Pert, "Inverse Bremsstrahlung Absorption in Large Radiation Fields During Binary Collisions -- Classical Theory," J. Phys. A **5**, 506 (1972).

156. H.T. Powell, A.C. Erlandson, and K.S. Jancaitis, "Characterization of High Power Flashlamps and Application to Nd:Glass Laser Pumping," in *Conference on Flashlamp Pumped Laser Technology*, (SPIE, 1986), Vol. 609, p. 78-94.

157. H.T. Powell, A.C. Erlandson, K.S. Jancaitis, and J.E. Murray, "Flashlamp Pumping of Nd:Glass Disk Amplifiers," in *Conference on High-Power Solid State Lasers and Applications*, (SPIE, 1990), Vol. 1277, p. 103-120.

158. W.H. Press, S.A. Teukolsky, W.T. Vetterling, and B.P. Flannery, *Numerical Recipes in C: The Art of Scientific Computing*, (Cambridge: Cambridge University Press, 1992).

159. D.F. Price, R.M. More, R.S. Walling, G. Guethlein, R.L. Shepard, R.E. Stewart, and W.E. White, "Absorption of Ultra-Short Laser Pulses by Solid Targets Heated Rapidly to Temperatures 1-1000 eV," Phys. Rev. Lett. **75**, 252 (1995).

160. S.C. Rae and K. Burnett, "Possible Production of Cold Plasmas Through Optical-Field-Induced Ionization," Phys. Rev. A **46**, 2077 (1992).

161. R. Rankin, C.E. Capjack, N.H. Burnett, and P.B. Corkum, "Refraction Effects Associated with Multiphoton Ionization and Ultrashort-Pulse Laser Propagation in Plasma Waveguides," Opt. Lett. **16**, 835 (1991).

162. J.F. Reintjes, *Nonlinear Optical Parametric Processes in Liquids and Gases*, (Orlando: Academic Press, 1984).

163. N.H. Rizvi, P.M.W. French, and J.R. Taylor, "Generation of 33 fsec Pulses from a Passively Mode-Locked Cr^{3+}:$LiSrAlF_6$ Laser," Opt. Lett. **17**, 1605 (1992).

164. I.N. Ross, J. Boon, R. Corbett, A. Damerell, P. Gottfeldt, C. Hooker, M.H. Key, G. Kiehn, C. Lewis, and O. Willi, "Design and PerFormance of a New Line Focus Geometry for X-Ray Laser Experiments," App. Opt. **26**, 1584 (1987).

165. C. Rouyer, E. Mazataud, I. Allais, A. Pierre, S. Seznec, C. Sauteret, G. Mourou, and A. Migus, "Generation of 50-TW femtosecond pulses in a Ti:Sapphire/Nd:Glass Chain," Opt. Lett. **18**, 214 (1993).

166. A.M. Rubenchik, T. Ditmire, and M.D. Perry, "Theoretical and Experimental Investigation of Phase Modulation Effects in Chirped Pulse Amplification," J. Opt. Soc. Am. B in preparation for submittal (1995).

167. P. Salières, T. Ditmire, K.S. Budil, M.D. Perry, and A. L'Huillier, "Spatial Profiles of High-Order Harmonics Generated by a Femtosecond Cr:LiSAF Laser," J. Phys. B: At. Mol. Opt. Phys. **27**, L217 (1994).

168. P. Salières, A.L. Huillier, and M. Lewenstein, "Coherence Control of High - Order Harmonics," Phys. Rev. Lett. **74**, 3776 (1995).

169. F. Salin, J. Squier, and G. Mourou, "Large Temporal Stretching of Ultrashort Pulses," App. Opt. **31**, 1225 (1992).

170. C. Sauteret, D. Husson, G. Thiell, S. Seznec, S. Gary, A. Migus, and G. Mourou, "Generation of 20-TW Pulses of Picosecond Duration Using Chirped Pulse Amplification in a Nd:Glass Power Chain," Opt. Lett. **16**, 238 (1991).

171. K.J. Schafer, B. Yang, L.F. DiMauro, and K.C. Kulander, "Above Threshold Ionization Beyond the High Harmonic Cutoff," Phys. Rev. Lett. **70**, 1599 (1993).

172. J.F. Seely and E.G. Harris, "Heating of a Plasma by Multiphoton Inverse Bremsstrahlung," Phys. Rev. A **7**, 1064 (1973).

173. R. Sheps, J.F. Myers, H.B. Serreze, A. Rosenberg, R.C. Morris, and M. Long, "Diode-Pumped Cr:$LiSrAlF_6$ Laser," Opt. Lett. **16**, 820 (1991).

174. A.E. Siegman, *Lasers*, (Mill Valley, CA: University Science Books, 1986).

175. V.P. Silin, "Nonlinear High-Frequency Plasma Conductivity," Sov. Phys. JETP **20**, 1510 (1965).

176. D.E. Spence, P.N. Kean, and W. Sibbett, "60-fsec Pulse Generation from a Self-Mode-Locked Ti:sapphire Laser," Opt. Lett. **16**, 42 (1991).

177. L. Spitzer and R. Härm, "Transport Phenomena in a Completely Ionized Gas," Phys. Rev. **89**, 977 (1953).

178. L. Spitzer., *Physics of Fully Ionized Gases*, (New York: Interscience, 1967).

179. M. Stalder, B.H.T. Chai, and M. Bass, "Flashlamp Pumped Cr:$LiSrAlF_6$ Laser," Appl. Phys. Lett. **58**, 216 (1991).

180. D.G. Stearns, O.L. Landen, E.M. Campbell, and J.H. Scofield, "Generation of Ultrashort X-ray Pulses," Phys. Rev. A **37**, 1684 (1988).

181. R.H. Stolen and C. Lin, "Self-Phase-Modulation in Silica Optical Fibers," Phys. Rev. A **17**, 1448 (1978).

182. D. Strickland and G. Mourou, "Compression of Amplified Chirped Optical Pulses," Opt. Comm **56**, 219 (1985).

183. B.C. Stuart, S. Herman, and M.D. Perry, "Chirped-Pulse Amplification in Ti:sapphire Beyond 1 μm," IEEE J. Quant. Elec. **QE-31**, 528 (1995).

184. A. Sullivan, H. Hamster, H.C. Kapteyn, S. Gordon, W. White, H. Nathel, R.J. Blair, and R.W. Falcone, "Multiterawatt, 100-fs Laser," Opt. Lett. **16**, 1406 (1991).

185. J.W.G. Tisch, R.A. Smith, J.E. Muffett, M. Ciarrocca, J.P. Marangos, and M.H.R. Hutchinson, "Angularly Resolved High-Order Harmonic Generation in Helium," Phys. Rev. A **49**, R28 (1994).

186. E.B. Treacy, "Optical Pulse Compression With Diffraction Gratings," IEEE J. Quant. Elec. **QE-5**, 454 (1969).

187. J.B. Trenholme and J.L. Emmett, "Xenon Flashlamp Model for Performance Prediction," in *Proceedings, Ninth International Conference on High Speed Photography*, (SMPTE, 1970), p. 299.

188. C.-G. Wahlström, "High-Order Harmonic Generation," in *X-Ray Lasers 1994*, ed. D.C. Eder and D.L. Matthews, (New York: American Institute of Physics, 1994),

189. C.-G. Wahlström, J. Larsson, A. Persson, T. Starczewski, S. Svanberg, P. Salières, P. Balcou, and A. L'Huillier, "High-Order Harmonic Generation in Rare Gases with an Intense Short-Pulse Laser," Phys. Rev. A **48**, 4709 (1993).

190. W.E. White, J.R. Hunter, L.V. Woerkom, T. Ditmire, and M.D. Perry, "120-fs Terawatt Ti:Al_2O_3/Cr:$LiSrAlF_6$ Laser System," Opt. Lett. **17**, 1067 (1992).

191. W.E. White, A. Sullivan, D.F. Price, J. Bonlie, and R. Stewart, "Production of > 10^{19} W/cm^2 Using 10 TW, 100 fs pulses from a Nd:glass Pumped Ti:sapphire Amplifier," in *CLEO '95*, Baltimore, MD, 1995, talk CPD45-1.

192. S.C. Wilks, W.L. Kruer, E.A. Williams, P. Amendt, and D.C. Eder, "Stimulated Raman Backscatter in Ultraintense, Short Pulse Laser-Plasma Interactions," Phys. Plasmas **2**, 274 (1995).

193. W.M. Wood, C.W. Siders, and M.C. Downer, "Measurement of Femtosecond Ionization Dynamics of Atmospheric Density Gases by Spectral Blueshifting," Phys. Rev. Lett. **67**, 3523 (1991).

194. J. Wörmer, V. Guzielski, J. Stapelfeldt, and T. Möller, "Fluorescence Excitation Spectroscopy of Xenon Clusters in the VUV," Chem. Phys. Lett. **159**, 321 (1989).

195. B.J.C. Wu, P.P. Wegener, and G.D. Stein, "Homogeneous Nucleation of Argon Carried in Helium in Supersonic Nozzle Flow," J. Chem. Phys. **69**, 1776 (1978).

196. K. Yamakawa, H. Shiraga, Y. Kato, and C.P.J. Barty, "Prepulse-free 30-TW, 1-ps Nd:glass Laser," Opt. Lett. **16**, 1593 (1991).

197. Y.B. Zel'dovich and Y.P. Raizer, *Physics of Shock Waves and High-Temperature Hydrodynamic Phenomena*, ed. W.D. Hayes and R.F. Probstein. Vol. 1, (New York: Academic Press, 1966).